# Bioengineered Silk Based 3D Matrices for Skin Regeneration and In Vitro Screening Applications

*A Thesis Submitted in Partial Fulfilment of the*

*Requirements for the Degree of*

**Doctor of Philosophy**

*by*

**Bibrita Bhar**


**Department of Biosciences and Bioengineering**

**Indian Institute of Technology Guwahati**

**Guwahati – 781039, Assam, India**

**August 2024**

**INDIAN INSTITUTE OF TECHNOLOGY GUWAHATI**

**DEPARTMENT OF BIOSCIENCES**

**AND BIOENGINEERING**

## STATEMENT

I do hereby declare that the research findings of this thesis are the result of research work carried out by me in the Department of Biosciences and Bioengineering, Indian Institute of Technology Guwahati, Guwahati, India, under the supervision of Prof. Biman B. Mandal.

As per the general norms of reporting research findings, due acknowledgements have been made, wherever the research findings of other researchers have been cited in this thesis.

Bibrita Bhar

**Date: 08.08.2024** **Bibrita Bhar**

**INDIAN INSTITUTE OF TECHNOLOGY GUWAHATI**

**DEPARTMENT OF BIOSCIENCES**

**AND BIOENGINEERING**

## CERTIFICATE

It is certified that the work described in this thesis entitled "***Bioengineered Silk Based 3D Matrices for Skin Regeneration and In Vitro Screening Applications***" by ***Ms. Bibrita Bhar*** for the award of the degree of **Doctor of Philosophy (Ph.D.)** is an authentic record of the results obtained from the research work carried out under my supervision in the Department of Biosciences and Bioengineering, Indian Institute of Technology Guwahati, India, and this work has not been submitted elsewhere for the award of any other degree.

Bibrita Bhar

**Bibrita Bhar**

(Candidate)

Roll No.: 186106002

**CERTIFIED**

**Biman B. Mandal, Ph.D.**

(Thesis Supervisor)

Date: 8/08/2024

# ACKNOWLEDGEMENTS

*The journey of my Ph.D. has been a tumultuous experience, changing me completely as a person. At times, I can hardly recognize myself, but I have come to realize that everything in life has meaning and purpose. At the end of this journey, I welcome all these changes. I accept the transformation, becoming more confident and readier to endure future turmoil. Reflecting on this juncture of my life, I am deeply appreciative of the support and guidance I received from numerous people on the way of this journey.*

*Foremost, I extend my heartfelt gratitude to my Ph.D. supervisor, Prof. Biman B. Mandal, for providing me with the opportunity and an incredible platform to be part of his research group. He has been a constant driving force in my Ph.D. journey, with his relentless pursuit of excellence and passion for achieving the highest standards. I am deeply grateful for his guidance and mentoring, which pushed me to my limits. I thank him for believing in me even when I doubted myself. His encouragement and support have been invaluable throughout this journey. His critical evaluations and insights, which were unparalleled, helped me become the best version of myself with the confidence to be an independent researcher. The time spent under his guidance throughout my Ph.D. was truly memorable and intensely influential, shaping both my personal and professional growth.*

*I would like to express my sincere gratitude towards my Doctoral committee members: Prof. Roy P. Paily from the Department of Electronics and Electrical Engineering, IITG; Dr. Rajkumar Thummer from the Department of Biosciences and Bioengineering, IITG; and Dr. Akshai Kumar A. S from the Department of Chemistry, IITG. Their invaluable suggestions, inputs, and discussions significantly enriched and refined my thesis work.*

*I would like to express my gratitude to the current and former Heads of the Department of Biosciences and Bioengineering, IIT Guwahati: Prof. Rakhi Chaturvedi, Prof. Latha Rangan, and Prof. Kannan Pakshirajan, for their support across various academic and research endeavours, as well as for departmental instrumentation facilities. I am thankful for the support received from the administrative and technical staff of the Department of Biosciences and Bioengineering, IIT Guwahati, in maintaining and providing research infrastructure. Additionally, I appreciate the assistance and support from the R&D section, Student Affairs, and Academic Affairs, IITG, throughout my Ph.D. tenure. I also acknowledge the Central Instrumentation Facility (CIF) IIT Guwahati for providing high-end instrumentation facilities.*

*I am thankful for the generous funding received from various funding agencies that supported my research studies. Specifically, I express my sincere gratitude to the Ministry of Education (MoE) for providing me with a fellowship throughout my Ph.D. tenure. I am grateful for the funding support from several research grants received by Prof. Mandal from the Department of Biotechnology (DBT), Department of Science and Technology (DST), and Ministry of Electronics and Information Technology (MeitY), Government of India. The support enabled the procurement of necessary consumables and equipment essential for my thesis work.*

*I extend my heartfelt gratitude to all my collaborators: Prof. Samit K. Nandi from West Bengal University of Animal and Fishery Sciences (WBUAFS), Kolkata, India, and Dr. Pavan Kumar Samudrala from National Institute of Pharmaceutical Education and Research Guwahati (NIPER-G) for their assistance in the animal experiments; Dr. Manoj Agarwala from GNRC Institute of Medical Sciences, Guwahati, India, for his help in collecting samples from the hospital. I also acknowledge Prof. Niranjan Karak from the Department of Chemical Sciences, Tezpur University, for our scientific collaborations. Special thanks are due to Dr. Nandana Bhardwaj from the Department of Science and Mathematics, IIIT Guwahati, for her help and scientific advice during my research work.*

*I am deeply grateful to all my lab mates for fostering a positive, collaborative, and scientific environment. They have been integral to my professional, academic, and personal growth, offering constant support through all challenges and achievements. I express my gratitude to all my respected seniors: Dr. Manishekhar Kumar, Dr. Jadi Praveen Kumar, Dr. Dimple Chouhan, Dr. Ankit Gangrade, Dr. Shreya Mehrotra, Dr. Bibhas Kumar Bhunia, Dr. Yogendra Pratap Singh, Dr. Joseph Christakiran Moses, Dr. Janani G. and Dr. Ashutosh Bandyopadhyay for their immense support and guidance throughout my journey. Their presence made the journey truly enjoyable and fulfilling. I extend my heartfelt thanks to all my current labmates: Chitra, Souradeep, Sayanti, Kodieswaran, Rajat, Sanu, Maheswari, Pooja, Victoria, Komal, and my former lab mates Dr. Rajiv, Dr. Aparajita, Dr. Chandramouli, Dr. Bhaskar, Dr. Priyanka, Dr. Avipsa, Dr. Namit, Suvro, Monisha, Sakshi, Princy, Priyanka, Sangeetha, Anupam, Nakhul, Vaishali, Swapnil, Rupam, Shubham, Saptarshi, Amritha, Vartik, Himanjal, Anushka, Shruti, Varnit, Pragya, Eshani, Sayantanee, Baishali, Animesh, Ananya, Saki, Richa, Ravi, Arnab, and Aman. I am deeply thankful for the camaraderie, valuable scientific insights, engaging discussions, and the countless memories we created together, all of which I will cherish forever. I would also like to extend my special thanks to Dr. Rajan singh (IITG), Bijayshree Chakraborty (WBUAFS), and Vaishak Kundudi Ramesh (WBUAFS) for their collaborations and help in research work.*

*I take this opportunity to express my gratitude to all my teachers throughout my life, whose guidance has brought me to where I am today. I also extend my heartfelt thanks to all my friends who supported my emotional well-being; without their help, I would not have come this far.*

*Finally, I would be indebted to my parents and other family members for their constant support. Maa, Baba, and Dada, your sacrifices, encouragement, and unconditional love have been the bedrock of my journey. I am immensely grateful for every moment we have shared, navigating challenges and celebrating triumphs together, which gave me the strength to persevere through this challenging journey. This endeavour would not have been possible without the support from my life partner, Soham. I am forever grateful for his love and motivation during vulnerable times and for being my pillar of strength.*

*I thank the creator of the universe for all the blessings from the outset and for guiding my path in life.*

***-Bibrita Bhar***

# THESIS ABSTRACT

Skin tissue serves as a critical protective barrier of our body against external factors, including pathogens, as well as thermal, mechanical, and chemical influences. The tissue is susceptible to various injuries, ranging from minor cuts and burns to chronic wounds, including diabetic ulcers and pressure sores. The non-healing chronic wounds pose a significant threat as they lose their self-repair ability and may lead to severe consequences if not treated timely. To address this urgent issue, we developed pro-regenerative matrices to meet the growing demand. This thesis presents possible silk-based strategies for fabricating matrices with inherent properties to support the growth of skin cells and accelerate regeneration. The developed silk-based hydrogel systems contained different biological molecules including extracellular matrix and phytochemicals which acted as instructive biochemical cues to accelerate the healing process. In addition, a breathable electrical bandage patch was developed as an active secondary dressing alongside the SF hydrogel. The patch provided low-intensity electrical pulses to the wound site through a silk-based antimicrobial ionogel interface. The promising outcomes of the *in vitro* and *in vivo* validations indicate immense translational potential of developed technologies for wound care. Further, reinforcing the understanding of the unique properties of SF hydrogel, the final objective focused on synthesizing a photopolymerizable SF-bioink for bioprinting. The formulation was utilized to fabricate a pre-clinical 3D bioprinted immunocompetent skin model which effectively classified skin irritative and non-irritative substances, thus establishing itself as a suitable rapid screening platform for skin sensitization tests. Therefore, along with SF-based regenerative strategies, the innovative technology of developing 3D skin models, demonstrated in the thesis, possess great promise for significant advancement in wound care technology and *in vitro* skin tissue modelling.

# Table of contents

# Abbreviations

| | | |
|---|---|---|
| 3D | : | 3-dimentional |
| AaSF | : | *Antheraea assamensis* silk fibroin |
| AgNPs | : | Silver nanoparticles |
| ANOVA | : | Analysis of variance |
| bFGF | : | Basic fibroblast growth factor |
| BmSF | : | *Bombyx mori* silk fibroin |
| BSA | : | Bovine serum albumin |
| CAD | : | Computer-aided design |
| CAM | : | Calcein-AM |
| CCR7 | : | C-C chemokine receptor type 7 |
| CD206 | : | Cluster of Differentiation 206 |
| CD31 | : | Cluster of differentiation 31 |
| CD68 | : | Cluster of differentiation 68 |
| cDNA | : | Complementary deoxyribonucleic acid |
| CK | : | Cytokeratin |
| cm | : | Centimeter |
| Col | : | Collagen |
| DAPI | : | 4′,6-diamidino-2-phenylindole |
| dECM | : | Decellularized extracellular matrix |
| DLP | : | Digital light processing |
| DMEM | : | Dulbecco's modified eagle medium |
| DMMB | : | 1,9-dimethylmethylene blue |
| DNA | : | Deoxyribonucleic acid |
| ECM | : | Extracellular matrix |
| ELISA | : | Enzyme-linked Immunosorbent Assay |
| EthD-1 | : | Ethidium homodimer-1 |
| FBS | : | Fetal bovine serum |
| FDA | : | Food and Drug Administration |
| FESEM | : | Field emission scanning electron microscope |
| FITC | : | Fluorescein isothiocyanate |

| | | |
|---|---|---|
| FTIR | : | Fourier transform infrared spectroscopy |
| g | : | gm |
| G′ | : | Storage modulus |
| G″ | : | Loss modulus |
| GelMA | : | Gelatin methacrylate |
| h | : | Hour |
| H&E | : | Hematoxylin and eosin |
| HCl | : | Hydrochloric acid |
| HDF | : | Human dermal fibroblasts |
| HEK | : | Human epidermal keratinocytes |
| HEMn | : | Human epidermal melanocytes |
| HUVEC | : | Human umbilical vein endothelial cells |
| IHC | : | Immunohistochemistry |
| IL-10 | : | Interleukin-10 |
| IL-1β | : | Interleukin-1β |
| IL-6 | : | Interleukin-6 |
| iPSC | : | Induced pluripotent stem cells |
| kDa | : | Kilodalton |
| kPa | : | Kilopascal |
| LAP | : | Lithium phenyl-2,4,6-trimethylbenzoylphosphinate |
| LiBr | : | Lithium bromide |
| M | : | Molar |
| MBC | : | Minimal bactericidal concentration |
| mg | : | Milligram |
| MIC | : | Minimum inhibitory concentration |
| min | : | Minute |
| mL | : | Milliliter |
| MMPs | : | Matrix metalloproteinases |
| mRNA | : | Messenger ribonucleic acid |
| MSCs | : | Mesenchymal stem cells |
| MT | : | Masson's trichrome |
| NCCS | : | National Centre For Cell Science |
| NF-κB | : | Nuclear factor kappa B |

| | | |
|---|---|---|
| nm | : | Nanometer |
| O.D. | : | Optical density |
| PBS | : | Phosphate buffered saline |
| PCL | : | Polycaprolactone |
| PDGF | : | Platelet-derived growth factor |
| PLA | : | Polylactic acid |
| PLGA | : | Poly(lactic-co-glycolic) acid |
| PPR | : | Photoactivated platelet releasate |
| RGD | : | Arg-Gly-Asp |
| s | : | Second |
| SDS | : | Sodium dodecyl sulfate |
| SF | : | Silk fibroin |
| sGAG | : | Sulfated glycosaminoglycan |
| SilkMA | : | Silk fibroin methacrylate |
| UNT | : | Untreated |
| UTS | : | Ultimate tensile strength |
| VEGF | : | Vascular endothelial growth factor |
| WVTR | : | Water vapour transmission rate |
| µg | : | Microgram |
| µL | : | Microliter |
| µm | : | Micrometer |
| µM | : | Micromolar |
| % | : | Percentage |

# List of Figure

**Appendix**

# List of Tables

# Chapter 1: Introduction and review of literature

*The chapter provides a comprehensive overview of the current status of skin tissue engineering. The introduction details the cellular composition and functions of different skin layers, discusses skin injuries, and outlines the thesis objectives. The literature review highlights the shift from conventional to advanced dressing materials, focusing on the significance of silk proteins from mulberry and non-mulberry sources. The review includes relevant cellular strategies, the impact of exogenous growth factors application, and innovative approaches such as nanotherapeutics, wearable devices, and 3D bioprinting. The importance of 3D bioprinted in vitro skin models is highlighted, showcasing their potential to mimic the complex structure and function of native skin tissue for drug testing, disease modeling, and personalized medicine. The clinical relevance and future trajectory of these advancements are emphasized, underlining their potential to provide cost-effective and efficient skin regenerative solutions, ultimately improving the outcomes and quality of life of patients. Lastly, the chapter outlines the motivation and objectives of the research, aiming to advance the field of skin tissue engineering by developing more effective and innovative solutions for skin regeneration.*

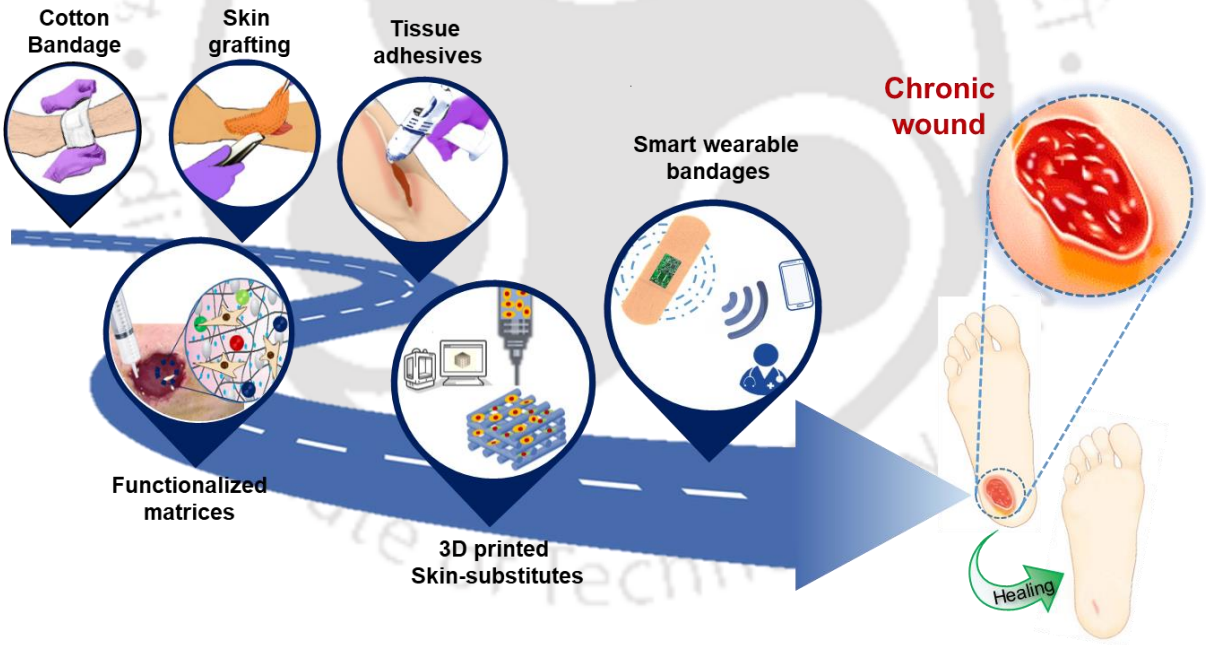


***Parts of this chapter have been published as:***

Bibrita Bhar, Dimple Chouhan, Nakhul Pai, and Biman B Mandal. "**Harnessing Multifaceted Next-Generation Technologies for Improved Skin Wound Healing**." *ACS Applied Bio Materials*. 2021;4(11):7738-63.

Reprinted (adapted) here with permission from *ACS Applied Bio Materials* (American Chemical Society), Copyright 2021.

## 1.1. Introduction

The skin is the largest organ of the body, constituting ~15% of total body weight and encompassing an area of 1.8 $m^2$ [1]. This substantial organ is responsible for numerous critical functions. It plays vital roles in sensation, preventing dehydration, temperature regulation, and most importantly, it acts as a physical barrier protecting internal organs from the external environment [2, 3]. It consists of three distinct layers: epidermis, dermis, and hypodermis (**Figure 1.1**.). The primary component of the epidermis is keratinocytes, which form a keratinized stratified squamous epithelium. The proliferating keratinocytes reside in the basal layer at the bottom of the epidermis, directly in contact with the basement membrane that separates the dermis from the epidermis. Through a sequential terminal differentiation process, these proliferative cells generate the stratified epidermis, resulting in the formation of corneocytes and lipid lamellae that constitute the barrier of the epidermal stratum corneum [4]. In addition, skin pigmentation is essential for efficient photoprotection and relies on melanin, a pigment produced by epidermal melanocytes and transferred to surrounding keratinocytes [5]. The epidermis also possesses several minor cell populations, comprising immune cells such as Langerhans cells and T-cells, along with nerve endings and glandular ducts. The dermis, located underneath the epidermis, is thick and fibrous and consists of protein fibers (collagen and elastin), glycosaminoglycans (GAG), and different types of cells such as fibroblasts, dermal dendrocytes, histiocytes, and mast cells [6]. This layer contains macrostructures, which include blood vessels, lymphatics, nerves, and appendages (sebaceous glands, hair follicles, and tactile corpuscles). Dermis maintains hydration and immunological response of skin and also functions as an insulator, thermosensor, and mechanosensor. The hypodermis, or the subcutaneous tissue, is the innermost layer and contains adipocytes, nerves, and blood vessels. It functions as a nutrient reservoir, shock absorber, and insulator [6]. The multi-layered anatomy of skin reflects the functional/physiological importance of the organ in the body. Nonetheless, skin as the outer covering of the body is prone to frequent injury. Skin wound is defined as a type of injury that causes the breakdown of the protective function of the skin due to loss of continuity of epidermis, with or without loss of underlying dermis, subcutaneous fat, fascia, and muscle layer. Skin injury can also be caused by blunt force trauma/genetic illness when epidermal continuity remains undisturbed but underlying layers are damaged. Additionally, intense thermal exposure can cause severe burn injury to the skin and the underlying tissue layers. The healing rate of these injuries depends on multiple factors, such as size, depth, and location of the wound, patient age, and the presence of local or systemic

disease [7]. Clinicians primarily aim for closure of the wound edges via suturing or using adhesives. The edges of the wounds with large size and depth cannot be closed with these strategies. These wounds remain open and heal by slowly being filled with new granulation tissue. Therefore, after injury, regeneration of the skin is essential for maintaining skin integrity and preventing infections to protect the internal organs. Tissue engineering focuses on developing advanced therapies to achieve effective tissue regeneration. Skin tissue engineering encompasses two primary domains: the fabrication of advanced wound dressings and the development of *in vitro* skin models. These two areas address distinct challenges yet possess interconnected aspects of skin tissue characteristics. Bioengineered wound dressings aim to provide effective and tailored solutions for promoting wound healing, often incorporating biomaterials with bioactive properties to facilitate tissue repair. In contrast, *in vitro* models serve as advanced platforms for studying skin biology, disease mechanisms, and drug testing, offering valuable insights into skin physiology and pathology. Through the integration of biological and engineering principles, skin tissue engineering addresses the challenges associated with skin injuries by developing advanced biomaterials, tissue-engineered constructs, and *in vitro* models that mimic the complexity of native skin tissue.

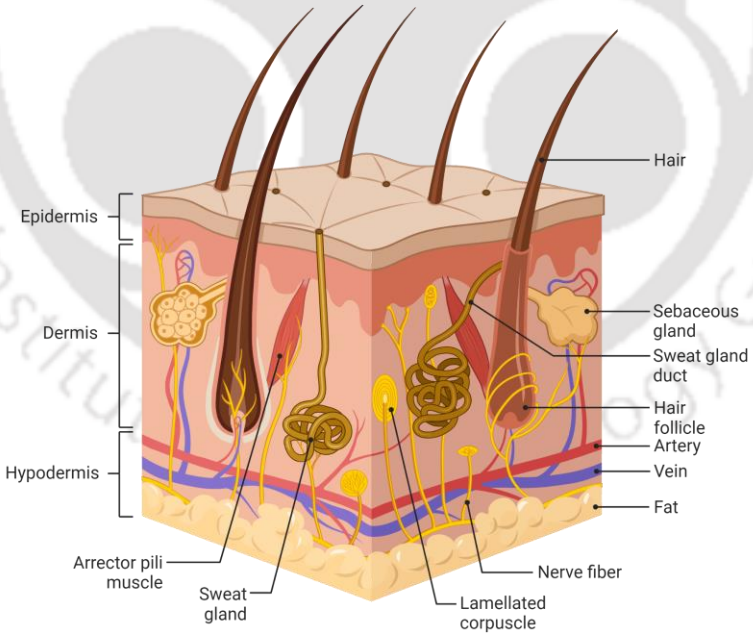


***Figure 1.1.*** *Diagram of the three-dimensional (3D) structure of skin tissue, consisting of three primary layers: epidermis, dermis, and hypodermis. The tissue comprises various important structures, including blood capillaries (arteries and veins), hair follicles, sebaceous glands, and sweat glands, that play major roles in the functions of the tissue. Created with BioRender.com.*

The current treatment regimen primarily relies on regular cleaning of the wound site for removal of debridement, topical/systemic administration of antibiotics, and covering the wound to eliminate the chance of further infection. Therefore, conventional wound management requires improvements in order to ensure more interactive therapeutics to boost the specific events of the healing cascade. Biomaterials offer a promising avenue for improving conventional wound management strategies. A range of natural and synthetic biomaterials have been explored for this purpose. The most commonly used natural biomaterials include fibrin, collagen, gelatin, silk, chitosan, and hyaluronic acid [8, 9]. Products using allogenic or xenogeneic cadaveric grafts are also commercially available; however, they have drawbacks of disease transmission, immune rejection, short shelf-life, and high maintenance cost [10]. To address the problems, numerous biomaterials have been explored with the goal of developing safe, affordable, but efficient strategies with better healing potential. Among various biopolymers, natural materials are preferred over synthetic materials because natural materials are biocompatible and biodegradable, and they tend to mimic the extracellular matrix (ECM) more efficiently than synthetic polymers [9]. Silk, a versatile protein biopolymer produced by various insects such as silkworms, spiders, scorpions, mites, and flies, has a rich history of use in surgery due to its biocompatibility and exceptional tensile strength. Over recent decades, silk has emerged as a promising biomaterial for tissue engineering applications, particularly regenerated silk fibroin (SF) sourced from *Bombyx mori* silkworm cocoons. FDA-approved silk-based bioengineered products, including SERI surgical scaffold® and Silk Voice® highlight its potential in regenerative medicine. With characteristics such as biocompatibility, tunable biodegradation, and remarkable mechanical strength, silk can be adapted into various formats like 3D scaffolds, hydrogels, and nanofibers, making it an attractive option for tissue engineering. Besides physical properties, SF also possesses cell-interactive properties crucial for healing and tissue regeneration. Certain varieties of silk, such as non-mulberry SF, contain cell binding motifs, Arg-Gly-Asp (RGD) tripeptide, which facilitates cell attachment and migration through integrin receptors [11]. SF is easily blendable with other natural and synthetic polymers, enabling the fabrication of composite materials with enhanced functionalities. As a newly explored biomaterial, non-mulberry silk holds immense promise, offering new avenues for research and discovery in the field of wound healing applications. Blending silk from different sources presents an opportunity to enhance the properties of the matrices based on requirements.

The thesis presents strategies to develop wound dressings using various SF varieties to fabricate different matrices to support cellular growth and ECM remodeling for skin regeneration and *in vitro* modelling. Initially, it details the fabrication of composite matrices from both mulberry (*Bombyx mori*) and non-mulberry (*Antheraea assamensis*) silk proteins. A decellularized extracellular matrix (dECM) was isolated from porcine omentum tissue for integration of dECM scaffold in the composite SF hydrogel system comprising both varieties of SF proteins. The fabrication approach aimed to combine the properties of SF hydrogel with the structural support provided by the collagenous ECM scaffold, offering a synergistic solution for addressing the problems associated with diabetic wounds. In order to achieve sustained delivery of bioactive molecule with long term stability, a silk-aloe composite matrix was developed, where these SF varieties blended with *Aloe vera* mucilage extract to formulate a delivery system for aloe phytochemicals molecules for the treatment of full-thickness wounds in a cost-effective manner. The SF formulation then further utilized to fabricate a SF-based electro-conductive hydrogel. An electrical bandage was applied on the SF hydrogel for efficient conduction of electrical pulses at the wound site. Therefore, the thesis also explored the potential of pulsed electrical stimulation (ES) at the wound site through the development of a wearable electrical bandage. The combined platform demonstrated rapid wound closure and regeneration in the full-thickness wound model. Continuing the exploration of silk-based innovations, the last objective focuses on synthesizing a photopolymerizable SF-based bioink for the bioprinting of an *in vitro* skin model. The study not only offers a new direction for skin tissue research but also provides invaluable insights into skin sensitization assessments, thereby providing new opportunities for *in vitro* screening in pharmaceutical studies. The detailed studies are organized into different chapters, which will be followed by an extensive review of the literature pertinent to the current research area. The literature review provides a detailed examination of the evolution of materials and technologies used in skin tissue engineering, emphasizing the shift from conventional to advanced biomaterials. Specifically, silk proteins from mulberry and non-mulberry sources are highlighted for their unique properties, including biocompatibility, mechanical strength, and support for cellular adhesion and proliferation. The review discusses various cellular strategies, including the use of keratinocytes, fibroblasts, and stem cells and the incorporation of exogenous growth factors to enhance tissue regeneration at the wound site. The advanced technologies comprising nanotherapeutics, smart bandages, and 3D bioprinting are explored for their potential to improve treatment efficacy. The review highlights the promise of 3D bioprinted *in vitro* skin models for drug testing, disease modeling, and personalized medicine, highlighting the clinical relevance and future potential of these advancements in improving patient outcomes and quality of life.

# *Review of literature*

## 1.2. Review of literature

The highly regulated wound healing mechanism consists of a sequence of progressive events, namely, hemostasis, inflammation, proliferation, and tissue remodelling (**Figure 1.2**) [12]. Superficial or epidermal injuries possess self-repair potential, and the healing cascade normally runs without any failure. After the injury, a blood clot covers the wound site, which acts as a natural provisional matrix that ultimately helps in the recruitment of various cells [13, 14]. The clot consists of a fibrin matrix, which aids in the sequestration of growth factors and thus supports cell adhesion, migration, and proliferation. The fibrin clot also helps in the slow release of sequestered growth factors and cytokines during the complete course of healing [13, 14]. Naturally, the wound milieu stimulates and regulates the healing progression through instructive biochemical cues and various types of cells under normal physiological conditions. During inflammation, neutrophils, macrophages, and lymphocytes clear debris and prevent infection. Subsequently, in the proliferation phase, fibroblasts synthesize collagen, angiogenesis forms new blood vessels, and keratinocytes re-epithelialize the wound. Finally, during the tissue remodeling phase, collagen fibers undergo maturation, enhancing the tensile strength of the newly formed tissue. Concurrently, myofibroblasts facilitate wound contraction, reducing the wound size. Matrix metalloproteinases (MMPs) play a crucial role in balancing matrix synthesis and degradation, thereby ensuring the restoration of proper tissue architecture

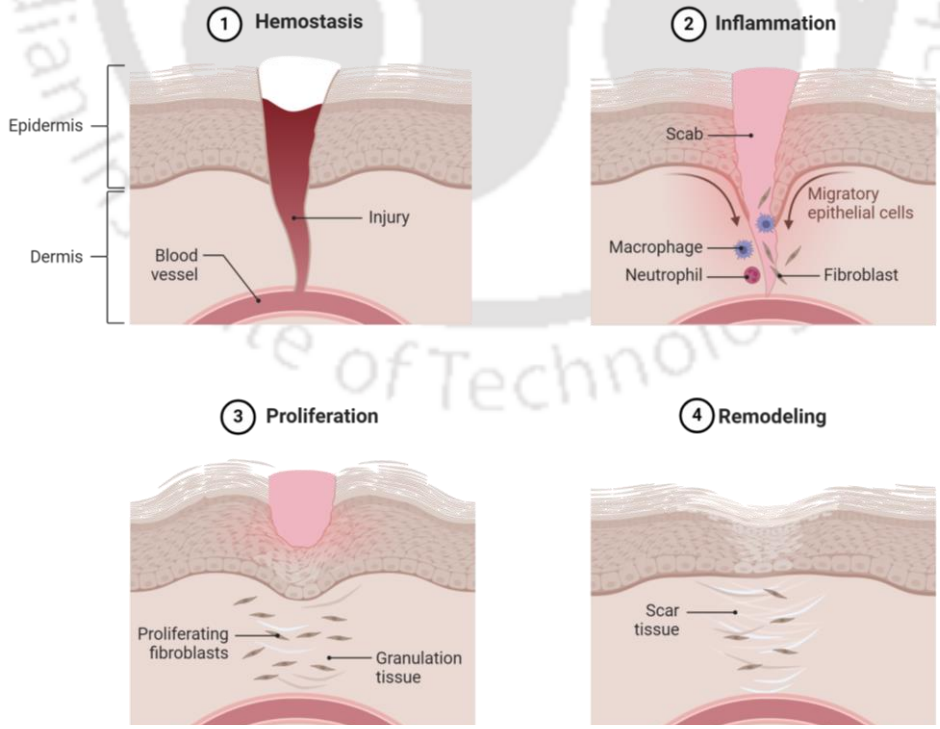


***Figure 1.2.*** *Schematic illustration of different stages of wound healing process. Created with Biorender.com.*

and function. Usually, the wounds that do not heal within 12 weeks are classified as chronic wounds [15]. These wounds predominantly affect the elderly and individuals with diabetes, are highly common, and pose a significant socioeconomic challenge. Various factors can impair the healing process. Broadly, these factors are divided into local and systemic categories. The local factors directly impact the wound characteristics, while systemic factors pertain to the overall health or disease state of the patient. Many of these factors are interconnected, with systemic factors affecting wound healing through their local effects (**Figure 1.3**). Therefore, influencing these local factors using active wound dressing can aid to restore the healing process. The biomimetic approaches inducing the natural healing mechanism has been considered efficient for the treatment of non-healing wounds in comparison to conventional therapies. Researchers have adapted the strategy to mimic the microenvironment of spontaneous healing wounds with the help of bioactive molecules and the structural framework of scaffolds in the form of smart dressing materials [16-18]. The essential factors for the fabrication of dressing materials include their ability to stop bleeding, absorb wound exudates, offer easy debridement of necrotic tissue, provide barrier properties against pathogens, and permeability to gases and water vapor [19].

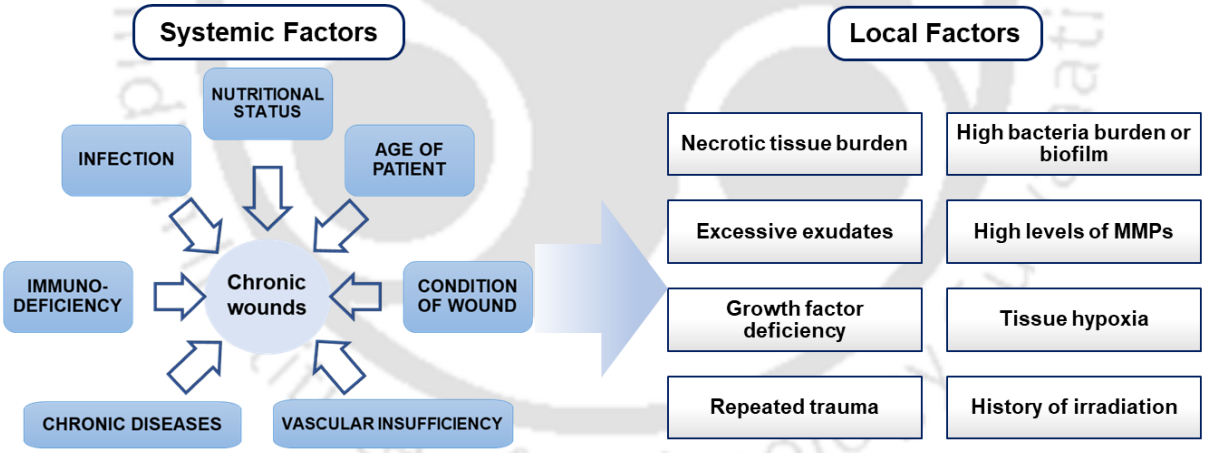


***Figure 1.3.*** *The systemic and local factors affecting healing process, which leads to generation of chronic wounds.*

### 1.2.1. The evolution of wound dressings

The ancient wisdom for wound management had been highlighted by many historians. Natural materials such as plant fibers (mostly cotton), animal fats, and honey pastes were regularly used in the past as bandages [20]. Johnson and Johnson developed the first commercial product using sterilized cotton yarn in 1891 [21]. Similar products have been widely used in the form of temporary dressings or for cleaning wounds. The cotton gauze is a sheer woven mesh, mostly

used to manage wound exudates because of its highly absorbent nature [22]. Its adherence to wound tissue led to the need for the impregnation of cotton fibers with petroleum or paraffin-like materials to reduce painful hassle while changing dressings. Other than cotton, synthetic or semisynthetic woven bandages made up of lyocell, viscose, cellulose acetate, polypropylene, polyethylene terephthalate (PET), and polyurethane (PU) are commonly used in commercially available bandages. In general, a usual bandage contains three basic layers: a wound contact layer, an absorbent pad, and a base material/adherent tap. The wound contact layer or primary dressing needs to maintain moisture level, permits gaseous exchange, and aids in epithelial migration. Multiple formats of primary wound dressings, such as thin films, porous sponges, hydrogels, and nanofibrous mats, have been developed for specific types of wounds [19, 22]. Semi-permeable thin films are commonly used for the management of minor burns, small injuries such as skin tears, abrasions, and lacerations, and partial-thickness wounds as well. These films are mostly made of synthetic polymers and are used to provide barrier properties to wounds to prevent pathogenic infection and dehydration. Although these film dressings allow the exchange of water vapor and gases, these are not appropriate for application on wounds with excess exudate; injudicious use can cause maceration of surrounding skin. Additionally, hydrocolloids and hydrogel-based dressings are being utilized to provide a moist environment at the wound bed [11, 21]. Alginate-based hydrocolloid dressings have been widely explored for heavily exudating wounds to absorb excessive exudates and keep the wound bed moist [23-25]. Hydrogel-based dressings provide a long-term moist environment to the necrotic burn tissue and trigger the cells towards a healing pathway [11, 26].

However, highly exudating wounds are difficult to manage by occlusive dressings because of excessive exudate accumulation in wounds. Exudate accumulation in the wounds and their leakage further attract bacterial infections [21]. In such cases, semi-occlusive dressings are beneficial as they provide optimum moisture properties along with barrier properties [27]. Fibrous matrices are semi-occlusive in nature and transport gases and moisture [27]. These dressings provide a large exposed surface area and porous ECM-like fibrous structure, favorable for cellular recruitment and attachment. These fibers can be generated via several techniques such as template-assisted synthesis [28], self-assembly [29], chemical vapor deposition [30], centrifugal spinning [31], wet/dry spinning [32], and electrospinning [33]. Among these fabrication methods, the spinning process has dominated the field of research, where viscous polymer solution is ejected through a spinneret to generate continuous filament. Advances in the fabrication of fibrous matrices using various natural and synthetic polymers

perfectly demonstrate successful transition in the development of porous substrates for providing required moisturization and aeration [34-36]. Wet/dry spinning is usually used to fabricate fibers with a diameter in the micrometer range, while electrospinning and centrifugal spinning can generate fibers in the nanometer range [37]. The properties of electrospun matrices such as morphology, distribution, and diameter size of the fibers are highly tunable and can be adjusted according to the properties of the polymer solution, process parameters, amount of applied voltage [38]. Unlike electrospinning, the jet formation of polymer is generated by centrifugal force instead of a high-voltage electric field [31]. Centrifugal spinning is a cost-effective alternative to electrospinning. The high rotational speed of centrifugal spinneret offers fast and scalable fiber fabrication required for high producibility in industrial applications [31]. These fibers have been incorporated with different types of bioactive molecules like antibiotics, growth factors, and other small molecules to further improve the functionality of the fibrous dressings [39]. Another format of semi-occlusive dressings is widely used foam dressing. Foam dressings are typically comprised of a non-adherent, hydrophilic PU-based wound contact surface with a semi-permeable hydrophobic backing. PU foam is highly absorbent and works as a wick for wound fluids, making it ideal for wounds with a lot of exudates [40]. Physical absorption allows wound fluid to enter the open pores of the foam structure and facilitates its uniform dispersion throughout the absorbent layer. An additional soft silicone wound contact layer is now incorporated in commercially available foam dressings. This layer is adhesive to peri-wound skin tissue; therefore, it ensures no leakage of wound exudate from the edges. However, it does not adhere to the wound bed, providing a less painful dressing removal [41]. Some foam dressings contain antibacterial agents such as silver and have been shown to reduce the microbial bioburden in wounds and shorten recovery time [42]. The current treatment regimen primally relies on regular cleaning of the wound site for removal of debridement, management of wound exudate, topical/systemic administration of antibiotics, and covering the wound to eliminate the chance of further infection. Therefore, conventional wound management requires improvements in order to ensure more interactive therapeutics to boost the specific events of the healing cascade.

### 1.2.2. Biomaterials for skin tissue engineering

Advances in biomaterials have boosted the field by developing various active wound dressings for deep open wounds or severe burns. For instance, the bioengineered substitutes are designed to not only provide barrier properties but also offer physical support for tissue regeneration. Matrices for skin regeneration are mostly designed using a 3D framework of hydrogels or

porous scaffolds, or nanofibrous mats, which integrate well with the tissue [43]. The 3D framework and interconnected pores provide a microenvironment that helps in the spatial distribution of cells for cellular growth, thereby guiding the development of neo-tissue on the framework [43]. Other physical properties such as biocompatibility, biodegradability, mechanical properties, and inherent architecture play major roles in the regeneration process [44]. The platform of constructs should be designed to offer cell recruiting properties to promote the migration of host cells toward the wound cavity. Therefore, the matrices are often designed to confer a physical connection between cells and material by modulating the surface properties, porosity, and mechanical strength [26]. A list of desired properties of biomaterials required for skin tissue engineering applications is presented in **Table 1.1**. To introduce these designed constructs in wound care market, the material needs to possess several desirable properties such as cost-effectiveness, easy handling, off-the-shelf availability, longer shelf-life, and high scalability. The recently developed matrices have explored applications of various biomaterials.

**Table 1.1.** Desired properties of biomaterials for skin regeneration [44-46].

| Property | Effect on Regeneration |
|---|---|
| **Biocompatibility** | The materials should interact with biological systems without causing harm. They should not trigger adverse reactions within biological systems. |
| **Biodegradability** | Biomaterials should break down slowly over time; the rate of degradability should match the regeneration of the following injury. They should be broken down into non-toxic components. |
| **Microarchitecture** | Interconnective ECM-mimicking microarchitecture is important to determine cell growth and tissue regeneration. |
| **Porosity** | The materials should have an interconnected porous structure to facilitate cell migration, nutrient flow, and waste removal. |
| **Mechanical Strength** | The biomaterials should possess mechanical properties similar to native skin. They should withstand the physiological forces at the wound site without premature breaking down, thus maintaining structural integrity during the healing process. |
| **Hydrophilicity** | They should maintain a moist environment to promote cell proliferation and migration. |
| **Shelf-life Stability** | The materials should be stable during storage, maintaining their properties until use. |

| | |
|---|---|
| **Ease of application** | The biomaterials should be easy to apply and conform to the wound site, providing comfort to the patient. |
| **Cost-effectiveness** | The biomaterials should be affordable to produce and use, ensuring accessibility for widespread clinical application. |

By exploring the unique properties of these biomaterials, researchers have been able to design innovative and effective wound care solutions. These advancements have been made possible by utilizing materials from diverse sources, each offering distinct advantages in the regeneration process. A list of natural and synthetic polymers being utilized in this field is presented in **Table 1.2**. The synthetic polymers are generally easier to customize to achieve desired mechanical properties and degradability. However, their use is limited by the absence of cell attachment motifs and the production of acidic degradation products [47]. In contrast, matrices derived from natural polymers are often better adapted and tolerated within the host body due to the presence of intrinsic biological cues and cell binding motifs, making them preferable for various biomedical applications.

**Table 1.2.** Details of widely used biomaterials for skin tissue engineering applications.

| Type | Material | Sources | Form | Findings | Ref |
|---|---|---|---|---|---|
| Natural | Fibrin glue | Derived from fibrinogen, a blood plasma protein, often from human or animal sources | Suspension, gel, membrane | Enhances wound closure and speeds up re-epithelialization | [48, 49] |
| | Collagen | Derived from animal tissues from bovine, porcine, rodents | Reinforced scaffolds, gels, electrospun dressings | Enhances early wound healing, accelerates wound closure | [50, 51] |
| | Gelatin | Derived from collagen by partial hydrolysis | Membrane, wound dressings, bilayered graft | Promotes re-epithelization and enhances neovascularization | [52-54] |
| | Chitosan | Derived from chitin, primarily found in the exoskeletons of crustaceans | Bio-inspired bi-layered hydrogels, Nano-membrane | Increases biostability of nanofibrillar dressings, aids stem cell delivery and wound healing | [55, 56] |

| | | | | | |
|---|---|---|---|---|---|
| | Hyaluronic acid | Derived from various sources such as rooster combs, human placenta, bacterial fermentation | Hydrogel based system, nanofibrous mats | Facilitates cytokine and growth factor release, improves wound healing | [57, 58] |
| | Silk fibroin | Derived from the silk of silkworms, spiders | Electrospun mats and bi-layered dressings, hydrogels | Improved re-epithelialization, wound closure, biological functions | [59, 60] |
| Synthetic | PCL | Derived from the chemical polymerization of caprolactone | Electrospun dressings | Facilitates healing of chronic wounds | [61] |
| | Polyurethane | Derived from the chemical reaction of diisocyanates and polyols | Nanofibrous mats, membranes | Enhances wound healing and re-epithelialization in diabetic wounds | [62, 63] |
| | Polyglycolic acid/poly lactic acid | Derived from the polymerization of glycolic acid and lactic acid | Nanofibrous mesh, knitted membrane | Improves healing of full-thickness diabetic foot ulcers | [64, 65] |
| | Polyvinyl alcohol (PVA) | Derived from the polymerization of vinyl acetate, followed by hydrolysis | Electrospun wound dressings, membranes | Enhances healing in full-thickness dermal defect models | [66, 67] |

### 1.2.3. Silk as biomaterial for skin tissue engineering

Silk is a protein polymer that is produced by a range of insects, including silkworms, spiders, mites, flies, and scorpions [68]. Among these, silk from silkworms and spiders has been extensively researched and utilized in various biomedical applications [68, 69]. Although the term "silk" generally refers to the protein fibers spun by insects, its properties and composition can significantly vary between different species and their functions [70]. Silkworms spin the fibers to generate protective cocoons during metamorphosis, while spiders use the fibers to build webs, capture prey, and aid their movements [70, 71]. The amino acid sequences of silk proteins differ markedly among species, resulting in varied silk fibers [70]. Silk fiber consists

of two main proteins: a central core of fibroin protein and an outer coating of sericin protein [72]. SF, extracted from the domesticated silkworm *Bombyx mori*, has been the most extensively explored and studied variety of silk [68, 69]. Over the past few decades, its physical properties, chemical composition, and biological characteristics have been thoroughly characterized [73]. Herein, fibrous silk biomaterials, particularly SF from different silkworms, is emphasized to understand their structural and biological properties, which make them highly desirable for applications in biomedical engineering (**Figure 1.4**). SF aids multiple key stages of the wound healing process [74]. The subsequent sections provide details of the different types of SF biomaterials, their properties, and their applications in wound healing and tissue regeneration. Silkworms are categorized into two broad groups based on their feeding habits: mulberry and non-mulberry silkworms [70]. This classification depends on the host plants that provide shelter and food for the worms. Mulberry silkworms, such as *Bombyx mori*, feed exclusively on mulberry leaves. Non-mulberry silkworms include various species such as *Antheraea assamensis* (Indian Muga silk), *Antheraea mylitta* (Indian Tasar silk), *Philosamia ricini* (Indian Eri silk), *Antheraea pernyi* (Chinese Oak Tussah silk), and *Antheraea yamamai* (Japanese silk). The primary differences in the protein sequences among these SF lead to variations in their physical, chemical, and biological properties.

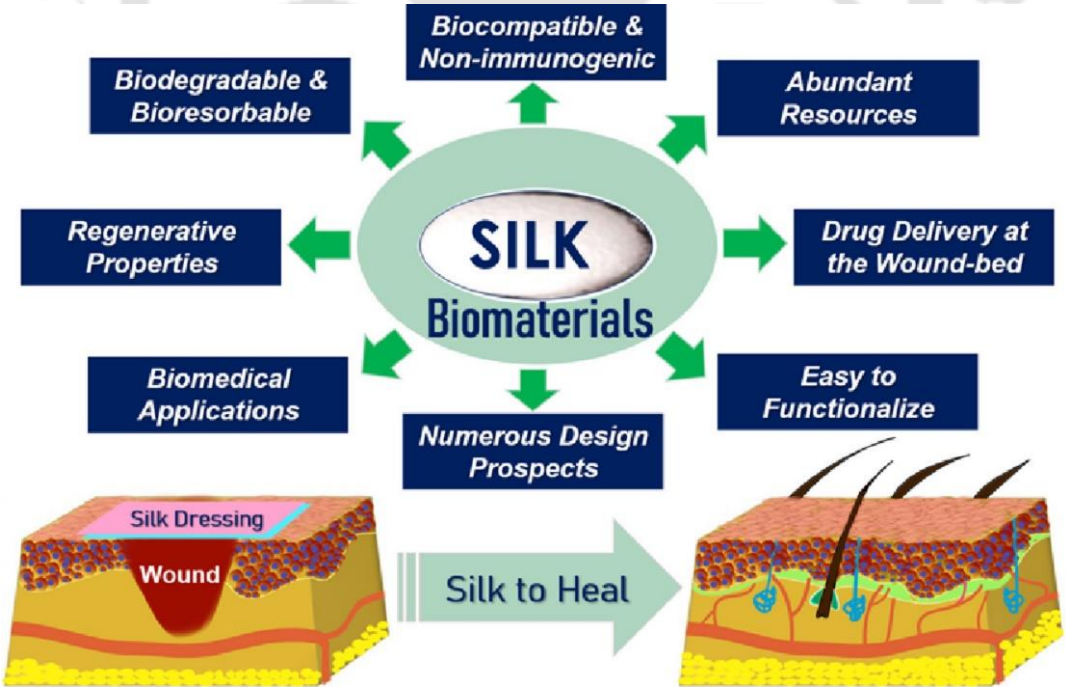


***Figure 1.4.*** *Beneficial properties of silk as a biomaterial, essential for wound healing applications. Reprinted with permission from [74]. Copyright 2020 Elsevier.*

### 1.2.3.1. Mulberry Silk

Mulberry silk, also known as *Bombyx mori* silk fibroin (BmSF), consists of two polypeptide chains: a heavy chain (391.367 kDa) and a light chain (25 kDa), along with a glycoprotein called P25 [75]. These components assemble in a 6:6:1 ratio, a characteristic feature of BmSF [75]. The SF protein exists in α-helix and random coil conformations within the silk glands of silkworms, transitioning to mechanically strong silk fibers during spinning [75]. The transition from random coils to β-sheet conformations stabilizes the silk fibers in cocoon construction, primarily due to the presence of repetitive (GAGAGS)n sequences in the protein [76]. The fibroin heavy chain consists of long crystallizable hydrophobic domains and amorphous hydrophilic domains. The hydrophobic glycine-alanine repeats confer high crystallinity and mechanical strength to the silk. BmSF is isolated from the silk cocoons (**Figure 1.5A**) which involves their degumming to remove sericin by boiling the cocoons in a sodium carbonate solution, followed by dissolving the silk fibers in a lithium bromide (LiBr) solution [73]. The degummed silk fibers dissolve in 9.3 M LiBr at 60°C, and subsequent dialysis against water yields an aqueous silk solution. This solution can be modulated into various designs by inducing β-sheet formation through physical or chemical methods. Several factors such as fibroin concentration, pH, temperature, solution aging, ionic strength, or blending with other polymers, influence β-sheet content and its structural stability. Physical methods such as mechanical shear, sonication, and electric field are being used to enhance β-sheet formation, making SF a versatile material for tissue engineering applications [77-79].

### 1.2.3.2. Non-Mulberry Silk

Non-mulberry silk fibroin (NMSF) differs from BmSF in its lack of the L-chain and P25 glycoprotein [70, 80]. NMSF contains polyalanine (AA)n and polyglycine (GG)n blocks, unlike (GAGAGS)n repeats of BmSF [70]. For instance, *Antheraea assamensis* SF (AaSF) comprises polyalanine (44.5% alanine) and polyglycine (30.1% glycine) motifs [80]. AaSF possesses a high arginine content and Arg-Gly-Asp (RGD) tripeptide, advantageous for tissue engineering applications due to its cell-binding properties [80]. The unique protein sequence of NMSF necessitates different dissolution methods compared to BmSF, with sodium dodecyl sulfate (SDS) surfactant being effective for solubilizing NMSF [81]. During cocoon spinning, silkworms extrude raw SF, which undergoes a conformational change from α-helix to β-sheets, making the fibers highly stable and difficult to dissolve. However, dissolving raw SF directly from the glands of the 5$^{th}$ instar larvae of silkworms (**Figure 1.5A**) is a simple method

applicable to various NMSFs from *Antheraea mylitta*, *Antheraea assamensis*, and *Philosamia ricini* [81, 82]. For example, AaSF exhibits superior tensile strength and can show 40% elongation at break, compared to only 15% elongation at break for BmSF [80]. Therefore, the unique polypeptides of NMSF and their molecular structural organizations collectively account for their extraordinary properties.

Conclusively, SF has gained significant attention in the fields of tissue regeneration and wound healing due to its unique properties. SF exhibits excellent biocompatibility, biodegradability, and mechanical strength. The ability of SF to transition from α-helix to stable β-sheet structures during processing contributes to its robust physical properties, such as high tensile strength and elasticity. This stability makes it suitable for various biomedical applications, through fabrication different formats including scaffolds, hydrogels, nanofibrous mats, printed constructs (**Figure 1.5B**). The structural adaptability and biological compatibility of silk make it a valuable biomaterial for regenerative applications.

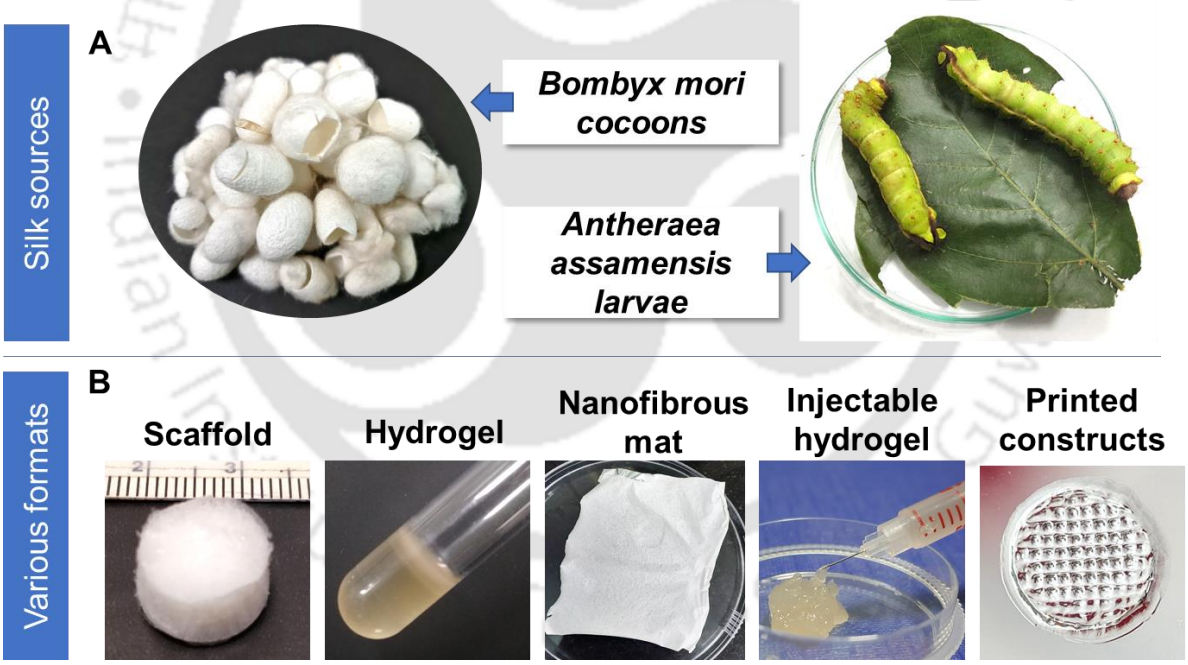


***Figure 1.5.*** *(A) Schematic presenting sources of silk protein and (B) its amenability to fabricate various 3D formats for applications.*

### 1.2.4. Cells used for skin tissue engineering applications

Cellular therapies in the field of skin tissue engineering emerged long ago with the advent of cell-laden collagen gels [83]. Cellular constructs hold great potential in treating chronic wounds that have senescent cells and fail to produce ECM in the wound microenvironment. Cellular matrices are applied to re-establish cellular events and stimulate cells towards the regenerative

pathway. Previously, cell-based therapies mostly included dermal fibroblasts and epidermal keratinocytes because the fabrication and maintenance of conventional bilayer structures are relatively straightforward. The matrices initially seeded with dermal fibroblasts were cultured for a few days to develop a dermal layer. Subsequently, keratinocytes were seeded on top and cultured, maintaining an air-liquid interface to generate a mature epithelial layer. This is the most common conventional strategy to develop a bilayer skin graft using hydrogels and porous scaffolds [83]. Similarly, further progress was achieved by adding endothelial cells (ECs) along with fibroblasts, which generated pre-vascularized skin grafts in a facile manner [84]. Further advancement in this field can be seen in stem cell therapy. A variety of stem cells have been used for wound healing, such as bone marrow-derived mesenchymal stem cells (BMSC), adipose-derived stem cells (ASC), epidermal stem cells (ESC), hair follicle stem cells (HFSC), sweat gland-derived stem cells (SGSC) and induced pluripotent stem cells (iPSC) [85-87]. In a recent report, a well-established dermal graft, Integra®, was used to culture human SGSCs that demonstrated enhanced vascularization in the regenerated dermal region [88]. A temporary matrix such as Apligraf® is also used as a carrier to deliver cells at the wound site to overcome the shortcomings of allogenic cell-laden permanent grafts [89]. Dermagraft is another commercially available product that serves the purpose of providing allogenic fibroblasts at the wound site while acting as a temporary bioactive dressing [89]. Other examples of commercially available matrices containing fibroblasts include OrCel®, TransCyte®, and Theraskin®. Similarly, well-known grafts containing epidermal cells include Epicel®, Epidex®, Laserskin®, Bioseed-S®, Cryoskin®, Myskin® [8, 10, 89]. Genome editing technology further advances cell-based therapies by genetic engineering of mammalian cells to produce specific proteins/growth factors to stimulate the healing process. A recent study has used Cas9-AAV6-mediated genome-editing tool to engineer MSCs that overexpress *PDGFB* and *VEGFA* genes. The combinatorial effect of both growth factors has shown promising results in the diabetic wound (DW) model [90].

### 1.2.5. Exogenous growth factors-based strategies

Various types of growth factors are involved in different stages of the natural healing process. However, chronic ulcers lack a sufficient amount of growth factors due to a high proteolytic environment and persistent inflammation [12, 14]. The researchers have developed wound dressings that supply desired growth factors to artificially create a growth factor pool in the wound microenvironment. The approaches taken to functionalize the matrices include recombinant technology, permanent immobilization, adsorption, and simple addition of growth

factor peptides [18, 39]. Several products containing growth factors have been approved and are currently available in the market, such as Regranex (FDA-approved gel containing recombinant PDGF) [91], Fiblast® (bFGF topical spray) [92], Easyef® and Citoprot P® (solutions containing recombinant EGF, rEGF) [93], and Regen-D® (topical gel with rEGF) [94]. However, growth factors have limited clinical application due to short half-life, inactivation in proteolytic microenvironment of wounds, and instability in physiological conditions. Moreover, the burst release of growth factors can lead to unintended cellular response [95]. Therefore, advanced delivery strategies have been developed to deliver the growth factors to the wound site in a prolonged and sustained manner. Growth factors are loaded onto film/membrane/mats/ scaffolds by physical adsorption or encapsulation during the preparation process to fabricate efficient delivery platforms. Sequential release of multiple growth factors can be achieved by incorporating them inside composite matrices due to varied loading and releasing efficiency. A research group incorporated four different growth factors, i.e., bFGF, EGF, VEGF, and PDGF, into a composite nanofibrous membrane containing collagen and HA fibers with gelatin nanoparticles [96]. *In vitro* release study showed rapid release of bFGF (incorporated in HA fiber) and EGF (incorporated in collagen fiber) from the composite membrane. In contrast, VEGF and PDGF, both encapsulated inside gelatin nanoparticles, showed a slower release profile due to the presence of an additional gelatin layer in the particles [96]. A particulate-based delivery system shows excellent controlled release ability, which reduces the risk of an oncogenic response associated with uncontrolled delivery of high dosages of growth factors.

### 1.2.6. Nanotherapeutics for skin regeneration

In conventional methods, porous scaffolds and hydrogels are used as matrices for drug release. However, most drug delivery systems suffer from passive release, and this leaky nature can lead to additional complications, i.e., antibiotic resistance, side effects, and toxicity for a drug overdose. The development of a precise and controlled delivery system made a significant impact on the treatment outcome. Nanotechnology provides an immense scope of delivering drugs and bioactive molecules like growth factors and nucleic acids through nanoparticles, thereby providing a promising tool in the field of wound healing [97]. The incorporation of nanoparticles in wound dressing materials is a smart approach to fabricate nanocomposite matrices that deliver the desired drugs in an efficient manner. Therefore, researchers have also developed wound dressings with a sequential release of multiple drugs, growth factors, and nucleic acids. Such matrices offer the additional advantage of controlled delivery of specific

drugs targeting different events of the healing process [98]. Silver nanoparticles (AgNPs) have gained much attention in wound healing applications owing to their antimicrobial activity and have been used for the treatment of infected burns and chronic ulcers [99]. They are also clinically used in hospitals because of their efficacy against hospital-acquired antibiotic-resistant bacterial infections [21, 100]. Acticoat$^{TM}$ membrane (Smith & Nephew) is an effective antimicrobial dressing with a flexible polyester layer coated with AgNPs designed and marketed for chronic and burn wounds [101]. Gold nanoparticles (AuNPs) have been demonstrated the ability to improve the wound healing process by diminishing inflammation, accelerating the wound closure rate, regenerating granulation tissue, and augmenting angiogenesis [102]. Another example of nanotherapeutics is nitric oxide (NO)-releasing nanoparticles due to their inherent antibacterial activity and property to stimulate cellular migration and proliferation [103]. NO-releasing nanoparticles have also shown accelerated wound healing in both healthy and DW in rodent models [104]. Likewise, nanoparticles have been prepared using natural polymers such as gelatin, chitosan, or synthetic polymers like polycaprolactone (PCL), polylactic acid (PLA), and poly(lactic-co-glycolic) acid (PLGA) as nanocarriers for sustained release of encapsulated bioactive molecules and are discussed in the next section.

### 1.2.7. Wearable devices as wound care dressings

Wound healing is a complex and dynamic process, and the rate of physiological processes differs at different stages. Chronic non-healing injuries impair tissue regeneration and affect the host immune response. The treatment for slow or non-healing wounds needs multiple evaluations at different healing stages for appropriate therapeutic outcomes. The wound management process requires several appointments with the clinician, which can lead to cumulative delays in the process with an increase in the cost of treatment. Hence, there is a need for a rapid evaluation system that can monitor and actively control the treatment process. This tailor-made and precise approach can lead to faster healing and lower the cost of treatment.

#### 1.2.7.1. Sensing systems

Evaluation of wound condition through sensing system with regard to its pH [105], temperature [106], moisture [107, 108], surface area [109], bacterial load [110], oxygenation [111], blood pressure [112], level of uric acid [113, 114] and level of specific enzymes [115] could enable personalized treatment for the patients. Flexible and stretchable biosensors offer solutions for designing wound-monitoring electronics [116]. Usually, normal healing wounds and chronic

wounds have pH in the range of 5.5–6.5 and 6.5-8.5, respectively [117]. As this pH change is directly relevant to the condition of the wounds, researchers have focused on developing an effective sensing system. Recently, Mostafalu *et al*. have designed a fully automated pH-responsive wound dressing that utilizes an electrochemical pH sensor and thermo-responsive drug carriers to control the drug release from a hydrogel. The dressing contains a microcontroller to process the data detected by the sensors and subsequently program the drug release protocol for individualized treatment [117].

For quick and precise detection, considerable attention is being paid to pH sensors using electrochemical and colorimetric sensors [116, 118]. The development of stretchable pH sensors for wearable point-of-care applications has drawn considerable attention. A group has fabricated a highly stretchable sensor containing serpentine polyaniline (PANI)/carbonized polyimide composite –interconnections on an Ecoflex substrate. The device showed a minimal (~4.2mV) deviation in output value at 100% strain condition when applied on a microfluidic setup with hydrogel, imitating pH fluctuation similar to the typical wound site [118]. The elevated level of IL-6 at the wound site acts as a biomarker of increased MMPs activity and inflammation [119]. IL-6 has been monitored using various systems, such as amperometric immunosensing [120], impedance [121], and optical sensing [122] based on microfluidic platforms. The rapid low-cost disposable detection system of *Pseudomonas aeruginosa* [123] and *Staphylococcus aureus* [123] in wound exudate has fulfilled the urgent need of sensing bacterial load in wound areas for point-of-care diagnostics. Omniphobic paper-based pH and uric acid sensing smart bandages have been fabricated to monitor chronic and pressure ulcers [124]. The recent advancements in wireless technology have boosted the sensing system by not only improving the real-time assessment of the healing process but also making it possible for physicians to remotely monitor patients' conditions [117, 124].

#### 1.2.7.2. Wearable devices for electrotherapy

The tissues of the human body inherently possess a bioelectric circuit. Intact skin possesses an inherent electrical potential and a transcutaneous current potential ranging from 20 to 50 mV (**Figure 1.6)** [125]. When the skin is injured, current flow through the wound, generating a lateral electrical field known as the current of injury, which is involved in multiple stages of wound healing [125, 126]. However, this endogenous electric field has been reported to be weaker in case of non-healing wounds which leads to failure of the healing process [127]. This problem is particularly grave and long-lasting in hard-to-heal wounds like diabetic ulcers [128].

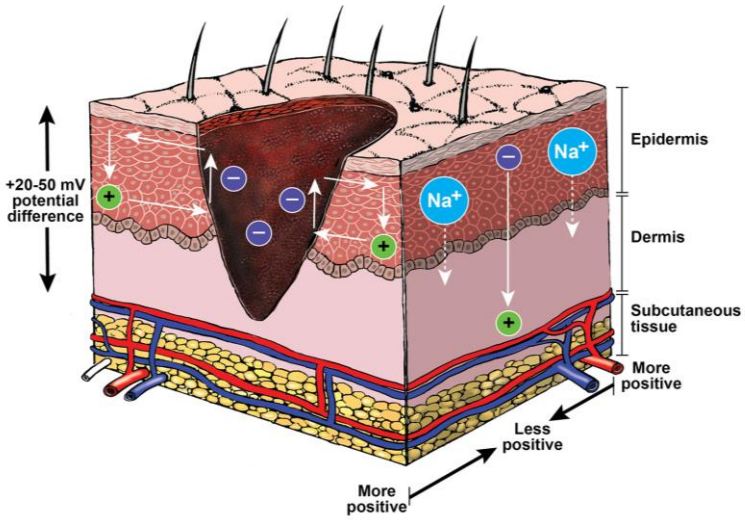


***Figure 1.6.*** *Schematic image of "current of injury" generated by the flow of current through the wound. The intact skin possesses the transcutaneous potential of 20-50 mV. Reprinted with permission from [125]. Copyright 2016 John Wiley and Sons.*

Electrotherapy aims to restore the endogenous potential by mimicking the naturally occurring signal. It also stimulates the proliferation and migration of different cell types, such as fibroblasts, macrophages, neutrophils, and ECs [129]. Exogenous application of electric current in the range of 200-800 µA has shown an accelerated wound healing process [130]. A low-intensity current can also stimulate the differentiation of ADSCs into fibroblasts and keratinocytes [130]. ES also promotes the galvanotaxis of keratinocytes to follow an electrical gradient toward a wound site [131]. Moreover, it can be applied to destroy multi-drug resistant biofilms present on the wound surface owing to its bacterial inhibitory effect [132]. *In vivo* experiments and clinical trials have shown faster healing by the application of exogenous electric fields, but the studies have utilized large devices for the therapy, which required hospitalization of patients [133]. Therefore, recent reports have aimed to miniaturize the devices for a lightweight, disposable format to eliminate the cost and inconvenience related to hospitalization [134]. For example, Howe *et al.* designed a wearable ES bandage consisting of a battery-operated PCB stimulator attached to a flexible hydrogel electrode set-up. This device could continuously deliver current pulses of 2 mA during a 7-day period [135]. Yu *et al.* designed a microcurrent dressing consisting of AgNPs and zinc particles arranged in a dot-matrix array. This dressing is able to deliver long-lasting ES and showed significant improvement in wound closure rates in a rat skin defect model due to the downregulation of TNF-α and IL-1β and upregulation of VEGF and EGF [136]. Sultana and co-workers developed a carbon-based conductive electrochemical scaffold. Application of -600mV

potential for 24 hours led to the conversion of oxygen to hydrogen peroxide at the scaffold surface and destroyed bacterial biofilm. The scaffold was able to achieve a significant reduction in the number of multi-drug resistant *Acinetobacter baumannii* and an 80% decrease in biofilm coverage [137]. In another study, Heald *et al.* developed a silk fabric-based patterned electroceutical dressing (PED) printed using Ag/AgCl ink. This dressing was connected to a 6V battery pack and 1kΩ resistor. A Bluetooth enabled circuit was also incorporated for real-time wound monitoring. It exhibited biofilm disrupting properties and infection inhibition due to weak acid production at the wound surface [138].

Several ES devices or dressings are commercially available to accelerate the wound repair and regeneration processes. For example, Accel-Heal® is a single-use device that delivers an automated sequence of micro-current pulses. It consists of skin-friendly electrode pads that provide ES continuously for a 48-hour time period. The treatment regimen is completed in 12 days. In a clinical trial evaluating its efficacy on hard-to-heal wounds, 95% of the subjects observed significant improvement in wound closure [139]. Fenzian™ is an FDA-registered and CE-approved device that detects changes in skin impedance and, using a biofeedback loop, adjusts the external microcurrent pulses to be delivered. A significantly improved wound contraction rate was seen in participants recruited in a pilot feasibility study that used this device. FDA has approved a redox-active Ag/Zn bioelectric dressing, Procellera™ (Vomaris, Wound Care, Inc., Chandler, AZ), for professional use as an antimicrobial bandage for partial-thickness and full-thickness wounds, first and second-degree burn wounds, surgical incisions, and graft donor sites. The product has shown effective biofilm-destructive properties in the case of *Pseudomonas aeruginosa*, one of the prevalent pathogens found at chronic wound sites [140]. Similarly, PosiFect RD® is a battery-operated single-use bioelectric dressing containing a two-electrode system that generates a continuous, direct current flow to the wound site. Its application involves a small cathode pad applied to the wound site and the ring-shaped anode encircling the cathode, embedded in hydrogel and applied to the adjoining undamaged skin. Another group has engineered a tunable laboratory prototype of a disposable low-cost bioelectric dressing that is made of silk fabric with electrodes, a resistor, a 6 V-battery as a power source, and a waterproof casing. The electrical dosage needed for this purpose is in a very low range (250–500 μC/s); therefore, enzymatic biofuel cells, which can generate low-intensity direct current for more than 12 hours using pre-loaded sugar as fuel, have been utilized to fabricate bioelectric plaster [141, 142]. A group has designed a disposable photovoltaic patch with organic solar cells to generate an electric field

of 70 mV/mm from light energy for cutaneous wound healing therapy [143]. Few research groups have made advances in developing self-sustainable wearable nanogenerators to harvest biomechanical energy from breathing [144] or locomotion-related muscle movements of animals for the generation of required electrical energy for healing [145]. An innovative approach has been developed to deliver ES without direct contact with the wound site. Wirsing *et al*. developed a non-invasive wireless microcurrent stimulation (WMCS) technique based on the electron-donating ability of nitrogen and oxygen. The WMCS device delivers 1.5 µA current to the wound site using a wrist strap wire placed far away from the wound. 95% of the wound area was reduced after eight weeks of treatment [146]. Therefore, it is only a matter of time when these advanced wearable devices providing exogenous electrical fields will be used in household settings.

### 1.2.8. 3D Bioprinting in skin tissue engineering

Scientists have been striving to engineer multi-layered skin architecture for the last two decades. In a recent study, a group fabricated *in vitro* innervated, immuno-competent skin-equivalent composed of epidermis, dermis with human-induced neural stem cells, and hypodermis with inherent immune cells from the lipoaspirate by manual casting of cells with hydrogel [147]. Manually seeded cells usually form non-homogeneous layers and are disadvantageous for large-scale production due to poor reproducibility. Therefore, most of the available skin equivalents at present lack a homogeneous distribution of cells and vascular networks, which leads to subsequent rejection of the construct in some cases [148]. Among the numerous techniques that have been successfully developed for skin grafting, 3D bioprinting technique provides the solutions to the mentioned challenges. The minute internal structures and variety of cellular distribution patterns can be recreated using 3D bioprinting to recapitulate the architectural and functional properties of native skin tissue. Due to its high degree of repeatability, reproducibility, and flexibility, numerous researchers have focused on exploiting various printing techniques such as inkjet, extrusion, and laser-based printing for this purpose [149-151]. The details of fabricated 3D bioprinted skin constructs are summarized in **Table 1.3**. Cell-laden soft biomaterial, known as ‘bioink’, gets deposited into desired shapes and architecture to fabricate tissue-like constructs. The ultimate focus of the field is to achieve the successful clinical application of constructs in patients. Researchers are trying to attain the goal through two different strategies. The first strategy relies on the *in situ* printing of bioink on the wound surface [152-155]; for example, handheld bioprinters with a microfluidic cartridge have been developed to deposit cellular bioink homogenously on the wound area in a clinically

relevant setup [154, 155]. The second strategy focuses on developing a suitable bioink and then *in vitro* culturing of printed skin, followed by *in vivo* application of the cultured constructs [156]. Both approaches are illustrated in **Figure 1.7,** representing advanced therapeutic ways of implanting living skin substitutes at the wound site for improved wound repair and regeneration.

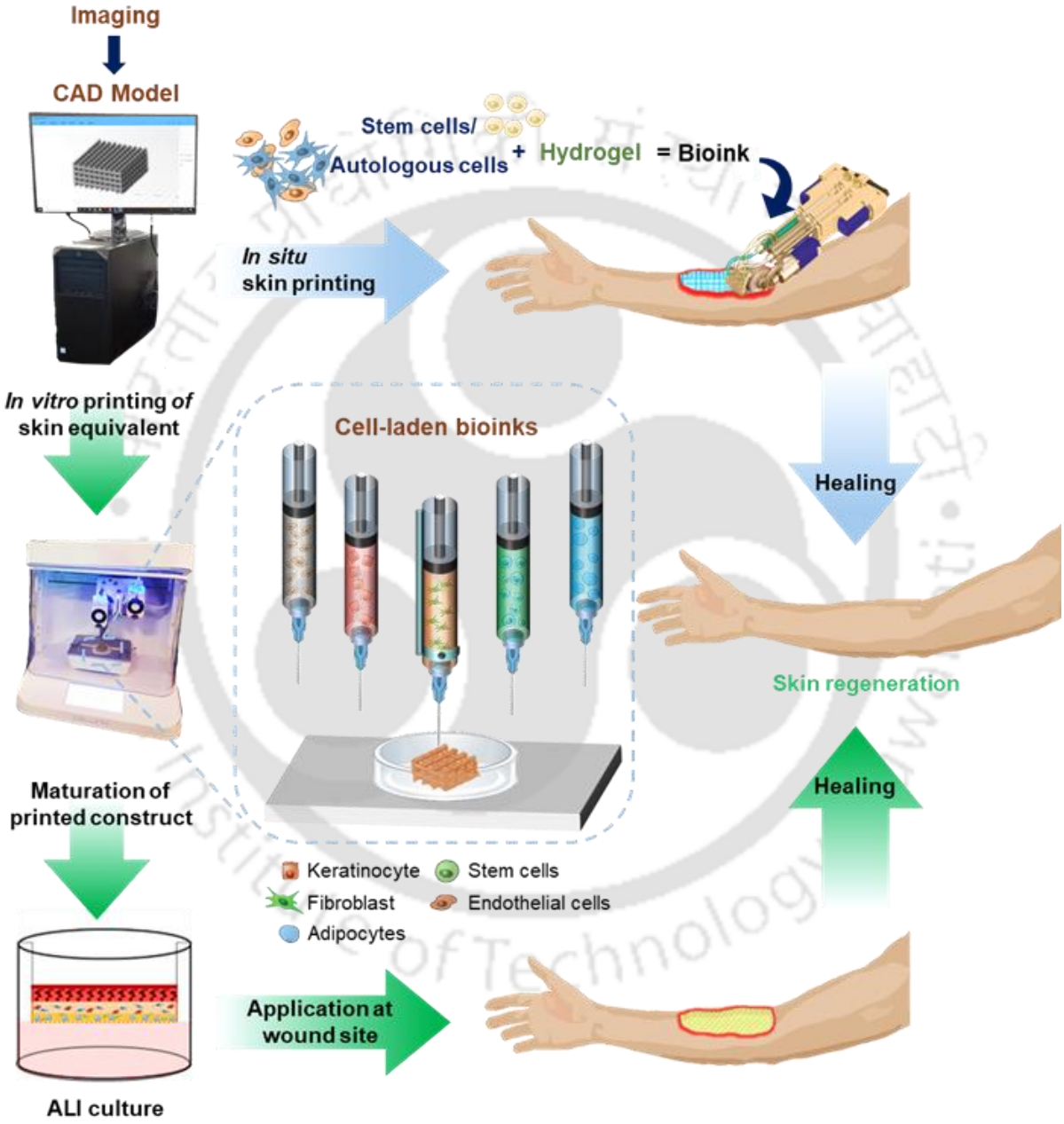


***Figure 1.7****. Conceptual diagram of two different strategies of 3D printing of skin equivalents for wound healing. After medical imaging of wounds, 3D CAD models are generated using various user interfaces. One strategy relies on the direct deposition of bioinks at the wound site using a handheld printer (top right). Alternatively, the second strategy develops 3D printed multilayered skin constructs for application at wound site after in vitro maturation (bottom right).*

### 1.2.8.1. Bilayered skin substitutes

The multiple anatomically distinct layers of skin tissue can be classified into three compartments: epidermis, dermis, and hypodermis, with each layer having its unique architectural and functional properties. To address full-thickness wounds, 3D organotypic reconstruction has been initially put forward by 3D printing bilayered constructs with dermal and epidermal layers [149, 157]. In 2009, Lee *et al.* first introduced robotic deposition of keratinocytes and fibroblasts in a layer-by-layer fashion using collagen hydrogel as bioink with an optimal printing resolution of 300 µm [157]. Binder *et al.* were the first to print cells-loaded bioink directly on 3 cm x 2.5 cm dorsal skin defect of a porcine model. The bioink containing collagen, fibrinogen, keratinocytes, and fibroblasts was deposited accurately to the previously scanned size of the wound using an ink-jet bioprinter [158]. Researchers exploited the laser-assisted bioprinting technique to develop bilayered skin constructs with NIH3T3 and HaCaT cells on top of Matriderm® and showed tissue formation with the generation of adhering and gap junctions among the cells [159, 160]. Cubo *et al.* have utilized the extrusion bioprinting process to develop a functional bilayered skin containing the dermal layer made by human fibroblasts embedded in a human plasma-derived fibrin matrix and an epidermal layer populated with human keratinocytes [150]. Scaffold free approach of printing demonstrated the fabrication of 3D-printed skin tissue that closely mimicked the bilayer structure of human skin, showing prominent epidermal and dermal markers [151]. Similarly, a bilayered skin has been printed with gelatin containing a silver-loaded epidermal layer to inhibit bacterial infection and a PDGF-BB loaded dermal layer for treatment of DW [161]. Autologous fibroblasts and keratinocytes layers were directly printed on the wound site to attain rapid wound closure of extensive burn injuries and excisional full-thickness wounds [153].

### 1.2.8.2. Multi-layered complex skin equivalents

Significant progress has been made in the bioprinting of bilayered skin structure, but all these constructs are still far from having native human skin architecture and lack vasculature, which is one of the most essential components to ensure graft survival in recipients. Several attempts have been made to overcome this challenge by utilizing multidisciplinary approaches of biomaterial engineering and microfluidic techniques for the development of *in vitro* vascularized tissue. Recent studies have fabricated skin-equivalents with integrated perfusable hollow vascular channels by removing nylon wire or sacrificial ink from the printed dermal layer, followed by coating with endothelial cells [162]. The incorporation of vascular beds in

the construct increased the relevance of 3D printed grafts for the treatment of non-healing cutaneous wounds. However, pre-patterned perfusable vascular channels are much larger than the native skin capillaries (< 50 µm). Abaci *et al.* were able to bioprint the perfusable channels with the lowest diameter of 80 µm [163]. An alternative approach has been reported to utilize the self-assembled ability of ECs derived from human cord blood endothelial colony-forming cells to generate a functional vessel-like structure of physiologically relevant dimensions *in vitro* [164]. Besides the use of 3D printed skin for therapeutic purposes, the fabrication of a vascularized skin-on-a-chip model shows the potential for recapitulation of native skin physiology. This could eventually help to develop a more reliable alternative model for drug and cosmetic testing [162]. Other than vascularization, the attempts to fabricate pigmented biomimetic human skin have been made by precise patterning of human epidermal melanocytes (HEMn) and keratinocytes in the epidermal layer [165, 166]. Most of the 3D printed skins have been fabricated with collagen matrix in the dermal layer, which makes the constructs unreliable to use for a longer period of time due to the inherent time-dependent contraction property of collagen. Kim *et al.* have evaded this challenge by using skin-derived dECM–fibrinogen bioink and printed vascularized construct containing all three layers, i.e., epidermis, dermis, and hypodermis on a polycaprolactone-based platform to mimic the complexity of skin anatomy [156].

#### 1.2.8.3. Stem cell-based 3D printed patches

Stem cell-based therapies for chronic wounds have shown excellent tissue repair and regenerative potential [167]. The primary characteristics of stem cells, such as multilineage differentiation and self-renewal capacity, have made them apt for utilization as cellular components in bioink to regenerate the skin tissue with vascular networks and ectodermal appendages. Angiogenesis or neovascularization is critical for the formation of provisional granulation tissue to provide oxygen and nutrition to the growing tissue cells. Bioprinted constructs with stem cells from multiple sources have been compared to examine their angiogenic property for the treatment of large-sized skin wounds. Amniotic fluid-derived stem cells (AFSCs) and BMSCs, embedded in fibrin-collagen gel, were printed onto the full-thickness wound on murine skin. The study has shown an increased vascular network in AFSCs-treated wounds in comparison to BMSCs-treated ones [168]. Similarly, ADSCs also promote neovascularization by upregulating VEGF-related signaling during the regeneration process [169]. Human ADSCs, together with endothelial progenitor cells, have been used for

the fabrication of 3D printed patch made up of porcine skin-derived dECM as bioink. The skin patch showed remarkably faster wound healing with improved neovascularization [156]. In addition to vascularization, 3D bioprinting of stem cell technology has been utilized for sweat gland regeneration. The sweat gland plays an important thermoregulatory role in our body. Hence, its regeneration possesses clinical relevance in the case of large-sized wounds covering substantial body surfaces. Due to its low regenerative potential, absence or damaged sweat glands pose a challenge for restoration of the gland structure after deep dermal injury. To address this problem, researchers adopted 3D bioprinting technique with MSCs or epidermal progenitor cells to arrange them in a defined spatial pattern in order to provide precise and instructive microenvironment for functional sweat gland regeneration [170, 171]. Although these strategies have shown promising therapeutic outcomes, further work is required to transfer the technology to clinical trials. For ease of clinical application, a research group developed a handheld bioprinter with a microfluidic printhead and a silicone wheel for precise deposition on the wound bed. The handheld bioprinter was used to directly print stem cells-based fibrin-HA matrix on burn wounds in a porcine model for improved regeneration [154]. Therefore, the utilization of MSCs in bioink preparation holds immense therapeutic value for skin regeneration. Recent evidence indicates that the regenerative property of MSCs primarily relies on their capability to secrete trophic factors, which stimulate neighboring host cells for the initiation of the regeneration process [172]. Therefore, recent studies are exploring the potential of stem cells-secreted extracellular vesicles or exosomes to accelerate the skin regeneration process instead of using the whole cells for the treatment [154, 173].

**Table 1.3.** List of 3D printed skin equivalents.

| Cells | Biomaterial/ Bioink | Biomolecules/ Additives | Bioprinting technique | *In vivo* model | Remarks | Ref |
|---|---|---|---|---|---|---|
| **Bilayered skin substitutes** | | | | | | |
| HDF, HEK | Collagen hydrogel | Human keratinocyte growth supplement | Robotic freeform fabrication | - | The cells retained their morphology; contraction of the collagen-cell matrix was observed in a two-week *in vitro* culture. | [157] |
| HDF, HEK | Hydrogel containing fibrinogen and type-I collagen | Thrombin | Inkjet (*in situ* printing) | Athymic mice | Complete closure of the wound was observed by 3 weeks. Human cells were found into the surrounding skin appendages of regenerated tissue. | [158] |

| | | | | | | |
|---|---|---|---|---|---|---|
| NIH 3T3 mouse embryonic fibroblasts, HaCaT cells | Collagen gel, Matriderm ® (stabilizing matrix) | - | Laser-assisted | - | Formation of basal lamina and adhering and gap junctions were observed by 10 days in *in vitro* culture. | [159] |
| NIH 3T3 mouse embryonic fibroblasts, HaCaT cells | Collagen, Matriderm ® (stabilizing matrix) | Hydrocortisone | Laser-assisted | Nude mice | Formation of skin-like tissue within 11 days on full-thickness wounds in nude mice and angiogenesis was observed at wound edge. | [160] |
| HDF, HEK | Plasma-derived fibrin | $CaCl_2$ | Extrusion-based | Skin-humanized mice. | Generation of 100 $cm^2$ of human skin-like tissue in less than 35 min; no contraction of printed construct after more than two weeks. | [150] |
| HDF, HEK | Bovine gelatin, alginate, fibrinogen | $CaCl_2$, thrombin | Extrusion-based | - | The printed construct supported the epidermal formation and neosynthesized ECM in dermal layer in *in vitro* culture. | [151] |
| HDF, HEK | Gelatin methacrylate (GelMA) | Silver (top layer), PDGF-BB (bottom layer) | Extrusion-based | 8 to 12-week-old female C57BL/6JNju DIO type II diabetic mice | Printed scaffolds were able to accelerate wound closure, re-epithelialization, and angiogenesis in DW | [161] |
| HDF, HEK (in mice), autologous cells (in porcine) | Fibrinogen, collagen | Thrombin | Inkjet-based | Athymic nude mice, porcine model | A novel mobile skin bioprinting system was designed for *in situ* printing and printed tissue accelerated regeneration in both models. | [153] |
| **Multi-layered complex skin equivalents** | | | | | | |
| HDF, HEK, iPSC-derived EC | Type-I collagen, alginate (sacrificial ink) | $CaCl_2$ | Inkjet-based | SCID mice | The study showed that the pre-organized vasculature in printed skin can promote the host neovascularization and induce vessel invasion when implanted. | [163] |
| HDF, HEK, HUVEC | Collagen gel | - | Inkjet-based | - | *In vitro* culture of perfused skin-equivalent showed high cell density and well-organized barrier function; the model can be used for drug permeation studies. | [162] |
| HDF, HEK, HEMn | Collagen gel | - | Microvalve-based | - | Presence of dendrites from cultured HEMn | [165] |

| | | | | | | |
|---|---|---|---|---|---|---|
| | | | pneumatic dispensing | | confirmed survival and proliferation of melanocytes in printed construct; non-uniform pigmentation was observed. | |
| HDF, HEK, HUVEC, Human preadipocytes (HPA) | Skin-derived and adipose-derived dECM, bovine fibrinogen | NaCl, aprotinin | Hybrid: both extrusion and inkjet-based | - | The skin equivalent showed stratified epidermis, ECM-secreted dermis, and lipid droplet-entailed hypodermis after in vitro maturation. | [174] |
| **Stem cell-based 3D printed patches** | | | | | | |
| BMSC, AFSC | Fibrinogen, collagen | Thrombin, triple antibiotic | Laser-assisted deposition | Nude mice | Accelerated wound closure was achieved with both cells. Strong angiogenic response and capillary diameters in the AFSCs-treated wounds compared with the MSCs-treated wounds | [168] |
| Human adipose-derived stem cells (ASC), endothelial progenitor cells | Porcine skin-derived dECM | Thrombin | Extrusion and inkjet-based | 8-week-old male BALB/cA-nu/nu mice | Improved re-epidermal organization, dermal ECM secretion, and barrier function were achieved. | [156] |
| Umbilical cord-derived MSC | Fibrinogen, hyaluronic acid | Thrombin | Extrusion-based (in situ deposition) | Porcine model | Designed a handheld 3D printer that was able to deposit material directly at wound sites that were inclined up to 45°, which showed improved re-epithelialization and increased dermal cell repopulation in pre-clinical setup. | [154] |

One of the key benefits of 3D bioprinting lies in its capacity to fabricate customized tissue models, precisely mimicking spatial microstructures of skin tissue. Among the common bioprinting techniques, laser-assisted bioprinting allows precise, high-density cell deposition without viscosity restrictions [175]. *Koch et al.* used this technique to print fibroblasts and keratinocytes in collagen, forming a bilayered skin-like structure with an epidermis-like layer [159]. Droplet-based printing, efficient with low-viscosity biomaterials, has also been used to create uniform epidermal layers and pigmented bilayered skin [165, 175]. Extrusion-based bioprinting, the most popular technique, is characterized by high speed, scalability, and

affordability, allowing the use of high-viscosity biomaterials [176]. Human plasma-based bioinks with primary human fibroblasts and keratinocytes were used to fabricate skin constructs resembling human skin architecture [150, 151]. The collagen-based printed construct supported cell growth and enhanced proliferation *in vitro* [177]. To address poor mechanical properties and contractibility of collagen, researchers provided additional support to collagen-based matrices. The collagen-based dermal bioink and PCL were co-printed to prevent collagen contraction during *in vitro* maturation. The fabricated skin model exhibited excellent biological properties, including a stable dermal layer with well-spread fibroblasts and stratified epidermis layers after 14 days of maturation [178]. *Shi et al.* enhanced the mechanical strength of the collagen-based matrix through two-step crosslinking of bioinks containing collagen and GelMA, using tyrosinase-based crosslinking and photo crosslinking of GelMA [179]. However, extrusion-based bioprinting faces challenges such as low resolution (≥100 μm), slow printing speed, and frequent nozzle clogging [180]. These limitations hinder the fabrication of functional biomimetic skin closely resembling human skin microanatomy. The complex microstructures such as hair follicles, sweat glands, and sebaceous glands remain difficult to replicate *in vitro*. Researchers attempted to use progenitor cells and growth factors to print skin constructs with an inductive niche capable of producing these appendages post-transplantation [171]. For instance, *Huang et al.* bioprinted epidermal progenitor cells with dermal bioink composed of gelatin, sodium alginate, dermal homogenate, and epidermal growth factor (EGF), restoring sweat gland function in a mice model with burnt skin [171].

#### 1.2.8.4. 3D printed skin tissue models for *in vitro* screenings

Over the past decade, a significant shift in drug-screening models has occurred due to international and national restrictions on animal testing for cosmetic products, leading to the development of alternative *in vitro* 3D skin tissue models [181]. These models offer more reliable and accurate assessments of drugs and cosmeceutical agents, providing a more physiologically relevant rapid screening platform compared to animal models. Various skin substitutes, including cellular monolayers, bilayers, and trilayers, have been explored for skin regeneration therapy and drug testing. Recent technological advancements in 3D printing technology hold great potential for engineering functional skin units with multiple layers and cellular components (**Figure 1.8**) [182]. Incorporation of immune cells into dermal bioink and within perfusable vasculature could make *in vitro* modelling of functional skin units a reality. This requires the development of perfusion-based systems or ‘skin-on-a-chips’ with dynamic flow systems, including vascular and lymphatic networks, to ensure proper physiological

transport of oxygen and nutrients *in vitro*. Additionally, 3D bioprinting enables automated, standardized, and large-scale production of *in vitro* models, beneficial for high-throughput drug screening on printed healthy or diseased skin models. Recently, a 3D diseased full-thickness skin model with properties of type 2 diabetes was developed using extrusion-based printing [183]. The study demonstrated an *in vitro* perfused model of wounded diabetic skin, capable of recapitulating the delayed healing process. Furthermore, anti-diabetic drugs such as metformin and eicosapentaenoic acid were perfused through vascular channels to evaluate their effects on the printed diabetic skin model. This perfusion alleviated inflammatory responses associated with diabetes and exhibited improved uptake of glucose by keratinocytes in metformin-treated models. Thus, while the development of multi-layered skin constructs, encompassing both healthy ECM and diseased components, is achievable with current bioprinting technologies, further advancements are necessary to produce physiologically relevant models in a cost-effective manner.

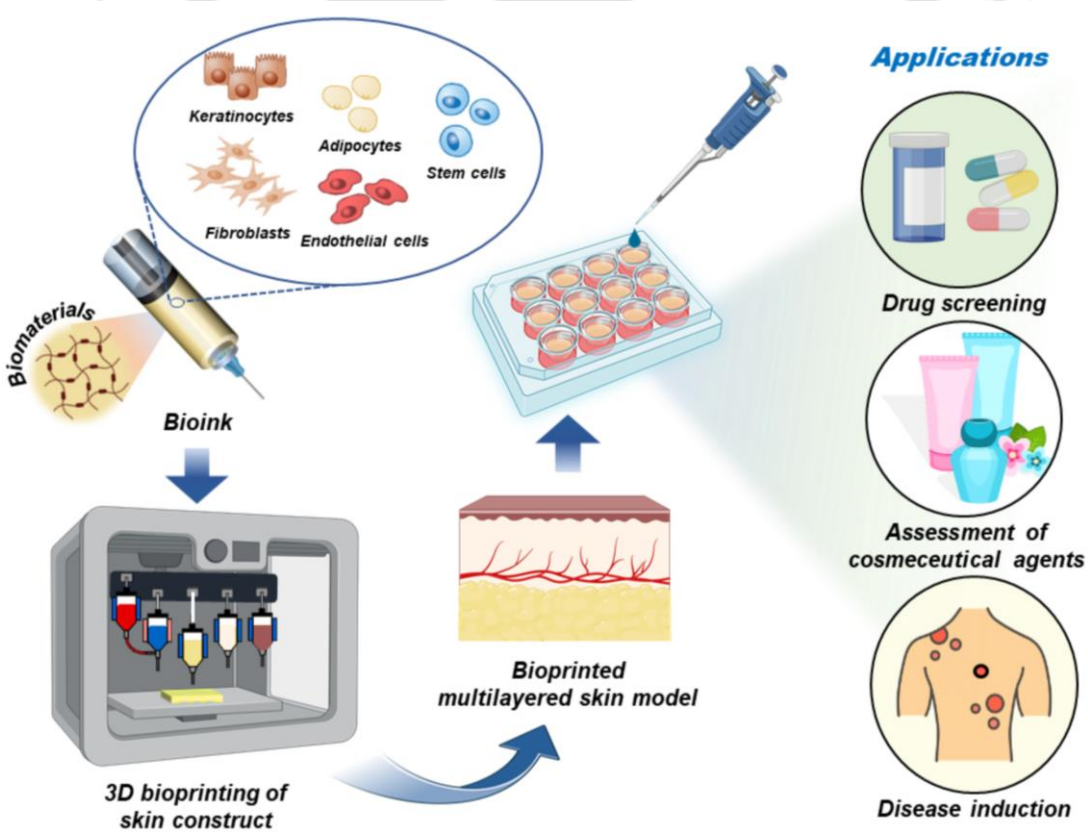


***Figure 1.8.*** *Schematic diagram showing the process of fabricating a 3D in vitro multilayered skin model using bioprinting technology and its various in vitro screening applications. Reprinted with permission from [182]. Copyright 2023 IOP Publishing.*

### 1.2.9. Relevant research directions

Advances in the fields of biomaterials, functionalization strategies, nanotechnology, drug delivery, and electronics have collectively improved the quality and efficacy of healthcare products. Although conventional therapies effectively provide barrier properties to open wounds and prevent infections, they are not so effective for chronic wounds. The advanced strategies support the development of multiple treatment options by modulating the microenvironments distinctly at different stages or conditions of the wound. To bridge the gap between technological innovations and clinical practices, it is essential to examine the applicability of the new technologies. Numerous novel strategies of artificial skin grafts and dressings have been developed in the past few decades, but only a limited number of technologies have reached the wound care market. The tissue-engineered grafts or dressings comprising different cells, growth factors, and nanotherapeutics create challenges in ethical approval or scaling up production for clinical practices. Besides expensiveness, the use of natural growth factors has limitations due to their short half-life and deactivation/low stability in the proteolytic wound environment [184]. To maintain the desired concentration, the dressings containing growth factors often require the use of a higher dose, which might lead to severe side effects, including oncogenesis [95, 184]. Similarly, the safety issues related to stem cell-based therapy are still debatable due to the chance of their unwanted differentiation and suppression of antitumor response [185]. On the other hand, the emergence of automated technology possesses tremendous clinical promise in wound care. Rapid advancements in integrated circuit technology aid in the miniaturization of medical instruments that will definitely reduce the time and cost of a hospital stay [186]. Recent advancements in electronics have significantly improved the data storage capacity and display in wearable technology. Further improvements in power sources, data management, stable sensors, and leakage-free delivery systems are yet to be achieved through multifaceted research activities. Although this innovative machinery indeed holds great potential, translating them from bench to bedside requires simplification of the technologies for regular clinical practices. User-friendliness and affordability are the key features that will help to introduce these innovations in the wound care market. More technical complexities could be added slowly to provide a variety of treatment options for specific wounds. The automated/semiautomated smart bandage technologies are at an accelerated pace to reach the patients due to lesser associated ethical issues for their non-invasive or minimally invasive nature. These therapeutics may be envisaged to revolutionize wound care regimens in the near future.

From the fabrication aspect, the emerging 3D printing technology has the potential to revolutionize the strategies of developing complex artificial skin grafts. However, a careful assessment is essential for the commercialization of this technology. Every stage of this process, such as the selection of bioink material, pre-processing and post-processing of 3D printed constructs, and sterilization prior to implantation, requires to be cautiously scrutinized according to the compliances of regulatory bodies. Concurrently, the introduction of technology as regenerative medicine also demands the evolution of regulatory sciences to hasten the clinical assessment of the products. Over the last decade, there has been significant scientific focus on developing 3D *in vitro* models to minimize the use of animals for drug testing. Regulatory agencies worldwide including U.S. Food and Drug Administration (FDA) are promoting the alternative techniques, providing guidelines for their validation and approval [187, 188]. The current marketed *in vitro* models lack essential components of skin tissue including immune cells, and blood vessels, highlighting the need for the development of advanced models. Compared to conventional strategies, 3D bioprinting technology offers an automated platform to simulate skin complexity with spatial precision by layering bioinks containing different types of skin cells [189, 190]. The technology possesses great potential to generate on-demand models with consistent and reproducible spatial architecture [191]. Therefore, the development of physiologically relevant skin components, from ECM microarchitecture to the microbiome, is feasible with current bioengineering technologies. However, further advancements in existing technologies and the development of novel approaches are essential to enable cost-effective and scalable fabrication of functional skin tissue *in vitro*. These developments will be pivotal in enhancing the utility of *in vitro* skin constructs for research, clinical applications, and reducing the reliance on animal models.

# *Motivation and objectives of thesis*

### 1.3. Motivation and objectives of the thesis

Skin serves as a protective barrier against external threats such as pathogens, physical trauma, and UV radiation. The tissue is susceptible to injuries ranging from minor cuts and burns to chronic wounds, including diabetic ulcers and pressure sores. After wounding, regeneration of the skin is essential for maintaining skin integrity and preventing infections to protect the internal organs. Tissue engineering focuses on developing advanced therapies to achieve effective tissue regeneration. Skin tissue engineering encompasses two primary domains: the fabrication of advanced wound dressings and the development of *in vitro* skin models. These two areas address distinct yet interconnected aspects of skin tissue. Bioengineered wound dressings aim to provide effective and tailored solutions for promoting wound healing, often incorporating biomaterials with bioactive properties to facilitate tissue repair. In contrast, *in vitro* models serve as advanced platforms for studying skin biology, disease mechanisms, and drug testing, offering valuable insights into skin physiology and pathology. Through the integration of biological and engineering principles, skin tissue engineering addresses the challenges associated with skin injuries by developing advanced biomaterials, tissue-engineered constructs, and *in vitro* models that mimic the complexity of native skin tissue.

The current treatment of wounds primarily involves regular cleaning to remove debris, applying topical or systemic antibiotics, and covering the wound to prevent infection. However, these conventional methods need enhancements to promote specific stages of the healing process. Biomaterials, particularly silk, offer a promising solution for improving wound management. The long history of the use of silk sutures in surgery has firmly established silk as a biocompatible material. Regenerated SF from *Bombyx mori* silkworm cocoons has gained attention in tissue engineering owing to its biocompatibility, tunable biodegradation, and mechanical strength. SF can be transformed into various formats, including 3D scaffolds, hydrogels, and nanofibers, based on the requirements for the applications. Certain silk varieties, such as NMSF, contain cell binding motifs, Arg-Gly-Asp (RGD) tripeptide, which facilitates cell attachment. Further, blending SF with other natural or synthetic polymers enhances the functionality of composite materials, making the composite a promising avenue for biomedical applications. Incorporating specific bioactive components tailored to each stage of wound healing can enhance the effectiveness of SF-based composite materials to actively support and induce multiple stages of healing. This approach ensures that the material not only provides a

scaffold for tissue growth but also modulates the wound environment to accelerate recovery through targeted therapeutic effects at each stage.

Initially, we integrated a dECM scaffold with composite SF hydrogel, where mulberry *Bombyx mori* and non-mulberry *Antheraea assamensis* silk varieties were infused into dECM scaffold. The fabrication technique was a chemical crosslinker-free approach, thus avoiding the possible toxicity and cost burden associated with it. This innovative approach combines the regenerative properties of SF with the structural support provided by the ECM scaffold, offering a synergistic solution for addressing the challenges of chronic diabetic wounds. By harnessing the biocompatibility and bioactivity of SF, along with the instructive cues provided by the ECM, this composite hydroscaffold can be an efficient dressing for promoting healing in diabetic wounds. Further, the hydrogel formulation was used to fabricate a silk-aloe composite matrix to formulate a sustained delivery system for aloe phytochemical molecules to induce the healing process. Due to its simple fabrication technique and easy application, the developed matrix holds significant translational potential. Further, a wearable e-Bandage was designed, which is directly involved in the healing mechanism by providing external ES at the wound site. *In vivo* studies demonstrated rapid wound closure with varying amplitudes of ES, supported by accelerated tissue formation, remodeling, vascularization, and reepithelization. The final objective focuses on synthesizing a photopolymerizable bioink hydrogel utilizing SF protein. Photopolymerizable silk composite, enriched with platelet releasate and primary skin This composite, enriched with platelet releasate and primary skin cells, was utilized to formulate a pre-clinical 3D bioprinted immunocompetent skin model for *in vitro* skin sensitization tests. This innovative approach not only offers a crucial facet of skin tissue research but also provides invaluable insights into skin sensitization, thereby providing new opportunities for *in vitro* screening in dermatological and pharmaceutical studies and the reliance on animal models. Throughout this study, SF protein emerged as a versatile and indispensable biomaterial, guiding the way toward novel therapeutic approaches and promising advancements in wound care and tissue engineering.

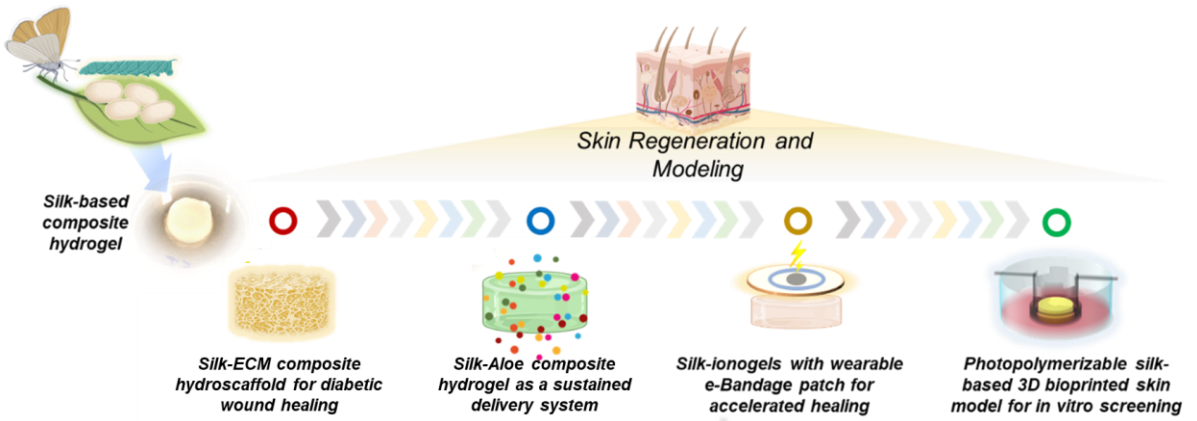


***Figure 1.9.*** *Outline of the thesis objectives/work of the thesis. Created using BioRender.com.*

## Objectives

1. Fabrication of composite hydroscaffold with silk and decellularized extracellular matrix derived from porcine omentum tissue to investigate its regenerative efficacy in diabetic wound healing.
2. Development of silk-aloe composite matrix for sustained delivery of bioactive molecules and assessment of its healing ability in full-thickness wound model.
3. Development of a wearable e-bandage patch with silk-based antibacterial ionogel to provide external electrical stimulation for accelerated healing in animal model.
4. Development of silk-based 3D bioprinted immunocompetent skin model as an advanced platform for skin sensitization assessment

भारतीय प्रौद्योगिकी संस्थान गुवाहाटी
Indian Institute of Technology Guwahati

# Chapter 2: Fabrication of composite hydroscaffold with silk and decellularized extracellular matrix derived from porcine omentum tissue to investigate its regenerative efficacy in diabetic wound healing

*The chapter describes the methodology to integrate omentum tissue-derived extracellular matrix in the silk hydrogel system to fabricate a hydroscaffold dressing that possesses both the properties of a collagenous fibrous scaffold and a hydrogel, aiming to mimic all aspects of provisional skin tissue-matrix. The work presents a facile single-step technique of fabrication of dECM-based matrix that can ensure adherence of the dressing at the wound site due to in situ gelation property of silk proteins. In vivo validation of SF-dECM establishes its applicability for the treatment of diabetic chronic wounds as the hydroscaffold demonstrated its ability to influence crucial steps of healing, including vascularization, inflammation, and tissue remodeling.*

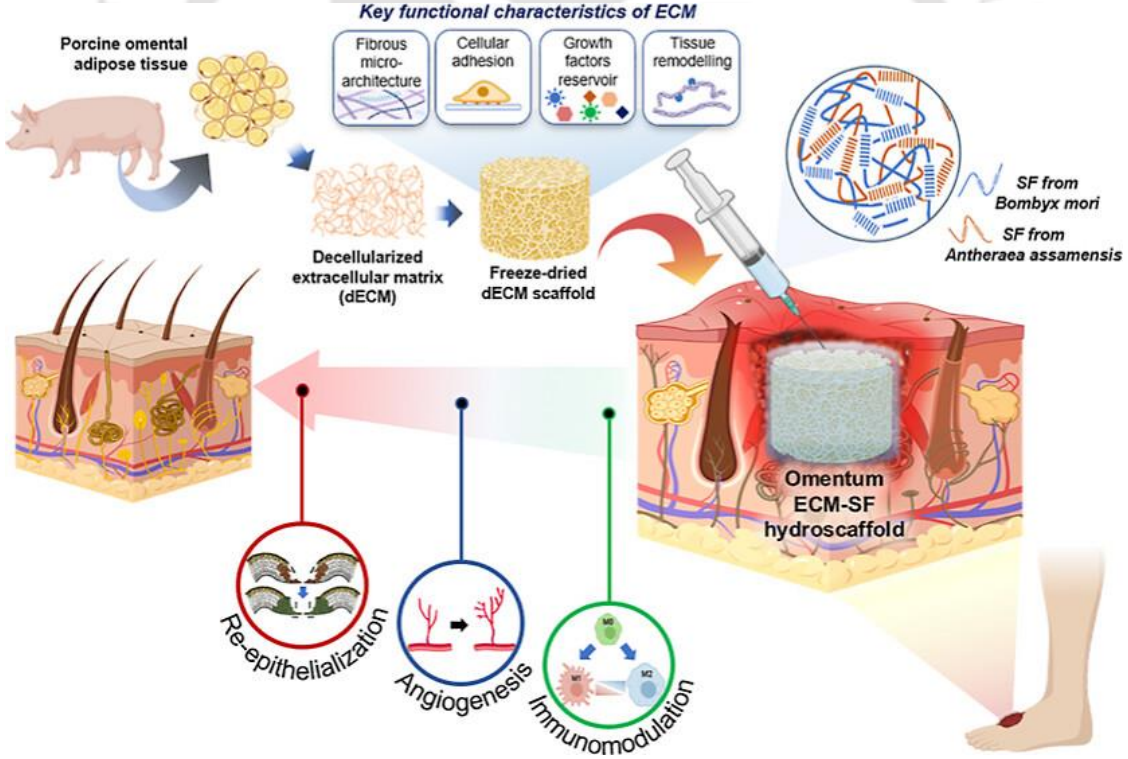


***The work embodied in this chapter is published as:***

Bibrita Bhar, Priyanka Ranta, Pavan Kumar Samudrala, and Biman B. Mandal. "**Omentum Extracellular Matrix-Silk Fibroin Hydroscaffold Promotes Wound Healing through Vascularization and Tissue Remodeling in the Diabetic Rat Model**." *ACS Biomaterials Science & Engineering*. 2024;10(2):1090–105.

**Abstract**

Nonhealing diabetic wounds are often associated with significant mortality and cause economic and clinical burdens to the healthcare system. Herein, a biomimetic hydroscaffold is developed using omentum tissue-derived dECM and SF proteins that associate the behavior of a collagenous fibrous scaffold and a hydrogel to reproduce all aspects of the provisional skin tissue matrix. The chemical cross-linker-free in situ gelation property of the two types of SF proteins from Bombyx mori and Antheraea assamensis ensures the adherence of dECM with surrounding tissue on the wound bed, circumventing further suturing. The physicochemical and mechanical properties of the composite hydroscaffold (SF–dECM) were thoroughly evaluated. The hydroscaffolds were found to support the growth and proliferation of human dermal fibroblasts and influence the angiogenic potential of endothelial cells under in vitro conditions. Furthermore, the healing efficacy of the composites was evaluated by generating full-thickness wounds on a streptozotocin-induced diabetic rat model. The presence of dECM components in the composite facilitated the rate of wound closure, granulation tissue formation, and re-epithelialization by providing intrinsic cues to advance the inflammatory stage and stimulating angiogenesis. Collectively, as an off-the-shelf wound dressing requiring only a single topical administration, the SF–dECM hydroscaffold is a promising, cost-effective dressing for the management of chronic diabetic wounds.

**Hypothesis**

The study aims to develop a silk-based composite dressing designed to enhance healing in diabetic conditions by incorporating additional biochemical cues along with SF hydrogel. The omental-derived dECM serves as a scaffold for the infusion of SF hydrogel from *Bombyx mori* and *Antheraea assamensis*. This synergistic combination is expected to support key processes of tissue regeneration, including angiogenesis and ECM remodeling, thereby accelerating wound healing and offering an alternative solution for chronic diabetic wound management.

## 2.1. Introduction

Diabetic wounds are difficult to treat owing to severe consequences of wound chronicity, hyperglycemia, and microbial infection, which worsen over time unless treated effectively. Diabetic patients possess a 15–25% lifetime chance of developing diabetic foot ulcer (DFU) [192]. The annual incidence of DFU worldwide is estimated to be 9.1-26.1 million [193]. The prevalence of diabetic foot ulcers is bound to inevitably rise as the number of newly diagnosed diabetics increases every year. Such chronic wounds cause a significant economic burden and a major healthcare problem as prolonged open wounds lead to substantial imbalance in physiological activities, resulting in disabilities or even death of the patient [194]. Management of DFU primarily involves the standard therapeutic regimen including control of blood glucose level, prevention of infection, wound debridement, and application of dressing. However, the closure of diabetic wounds often remains incomplete even after 20 weeks for the patients receiving only standard therapy [195]. The persistent inflammatory environment with high levels of MMPs results in instability of ECM at the wound site [196]. The commonly used wound dressings for the management of these wounds are foam dressings, hydrocolloids, and hydrogels, that can absorb wound exudates, but lack bioactive components to influence the wound microenvironment. Although several bioactive molecules, including stem cells, growth factors, and platelet-rich plasma, have been clinically employed for the treatment, they have certain drawbacks, including easy deactivation, low bioavailability, and high cost of production [197]. In this case, adjuvant therapies with skin substitutes from autologous, allogenic, and xenogeneic sources are used as ECM replacements to expedite wound closure [198, 199]. The usage of autografts demonstrates a lower rejection rate, but their harvesting is limited and may result in secondary infection and pain at the donor site. On the other hand, allografts and xenografts overcome these limitations, but they pose a risk of immunological rejection and disease transmission [200]. To address the issue, researchers have focused on developing acellular tissue matrices using appropriate decellularization processes to minimize the risk of

immune response leading to rejection of grafts [201]. Acellular dermal matrices derived from human skin tissues such as Alloderm, Graft Jacket, and Epiflex are available in the market for tissue regeneration and have been clinically proven to accelerate the regeneration process [202]. Grafting of adipose tissue has also been extensively studied and applied in addressing soft-tissue defects and regenerative purposes, including the treatment of open wounds and anti-scarring interventions [203]. Several clinical trials and case reports demonstrated improved healing of diabetic wounds treated by lipografting [203-205]. However, the global shortage of human tissue leads to high costs and limited availability of these matrices, especially in developing countries. The limitation of tissue supplies and the need to scale up manufacturing such grafts for industrial production have spurred the research for finding alternatives of human skin. Animal tissue, particularly porcine tissue, has the potential to alleviate human tissue scarcity. The global production of porcine adipose tissue has been estimated to be 6.8 million tonnes, and considerable quantities of omental adipose tissue are discarded as food waste on a regular basis [206]. Therefore, repurposing this tissue to develop new biomaterials might have economic benefits. The dECM from porcine omentum possesses great potential to be used as a scaffold material for skin regeneration. It contains various structural ECM components, including type I-VI collagen fibers, fibronectin, elastin, laminin, and GAG [206]. Adipose tissue ECM has been used to develop injectable hydrogels for regenerative applications [207]. However, only dECM scaffolds lack mechanical robustness, which limits their application to be used as wound dressing for deep chronic wounds. Incorporation of biomaterials with superior mechanical properties has potential to overcome this issue. SF can be a rational choice for preparing such composite biomaterials due to its tunable mechanical properties. SF not only can aid in maintaining structural integrity but also support and interact favorably with surrounding biological tissues. In addition, its biodegradability, low immunogenicity, and active participation in tissue regeneration make it an excellent option for fabricating wound dressing [208]. Specifically, the activation of NF-κB signaling has been demonstrated as the mechanistic basis of SF-induced wound healing process[209]. SF-based wound dressings have been fabricated in different formats such as films [210], sponges [211], nanofibrous mat [27], and hydrogels [11]. Besides bioactive properties, hydrogel dressings have their own beneficial characteristics as these dressings aid in maintaining a moist wound healing environment, which facilitates autolytic debridement and promotes granulation tissue formation and re-epithelialization [212]. SF-based hydrogels have been reported to be an effective candidate for many regenerative applications, especially in the field of wound healing [213, 214].

Development of hybrid biomaterials combining dECM and SF possesses potential to provide matrices with biological cues of dECM, alongside the tunable mechanical properties of SF[215]. In previous reports, placental dECM was blended with SF to fabricate a hybrid sponge for the treatment of full-thickness wounds in rat model[216]. Decellularized amniotic membrane has also been incorporated in electrospun nanofibrous SF mat to develop composite membrane as dressing material. The membrane not only expedited the healing process but also contributed to a significant reduction in scar formation by influencing collagen deposition and MMP1 expression in full-thickness wounds in rabbit ear model[217]. The fabrication process for both composites involved a chemical crosslinking method using 70% ethanol, which could potentially affect the biological activity of ECM components. The present study utilizes the chemical crosslinker-free in situ gelation property of two types of SF proteins to ensure the adherence of dECM scaffold with peripheral tissue on the wound site, thereby circumventing further suturing. We previously explored the temperature-induced self-assembly property of mulberry BmSF and non-mulberry AaSF [11, 218]. The goal of the study is to develop a biologic composite dressing using omental dECM and SF composite, leveraging the synergistic effects derived from the inherent properties of both pristine biomaterials. The omentum is a large flat adipose tissue layer located in abdomen and characterized by highly vascular network. The pro-angiogenic and regenerative properties inherent in omental tissue derivatives have prompted their utilization in cardiac tissue engineering applications[219, 220]. Herein, we utilized omental dECM to fabricate the composite dressing which can serve as a stable provisional matrix to compensate for the intricate disruptions in diabetic wound microenvironment by providing missing cues to peripheral cells and guiding in situ responses to influence the healing process. We first thoroughly characterized the decellularized porcine omentum ECM to ensure the complete elimination of cellular components to elude any xenogeneic response. To preserve integrity of ECM and minimize essential component loss, we utilized freeze-dried dECM directly after the decellularization process, avoiding further enzymatic digestion and chemical crosslinking steps. We utilized the freeze-dried dECM to fabricate a composite hydroscaffold by injecting a blend of SF proteins, leveraging their inherent temperature-induced self-assembly property at physiological temperature (37 °C). Furthermore, the hydroscaffold was systematically characterized and assessed in terms of gelation kinetics, surface morphology, degradation properties, hydrophilicity, and mechanical properties to ensure its stability and utility in skin tissue engineering. In addition, the biocompatibility, cellular proliferative, and angiogenic potential of the tissue-engineered composite were investigated under *in vitro* conditions. Subsequently, a detailed *in vivo* study was performed in a diabetic rat model to explore its angiogenic and regenerative efficacy and compared with the commonly used collagen (Col) gel-based dressing as positive control group. The results of the wound closure rate, histological and immunostaining analysis infer the potential usefulness of the fabricated hydroscaffold as a cost-effective alternative for the treatment of diabetic wounds.

## 2.2. Materials and methods

### 2.2.1. Isolation of silk fibroin solutions

Silk cocoons of *Bombyx mori* and worms of *Antheraea assamensis* were obtained from local sericulture farms. BmSF was isolated from the silk cocoons following the previously published method [73]. The cocoons were chopped and degummed by boiling in 0.02M sodium carbonate ($Na_2CO_3$, Merck, India) solution for 15 min. Next, the degummed fibers were dried and dissolved in 9.3 M LiBr (Sigma-Aldrich, USA) solution at 60 ℃, followed by dialysis using 12 kDa cutoff dialysis cellulose membrane (Sigma-Aldrich, USA) against distilled water for 48 h. The obtained SF solution was stored at 4 ℃ until usage. AaSF was extracted from the silk glands harvested from silkworms at $5^{th}$ instar larval stage, following the established lab protocol [221]. Briefly, the glandular silk glands were squeezed using a tweezer to extrude out the fibroin protein. The protein was dissolved in 1% (w/v) sodium dodecyl sulfate (SDS, Himedia, India) aqueous solution. Next, the solution was dialyzed using a cellulose membrane dialysis tubing (molecular weight cut-off 12 kDa; Sigma-Aldrich, USA) against chilled Milli-Q water for 4 h at 4 °C for to remove excess surfactant. Percentage of SF solution was quantified using gravimetric method and the solutions were stored at 4 ℃ until usage.

### 2.2.2. Decellularization of porcine adipose tissue

Pig omentum tissue was collected from the local butcher shop and cleaned meticulously with autoclaved water for removing any other residues such as blood, muscle, dirt, and debris. Decellularization of the porcine omental adipose tissue was carried out by following a previously reported protocol with brief modifications [206]. The adipose tissue was excised into smaller pieces and subjected to freeze-thaw cycles twice for better removal of the cells by thermal shock-induced cell death and disruption of cellular membranes through ice crystal formation [222]. Further, the tissue slices were homogenized, followed by centrifugation at 6500 rpm for 15 min. The upper oil layer was removed, and the process was repeated till the whole oil content was taken out. The obtained pellet was then freeze-dried. For decellularization, the pellets were treated with a hyperosmolar solution of 1.5 M sodium chloride (NaCl, HiMedia, India), 0.5% SDS (HiMedia, India), and enzymatic mixture of 0.1 mg/mL DNase-1 (Sigma-Aldrich, USA) and 20 µg/mL RNase –A (Sigma-Aldrich, USA) for 24 h on a shaker at 37 ºC. The sample was then centrifuged and thoroughly washed with autoclaved Milli-Q. The ECM pellets were frozen in molds and lyophilized to fabricate dECM scaffolds and stored at -20°C for further experiment.

### 2.2.3. DNA quantification and biochemical estimations of native and dECM

For DNA and sulfated GAG (sGAG) estimations, lyophilized samples of porcine omentum before and after decellularization were digested at 60°C for 16 h in papain digestion buffer consisting of 125 µg/mL papain (Sigma-Aldrich, USA), 5 mM l-cysteine (Sigma-Aldrich, USA), 100 mM $Na_2HPO_4$ (Merck, India), and 5 mM ethylenediaminetetraacetic acid (EDTA, Sigma-Aldrich, USA). The digested ECM solution was centrifuged at 12,000 rpm for 3 min and supernatant was used for further estimations. DNA quantification of the samples was performed using Quant-iT™ PicoGreen® dsDNA assay kit (Invitrogen, Life Technologies, USA) according to the manufacturer's protocol. The amount of sGAG was estimated using 1,9-dimethylmethylene blue (DMMB, Sigma-Aldrich, USA) assay following previously established protocol [223] by measuring the absorbance at 525 nm using Thermo Scientific™ Multiskan™ Sky Microplate, with reference to bovine tracheal chondroitin sulfate (Sigma-Aldrich, USA) as standard. Collagen estimation of the samples was performed using Sirius red assay[224]. Briefly, 100 µL of pepsin digested sample solution per well was kept for drying at 37 °C for 24 h. Next, the samples were treated with 100 µL of Sirius red dye (1mg/mL) solution for 1 h and fixed with a fixing solution for 10-20 min (1 mL of glacial acetic acid, 5 mL of 35% formaldehyde, and 15 mL of picric acid). The samples were washed with 0.01 N HCl and kept for drying at room temperature. The samples were then dissolved in 0.1 N NaOH and absorbance was recorded at 550 nm. A standard calibration curve was plotted taking rat collagen type-1 (0-100 µg/mL) as standard for the estimation. The total protein concentration of the samples was measured using Bradford reagent (Sigma-Aldrich, USA). 20 µL of samples was incubated with 200 µL of Bradford reagent for 5 min and the absorbance was measured at 595 nm. Bovine serum albumin (BSA) was used for plotting a standard curve for the protein estimation.

### 2.2.4. Histological and immunohistochemical analysis of dECM

The samples of porcine omentum before and after decellularization were fixed in 10% neutral buffered formalin (NBF) solution and cryosectioned into 10 µm thickness for further staining. hematoxylin and eosin (H&E) and Masson's trichrome (MT) staining were performed to assess the removal of cellular components and collagen preservation, respectively. The sections were also immunostained with specific markers against ECM components (i.e. Col I and IV, fibronectin, elastin) and counterstained with 4',6-diamidino-2-phenylindole (DAPI) to evaluate their retention after the decellularization process. The images were captured using a Nikon

ECLIPSE Ti2 inverted microscope (Nikon Instruments Inc., Japan) and processed using ImageJ software (NIH, USA).

### 2.2.5. Fabrication SF-dECM scaffold and its characterization

The aqueous solutions of BmSF (3% w/v) and AaSF (3% w/v) were mixed in equal volume and kept 37 °C for 10 min to form pregel solution. 350 µL of pregel solution was then injected into per 50 mg of freeze-dried dECM scaffolds and kept at 37 °C for 20 min for completion of temperature-induced self-assembly of two varieties of SF protein chains [11]. The gelation time of blended SF hydrogel was estimated through turbidity analysis at 600 nm. Fourier transform infrared (FTIR) spectroscopy of the matrices was performed using ATR- FTIR spectroscopy (PerkinElmer, USA) in the spectral range of 600 and 4000 $cm^{-1}$ and averaged over 20 scans. The obtained spectra were normalized using OriginPro 2019 (OriginLab Corporation, USA). To ascertain the alteration in the secondary structure of SF proteins after gelation, the characteristic peaks of amide regions were examined. MT staining of dECM scaffold, SF hydrogel, and SF-dECM hydroscaffold was performed to analyze the distribution of dECM and SF inside the fabricated hydroscaffold. For the control groups of the study, the widely used rat tail collagen type I (Thermo Fisher scientific, USA) was used to prepare the Col pregel solution, following manufacturer's protocol. The pH-neutralized Col pregel solution was kept at 37 °C for 20 min to fabricate Col gel. In case of Col-dECM hydroscaffold, 350 µL of pregel Col solution was injected into per 50 mg of dECM scaffold and kept at 37 °C for 20 min for gelation, mirroring the fabrication process used for SF-dECM. The surface morphology of lyophilized matrices was analyzed using field emission scanning electron microscopy (FESEM; Zeiss Sigma, Carl Zeiss AG, Germany).

### 2.2.6. *In vitro* degradation study

*In vitro* degradation and integral stability of the fabricated scaffolds were assessed by immersing them in 2 U/mL of protease XIV solution (Sigma–Aldrich, USA, ≥3.5 U/mg) from *Streptomyces griseus* at 37 °C. The scaffolds were retrieved at regular intervals and weighed. The percentage of weight remaining of the scaffolds was calculated using following formula,

$$Weight\ remaining\ (\%) = \frac{Wt}{Wi} \times 100$$

Where $W_i$ and $W_t$ are the initial weight and weight of the construct at the particular time (t), respectively.

### 2.2.7. Assessment of moisture retention ability

For assessment of moisture retention ability, the weights of the samples were recorded initially and then dipped in phosphate buffered saline (PBS) for 30 min. Next, the wet matrices were kept in a dry incubator at 37 °C. After 0, 6, 12, 24, 36, 48, 60, and 72 h, the weights of matrices were measured, and the scaffolds were freeze-dried to measure their dry weights at last. The following formula was used to calculate the remaining water content percentage in the matrices at specific time intervals,

$$Remaining\ water\ content\ (\%) = \frac{Wt - Wd}{Wi - Wd} \times 100$$

Where $W_i$, $W_t$, and $W_d$ are the initial weight of wet scaffold, the weight of the wet scaffold at the particular time (t), and weight of the lyophilized dry scaffold, respectively.

### 2.2.8. Assessment of mechanical property

The mechanical property of the scaffolds was characterized through assessment of tensile properties of the scaffolds. All tests were performed on a computer-controlled universal testing machine (Instron 5944, USA). The scaffolds were prepared in rectangular shapes (5×2×T $cm^3$; T is the thickness of the scaffolds, measured by vernier caliper). Before the test, the scaffolds were soaked in PBS (pH 7.2) for 30 min, followed by removing the excess water using filter papers. The uniaxial tension experiment was performed with a deformation rate of 1 mm/min at room temperature until the scaffolds ruptured. tensile modulus, and ultimate tensile strength (UTS) were estimated from the stress-strain curves. The reported results were expressed as mean ± standard deviation (n = 5).

### 2.2.9. Assessment of cellular viability and proliferation

The cellular proliferation assessment of the matrices was performed by using HDF (Himedia, India). The cells were sub-cultured in high glucose Dulbecco's Modified Eagle's Medium (DMEM; Gibco, USA) supplemented with 10 % FBS. Next, the UV-sterilized matrices were conditioned with media for overnight and seeded with $10^5$ cells/$cm^2$ using static seeding technique. The cell-seeded constructs were kept in incubator (37 °C in humid atmosphere with 5 % $CO_2$) for 2 h to enable cellular adherence on the matrix, followed by adding more media in the wells to immerse the matrices in culture media. To evaluate the number of live cells, the cell seeded matrices after day 1 and 14 were stained with 2 µM ethidium homodimer-1 (EthD-1) and 2 µM calcein-AM (Sigma-Aldrich, USA) in PBS for 15 min. The constructs were washed with PBS gently and were imaged under hydrated conditions using a fluorescent

microscope (Nikon ECLIPSE Ti2, Japan). The representative images are presented with live cells exhibiting green fluorescence of calcein-AM dye and dead cells appearing red due to penetration of EthD-1 through damaged cell membrane. Further, proliferation of seeded cells was quantified by DNA quantification assay using Quant-iT™ PicoGreen® dsDNA Kit (Invitrogen, Life Technologies, USA), following the manufacturer's instruction.

### 2.2.10. Angiogenic potential assessment

The leachate was collected after immersing the matrices into media for 48 h and used for tube formation assay following previously reported protocol [225]. Briefly, human umbilical vein endothelial cells (HUVEC) were seeded (1 x $10^4$ cells/well) on 100 µL of preformed Col gel in each well of a 96 well plate. The endothelial culture media mixed in the ratio of 1:1 with leachate media were added in the wells and the *in vitro* tube formation was assessed after 16 h by calcein-AM staining as per protocol mentioned earlier. The obtained fluorescent images were analyzed to calculate the number of node formations. The representative fluorescent images from all groups are presented. The amount of vascular endothelial growth factor (VEGF) in dECM was measured by enzyme-linked immunosorbent assay (ELISA) following the manufacturer's protocol.

### 2.2.11. *In vivo* wound healing assessment in rat model

All animals were procured from Palamur Biosciences, Telangana, and the experiments were performed as per the ''Principles of laboratory animal care approval no. NIPS/NIPER/PC/2018-03-07. The protocol was approved by 'Institutional Animal Ethics Committee (IAEC) NETES NITS, Animal Facility Mirza Assam (CPCSEA Approval no.1996/PO/Re/S/17/CPCSEA). Male Wistar rats were used for the animal experiments, with weights ranging from 200-300 g. Diabetic induction of the animals was carried out by injecting streptozotocin (STZ; Sigma Aldrich, USA) drug solution (45 mg/kg) intraperitoneally [226]. All the animals are continuously monitored for toxicity symptoms such as dehydration, nausea and vomiting, weight loss, etc., and also after every 72 h the blood glucose levels were examined using a glucose meter (Accu-Chek® Inform II system, Roche Diagnostics, UK). Diabetic condition of rats was confirmed by monitoring constant high blood glucose level (>250 mg/dL) for a period of at least 3 weeks. The animals were randomized into three groups for different time points (7, 14 and 28 days). Intraperitoneal co-administration of xylazine hydrochloride (12 mg/kg; Xylaxin®, Indian Immunologicals, India) and ketamine (80 mg/kg; Ketalar®, Parke-Davis, India) was performed for anesthesia prior to wounding. The full-thickness skin excision was carried out using a biopsy punch of diameter 10 mm on the dorsal

side of each animal. The generated wounds were divided into the following groups: untreated control (UNT), Col gel, SF gel, Col-dECM and SF-dECM. dECM scaffolds were placed gently on the wound bed and Col and SF pregel solutions were injected in case of Col-dECM and SF-dECM groups. After application of matrices, a secondary dressing, Tegaderm (transparent film dressing), was employed, followed by the application of sterile gauze and an adhesive medical bandage to securely cover the wound area. On days 1, 3, and 5 following the injury, all of the animals received intramuscular injections of ceftriaxone (20 mg/kg) and meloxicam (5 mg/kg) during the treatment. The wounds were monitored and photographed on 0, 3, 7, 14, 21, and 28 days. The wound tissues were collected at different time points (day 7, 14, and 28). The experimental procedure was performed with care to reduce the distress of animals. Next, the wound areas were estimated from the gross wound images using ImageJ software, and the relative percentage area of wound was calculated using the following formula,

$$Relative\ area\ of\ wound\ (\%) = \frac{At}{Ai} \times 100$$

Where $A_i$ and $A_t$ are initial wound area and wound area at the particular time (t), respectively.

### 2.2.12. Histological and immunostaining of healing tissue

The collected wound tissues were fixed using 10 % NBF, followed by cryosectioned with a thickness of 10 µm using cryomicrotome (Leica Biosystems, Germany) to investigate the healing process. Initially, the histological analysis of healing tissue was performed through H&E staining of the tissue sections. The total collagen of the sections was examined by MT staining using a Trichrome Stain (Masson) Kit (Sigma–Aldrich, USA) according to the manufacturer's protocol. Immunohistochemistry (IHC) of collagen type I was performed to evaluate the extent of Col I deposition in the regenerated skin, using Vectastain Elite Universal ABC kit (Vector Laboratories Inc., USA) following the manufacturer's protocol. The sections were counterstained with hematoxylin and images were captured using Nikon ECLIPSE Ti2 inverted microscope (Nikon Instruments Inc., Japan). Similarly, the sections were also stained with antibodies against cytokeratin 14 (CK14), and cytokeratin 10 (CK10) for the analysis of epithelial regeneration. Further, the sections of excised tissues were analyzed by immunofluorescence using following antibodies: anti-CD31, anti-αSMA, anti-CCR7, and anti-CD206 (Abcam, UK). The sections were then incubated with DyLight® 594 and Alexa Fluor® 488 labelled secondary antibody, counterstained with DAPI, and imaged using the fluorescence microscope.

### 2.2.13. Statistical Analysis

Reported data were expressed as mean ± standard deviation. The statistical analysis of data was done using OriginPro 2019 software (OriginLab Corporation, USA) at multiple significance levels, * $p \leq 0.05$, ** $p \leq 0.01$, *** $p \leq 0.001$. The significance levels were calculated by comparing the data between the groups and within groups validated using one-way analysis of variance (ANOVA) followed by Tukey's test. The microscopic images were taken at least 6 fields per section for histological analysis and ImageJ software was used to analyze these images.

## 2.3. Results and discussion

### 2.3.1. Porcine omental adipose decellularization and biochemical characterization

Xenogenic dECM was isolated from porcine omental adipose tissue using a combined process of mechanical and chemical treatments **(Figure 2.1A)**. The purpose of decellularization is to

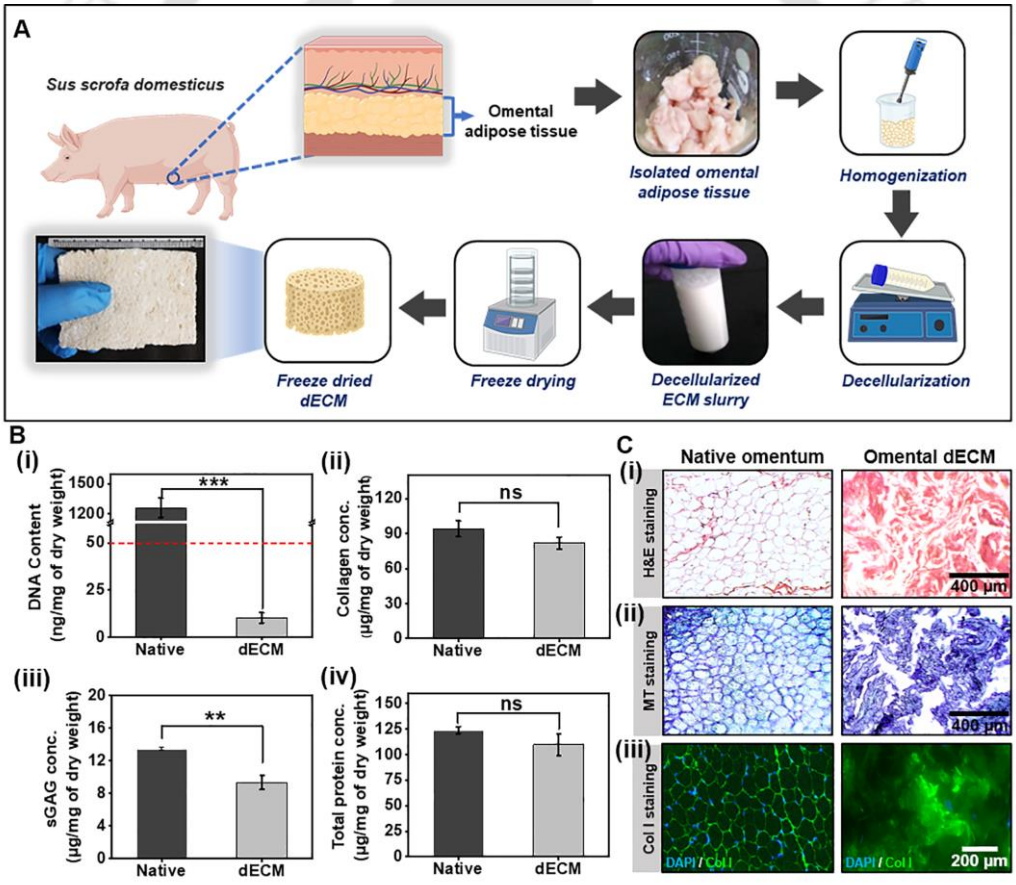


***Figure 2.1. Decellularization of omental tissue and its characterization.*** *(A) Schematic representation of decellularization process of porcine omental adipose tissue to prepare freeze-dried dECM scaffold (Created with BioRender.com). (B) Biochemical characterization of native omental adipose tissue and dECM (i) DNA content (the red dashed line represents previously reported permissible limit of DNA (50 ng) in decellularized matrix), (ii) collagen concentration, (iii) sGAG content, and (iv) total protein content. (C) (i) H & E, (ii) MT, and (iii) Col I immunofluorescence stained images of native omental adipose tissue and dECM. Values are plotted as mean ± standard deviation, where **$p \leq 0.01$, and ***$p \leq 0.001$.*

effectively eliminate all cellular and nuclear components [227], because cellular antigens may elicit immune-mediated rejection after implantation due to xenogenic immune response[228]. To assess the efficiency of the decellularization process, the presence of DNA in dECM was quantified. The DNA content of the dECM (10.2 ± 2.8 ng/mg of dry weight) was significantly reduced in comparison to the native porcine adipose tissue (1260.7 ± 95.3 ng/mg of dry weight), suggesting effective removal of cellular components ($p \leq 0.001$) **(Figure 2.1B.i)**. The isolated dECM satisfies the standard criteria of containing less than 50 ng of DNA/mg of its dry weight[229]. In addition, the dECM contains essential ECM components such as collagen (81.8 ± 5.2 µg/mg ECM dry weight) **(Figure 2.1B.ii)** and sGAG (9.4 ± 0.8 µg/mg ECM dry weight) **(Figure 2.1B.iii)**. The total protein was also not significantly different among native and dECM **(Figure 2.1B.iv)**. H&E staining also revealed the absence of nuclear material in dECM, validating effective removal of cells **(Figure 2.1C.i)**. MT staining and Col I (counterstained by DAPI) staining further confirm the retention of protein components and collagen in dECM after decellularization, indicating minimal loss of the matrix **(Figure 2.1C.ii&iii)**. Notably, other structural proteins Col IV, elastin, and fibronectin were maintained in dECM, hence preserving microarchitecture of the native tissue **(Figure 2.2)**.

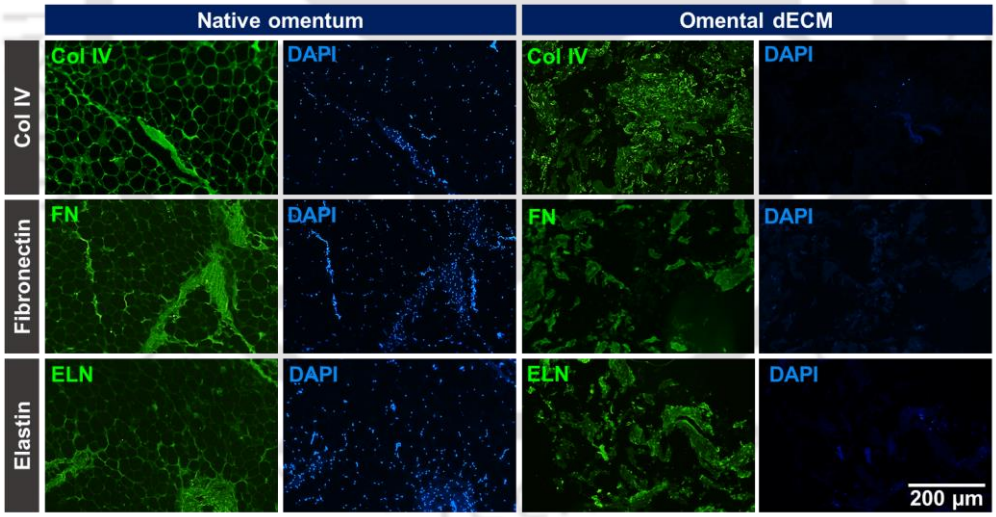


***Figure 2.2. Assessment of other ECM components in isolated dECM.*** *Representative immunofluorescence images of native omental adipose tissue and dECM, showing retention of essential ECM proteins (Col IV, fibronectin, and elastin) after decellularization process.*

### 2.3.2. Fabrication of SF-dECM scaffolds and physicochemical characterization

SF-dECM hydroscaffolds were fabricated by injection of 3% (w/v) blend solution (1:1 ratio) of two different naturally derived SF proteins isolated from *Bombyx mori* cocoons and *Antheraea assamensis* silkworms into the freeze-dried dECM scaffold at pregel condition

**(Figure 2.3A)**. The composite was then kept at 37 °C for 20 min for gelation. The gelation mechanism of SF hydrogel was assessed by detecting turbidity change through UV-visible spectroscopy. The rise in absorbance in blend solution at 10-20 min suggests rapid increase in crosslinking between SF protein chains **(Figure 2.3B)**. Blending of two types of SF fibroins together leads to self-assembly of SF chains and transformation into hydrogel in the absence of any chemical cross-linker [218]. The spontaneous formation of the SF hydrogel occurs through a conformational transition of SF chains from an amorphous to β-sheet structure. When two SF proteins with varying hydropathicities are combined, the protein chains are intended to interact with each other through hydrophobic interactions. During the initial stage of gelation, the hydrophobic regions within the protein chains undergo reorganization, promoting interchain interactions. As the gelation process continues, the intrachain interaction further enhances this phenomenon [218]. The crosslinking between BmSF and AaSF proteins in SF hydrogel was further validated using FTIR spectroscopy. The FTIR data showed the conformational changes with respect to change in secondary structure (β-sheets formation) in SF hydrogel with the signature peak shifts at amide I (from 1640 $cm^{-1}$ to 1620 $cm^{-1}$) and II (from 1538 $cm^{-1}$ to 1515 $cm^{-1}$) regions, corresponding to C = O stretching vibration of the peptide group and N – H bending with a contribution from C – N stretching vibrations, respectively **(Figure A2.1)** [230, 231]. After blending of SF with dECM scaffolds, similar protein-specific peak shifts at amide I (from 1640 $cm^{-1}$ to 1622 $cm^{-1}$) and amide II (from 1535 $cm^{-1}$ to 1514 $cm^{-1}$) regions were observed after temperature-induced crosslinking of SF **(Figure 2.3C&D),** indicating increase of β-sheet structure due to the gelation process [232]. In addition, dECM, SF-dECM uncrosslinked and crosslinked scaffolds showed prominent characteristic peaks of ECM components. The collagen-specific amide A and amide B band peaks were observed at around 3826 and 3065 $cm^{-1,}$ corresponding to stretching vibrations of N – H and O – H [233] **(Figure 2.3C)**. The peaks observed at 2920 and 2854 $cm^{-1}$ are assigned to the symmetric and asymmetric modes of $CH_2$ bending[234] and the peak observed at 1740 $cm^{-1}$ corresponds to ester C = O stretching vibrations of phospholipids [230]. The alterations in microarchitecture of dECM scaffolds when infused with SF blend to fabricate the composite hydroscaffold, were examined through histological analysis. MT staining of SF-dECM demonstrated the distribution of SF network within the composite **(Figure 2.3E)**. The predominantly blue-stained collagenous dECM was supported by the fibrous SF hydrogel network, suggesting potential enhancement of mechanical robustness of the composite scaffold.

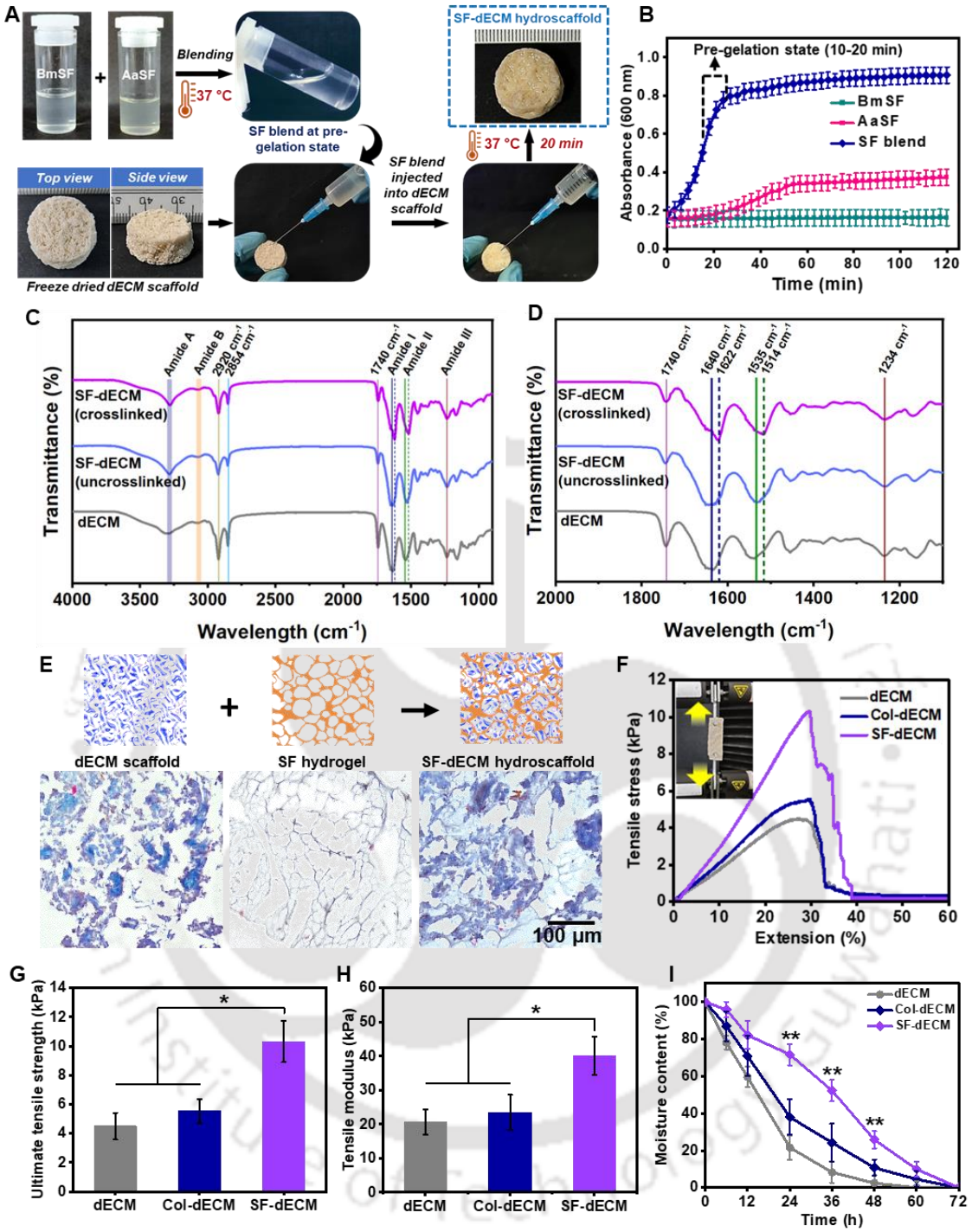


***Figure 2.3. Fabrication and physicochemical characterization of SF-dECM hydroscaffold.*** *(A) Stepwise photographic images of SF-dECM hydroscaffold preparation process. (B) Gelation kinetics analysis of the pristine BmSF and AaSF solutions and blend solutions at 37 °C. (C) FTIR spectra of dECM, SF-dECM uncrosslinked and crosslinked hydroscaffolds in whole mid-infrared region (4000-1000 $cm^{-1}$), (D) the corresponding spectra in the region of 2000-1000 $cm^{-1}$. (E) i) Schematic representation depicting microarchitecture of dECM scaffold, SF hydrogel, and SF-dECM hydroscaffold.* ***ii)*** *Histological analysis of the fabricated matrices through MT staining, showing the distribution SF inside the hydroscaffold structure. (F) Tensile stress curve of dECM scaffold and hybrid scaffolds and (G) the corresponding ultimate tensile strengths (UTS), (H) tensile modulus. (I) Assessment of moisture retention ability of the dECM scaffold and hydroscaffolds. Values are plotted as mean ± standard deviation, where * $p \leq 0.05$, ** $p \leq 0.01$.*

### 2.3.3. Assessment of mechanical properties and moisture retention ability

The mechanical properties of the dECM and hydroscaffolds were assessed from stress vs strain curves plotted from the obtained data through a uniaxial tensile test **(Figure 2.3F)**. UTS of SF-dECM hydroscaffolds (10.32 ± 1.42 kPa) was significantly higher ($p \leq 0.05$) than the UTS of dECM (4.50 ± 0.90 kPa), Col-dECM (5.53 ± 0.84 kPa) **(Figure 2.3G)**. Therefore, a noticeable enhancement of mechanical strength of dECM was observed when SF hydrogel was incorporated. The tensile moduli of the scaffolds were calculated and SF-dECM (40.13 ± 5.73 kPa) was significantly ($p \leq 0.01$) higher than that of only dECM (20.64 ± 3.78 kPa) and Col-dECM (23.45 ± 5.22 kPa) **(Figure 2.3H).** It can be concluded that the SF biopolymer aided in improving the mechanical properties of the fabricated hybrid scaffold. SF, with more mechanical strength than collagen [11], also improved the physical properties of the fabricated composite over Col-dECM, enabling easier handling with forceps in wet conditions and benefiting practical applications. Additionally, an ideal wound dressing must possess optimum hydrophilicity to prevent dehydration at the wound bed. The surface wettability of the dressing modulates the adsorption of proteins and cellular adhesion, migration, and proliferation [235]. Analysis of the moisture retention ability of the constructs demonstrated significantly higher ($p \leq 0.001$) water retention ability of SF-dECM compared to dECM and Col-dECM after incubating them in a dry incubator at 37 °C. After 24 h, the moisture content of dECM, Col-dECM, and SF-dECM were 21.60 ± 6.65 %, 37.99 ± 9.59 %, and 71.71± 5.75 %, respectively. A similar significant difference ($p \leq 0.001$) in moisture content was observed even after 36 h, when moisture content percentages of dECM, Col-dECM, and SF-dECM were 8.23 ± 5.69 %, 24.24 ± 10.11 %, and 52.29 ± 5.72 %, respectively **(Figure 2.3I)**. Therefore, the presence of SF hydrogel component in SF-dECM aided in improving water holding capacity of the construct[11] and can offer a moist environment to the wounds for a prolonged period of time, which can facilitate the overall healing process.

### 2.3.4. Analysis of surface morphology and *in vitro* degradability of hydroscaffolds

The surface morphology of the fabricated hydroscaffolds along with the corresponding pristine materials was investigated through FESEM analysis **(Figure 2.4A)**. The FESEM images of the hydrogels showed formation of three-dimensional porous hydrogel networks in both Col and SF gels, with SF displaying network characterized by larger pores than Col gel. All the dECM-based matrices showed random alignment of the collagenous fibers of ECM, resembling anisotropic alignment of collagen fibers of skin tissue. Presence of a distinct SF network supporting dECM structure inside the SF-dECM composite corroborates the enhancement of the mechanical properties and stability of the matrix. The stability of the fabricated constructs was evaluated under *in vitro* condition, immersed in a protease solution as the dressing material became exposed to a highly proteolytic microenvironment of a chronic wound after application on the wound bed. A highly significant difference ($p \leq 0.01$) was observed in remaining weight when the constructs were immersed in protease solution compared to the control group (constructs immersed in PBS) **(Figure 2.4B)**. In protease treatment, silk-based matrices

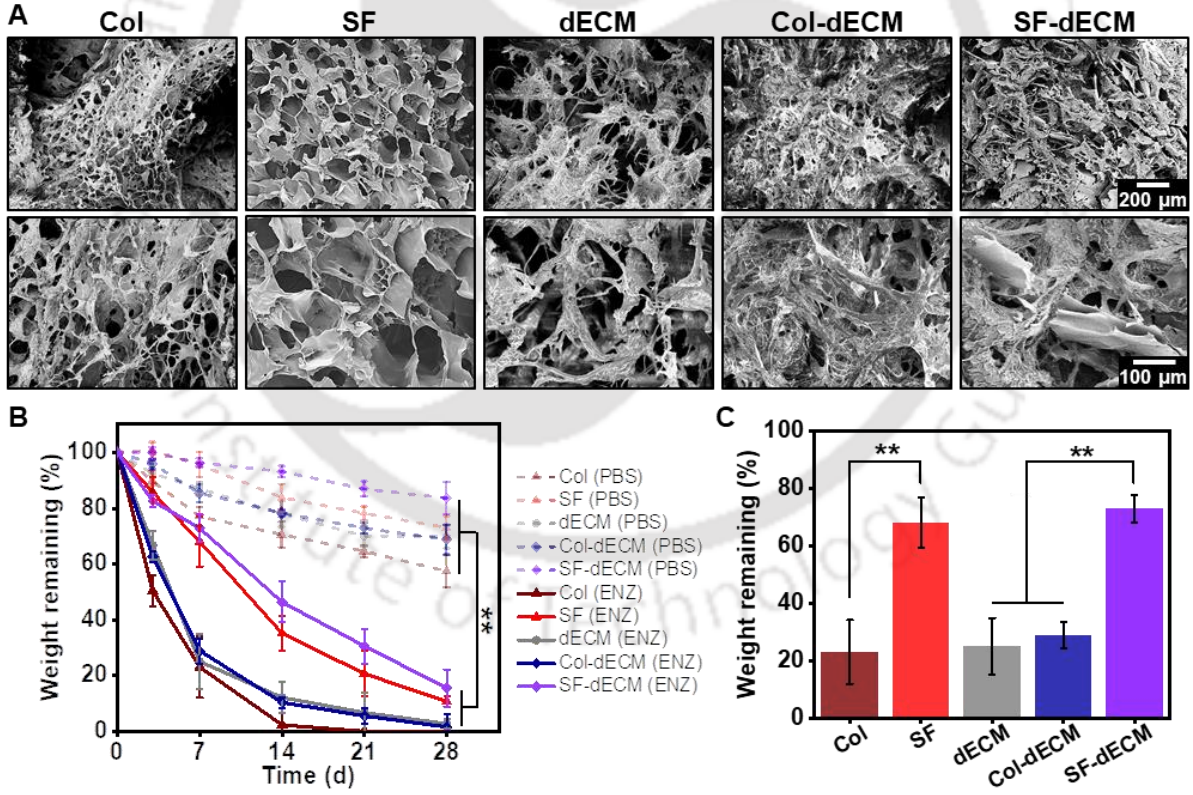


***Figure 2.4. Analysis of surface morphology and in vitro stability of hydroscaffolds and their respective discrete forms.*** *(A) FESEM images of the fabricated matrices at different magnifications, showing their porous fibrous microarchitecture. (B) In vitro degradation analysis of the matrices immersed in PBS and enzymatic solution at 37 °C for 28 days. (C) Weight remaining percentages of the matrices immersed in enzymatic solution at 37 °C on day 7, showing significant improvement of stability of SF-dECM due to presence of SF hydrogel. Values are plotted as mean ± standard deviation, where ** $p \leq 0.01$.*

demonstrated higher stability than the Col-based matrices. Remaining weights of Col, SF, dECM, Col-dECM, and SF-dECM on day 7 were 23.03 ± 11.06 %, 68.05 ± 8.86 %, 25.03 ± 9.87 %, 28.84 ± 4.52 %, and 72.84 ± 4.86 %, respectively **(Figure 2.4C)**. The significant difference ($p \leq 0.01$) in remaining mass between SF-dECM and other dECM-based scaffolds highlights the stability of hydrogel networks attributed to the formation of β-sheet structures in SF gel.

### 2.3.5. Biocompatibility and cellular proliferation assessment

HDF were seeded on the following matrices: Col gel, SF gel, dECM scaffold, Col-dECM hydroscaffold, and SF-dECM hydroscaffold for comparative analysis. Due to lack of crosslinking, rapid dissolution of dECM has been observed within 7 days in culture media. Live/dead staining was performed to evaluate the cellular viability of HDF remaining groups, and z-stack staining images on day 14 showed that the majority of cells were viable for all the groups **(Figure 2.5A)**. For quantitive analysis, DNA quantification of HDF cultured on hydrogels and hydroscaffolds suggested that all variants augmented the proliferation of HDF till 14 days, except dECM group due to disintegration. A Significant difference was observed in the proliferation of HDF between the hydrogel variants and hydroscaffold on day 7 ($p \leq 0.05$). HDF proliferation was significantly higher ($p \leq 0.01$) in Col-dECM and SF-dECM than in the hydrogels Col and SF on day 14 **(Figure 2.5B)**.

### 2.3.6. *In vitro* assessment of angiogenic potential of hydroscaffold

Newly formed blood vessels deliver nourishment and oxygen across the provisional granulation tissue during wound repair [236]. In this context, proliferation of endothelial cells and tube formation are critical steps in the angiogenesis process, which directly corresponds to the rate of healing process. Initially, human umbilical vein endothelial cells (HUVEC) were cultured with dECM extract to evaluate its effect on endothelial cells. A significant increase in HUVEC proliferation was observed in cells treated with dECM extract ($p \leq 0.05$) in comparison to control group cultured with basal endothelial medium on day 3 **(Figure A2.2)**. The effect could be attributed to presence of regenerative ECM components combined with growth factors sequestered in sGAG [237]. In particular, expression of VEGF in adipose tissue has been investigated in rodent models[238] and VEGF has been identified as a major contributor to the angiogenic activity of omental adipose tissue [239]. Quantification of VEGF in porcine omental adipose dECM extract through ELISA showed presence of 48.3 ± 5.8 pg of VEGF in per mg of dry dECM **(Figure A2.3)**. Presence of VEGF indicates pro-angiogenic property of omental dECM, therefore, a tube formation assay has been performed to evaluate

the efficacy of hydroscaffolds in angiogenesis **(Figure 2.5C)**. Extracts from the groups containing omental ECM showed higher efficiency than hydrogel groups in promoting cell tube formation, characterized by more visible tube-like structures **(Figure 2.5D)**. Quantitative image analysis also supported that the number of tubular structures was significantly higher ($p \leq 0.05$) in dECM, Col-dECM, and SF-dECM than in the Col, SF, and negative control group **(Figure 2.5E)**. The formation of tube-like structures is an indication of angiogenesis under *in vitro* condition. The improved tube formation in presence of dECM highlights the inherent efficacy of omental ECM in influencing the angiogenic potential [240]. This observation also suggests that the engineered SF-dECM hydroscaffolds retain critical properties of the ECM after the fabrication process. This implies the potential of these hydroscaffolds to exert a pro-angiogenic effect during the granulation tissue formation, a crucial phase of healing process.

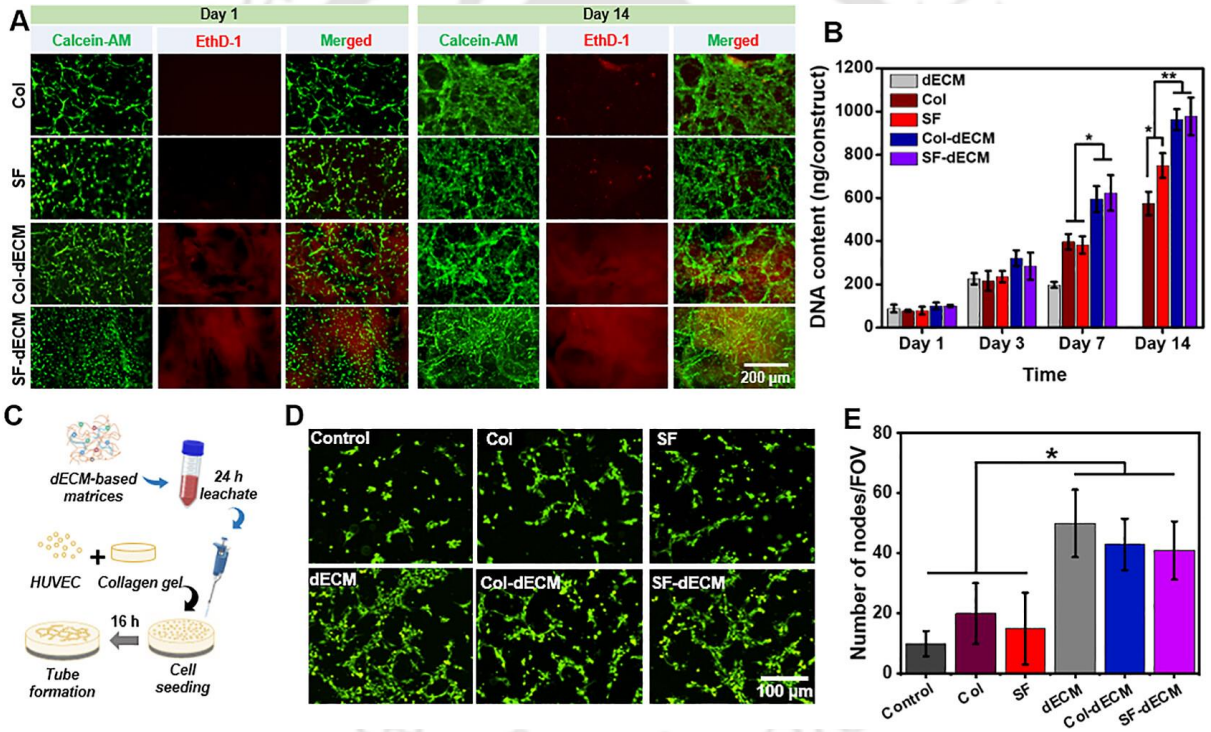


***Figure 2.5. Biocompatibility and angiogenic assessments of hydrogels and hydroscaffolds.*** *(A) Live/dead assay of HDF seeded on the hydrogels and hydroscaffolds. Live cells are shown in green (calcein-AM) while dead cells and matrices are shown in red (ethidium homodimer-1). (B) DNA quantification of HDF seeded on scaffolds and hydrogels after days 1, 3, 7, and 14. (C) Diagrammatic representation of the procedure of assessment of angiogenic efficacy of fabricated matrices. (D) Representative images of tube formation assay in HUVEC cultivated with leachates of hydrogels and hydroscaffolds. (E) Quantification of corresponding nodes/field of view (FOV) for comparison of angiogenic property among the experimental groups and control (treated with low serum medium). Values are plotted as mean ± standard deviation, where *$p \leq 0.05$, **$p \leq 0.01$.*

### 2.3.7. Planimetry analysis of diabetic wound closure

A diabetic rat model was first established by STZ injection **(Figure 2.6A)**. STZ is a highly selective pancreatic β-cell cytotoxic agent widely used to induce diabetes in rodents[241]. After STZ injection, the blood glucose level of the rats was monitored for 3 weeks and rats with blood glucose levels > 250 mg/dL were considered diabetic and chosen for the study. The animals were divided into the following groups: UNT, Col, SF, Col–dECM, and SF–dECM, and the matrices were applied on the full-thickness wounds generated on the dorsal side of the rats. In the case of the hydroscaffold groups, either Col or SF blend pregel solutions were injected into dECM scaffolds placed at wound site. In situ gelation of the pregel solutions at physiological temperature (37°C) ensured grafting of dECM scaffolds at wound site circumventing the need of additional suturing for attachment. Due to the absence of binding polymers such SF and Col or crosslinking agents, the bare dECM loses its integrity in the hydrated condition of wound bed. This led to disintegration of the dECM scaffolds and causing partial detachment, particularly during dressing changes every alternate day, as the parts of scaffolds tend to adhere to the secondary dressing rather than remaining securely attached to the wound bed. The other matrices were applied single time after wound generation in all the groups but the dECM scaffold required repeated applications after dressing changes. Hence, the only dECM group has been omitted for the *in vivo* analysis to ensure fair comparison among the groups. The gross examination of digital images of wounds revealed that the healing of untreated wounds was significantly delayed even after 20 days. The wound contraction was apparent for all the groups between days 7 and 14 **(Figure 2.6B)**. The wound areas were calculated from the photographic images using Image J software for quantitative analysis **(Figure 2.6C)**. The relative percentage areas of wounds on postoperative day 7 were 94.7 ± 6.9% in untreated group, 80.6 ± 5.2% in Col group, 75.5 ± 6.1% in SF group, 69.5 ± 4.7% in Col-dECM group, and 64.5 ± 4.7% in SF-dECM group. Meanwhile, a distinct difference in wound areas was observed between the untreated control group and experimental groups on day 14. The relative percentage areas of wounds on postoperative day 14 were 41.0 ± 5.4% in untreated group, 25.1 ± 3.1% in Col group, 26.9 ± 4.1% in SF group, 15.9 ± 3.4% in Col-dECM group, and 16.3 ± 3.4% in SF-dECM group **(Figure 2.6D)**. There were significant differences in the wound area percentages among the dECM containing composite groups (Col-dECM, SF-dECM) and the hydrogel-treated groups (Col, SF) ($p \leq 0.05$) and the untreated group ($p \leq 0.01$) on postoperative day 14 **(Figure A2.4)**. Therefore, presence of dECM was observed to be favorable for faster closer of the wounds in comparison to that of the hydrogels-treated

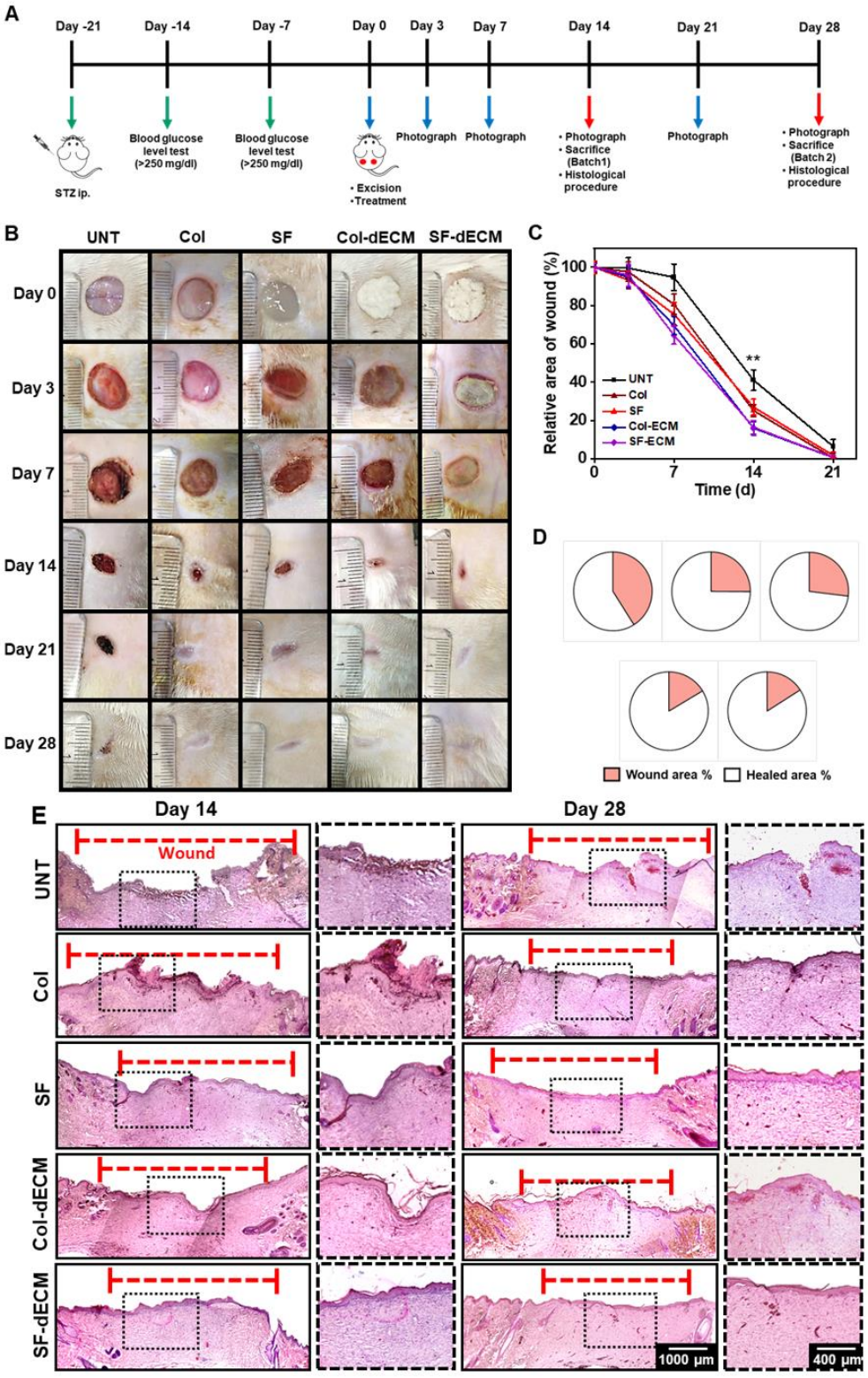


***Figure 2.6. In vivo assessment of hydrogels and hydroscaffolds in diabetic rat wound model.*** *(A) Diagrammatic representation of experimental plan of animal experimentation. (B) Photographic images of wound closure in different treatment groups and untreated control group on days 0, 3, 7, 14, 21, and 28. (C) Quantification of the wound area, determined by calculating the area of wounds using ImageJ software. (D) Fractions of area healed (mean value) in different treatment groups after day 14. (E) H&E staining of regenerated tissues to depict the wound morphologies after treatment on days 14 and 28. Values are plotted as mean ± standard deviation, where **p ≤ 0.01 for comparison between SF-dECM and untreated groups.*

wounds and untreated wounds, indicating influence of ECM components on cellular survival, proliferation, migration, and differentiation, essential for the proliferative stage of healing process [242, 243]. On day 21, the wounds treated with hydrogels and hydroscaffolds were observed to be completely closed whereas the untreated wounds showed delayed closure and took another 3-5 days for complete closure. The wound healing process is characterized by the formation of provisional granulation tissue, re-epithelialization, and regeneration of mature epidermo-dermal junction [189]. The granulation tissue formation and regenerated-tissue maturation were examined histologically on 14 and 28 days **(Figure 2.6E)**. Hydroscaffolds treated wounds showed more defined and thicker granulation tissue on day 14. Further, an intact neo-epidermis layer was formed at the wound sites in all treated groups except untreated group on day 28.

### 2.3.8. Collagen deposition and ECM remodelling

Production of collagen at the wound site is also an indication of restoration of damaged skin tissue. MT staining is an essential indicator for qualitative assessment of collagen deposition in the regenerated tissue. The deposited collagen stains blue, indicating collagen deposition and the structure of deposited collagen [244]. The SF-dECM group showed an even distribution of collagen fibers comparable to Col-dECM group, and fibers were thicker than that of untreated wounds on day 14 **(Figure 2.7A)**. Col I immunostaining confirms prominent deposition of Col I fibers in regenerated tissues in case of Col-dECM and SF-dECM groups **(Figure 2.7B)**. Quantification of the percentage area of Col I showed a significant difference ($p \leq 0.05$) in percent area in the field of view (FOV) in hydroscaffolds treated groups in comparison to other groups **(Figure 2.7C).**

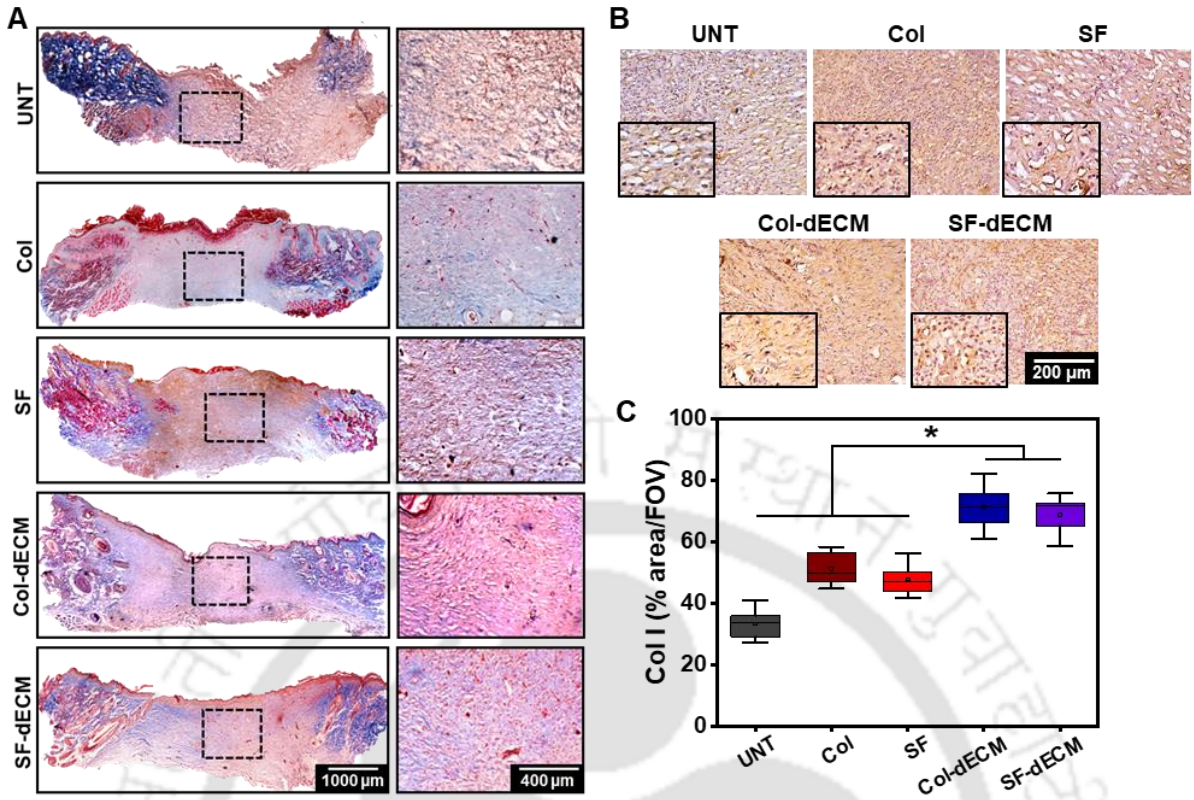


***Figure 2.7. Assessment of collagen content in dermal layer of regenerated tissue.*** *(A) MT staining of whole regenerated tissue after day 14 (left panel). Magnified images of the marked area showing newly formed collagen fibres at wound site. (B) Representative images of immunohistochemical staining of regenerated tissues showing expression of Col I on day 14. (C) Quantification of percentage area of Col I expression per FOV processed from immunohistochemical images. Values are plotted as mean ± standard deviation, where * $p \leq 0.05$.*

### 2.3.9. Angiogenic potential and immunomodulatory effect of SF-dECM

Angiogenesis is a critical step for tissue regeneration during the healing process. The angiogenic blood vessels penetrate the wound site from peripheral intact host tissue and form a microvascular network across the granulation tissue to supply oxygen and nutrients[245]. MT-stained images **(Figure 2.8A)** showed a higher number of blood vessels in the granulation tissue of the wounds treated with the hydrogels and hydroscaffolds in comparison to untreated wounds on day 14. Angiogenesis is specifically characterized by expression CD31 (a transmembrane protein) and α-SMA (a cytoplasmic protein), indicating neovascularization and maturation of vascular smooth muscle cells, respectively. As shown in **Figure 2.8A**, the relative fluorescence intensity of anti-CD31 and anti-α-SMA antibodies indicated a higher density of vessels in the dermis of wounds treated with Col-dECM and SF-dECM, compared with that in control and hydrogels–treated groups **(Figure 2.8B)**. Correspondingly, the quantification of fluorescence intensity of anti-CD31 from the captured images demonstrated

significantly higher expression of CD31 in Col-dECM and SF-dECM treated groups, in comparison to untreated control ($p \leq 0.05$) **(Figure 2.8C)**, correlated with the formation and maturation of newly formed blood vessels in the regenerated tissue. The obtained data validated the angiogenic potential of omental ECM, attributed to the presence of pro-angiogenic factors in the highly vascularized adipose tissue [237, 246]. The promotion of angiogenesis by dECM-based hydroscaffolds in early phase of healing holds substantial significance as the phenomenon aided in the formation of new blood vessels in the wound bed, essential for

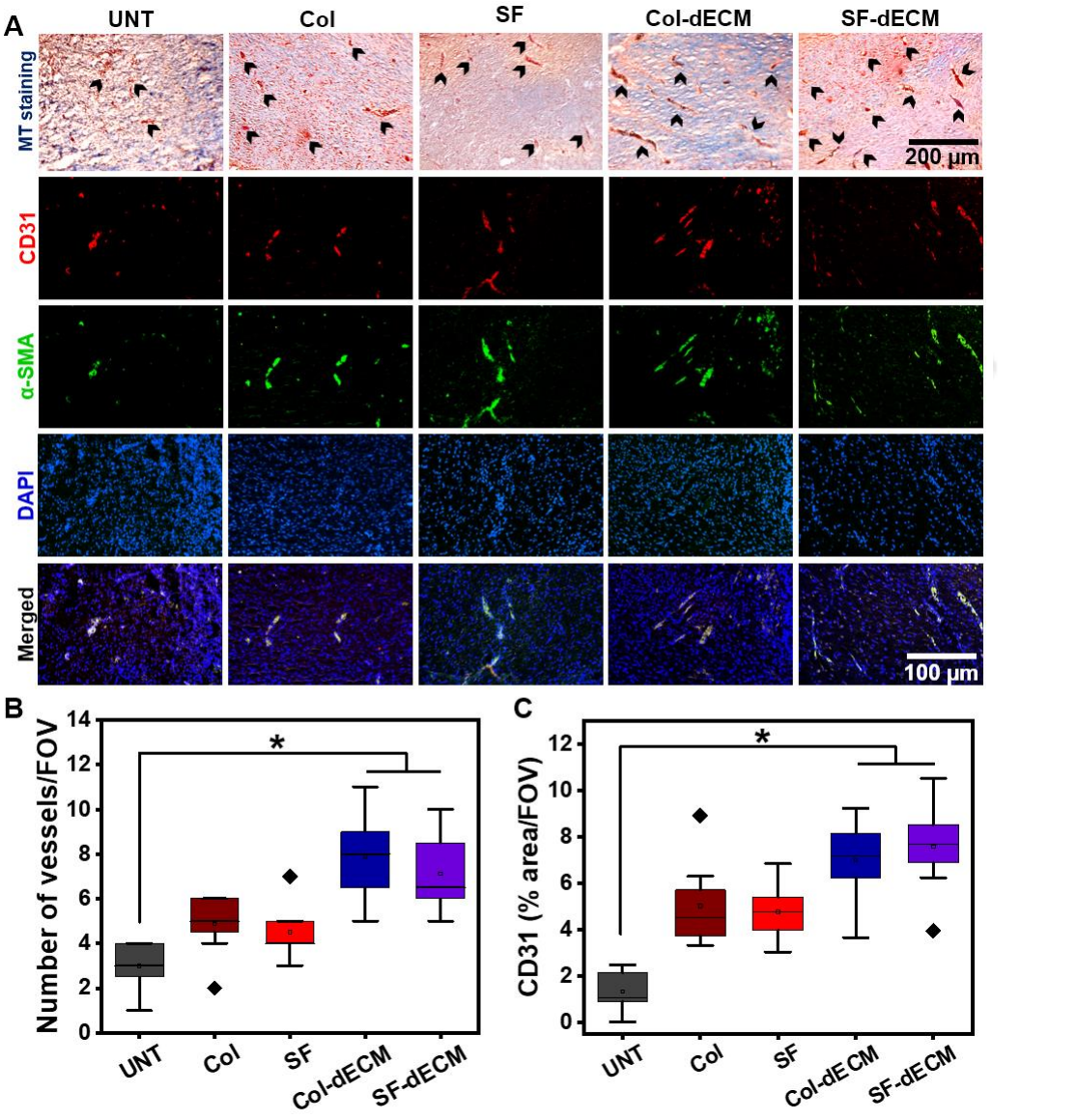


***Figure 2.8. Assessment of angiogenic effect of hydroscaffolds on wound sites.*** *(A) MT staining and immunostaining of regenerated dermal tissues for CD31 and α-SMA markers, showing newly formed blood vessels to provide nutrition and oxygen to growing tissues in proliferative phase of healing. Black arrows indicate the blood vessels in the tissue sections. (B) Measurement of number of blood vessels per FOV counted from the images. (C) Quantification of percentage area of fluorescent CD31 expression per FOV processed from the images. Values are plotted as mean ± standard deviation, where * $p \leq 0.05$.*

cellular sustenance [247]. Consequently, the hydroscaffolds facilitated a microenvironment conducive to the growth of newly formed granulation tissue, supporting the intricate processes involved in tissue regeneration and ultimately promoting the healing process.

In case of non-healing chronic wounds, one of the major challenges in treatment is the persistence of the chronic inflammatory stage, while normal wounds show acute inflammation that resolves within a few days [248]. The proinflammatory milieu of the wound bed is dominated by M1-type macrophages (pro-inflammatory) during the early stage of healing, and changes to M2-type macrophages (pro-remodelling) later stage, favouring cellular proliferation and tissue remodelling[249]. Inability of the macrophages to switch from M1-type to anti-inflammatory M2-type combined with prolonged inflammation, is a hallmark of chronic diabetic wounds [249]. Therefore, we investigated macrophage response towards the fabricated hydroscaffolds through immunostaining of $CCR7^+$ cells (M1-type macrophages) and $CD206^+$ cells (M2-type macrophages) **(Figure 2.9.A)**, along with quantification of the percentage areas of respective expression**.** On day 7, the presence of $CCR7^+$ M1-type macrophages was visible in all the groups during the early stage of healing in diabetic condition. Interestingly, the groups containing dECM, i.e. Col-dECM and SF-dECM showed significantly lower ($p \leq 0.01$) percentage areas of $CCR7^+$ macrophages compared to untreated group. A similar trend was observed on day 14 as well **(Figure 2.9.B)**. The data indicates rapid resolution of the inflammatory stage in the healing process in presence of dECM scaffolds. A significant difference ($p \leq 0.05$) between the percentage areas of $CCR7^+$ macrophages between SF and SF-dECM on day 14 was observed, suggesting immunomodulatory effect of the omental dECM, similar to other tissue-derived ECM [250, 251]. A limited number of $CD206^+$ M2-type macrophages was observed in the wounds treated with the hydroscaffolds on day 7, and the quantification showed a substantial increase ($p \leq 0.01$) of $CD206^+$ population in hydroscaffolds-treated groups compared to untreated group on day 14 **(Figure 2.9.C)**. The dynamic shift in the macrophage population from M1 to M2 reflects transitioning of wound microenvironment from inflammatory state to proliferative phase. The expedited M2 polarization suggests an immunomodulatory effect facilitated by the dECM present in the hydroscaffolds. Therefore, the regulation of macrophage polarization by the ECM components efficiently alleviated inflammation and accelerated regeneration, highlighting the potential of dECM hydroscaffolds as a promising immunomodulatory strategy for enhancing tissue repair.

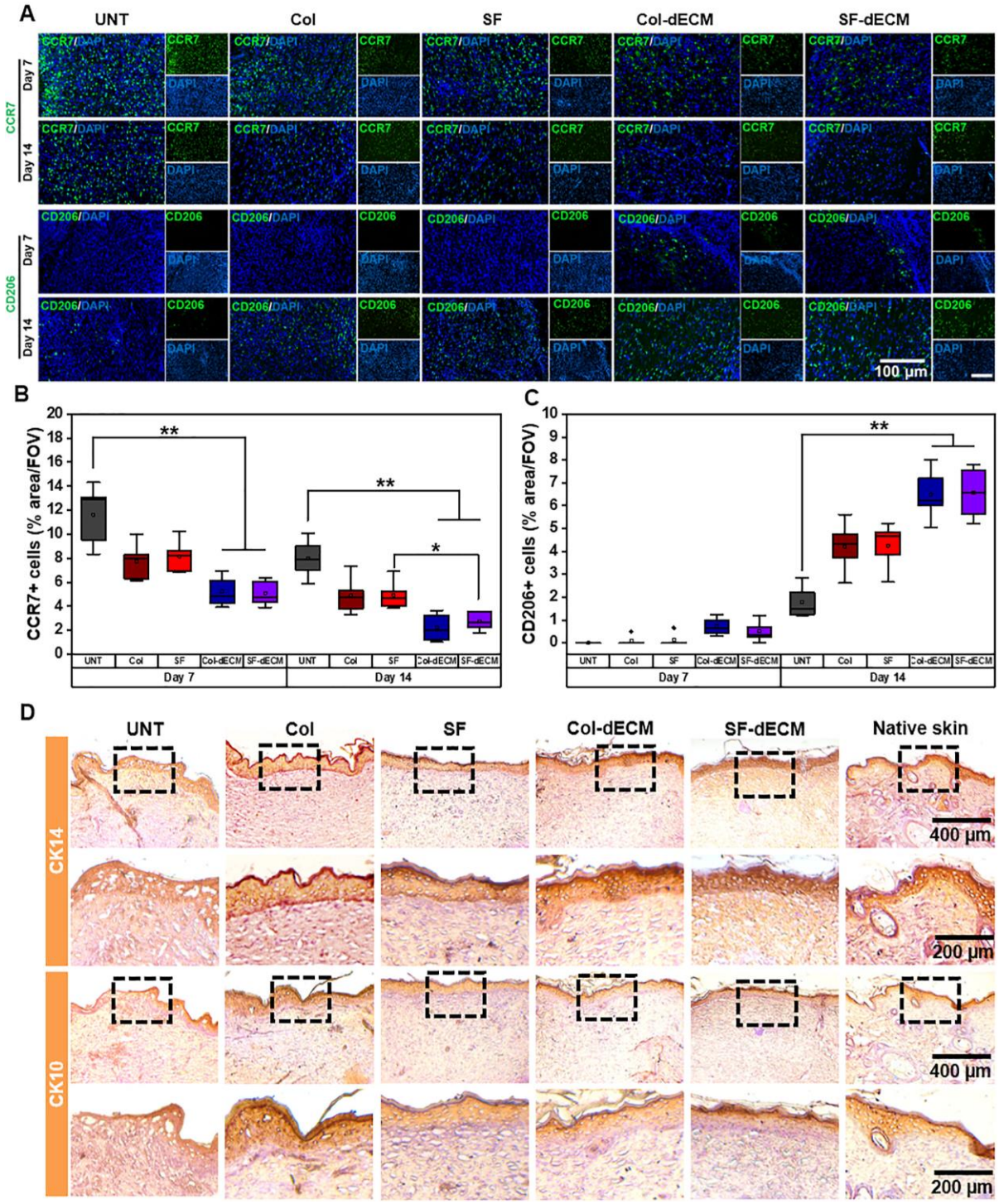


***Figure 2.9. Assessment of immunomodulation and reepithelization.*** *(A) Representative immunofluorescence images of granulation tissues on day 7 and 14 showing the expression of CCR7 (M1 phenotype) and CD206 (M2 phenotype), and quantification of percentage area of (B) CCR7+ and (C) CD206+ cells per FOV processed from the images. (D) Representative IHC images of regenerated tissue stained against CK14 marker (for proliferating basal keratinocytes) and CK10 marker (for terminally differentiated keratinocytes) after day 28. Values are plotted as mean ± standard deviation, where * $p \leq 0.05$, and ** $p \leq 0.01$.*

### 2.3.10. Examination and analysis of epithelial regeneration

Reepithelization is one of the most significant processes of the repair mechanism in the later stages of healing. After 28 days of wound healing, the expression of basal epithelial cell marker, CK14, and suprabasal epithelial cell marker, CK10, were assessed by immunostaining of the collected regenerated tissues. As shown in **Figure 2.9.D**, the expression of CK14 was prominently visible for all experimental groups. In contrast, the regenerated tissues in the untreated group possess breaches in epidermal layer, and the expression of CK10 was significantly lower than other experimental groups, validating incomplete maturation of epidermal layer even after 28 days. The CK10 expression in the regenerated tissue treated with Col-dECM and SF-dECM hydroscaffolds exhibited a deeper yellow colour at the outer edge of epidermal layer than the control group, representing more structural integrity of the keratinocyte layer and a higher degree of keratinization. Together, dECM-containing hydroscaffolds could expedite the regeneration of diabetic wounds by promoting the maturation of the epidermis layer and reconstruction of the dermis characterized by ordered collagen fibrils, improved angiogenesis, and differentiated epidermal layer, respectively.

Overall, the study validates the healing potential of SF-dECM-based hydroscaffolds without any xenogenic inflammatory response. However, previous studies reported that the extraction of adipose dECM requires pepsin-based digestion to solubilize it in a dilute acidic solution to prepare a hydrogel system [252, 253]. As the acidic solution might affect the biophysical properties of body fluids and hinder the healing process, therefore, adjustment of pH values is necessary before the application of the material[254]. The enzymatic digestion and acid-base neutralization not only weaken the mechanical properties of the ECM but also entailed a concurring risk of losing intrinsic cues, including paracrine signalling molecules [255, 256]. In order to retain the integrity of ECM and minimize the loss of essential ECM components, we utilized lyophilized dECM directly after the decellularization process. However, lack of physical/chemical crosslinking led to poor stability under *in vitro* and *in vivo* conditions, limiting its application as dressing; the inclusion of SF hydrogel not only ameliorated the stability of the composite but also improved the tensile property, which is a crucial characteristic of dermal matrices. In addition, SF protein from *Antheraea assamensis* possesses Arg-Gly-Asp (RGD) cell-binding motif, aiding in improved cellular recruitment at the wounded site. Thus, the combination dECM and SF hydrogel resulted in accelerated healing in diabetic conditions by providing necessary intrinsic cues to modulate the multiple stages of healing process. Matrices commonly available for skin tissue engineering are collagen-based

gels as they form regenerative templates intrinsically mimicking tissue microarchitecture. However, the efficacy of these matrices is compromised due to their inferior mechanical properties, resulting in faster graft contraction [11, 257]. Moreover, the high expenses associated with collagen matrices due to their intricate production and purification process, cause a significant disparity between the demand for these matrices and their availability [258]. The comparable healing efficacy of Col-dECM and SF-dECM supports the postulation of utilizing SF-dECM based matrices as low-cost and easily producible alternatives to these current treatment modalities. Further, validation of fabricated composite with larger animal models, followed by clinical studies, is essential to definitively corroborate the efficiency of the hydroscaffold in diabetic wound healing. Alternatively, the hydroscaffold system can be further explored for the fabrication of *in vitro* skin model due to its similarities with native tissue ECM in their physico-chemical properties. The composite can also be easily functionalized with drug molecules and/or antibiotic agents for localized drug delivery applications and the treatment of infected wounds, respectively.

## 2.4. Salient findings and outcomes

1. The developed SF-dECM possesses exceptional combinatorial characteristics of both collagenous scaffold and hydrogel systems beneficial for inducing wound healing and can be explored in wide applications of regenerative medicine and other tissue engineering applications.

2. The study presents a facile single-step technique of application of dECM scaffold infused with SF proteins that can ensure adherence of the dressing at the wound site due to in situ gelation property of silk proteins.

3. The decellularized omental ECM was thoroughly characterized to ensure elimination of xenogenic cellular components; however, the isolation technique ascertains retainment of the essential regenerative components and integrity of ECM, required for further application.

4. In vitro cellular response infers the ability of SF-dECM to support the growth and proliferation of HDF and endothelial cells.

5. *In vivo* validation of SF-dECM establishes its applicability for the treatment of diabetic chronic wounds as the hydroscaffold demonstrated its ability to influence crucial steps of healing, including vascularization, inflammation, and tissue remodeling.

### *Limitation of the chapter*

Although the study demonstrates promising outcomes, its reliance on a rat model introduces limitations due to interspecies variations in wound healing physiology and immune responses, which may affect the direct applicability of the findings to human clinical settings. Additionally, the controlled experimental conditions in animal models may not fully replicate the complexity of chronic diabetic wounds in human patients, which are often influenced by comorbidities, varying wound environments, and patient-specific factors. Further studies involving large animal models and clinical trials are essential to validate the efficacy, safety, and scalability of the SF-dECM hydroscaffold for human applications. Despite these limitations, the findings of the study pave the way for future research and clinical translation, promising advancements for improved treatment options in wound care.

# Chapter 3: Development of silk-aloe composite matrix for sustained delivery of bioactive molecules and assessment of its healing ability in full-thickness wound model

*The chapter presents fabrication of a phyto-hydrogel dressing by integrating Aloe vera mucilage extract into SF proteins from Bombyx mori and Antheraea assamensis, with polyvinylpyrrolidone as a stabilizer. The fabrication technique is a chemical crosslinker free approach and provides a long-term stable hydrogel system with property of delivering active aloe phytochemicals. The work initially explores the physicochemical properties and in vitro analysis of the hydrogels. Further, it demonstrates the healing efficacy of composite hydrogels in full-thickness wound model in rabbits.*

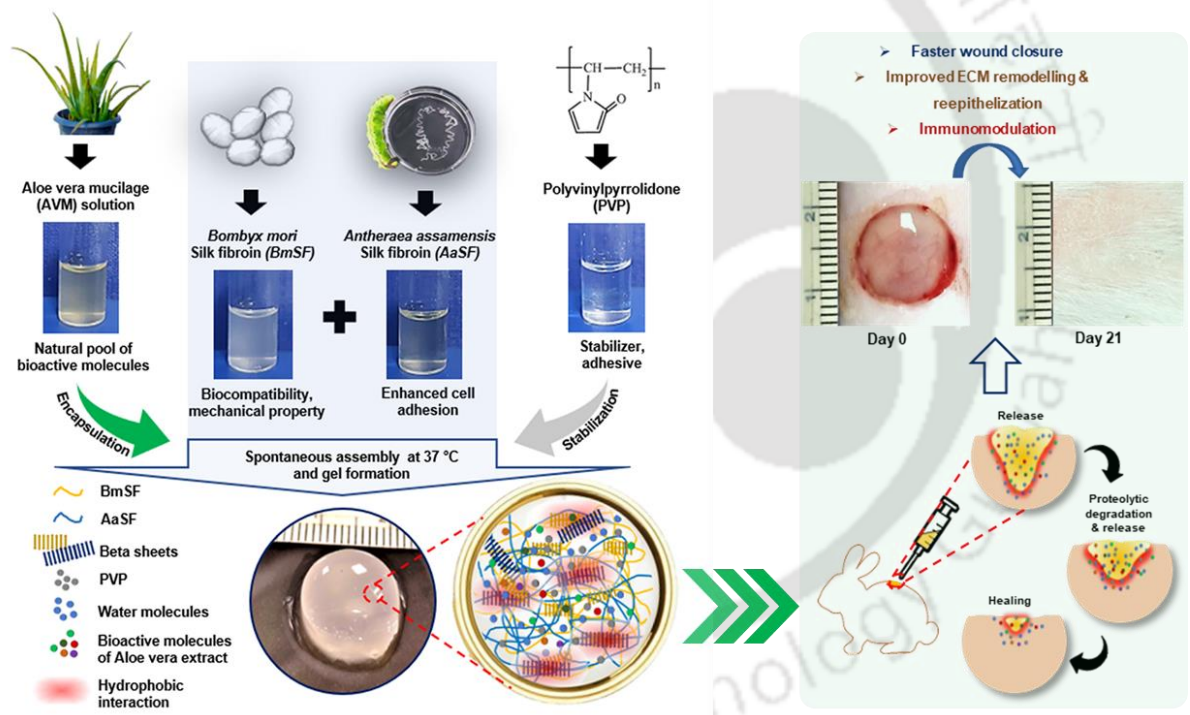


***The work embodied in this chapter is published as:***

Bibrita Bhar, Bijayashree Chakraborty, Samit K Nandi, and Biman B Mandal. "**Silk-Based Phyto-Hydrogel Formulation Expedites Key Events of Wound Healing in Full-Thickness Skin Defect Model**." *International Journal of Biological Macromolecules*. 2022; 203: 623-37.

**Abstract**

Immense socio-economic burden of chronic wound demands effective, low-cost strategies for wound care. Herein, we have developed a chemical crosslinker-free phyto-hydrogel by encapsulating phytochemicals of *Aloe vera* mucilage extract (AVM) in the self-assembled polymeric chains of two different SF proteins (from *Bombyx mori* and *Antheraea assamensis*). Additionally, polyvinylpyrrolidone (PVP) has been used as a stabilizer that also contributed to the mucoadhesive property of the composite (SAP; made of SF, AVM, and PVP) hydrogel. The physicochemical properties of the hydrogel were evaluated and compared with SF hydrogel containing only SF proteins without any additives. The biocompatibility assessment of the hydrogel under *in vitro* conditions has shown improved cellular proliferative and migratory responses, suggesting faster tissue repairability of the hydrogel. A detailed *in vivo* comparative study with a commercially available DuoDERM® gel revealed that SAP hydrogel not only promoted wound closure but also showed better deposition and remodeling of the ECM. Moreover, the hydrogel also demonstrated its ability to downregulate pro-inflammatory markers (IL-1β, TNF-α) and upregulation of anti-inflammatory markers (IL-10, TGF-β) at the early stage of healing. Therefore, the bioactive proteins-carbohydrates composite efficiently accelerates skin regeneration and possesses great translational potential to offer a low-cost alternative wound care therapeutic.

**Hypothesis**

The study aims to develop a silk-based cost-effective composite hydrogel matrix incorporating bioactive agents for topical application in wound healing. By utilizing different varieties of silk with temperature-induced self-assembly properties, the need for chemical crosslinkers can be eliminated. The inclusion of aloe vera phytochemicals is expected to ensure the sustained release of bioactive factors at the wound site, thereby supporting tissue regeneration. This composite hydrogel is anticipated to serve as a biodegradable and immuno-compatible alternative to traditional wound care products, potentially offering improved wound healing outcomes.

## 3.1. Introduction

Treatment of chronic wounds is a daunting healthcare challenge due to its non-healing physiology with associated pathological complications. The gold standard treatments of chronic wounds using autografts and allografts often lead to greater mortality risk, the transmission of pathogens, prolonged hospital stays, and are highly expensive. A recent report estimated that 1-2% of the population in developed countries might experience a chronic wound in their lifetime [259]. Chronic wounds affect over 6.5 million patients annually only in the USA [260]. It is estimated that almost 10% of the population develops a chronic wound at least once in a lifetime, with a wound-related mortality rate of 2.5% [261]. The high price of advanced wound care products and the rising incidences of chronic diseases are accelerating the growth of the wound care market, which is poised to reach nearly $22 billion by 2024 [262, 263]. However, developing countries are still holding a significant gap between supply and demand due to the unavailability of cost-effective treatments. Also, poor local hygiene, limited access to health care, inadequate health infrastructure, and infections further complicate the surgical procedures in patients. Insufficient treatments of acute wounds are the common cause of chronic injuries in low-middle-income countries. The substantial increase in the number of patients suffering from such conditions demands a large-scale and low-cost strategy in addition to effective treatments. Collagen-based Zyplast® and hyaluronic acid (HA)-based Juvederm® are being used as dermal fillers. Besides expensiveness, these fillers have been reported to show late-onset adverse immune reactions in several clinical applications [264, 265]. Therefore, the development and therapeutic assessment of affordable novel matrices with required physical and biological properties are the need of the hour [34].

Utilization of locally available materials from natural resources offers alternative solutions to fabricate affordable formulations. Natural plant extracts have been of great importance since

ancient times in traditional medicine in treating many pathological conditions. In the past few decades, there has been a renaissance in the use of medicinal plants in many countries, including developed countries [266]. Modern medicines focus on the isolation and purification of individual active components instead of using concoctions of extracts. However, complex isolation processes of active ingredients often lead to structural changes in the molecules, followed by loss of functionality of the compounds. The therapeutic activity of natural extracts is often the result of synergistic and simultaneous action of multiple chemicals [267, 268]. Microencapsulation of this pool of bioactive phytochemicals in tissue-engineered matrices could achieve sustained release of the molecules as well as increased stability during storage and extended shelf life. Advanced wound care emphasizes the sustained delivery of multiple components to regulate different stages of the wound healing process [269-271]. Hydrogels could be excellent delivery platforms of active ingredients aiming at accelerated wound healing [272]. The hydrogel dressings have attracted attention in wound care due to their unique physical properties of mimicking native ECM networks, tunable rheological properties, and ability to retain a large quantity of fluid to maintain an optimally moist environment at the wound site [273]. Additionally, the matrix also prevents the entrance of microbes to the wound as a physical barrier and allows the transport of functional molecules to the site of interest [272]. Therefore, we aim to develop an affordable, biocompatible, and biodegradable silk-based phyto-hydrogel system to accelerate the healing mechanism. The leaf extract from *Aloe barbadensis Miller* (*Aloe vera*) has been widely used in therapeutic fields for its anti-inflammatory, antiseptic, analgesic, and antimicrobial properties [274]. The innermost jelly-like mucilage portion of *Aloe vera* leaf (AVM) contains water-soluble monosaccharides, polysaccharides, essential amino acids, polypeptides, vital enzymes (oxidase, amylase, carboxypeptidase, and catalase), glucomannans, minerals (calcium, sodium, magnesium, zinc, copper, and chrome), vitamins ($B_1$, $B_2$, $B_6$, C, E, and folic acid), and antioxidants [275]. Topical application of the extract has proven its ability to stimulate the cutaneous wound healing process in animal models and clinical trials as well [275, 276].

In addition, the ECM of human tissue is a combination of three basic components: proteins, carbohydrates, and water. The precise balance of these three components, along with the cells, aids in the formation of functional tissue units [277]. Provisional composite hydrogels made up of proteins and carbohydrates are able to mimic native ECM architecture to support tissue regeneration. Herein, two types of SF, i.e., BmSF and AaSF, have been utilized to fabricate the structural base of the hydrogel matrix to encapsulate AVM phytochemicals. The phyto-

hydrogel might serve as a robust ECM mimic to support skin regeneration for wound healing applications. SF, being less expensive, immuno-compatible, and biodegradable, serves as one of the best biomaterials for skin tissue engineering [34]. Moreover, the beneficial properties of AaSF (endemic to North-East India), containing inherent cell-binding Arg-Gly-Asp (RGD) motifs, can be utilized for an enhanced regeneration process [80]. The temperature-induced self-assembly property of hydrophobic blocks of these two different types of SF circumvents the need for chemical crosslinkers for gelation [218]. The presence of long hydrophilic polysaccharide chains of AVM hinders hydrophobic interactions between SF molecules; therefore, polyvinylpyrrolidone (PVP) was used as a binder and stabilizer in the formulation. Subsequently, we evaluated the efficacy of the novel composite (SAP; containing SF, AVM, and PVP) hydrogel matrix for skin regeneration through *in vitro* assessment and later using an animal wound model. Initially, gelation kinetics and physical properties of SAP hydrogel were evaluated to assess its applicability in soft tissue engineering. The release profile of acemannan from SAP was examined to ensure the sustained delivery of bioactive factors at the wound site. Next, we evaluated biocompatibility of SAP hydrogel under *in vitro* conditions, followed by a 21-day study in a full-thickness rabbit skin defect model. Comparable results with a widely used commercial product substantiate the potential of SAP hydrogel to be used as a cost-effective alternative for wound care.

## 3.2. Materials and methods

### 3.2.1. Isolation of silk fibroin solutions

BmSF was extracted from the silk cocoons following the standard protocol [73]. In brief, *Bombyx mori* cocoons were degummed in boiling 0.02 M sodium carbonate (Merck, India) solution twice for 15 min. The dried silk fibers were dissolved in 9.3 M lithium bromide (Sigma-Aldrich, USA) solution at 60 °C for 4 h. Next, the mixture was dialyzed against Milli-Q water using a 12 kDa cellulose membrane dialysis tubing (Sigma-Aldrich, USA) for 48 h at room temperature to obtain an aqueous BmSF solution. AaSF was isolated from the silk glands harvested from 5$^{th}$ instar silkworms, following the established lab protocol [81]. Briefly, the fibroin was squeezed out from the glands using forceps, and the solution was dissolved in 1% (w/v) sodium dodecyl sulfate (SDS) (Himedia, India) aqueous solution. Further, the solution was dialyzed against Milli-Q water using a 12 kDa cellulose membrane dialysis tubing (Sigma-Aldrich, USA) at 4 °C for 4 h to obtain an aqueous AaSF solution. The concentration of the silk solutions was measured using the gravimetric method. All solutions were freeze-dried and lyophilized for future use.

### 3.2.2. Isolation of AVM extract

Fully grown leaves of *Aloe barbadensis Miller* were collected from a local garden. Fresh leaves were washed thoroughly with distilled water, and rinds were removed. The jelly-like innermost portion (known as mucilage) was collected by peeling to skim the surface of *Aloe vera* leaf and minced in pieces. The pieces were soaked in water for 30 min to remove latex. Then, the pieces were centrifuged at 10,000 rpm for 30 min at 4 °C for removal of long fibers. The supernatant was collected, and the pH of the solution was adjusted to 7.2-7.4 and freeze-dried for storage. The lyophilized AVM powder was dissolved in Milli-Q water to a stock solution of 10 mg/mL and UV sterilized for further use.

### 3.2.3. Fabrication of SAP hydrogel

Two varieties of SF (BmSF and AaSF) were mixed in an equal ratio (1:1), maintaining the total protein concentration of 2% (w/v) in the mixture. Different concentrations of PVP were mixed to measure gelation time and assess gel texture **(Table 3.1)**. The solution containing 2% (w/v) PVP (povidone K 90, $(C_6H_9NO)_n$, Sigma-Aldrich, USA) was chosen for the final preparation based on its fastest gelation property and appropriate gel consistency for topical application. AVM solution was mixed from a 10 mg/mL stock solution, maintaining the final concentration of 1000 µg/mL in the mixture. The pH of the mixture was adjusted to 7.2-7.4. Then, the solution was kept at 37 °C for gelation. 1 mL of the solution takes 20 min to reach the gelation stage. To compare the properties of the novel hydrogel, SF hydrogel containing only silk proteins, i.e., BmSF and AaSF (1:1), were also fabricated similarly.

**Table 3.1:** Preparation of different ratios of 1 mL of blend solutions.

| Sl no. | BmSF: AaSF ratio | Final SF conc. % (w/v) | PVP conc. % (w/v) | Gelation time (min) | Gel formation | Gel consistency |
|---|---|---|---|---|---|---|
| **1** | 1:1 | 2 | 0 | 25-30 | Yes | Soft; translucent |
| **2** | 1:1 | 2 | 0.5 | 25-30 | Yes | Soft; translucent |
| **3** | 1:1 | 2 | 1 | 20-25 | Yes | Soft; translucent |
| **4** | 1:1 | 2 | 2 | 20-25 | Yes | Soft; translucent |
| **5** | 1:1 | 2 | 4 | 25-30 | Yes | Very soft; fluidic |
| **6** | 1:1 | 2 | 6 | - | No | Viscous liquid |

### 3.2.4. Rheological properties of hydrogel

Rheological assessments of the hydrogels were performed using a parallel plate Rheometer (MCR 302, Anton Paar) with a round stainless-steel plate (25 mm diameter) at a distance of 1

mm from the sample stage. The gelation point was determined by placing the blended solution at the sample stage, maintaining the temperature 37 °C for the time sweep test. The data points were collected at a low strain (γ = 1%) amplitude with a specific angular frequency (ω = 10 rad/s) to prevent shear-induced gelation of blended solutions. A strain amplitude sweep test (1% to 1000%) was performed to determine the linear viscoelastic (LVE) region for the SF and SAP hydrogels. The determination of LVR is important for frequency sweep analysis where storage modulus (G′) and loss modulus (G″) were independent of strain amplitude. Frequency sweep for assessment of viscoelastic property of the hydrogels was noted over a frequency range of 1−100 rad/s at a low strain (γ = 1%).

### 3.2.5. Assessment of adhesive property of hydrogel

The adhesion strength of hydrogels was estimated by tensile pull-off adhesion test using Instron 5944 (Norwood, MA, USA.). 500 µL of hydrogels were placed between two porcine skin explants with a 20 mm × 20 mm contacting area. The skin explants were fixed, whereas placed hydrogel samples were stretched with a strain rate of 1 mm/min. Unidirectional tension was applied, while recording the extension and force. All measurements were performed three times.

### 3.2.6. Fourier transform infra-red (FTIR) spectroscopy

Infra-red spectra of precursor solutions and hydrogels were obtained using ATR-FTIR spectroscopy. The spectra were recorded in the spectral range of 4000-400 $cm^{-1}$ with a resolution of 4 $cm^{-1}$ and 32 scans. Normalization of the curves was performed using OriginPro 8.5 (OriginLab Corporation, USA). Amide regions in the spectra were inspected to determine the structural change of the hydrogels.

### 3.2.7. Examination of micro-architecture of hydrogel

The internal micro-architecture of the freeze-dried hydrogels was observed using a field-emission scanning electron microscope **(**FESEM; Carl Zeiss Sigma, Germany) at an operating voltage of 3 kV. The cross-sectioned freeze-dried hydrogels were coated with gold prior to observation. The pore sizes of the hydrogels were measured using image visualization software (ImageJ, NIH Image, USA).

### 3.2.8. Integral stability assessment in enzymatic condition

Comparative integral stability of hydrogels was assessed by placing 500 µL of each hydrogel in both 2 U/mL of Protease type XIV (from *Streptomyces griseus*, Sigma–Aldrich, USA) solution and phosphate buffered saline (PBS) solution at 37 °C. Weights of hydrogels were

measured after every alternative day, and the protease solutions were replaced by freshly prepared solutions. Percent mass remaining was calculated by following the equation.

$$Mass\ remaining\ (\%) = \frac{Mt}{Mi}\ x\ 100$$

Where $M_i$ and $M_t$ are the initial mass and mass of the construct at the particular time, respectively.

### 3.2.9. Measurement of water retention ability

1 mL of each hydrogel was kept in a dry incubator at 37 °C. Weights of wet hydrogels were measured after several intervals (0, 6, 12, 24, 36, 48, and 60 h), and the hydrogels were lyophilized at last to measure their dry weights. The remaining percentage of water content at respective time points was calculated using the following equation.

$$Remaining\ water\ content\ (\%) = \frac{Wt - Wd}{Wi - Wd} \times 100$$

Where $W_i$, $W_t$, and $W_d$ are the initial weight of the hydrogel, the weight of the hydrogel at the particular time, and the weight of the lyophilized dry hydrogel, respectively.

### 3.2.10. Release profile of SAP hydrogel

To analyze the quantity of aloe molecules being diffused from the SAP hydrogel, the release of acemannan was quantified for all the samples using a standard protocol [278]. Briefly, lyophilized AVM powder was re-dissolved in 1X PBS solution to make a stock concentration of 10 mg/mL and a calibration curve was plotted within the range of 0 to 2 mg/mL. 40 µL of each AVM concentration was mixed with 10 µL of Congo red dye and 50 µL of 0.2 M NaOH, and absorbance was detected at 540 nm wavelength using Multiskan Sky microplate spectrophotometer. Next, SF, SF+AVM, and SAP hydrogels were kept in 1 mL of 1X PBS at 37 °C. At regular intervals, 40 µL of the PBS solution was collected and mixed thoroughly for detection and replaced by fresh 1X PBS.

### 3.2.11. Cellular proliferation and migration study

Cell viability and proliferation studies were carried out separately with human dermal fibroblast (HDF procured from Himedia, India) and human keratinocyte cell line (HaCaT cells procured from NCCS, India) in 24-well transwell plates (Corning Transwell® 6.5 mm, 0.4 µm pore size with a polycarbonate membrane insert). The cells ($10^4$ cells/$cm^2$) were seeded onto a gelatin-coated 24-well plate and incubated for 24 h in 500 µL high glucose (25 nM) Dulbecco's Modified Eagle's Medium (DMEM) at 37 °C with 5% $CO_2$. Next day, 100 µL of hydrogels

were placed on each insert, and the cells were cultured in high glucose DMEM with 2% fetal bovine serum (FBS). Further, cell viability was measured after days 1,3, 5, and 7 of incubation using alamarBlue™ Cell Viability Reagent (Invitrogen). The cells were also stained with a solution containing 4 μM calcein–AM and 2 μM ethidium homodimer-1 (Sigma-Aldrich, USA) for 10–15 min. Due to the intracellular esterase activity of live cells, they take up calcein-AM stains and exhibit bright green fluorescence, whereas ethidium homodimer-1 penetrates through the damaged cell membrane of dead cells and binds to DNA and stains red. Next, the cells were gently washed with PBS, and images were captured using an inverted fluorescent microscope (EVOS FL, Life Technologies, USA).

Similarly, cell migration was evaluated using 24-well transwells. Briefly, cells were seeded at a density of $2.5 \times 10^5$ cells/ $cm^2$ into the lower chamber and kept in an incubator at 37 °C with 5% $CO_2$ for 24 h to form a monolayer of cells. Next, scratches were made using a sterile P200 micropipette tip and gently washed with PBS to remove unattached cells. Next, the cells were treated with hydrogels (100 μL/insert) kept in the upper chamber, and lower chamber containing the cells was filled with serum-free DMEM. HDF and HaCaT cells were photographed using optical microscope at 0, 12, and 24 h after wounding. The scratched area was measured using ImageJ software, and the normalized value of wound area was obtained by the following equation.

$$Wound\ area\ (normalized\ value) = \frac{At}{Ai}$$

Where $A_i$ and $A_t$ are initial wound area and wound area at the particular time (t), respectively.

### 3.2.12. *In vivo* full-thickness wound model generation and efficacy assessments of SAP hydrogel

The animal experiment was conducted in accordance with ‘‘Principles of laboratory animal care” from the Institutional Animal Ethics Committee (IAEC), West Bengal University of Animal and Fishery Sciences (WBUAFS), West Bengal, India (Registration No. 1828/po/Bt/S/15/CPCSEA dated 27.07.2020). Adult rabbits of either sex each weighing 1.5-1.8 kg were used for the experiment. The full-thickness skin wounds were made by incision (10 mm diameter) on the dorsum skin layer of the rabbits under anesthesia with Xylazine hydrochloride (5 mg/kg body weight; Injection xylaxin, Indian Immunologicals, Ahmedabad, India) and ketamine hydrochloride (33 mg/kg body weight; Ketalar, Parke-Davis, Hyderabad, India) intramuscularly. The negative control group or untreated wounds were covered with only Tegaderm™ dressing. The wounds were treated with DuoDERM® hydroactive gel in case

of positive control group, and the experimental groups were treated with 250 µL of respective hydrogels and covered with Tegaderm™ film dressing. The wounds were monitored and photographed on 0,3,5,7,9,11,14,17 and 21 days. After the closure of the wounds, the remaining detached dry hydrogels were cleaned. The wound tissues were collected using biopsy punch of 10 mm diameter at 3 different time points (day 7, 14, and 21) from the sacrificed animals containing four treatment groups (untreated, SF, SAP, and DuoDERM®). The whole procedure was performed carefully to minimalize the suffering of animals. Animals of each group received injection Meloxicam (0.3 mg/kg body weight; Injection Melonex, Intas Pharmaceuticals India, Ahmadabad, India) daily intramuscularly for 3 days. Next, the area of wounds was measured from the gross wound images using ImageJ software, and relative wound area (%) was calculated using the following equation.

$$Relative\ area\ of\ wound\ (\%) = \frac{At}{Ai} \times 100$$

Where $A_i$ and $A_t$ are initial wound area and wound area at the particular time (t), respectively. Collected tissue samples were fixed using 10% Neutral buffered formalin. The samples were cut into sagittal sections of 8 µm using cryomicrotome to investigate the wound regeneration process, and the sections were further stained with H&E. Total collagen of the sections was stained with Masson's trichrome kit (Sigma–Aldrich, USA) according to the manufacturer's protocol. Collagen content of the sections was immunostained with antibody against collagen type I (Col I). In addition, the sections were also used for immunohistochemistry (IHC) staining with antibodies against cytokeratin 10 (CK10), cytokeratin 14 (CK14), CD31, CD 206, and CCR7. Hydroxyproline estimation of tissue samples was performed according to previously reported biochemical hydroxyproline assay [279]. In brief, tissue hydrolysates were vigorously mixed with 0.01 M $CuSO_4$, 2.5 N NaOH, and 6% $H_2O_2$ and placed at 80 °C for 15 minutes. After cooling down, the samples were mixed with a freshly prepared 5% solution of paradimethyl amino-benzaldehyde in propanol with 3 N $H_2SO_4$ and placed at 75 °C for 15 minutes. The samples were further cooled, and absorbance was measured at 540 nm.

### 3.2.13. Gene expression analysis using qRT-PCR

The mRNA of the wound tissue was extracted using TRIzol reagent (Invitrogen) according to the manufacturer's protocol. The complementary DNA (cDNA) was obtained by reverse-transcribing total RNA using a reverse transcription kit and PCR equipment (Applied Biosystems). The cDNA was further used for qRT-PCR with a High Capacity cDNA Reverse Transcription Kit (Applied Biosystems) performed on a QuantStudio™ 5 Real-Time PCR

System (Applied Biosystems) for the analysis of following gene expression, Col I, MMP-1, MMP-2, MMP-9, IL-10, TGF-β, IL-1β, TNF-α, and IL-6. The $2^{-\Delta Ct}$ method was used to calculate the relative gene expression. The housekeeping gene, β -actin, was used as an internal control to normalize the expression of the target genes. **Table 3.2** enlists the sequences of primers used in the qRT-PCR reaction.

**Table 3.2:** Primer sequences used for the gene expression study.

| Target gene | Forward primer | Reverse primer |
|---|---|---|
| **Rabbit β-actin** | 5′-AGGAGAAGCTGTGCTACGTG-3′ | 5′-CAGGAAGGAGGGCTGGAACA-3′ |
| **Rabbit Col I** | 5'-CCTGGCACCCCAGGTCCT CA-3’ | 5'-TCGCTCCCAGGGTTGCCATC-3' |
| **Rabbit MMP-1** | 5'-TCAGTTCGTCCTCACTCCAG-3’ | 5'-TTGGTCCACCTGTCATCTTC-3' |
| **Rabbit MMP-2** | 5’-TTGGATCCTCCTACAGCAGCT GCACCAG-3’ | 5’-AAGAATTCCCGTAGAGCTCTT GAATGC-3’ |
| **Rabbit MMP-9** | 5'-TGCCAGGAGTACCTGTTCC GCTATG-3’ | 5'-TGCCACTTGAGGTCACCC TCGAA-3' |
| **Rabbit IL-1β** | 5′-TTGAAGAAGAACCCGTCCTC TG-3′ | 5′-CTCATACGTGCCAGACAA CACC-3′ |
| **Rabbit IL-6** | 5′-GAACAGAAAGGAGGCACT GG-3′ | 5′-CTCCTGAACTTGGCCTGAAG-3′ |
| **Rabbit IL-10** | 5′-CAAGCCTTGTCGGAGATGAT-3′ | 5′-TTTTCACAGGGGAGAAATCG-3′ |
| **Rabbit TNF-α** | 5′-CTGCACTTCAGGGTGATCG-3′ | 5′-CTACGTGGGCTAGAGGCTTG-3′ |
| **Rabbit TGF-β** | 5′-CAGTGGAAAGACCCCACAT CTC-3′ | 5′-GACGCAGGCAGCAATTATCC-3′ |

### 3.2.14. Statistical Analysis

Data of all the experiments were performed for n = 3 samples unless otherwise specified. Data analysis was done using statistical software OriginPro 8.5 (OriginLab Corporation, USA). All graphical data are reported as mean ± standard deviation. The statistical analysis was conducted by comparing the data between the groups and within groups by using one-way analysis of variance (ANOVA) followed by Tukey’s test at multiple significance levels, * $p \leq 0.05$, ** $p \leq 0.01$, *** $p \leq 0.001$. Histological examination was performed by capturing images of 5 fields per section, and the images were analyzed using ImageJ software.

## 3.3. Results and discussion

### 3.3.1. Fabrication of SAP hydrogel

The aqueous solubility of lyophilized AVM allowed it to mix homogenously with SF solutions of BmSF and AaSF. The phytochemicals present in AVM extract were incorporated into the hydrogel matrix using inherent self-assembling properties of two different varieties of SF proteins. The two types of SF proteins with different hydropathicity interact with each other at the hydrophobic stretches of two chains. The hydrophobic regions of both proteins are postulated to rearrange themselves with the increase of temperature and interact with each other through interchain hydrophobic interactions. The phenomenon leads to spontaneous assembly of two proteins and induction of β-sheet conformation to form a hybrid hydrogel **(Figure 3.1)** [218]. The addition of AVM solution in the blend resulted in entrapment of AVM molecules within the interpenetrating hydrogel network of SF chains. The blend solution was transparent with flowing property at room temperature. When 1 mL of the mixed solution was kept at 37 °C for ~20 min, the solution became translucent at pre-gelation stage and transformed into an

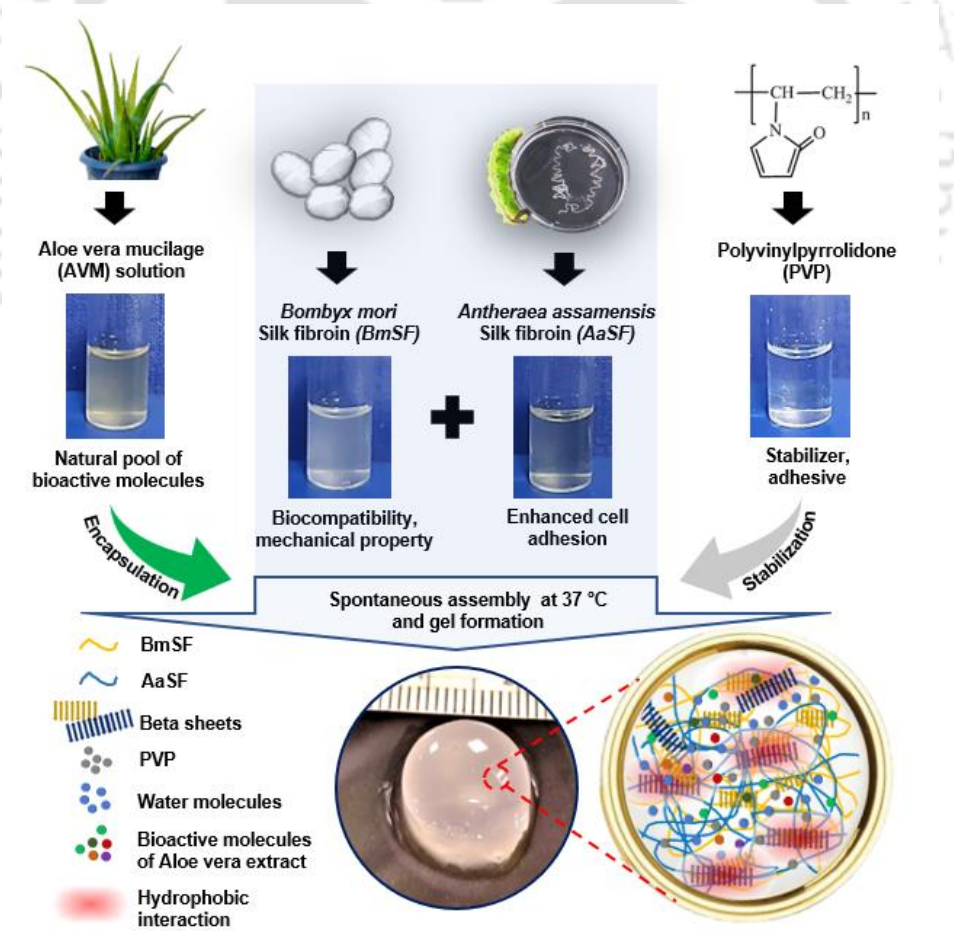


***Figure 3.1: Schematic representation of fabrication technique.*** *Pristine silk solutions from two different sources, BmSF and AaSF were blended with AVM and PVP solutions at 37 ˚C for 15-20 min to develop SAP hydrogel.*

opaque hydrogel. The concentration of AVM used for the fabrication of SAP hydrogel was optimized from its cytotoxicity assessment and release profile of aloe molecule **(Figure 3.2A&B).** The regenerative properties of *Aloe vera* are attributed to a glucomannan called acemannan, which was quantified using the Congo Red reagent [280]. Its release profile of SAP showed that 34.85 ± 4.12% of acemannan were released within 48 h while dipped in PBS at 37 °C **(Figure 3.2B)**. The result suggested that the incorporation 1000 µg/mL of AVM can provide optimal release (~35%) of aloe molecules for 48 h, which is within the range of effective concentration required for effective cellular response **(Figure 3.2A)**. Hence, the hydrogel can persist as a reservoir for sustained and slow release of aloe molecules to maintain an optimum concentration at wound bed for a prolonged period of time. The host cells can utilize the remaining entrapped aloe molecules after their recruitment into the gel and followed by cell-mediated enzymatic degradation of the matrix.

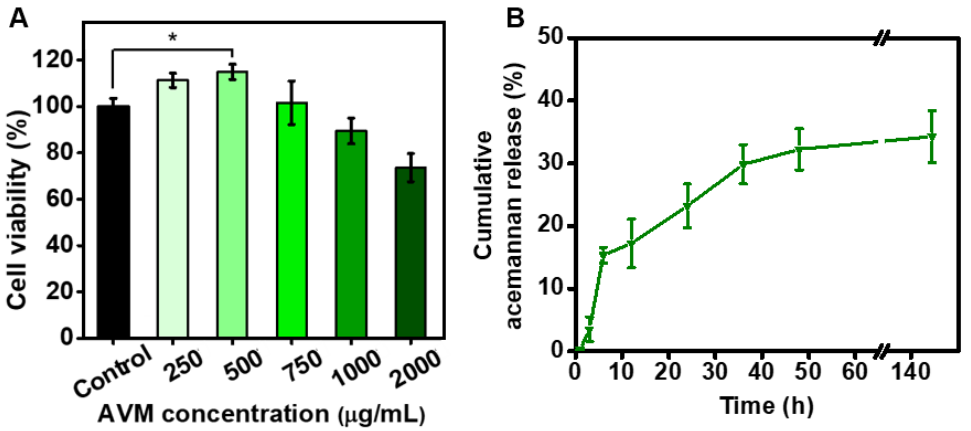


***Figure 3.2. Evaluation of efficacy of AVM. (A)*** *Cytotoxicity assessment of different concentrations of AVM extract on HDF after 24 h. (B) Release profile of acemannan from the fabricated SAP hydrogel. Values are plotted as mean ± standard deviation, where * p≤ 0.05.*

### 3.3.2. Gelation and rheological property

The gelation mechanism of hydrogels and pristine materials was observed by detecting the changes in absorbance value at 600 nm. Significant changes in absorbance were detected in blended solutions within 15-40 min of incubation at 37 °C in contrast to precursor solutions, i.e., BmSF, AaSF, and AVM extract. Turbidity of the blend solutions increases as monomers of transparent solutions transform into fibrillar polymer networks that scatter significant amounts of light. The rapid rise in absorbance in blend solutions indicates the increase in cross-linking among the protein chains of two types of SF proteins (BmSF and AaSF). After reaching the highest optical density (O.D.) values, the curves of blended solutions reached a plateau which demonstrated completion of the gelation process. The addition of AVM with SF solution showed a delayed gelation process (40 min) compared with only SF blend. In contrast, the

presence of PVP led to faster gelation of SAP hydrogel (20 min) in comparison to the SF+AVM group without PVP **(Figure A3.1)**. The gelation behavior of the SF and SAP hydrogels was studied to analyze the flow property or deformation of the hydrogels at various physical conditions using a rheometer. Time sweep analysis was performed to determine the gelation point of the hydrogels. Initially, G″ was greater than G′ for the blend solutions implying the viscous behavior of the solution. After a certain time, G′ quickly increased and crossed G″ resulting in the formation of elastic intermolecular cross-links among the protein chains, which led to temperature-induced gelation of blend solutions [218]. Subsequently, the samples showed solid-like properties, attributed to a successful gelation process **(Figure 3.3A)**. Next, the hydrogels were subjected to an amplitude sweep test where γ is varied while keeping frequency at a constant value. The increase of γ led to a decrease of G′ value and crossed the curve of G″. The point where G′ starts to decrease corresponding to the deformation of hydrogel is known as the limit of LVE region. From **Figure 3.3B,** it was observed that SAP hydrogel retained its stability up to application of ~14% strain, whereas SF hydrogel showed a lower strain value (γ ~ 9%) for the LVE region. This region indicates the range of strain values within which a test can be performed without destroying the structure of the matrix. Frequency sweep analysis was carried out from 1-100 rad/s within the LVE region **(Figure 3.3C)**. The observation further substantiates that both hydrogels remain stable, and their responses are elastic in the mentioned frequency range.

### 3.3.3. FTIR analysis and Microstructural property

The cross-linking between BmSF and AaSF in SAP hydrogel was validated using FTIR spectroscopy **(Figure 3.3D)**. Both proteins in pristine condition showed characteristic amide peaks of SF, i.e., amide-I at 1655 $cm^{-1}$ corresponding to C—H stretching and N—H deformation, amide-II at 1540 $cm^{-1}$ corresponding to C=N stretching, and amide-III at 1230 $cm^{-1}$ corresponding to C—N stretching [281][27]. These signature peaks are also observed in blend SAP hydrogel. The right shift of the signature peaks from 1655 $cm^{-1}$ to 1624 $cm^{-1}$ at amide I region and from 1540 $cm^{-1}$ to 1515 $cm^{-1}$ at amide II region implies the conformational changes in the polymeric chains of SAP hydrogel to obtain β-sheet transition. The internal micro-architecture of hydrogel, studied using FESEM of cross-sectioned freeze-dried SF and SAP hydrogels, are presented in **Figure 3.3E**. The pores in SF and SAP hydrogels were interconnected with an average pore size of 98 ± 27.18 $\mu$m and 112 ± 34.26 $\mu$m, respectively, suitable for cellular infiltration and migration as also reported in similar studies [282, 283].

### 3.3.4. Stability and moisture retention ability of hydrogel

The application of hydrogels on wounds exposes the material contents to a proteolytic-rich wound microenvironment. Enzymatic degradation of the hydrogels at wound site also aids in releasing its bioactive components and regeneration of neo-tissue to seal the wound cavity. In order to recapitulate the wound microenvironment under *in vitro* condition, the hydrogels were subjected to protease treatment for 21 days **(Figure 3.3F)**. A significant difference ($p \leq 0.001$) was observed in remaining mass when the hydrogels were treated with protease solution than the control group (hydrogels in PBS). In protease condition, SF hydrogel showed 32% weight retention on day 7 and entirely degraded on day 14, whereas SAP showed 58% weight retention on day 7 and complete degradation on day 21. Therefore, slower degradation or higher stability of SAP hydrogel might correspond to the presence of additive components, i.e., AVM and PVP, which are not subjected to proteolytic degradation. In the context of translational aspect of the technology, the long-term stability of the hydrogels was evaluated by storing them at 4 °C, and their physical appearance and odor were assessed after different time intervals. The fragmentation and liquefaction of SF hydrogel were observed after 60 days, but it was not apparent in SAP hydrogel, indicating its better translational potential as a wound care product **(Figure A3.2)**. Further analysis of water retention revealed higher water content in SAP hydrogel ($58.29 \pm 5.72\%$) as compared with SF hydrogel ($33.23 \pm 5.69\%$) post 36 h ($p \leq 0.01$) **(Figure 3.3G)**. Therefore, the superior water-retaining ability of SAP hydrogel can provide a moist environment to the wounds for a longer period of time

### 3.3.5. Assessment of adhesive properties of hydrogels

The adhesion strengths of the hydrogels were measured by the tensile adhesion test (**Figure 3.3H**). **Figure 3.3I and A3.3** show representative stress-extension curves of hydrogels and control groups, respectively. The maximum value of adhesion stress or the adhesion strength of SF and SAP hydrogels were $7.6 \pm 1.26$ kPa and $11.68 \pm 1.05$ kPa, respectively, suggesting significantly better adhesion property of SAP hydrogel ($p \leq 0.05$) than that of SF hydrogel (**Figure 3.3J**). This result indicates that the presence of PVP in SAP hydrogel improved the mucoadhesiveness of the hydrogel. Applied SAP hydrogel was firmly retained on the wound site (**Figure 3.3K**); however, the adhesiveness was mild enough to create no issue while changing the secondary dressing.

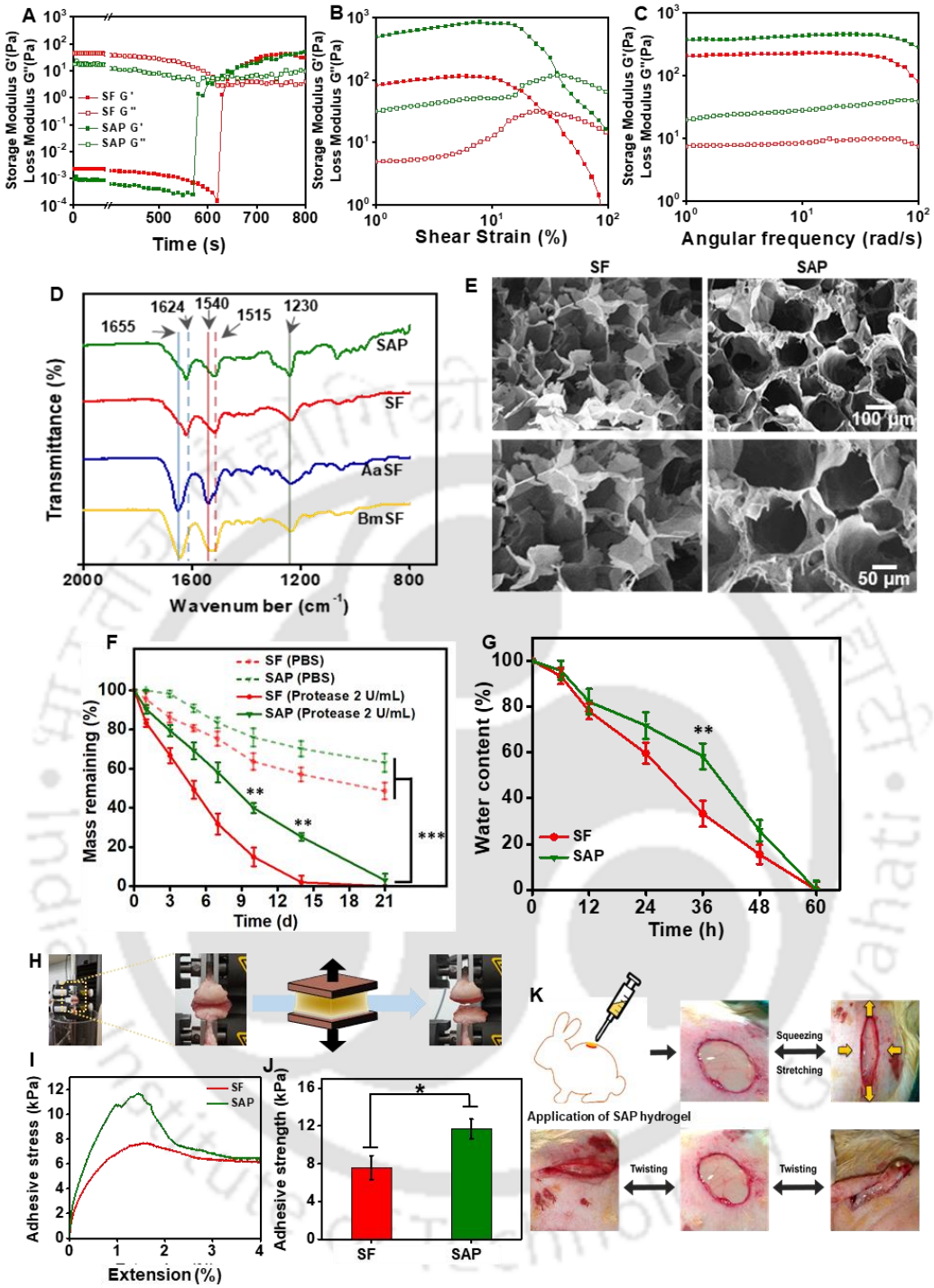


***Figure 3.3. Physicochemical properties of SAP hydrogel.*** *(A) Time sweep test, (B) determination of LVR region, (C) frequency sweep test. (D) FTIR spectra of pristine silk proteins (BmSF & AaSF) and the composite hydrogels. (E) FESEM images of SF and SAP hydrogel at different magnifications. (F) In vitro enzymatic degradation analysis of SAP in comparison to SF hydrogel. (G) Assessment of water retention capacity of the hydrogels. (H) Description of the tensile adhesion test performed with porcine skin explants. (I) Adhesive stress curve of SF and SAP hydrogels on porcine skin, (J) the corresponding adhesive strength. (K) Application of SAP hydrogel on wounds showed that it retained firmly on wound despite being squeezed, stretched, and twisted. Values are plotted as mean ± standard deviation, where * p≤0.05 ** p≤0.01, and *** p≤0.001.*

### 3.3.6. Cellular proliferation and migration study

To recapitulate the topical application of fabricated hydrogels at wound site, we have examined the effect of releasate of hydrogels on HDF and HaCaT cells in transwell system under *in vitro* condition. The hydrogels were placed on the inserts, and cells were seeded in lower chambers **(Figure 3.4A)**. A previous study reported cytocompatibility of SF hydrogel by determining the improved proliferation rate of encapsulated HDF inside the hydrogel [11]. Herein, we focused on mimicking the actual scenario of application of acellular matrix on top of host tissue at wound site. The diffused molecules from the phyto-hydrogel acted on the cells seeded on the bottom surface of the well plate. In both types of cells, i.e., fibroblasts and keratinocytes, hydrogels treated cells showed significantly higher ($p \leq 0.05$) cell numbers after 7 days, indicating the proliferative effect of the hydrogels on human skin cells **(Figure 3.4B&C)**. In case of HaCaT, SAP hydrogel showed a superior proliferative effect than that of SF hydrogel ($p \leq 0.05$), which suggests synergistic effects of released silk and AVM molecules in the media. Live-dead images of HDF and HaCaT cells grown in presence of hydrogels at 1,3 and 7 days of incubation are shown in **Figure 3.4D and 3.4E**. Most of the cells were viable and proliferated in presence of hydrogel releasates and the standard spindle-shaped morphology of HDF cells indicated healthy condition of the cells after incubation of 7 days. Similarly, we performed a cellular migration study with the fabricated hydrogels in transwell system **(Figure 3.4F)**. The intricate healing process involves active cell migration; therefore, it is an important parameter to be assessed in presence of the developed composite. During the remodeling of regenerated tissue, the fibroblasts and keratinocytes residing in wound edges migrate through the provisional matrix toward the wound center to heal the injury [284]. Interestingly, SAP hydrogel treatment showed significantly faster closure ($p \leq 0.01$) of scratch area compared to untreated control groups in case of both HDF and HaCaT cells **(Figure 3.4G-J)**. Moreover, SAP hydrogel showed an improved migration-inducing effect than that of SF hydrogel. The findings led us to perform a functional assessment of SAP hydrogel through detailed animal experimentation for wound healing application.

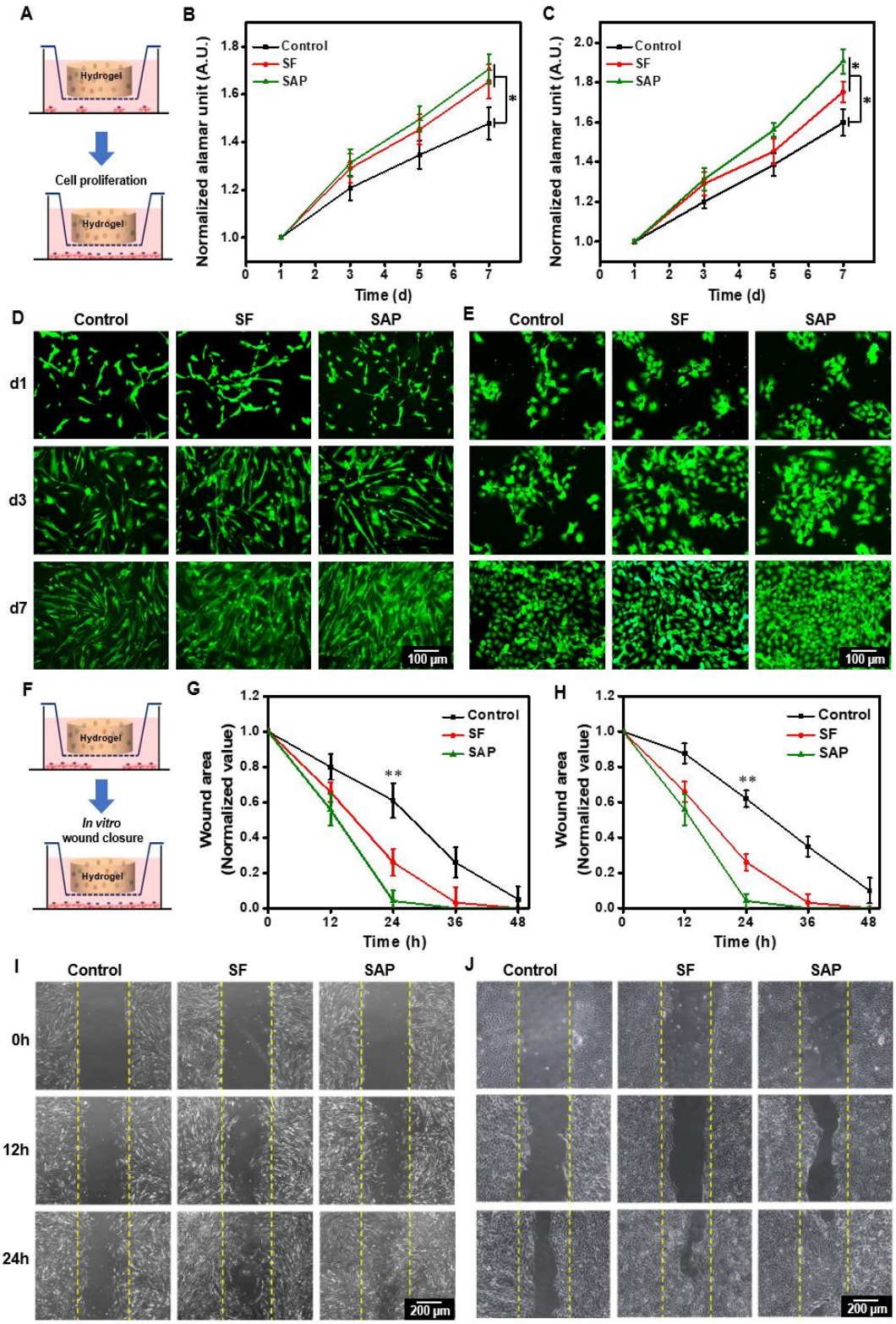


***Figure 3.4. Cellular proliferation and migration assay****. (A) Schematic representation of experimental setup of transwell proliferation assay. Proliferation rate of HDF (B) and HaCaT (C) was determined by alamar blue assay. Live/dead staining of HDF (D) and HaCaT (E) showed improved proliferation in presence of the hydrogels. (F) Schematic representation of transwell cell migration assay. Migration rate of HDF (G) and HaCaT (H) were evaluated through scratch assay. The Microscopic images of HDF (I) and HaCaT (J) at 0, 12h and 24h showed faster in vitro healing of the scratches in presence of hydrogels. Values are plotted as mean ± standard deviation, where * $p \leq 0.05$, ** $p \leq 0.01$.*

### 3.3.7. Efficacy assessment of hydrogel in a full-thickness wound model

As shown in **Figure 3.5A,** the hydrogels were applied on the incised wounds. The wound sizes were digitally photographed and processed for statistical comparison (**Figure 3.5B)**. It was observed that wound diameters were similar on day 3 to their original size (after incision at day 0). This could be attributed to the inflammatory stage of the healing process while contraction

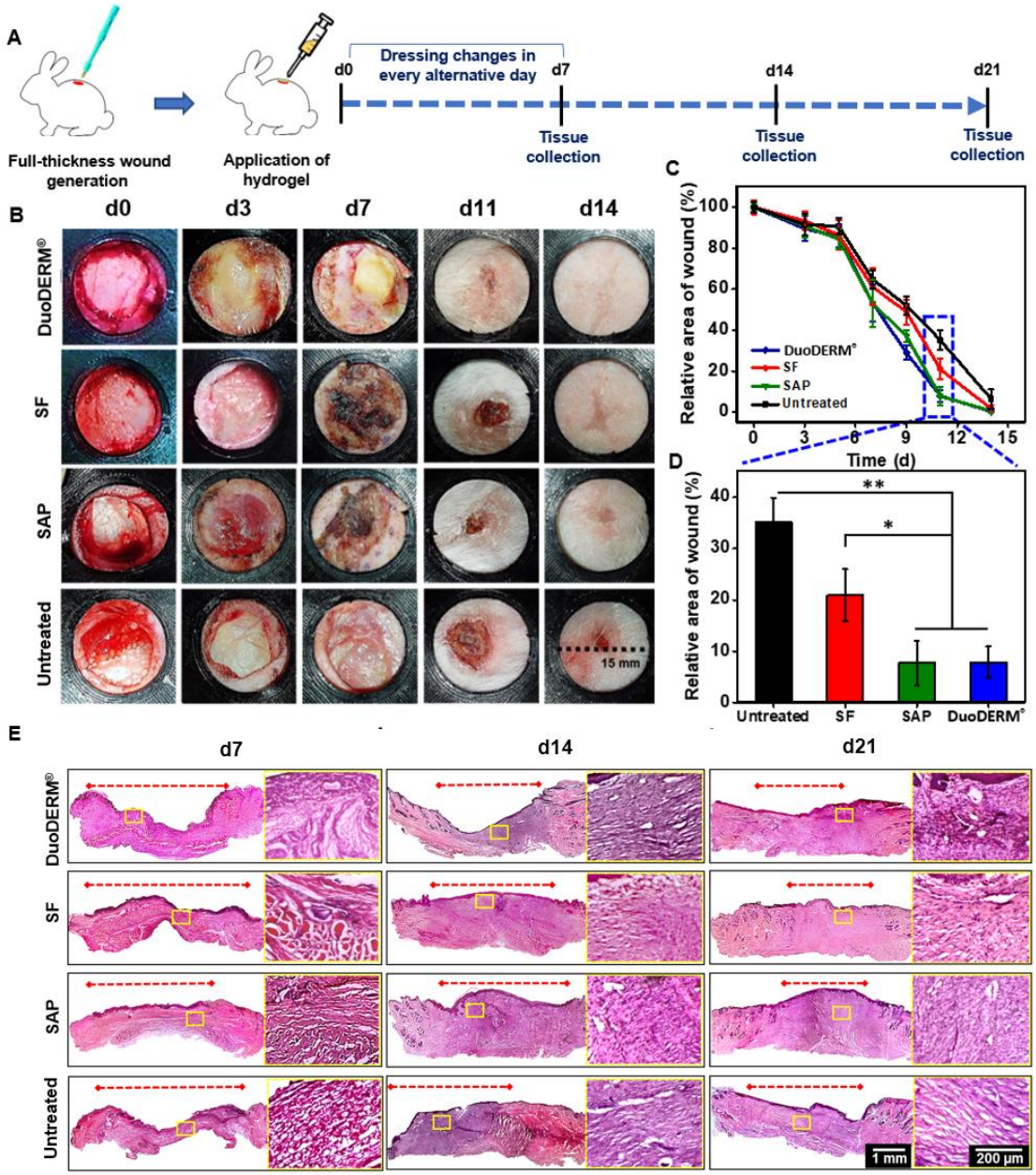


***Figure 3.5. In vivo assessment of overall healing efficacy of the hydrogels.*** *(A) Diagrammatic representation of timeline of animal experiments. (B) Representative images of full-thickness wounds (diameters 10 mm with error within 2 mm) in rabbit models with different treatments during the 21-days of wound healing period. (C) Quantification of wound area is determined by calculating the area of wounds on particular time-point using ImageJ software. (D) Significant differences among the wound area of the untreated control and experimental samples were observed at day 11. (E) Histological analysis of healed skin tissues on days 7, 14, and 21 to assess wound morphology at various stages of wound healing. Magnified images showed regenerated tissue at wound site. Values are plotted as mean ± standard deviation, where * $p \leq 0.05$, and ** $p \leq 0.01$.*

of the wound does not occur. The hydrogels treated wounds were observed to have significantly smaller diameters than the untreated group by day 11 (**Figure 3.5C)**. Precisely, the average values of the relative area of wounds (%) were 35.13 ± 4.83, 20.87 ± 5.08, 7.71 ± 4.34, 7.87 ± 3.08 in untreated, SF, SAP, and DuoDERM® treated wounds, respectively, on day 11 **(Figure 3.5D)**. Therefore, the accelerated wound closure was prominent in the SAP, and DuoDERM® treated wounds, as their wound areas were reduced by more than 90% of their original size after 11 days. It was apparent that the wounds treated with the hydrogels closed completely on day 14 whereas most of the untreated wounds took another 2-4 days for complete closure. **Figure 3.5E** depicts H&E stained images of cross-sections of wound tissues. Between days 7 to 21, the contraction of wound edges was apparent for all the groups. The hydrogel groups were observed to be propitious for granulation tissue formation and significantly faster epithelial migration to close the wound in comparison to that of the untreated group. Hydrogel-treated groups showed thicker and more defined granulation tissue.

### 3.3.8. Collagen deposition and ECM remodeling analysis

The deposition and breakdown of ECM, both processes, play pivotal roles in healing process [285]. Collagen is a primary constituent in dermal ECM and plays a fundamental role in the repair mechanism. MT stained images of untreated group showed significantly lower total collagen content in comparison to hydrogel-treated wounds **(Figure 3.6A)**. For quantification of total collagen, its biochemical marker hydroxyproline level was estimated **(Fig. 3.6B)**. In correlation to the MT stained images, the quantity of hydroxyproline was significantly ($p \leq 0.01$) high on day 14 and day 21. The result suggests higher collagen deposition at SAP hydrogel treated wounds than that of SF hydrogel treated and untreated groups, implying synergistic effect of SF and aloe phytochemicals in the healing process. Specifically, Col I, the most abundant collagen in skin ECM, was assessed by IHC staining of tissue sections. The images showed evidently visible mature Col I fibers in the hydrogels treated wounds after day 14 **(Figure 3.6C)**. Comparatively, lesser collagen deposition was observed in untreated wound tissues. Col I expression was significantly higher in all hydrogels treated groups in comparison to untreated group on days 14 and 21 **(Fig. 3.6D)**, suggesting better ECM deposition. The SAP treated wounds showed significantly higher expression of Col I than SF treated wounds ($p \leq 0.01$) on day 14. This demonstrates the combinatorial proliferative effect of SF proteins and active aloe components in SAP group. DuoDERM® showed a comparable expression pattern as SAP group. The Col I expression remained higher in all hydrogels treated groups in comparison to untreated group ($p \leq 0.01$) on day 21. The deposition and breakdown of ECM,

both the processes, play pivotal roles in healing process [285]. MMPs are involved in the breakdown of ECM by catalyzing the hydrolysis of major components of ECM and regulating the cytokines and growth factors [285, 286]. Therefore, the secretion of MMPs needs to be synchronized with the ECM deposition from fibroblasts in order to achieve scar-less healing. MMP-1 or collagenase-1 mediates the proteolysis of the triple helical structure of collagen chains between Gly775 and Leu776 [285]. Gene expression study showed higher expression of MMP-1 during the initial time point (after day 7) for all the groups, and the expression was downregulated with time in hydrogels treated groups **(Figure 3.6E)**. On contrary, the MMP-1 level of untreated wounds remained high at day 21 compared to the levels of hydrogels treated

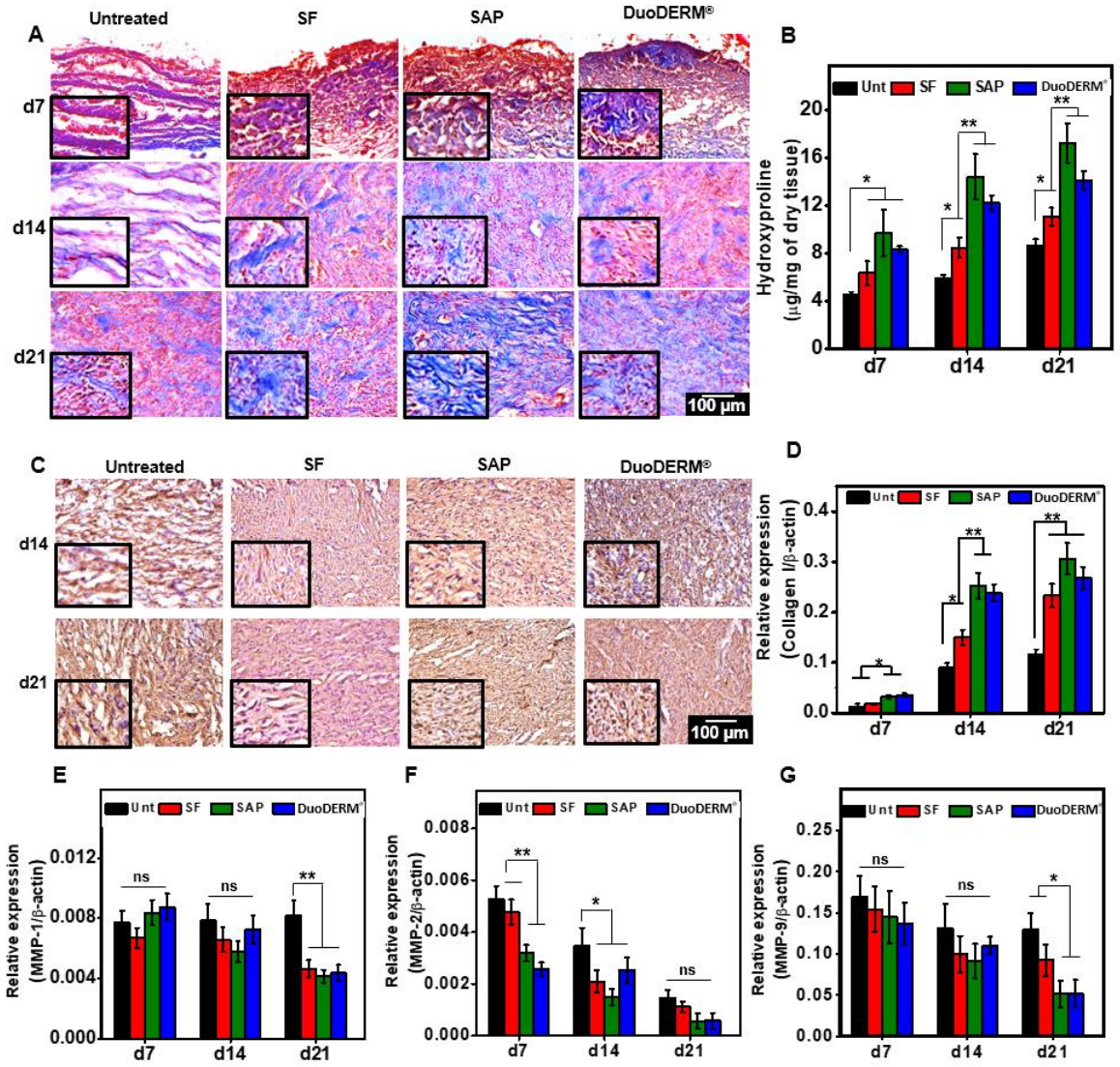


***Figure 3.6. Assessment of ECM components.*** *(A) Histological analysis of healed skin biopsies on days 7, 14, and 21 by MT staining. Magnified images showing blue collagen fibers in regenerated tissue. (B) Quantification of hydroxyproline after 7, 14, and 21 days of treatment. (C) IHC of Col I of wound tissues showing distribution of collagen fibers in the regenerated dermis supported by the hydrogels. (D-G) Gene expression analysis of Col I, MMP-1, MMP-2, MMP-9 genes. Values are plotted as mean ± standard deviation, where * p≤0.05, ** p≤0.01, and ns = not significant.*

wounds, indicating a slower healing process. The result shows simultaneous secretion of Col I fibers and its degradation by MMP-1, indicating protease-mediated remodeling of regenerated tissue in hydrogels treated groups, crucial for attaining native skin architecture [287]. Collagenases cleave collagen fibrils to denature them into gelatins which is further degraded by other MMPs, such as MMP-2 and MMP-9 [35]. Expression of MMP-2 was maximum at day 7 for all the groups and significant differences were observed between the untreated group and SAP hydrogel treated group at day 7 and 14, suggesting accelerated healing in the latter group **(Figure 3.6F)**. Untreated wounds also showed significantly higher expression of MMP-9 on day 21, demonstrating a slower rate of healing than that of SAP and DuoDERM® treated wounds **(Figure 3.6G)**.

### 3.3.9. Anti-inflammatory and immunomodulatory response of SAP hydrogel

Considerable evidence has been found that suggests macrophages to be one of the primary regulators of the healing process [288, 289]. The pro-inflammatory microenvironment of the wound bed at the early inflammation stage (1-3 days) is predominated by M1-type macrophages (pro-inflammatory) and switches into M2 type (anti-inflammatory) within 3-7 days, which favors tissue remodeling **(Figure 3.7A)** [288, 290]. The quantitative gene expression of pro-inflammatory (IL-1β, IL-6, and TNF-α) and anti-inflammatory (IL-10 and TGF-β) cytokines were further studied to analyze the effect of SAP hydrogels on the inflammatory stage of healing. Time course and sequential expression of these cytokines are essential to understand the rate of the healing process. The regenerative property of SF proteins has influenced the progression of the healing process from inflammation to regeneration stage in both SF and SAP groups. Significant reduction in the expression of IL-1β ($p \leq 0.01$) and TNF-α ($p \leq 0.05$) was observed in SF treated group compared to untreated wounds indicating faster initiation of proliferation stage at wound site. In case of SAP hydrogel, the expression of the pro-inflammatory cytokine, TNF-α was significantly lower than the SF group ($p \leq 0.05$), indicating an additive anti-inflammatory effect of aloe phytochemicals present in SAP hydrogel **(Figure 3.7B. i-iii)**. DuoDERM® treated wounds have shown a similar expression pattern of the M1 markers as in SAP treated wounds. High expression of both M1 markers in the untreated group indicates persistence of inflammatory response at the wound sites on day 7. Interestingly, the expression level of IL-6 was not significantly different between the experimental groups and the untreated group. Although the importance of IL-6 for the regulation of initial inflammatory response is well reported, it also stimulates the migration of fibroblasts in the

later regeneration phase [291]. Therefore, the data revealed the dynamic function of IL-6 in the healing process as its expression remained consistent in the experimental groups though their healing mechanisms were progressed to the next phase with a suppressed level of other pro-inflammatory markers. On the contrary, the significant upregulation of anti-inflammatory genes, such as IL-10, TGF-β, was observed in SF and SAP groups in comparison to the untreated group **(Figure 3.7B. iv-v)**. As the expression of M2 markers is more prominent in SAP treated wounds among all the hydrogels treated groups, we postulated the direct contribution of active aloe molecules in M2 macrophage polarization which further promotes the regeneration process. DuoDERM® treated wounds showed significantly lower expression of both the markers compared to SAP group ($p \leq 0.05$) due to lack of potential immunomodulatory component in the gel. Similarly, immunostaining of wound tissue sections showed the presence of more CCR7+ cells (representing M1 phenotype) in the untreated group

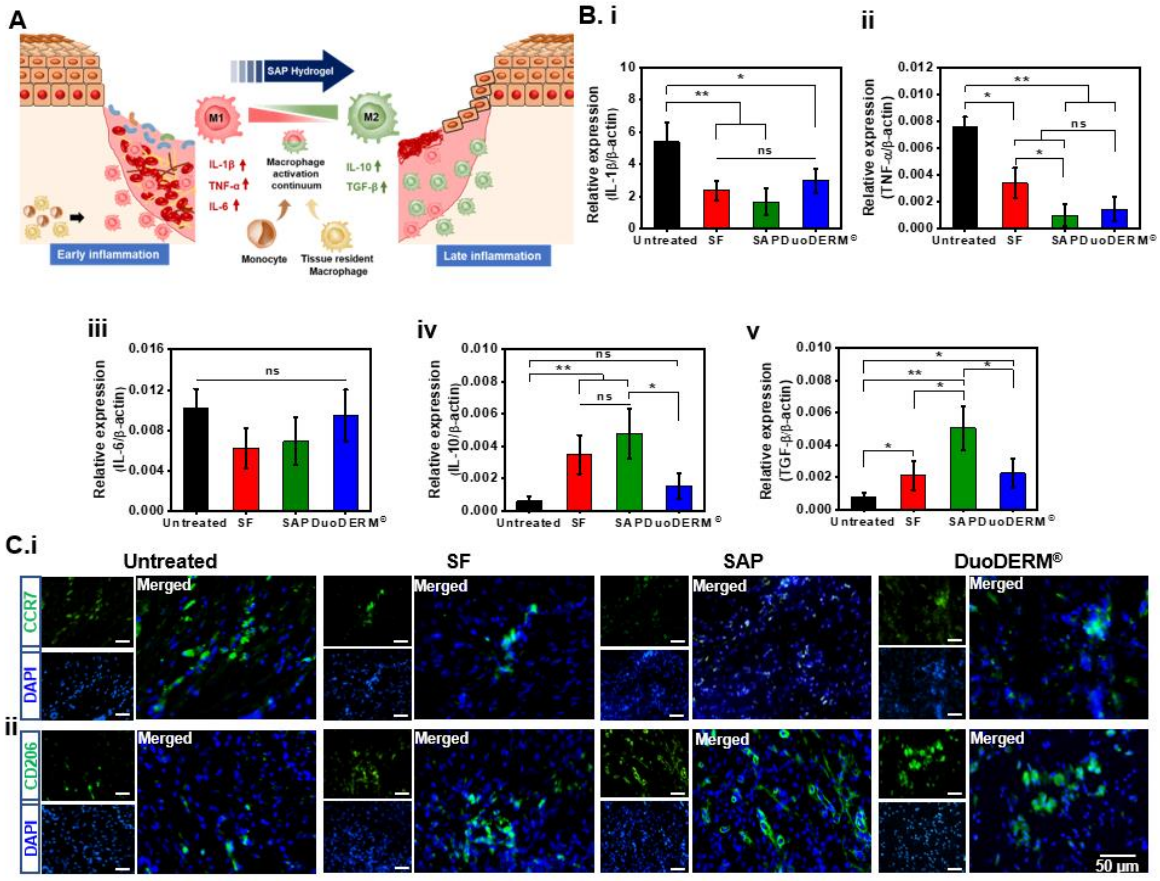


***Figure 3.7. Immunomodulatory effect of SAP hydrogel.*** *(A) Diagrammatic representation of immune cell recruitment at wound site and changes in macrophage phenotype during the time course of early and late inflammatory stages. (B.i-v) Quantification of real-time gene expression of M1 (IL-1β, TNF-α, and IL-6) and M2 (IL-10 and TGF-β) phenotypic markers of collected wound tissue on day 7. Immunofluorescence staining of wound tissue sections of day 7for (C. i) CCR7 (M1 phenotype) and (C. ii) CD206 (M2 phenotype) markers. Values are plotted as mean ± standard deviation, where * $p \leq 0.05$, ** $p \leq 0.01$, and ns = not significant.*

compared to other hydrogels treated groups. SAP-treated wound tissue showed a prominent and homogeneous presence of CD206+ cells (representing M2 phenotype) at day 7, indicating improved anti-inflammatory activity of SAP hydrogel in comparison to other hydrogel groups **(Figure 3.7C)**.

### 3.3.10. Assessment of angiogenic and reepithelization potential

During the early healing stage, MMP-2 and MMP-9 are also involved in the proteolysis of collagen IV, which leads to exposure of cryptic epitopes for integrin-ligand interactions necessary for angiogenesis [292]. The angiogenic blood vessels invade the wound site from intact, healthy tissue and grow into an organized microvascular network across the granulation tissue within a few days. Hydrogel-treated wounds showed improved angiogenic responses compared to untreated wounds **(Figure 3.8A),** which involve rapid migration of endothelial cells and faster revascularization at moist wound bed than that of dry-untreated wound tissue [293]. In the later phase of healing, reepithelization of wounds is one of the most important events of the repair mechanism. The primary epidermal markers such as basal keratin marker, CK14, and suprabasal keratin marker, CK10 were assessed by immunostaining of the wound tissues after 21 days of healing. It was apparent that hydrogel-treated wounds showed comparable regeneration of the epidermis **(Figure 3.8B)**. The expression of both the markers was clearly visible for all hydrogel-treated groups. In contrast, the untreated group showed breaching of epidermal layers in multiple wounds at higher magnification, indicating a delayed healing process. Expression of terminal differentiation marker CK10 was significantly lower in untreated wounds, validating incomplete epithelial maturation after 21 days **(Figure 3.8C)**. SAP-hydrogel-treated wound tissues showed prominent suprabasal keratinocytes at the upper part of the epithelial layer. Therefore, stained images substantiate the accelerated healing process of SAP hydrogel-treated wounds by inducing the differentiation of keratinocytes.

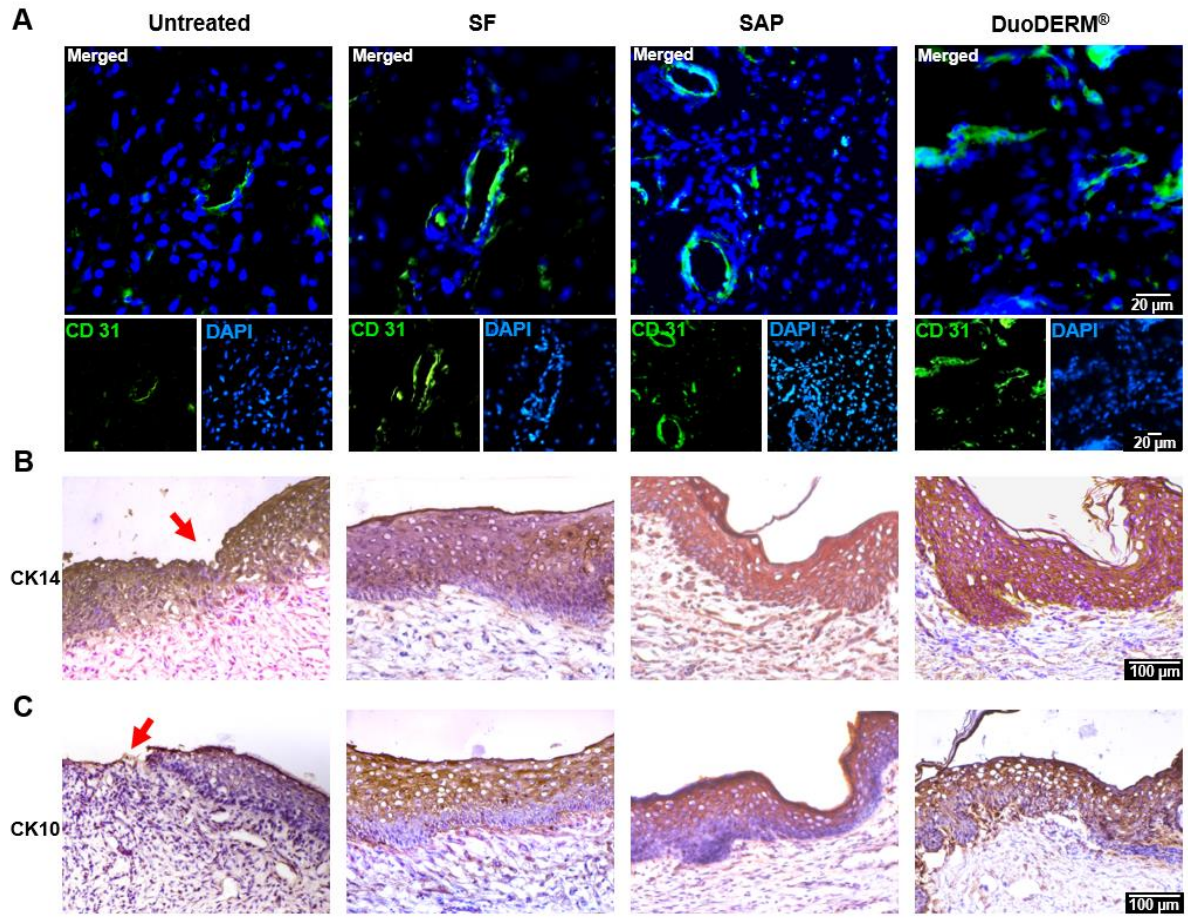


***Figure 3.8. Assessment of angiogenic and reepithelization potential of hydrogels.*** *(A) Immunostaining wound tissues for CD31 marker demonstrating vascular ingrowth in hydrogels treated wounds on day 7. Green depicts CD31 positive endothelial cells and blue depicts nuclei stained with 4',6-diamidino-2-phenylindole (DAPI). (B) Representative IHC images of wound tissue stained against CK14 marker of proliferating basal keratinocytes on day 21. (C) Stained images of CK10 marker of terminally differentiated keratinocytes, depicting its suprabasal expression in epidermis of regenerated tissues after day 21. Red arrows indicate incomplete epithelialization at wound sites in untreated group.*

Overall, we aimed to incorporate additional bioactive components into silk-based hydrogel system, which can be used for the treatment of critical deep open wounds. Incorporation of growth factors (GFs) as bioactive components for wound care applications has shown better healing potential [92, 94]. Albeit, therapeutics containing GFs are associated with high cost, short half-life, low stability or rapid deactivation in proteinase-rich wound microenvironment and require repeated applications and/or administration of high doses over a period of time, which could lead to severe side effects, including oncogenesis [95, 184]. On the contrary, phytochemicals from plants extracts are economical and non-toxic alternatives to growth factors. The functional polysaccharides present in AVM, such as glucomannans and mannose derivatives, majorly contribute to the biological activity of the extract [275]. Previous literature suggested that the biological functionality of these phytochemicals arises from the synergistic

actions of multiple components rather than a single component [275]. However, the extracted aloe gel is highly unstable and has poor mechanical properties limiting its application in tissue engineering. Regenerative research focused on these phytochemicals-incorporated tissue-engineered matrices is still in its infancy. Few studies have explored the efficacy of films of blended BmSF and *Aloe vera* solution, suggesting definite healing properties of the composite [294, 295]. We focused on developing a clinically reliable chemical cross-linker-free phyto-hydrogel matrix containing two types of SF proteins, AVM, and PVP. Besides the bioactivity of phytochemicals of AVM and SF, the composite hydrogel matrix has the potential to regulate moisture content at the wound site and provide an ECM-like three-dimensional provisional matrix for tissue regeneration. PVP, as a stabilizing agent in the composite, offers prolonged stability of the active components by associating with the particle surface to eliminate their precipitation or agglomeration. Therefore, the developed hydrogel can be utilized as topical formulation as it meets basic requirements of routine clinical applications of a topical gel, including ease of use, cost-effectiveness, stability, and three-dimensional shape conformation to fill the wound site. The fabrication process is straightforward and minimalistic, i.e., it does not necessitate any complex chemical steps or machinery, which aids in the easy translation of the technology for clinical practice. The formed SAP hydrogel not only ensures the availability of the pristine materials to cellular growth but also stabilizes and delivers the active molecules of AVM to provide prolonged effective concentrations at the wound bed.

The findings of this study validate the potential of using the SAP hydrogel for enhanced wound healing without any substantial inflammatory complications, suggesting excellent biocompatibility of the composite. In addition, the hydrogel system provides moist conditions, which promotes an efficient healing process. The water content of hydrogels aids in cooling and soothing sensation to relieve pain at the wound site. However, the application of hydrogel in more quantity and tightly covering of the wound might lead to excessive exudate production at the wound site. It can cause maceration of skin tissue around the periphery of injuries and impede the healing process. Therefore, an optimum quantity of hydrogel needs to be applied to obtain the desired condition. The secondary bandage needs to be applied firmly on top of the hydrogel but not too tightly to hinder circulation. The bandage also needs to be porous enough to allow the exchange of moisture vapor and gas. Further, the efficacy of the hydrogel system can be investigated with more critical wound models, such as diabetic wounds. The incorporation of antibiotics or stage-specific drugs might broaden its applications for other drug delivery applications.

## 3.4. Salient findings and outcomes

1. A novel phyto-hydrogel matrix was developed which could modulate multiple regeneration events by virtue of its topological and chemical cues to accelerate the overall healing process.
2. Fabricated SAP hydrogel showed synergistic effects of both of its pristine biomaterials, i.e., silk and AVM extract. The AVM was processed minimally and encapsulated in a hydrogel system to adopt a greener technology to preserve its bioactive moieties.
3. The higher water retention capacity of SAP hydrogel provided an optimum moist environment on the wound bed.
4. The released aloe phytochemicals showed enhanced cellular proliferation and migration. The remaining portion of hydrogel acted as a supportive provisional matrix for regeneration of neo-dermis and enhancing the reepithelialization process.
5. At the early stage of wound healing, SAP hydrogel also demonstrated its ability to reduce inflammation and induce the formation of granulation tissue. Downregulation of M1 phenotypic markers and upregulation of M2 phenotypic markers substantiates the anti-inflammatory and immunomodulatory aspects of the SAP matrix.
6. The comparable healing efficacy of the hydrogel with a widely used commercial product suggests its potential to be used as an alternative natural remedy for wound care at an affordable cost.

***Limitations of the chapter***

While the study demonstrates the potential of the silk-based composite hydrogel for wound healing, several limitations must be considered. The study was conducted using a rabbit model with normal wounds, and the findings may not fully translate to more complex wound conditions such as diabetic or infected wounds, which involve different healing challenges. The use of small animal models introduces inherent interspecies differences in wound healing physiology and cellular responses, which may limit the direct extrapolation of the findings to human clinical scenarios. However, the promising results observed in the preclinical model demonstrate potential of the hydrogel to support tissue regeneration, paving the way for future research and development aimed at translating this technology into clinical applications.

# Chapter 4: Development of a wearable e-bandage patch with silk-based antibacterial ionogel to provide external electrical stimulation for accelerated healing in animal model

*The chapter presents the development and application of a wearable e-bandage patch integrated with a silk-based antibacterial ionogel. This innovative patch provides external pulsed ES to accelerate wound healing in an animal model. The study includes the design and fabrication of the patch, the incorporation of the ionogel to enhance antibacterial properties and signal transmission, and the optimization of ES parameters. The efficacy of the e-bandage in promoting wound closure and tissue regeneration was thoroughly evaluated, demonstrating its potential as a promising tool for advanced wound care.*

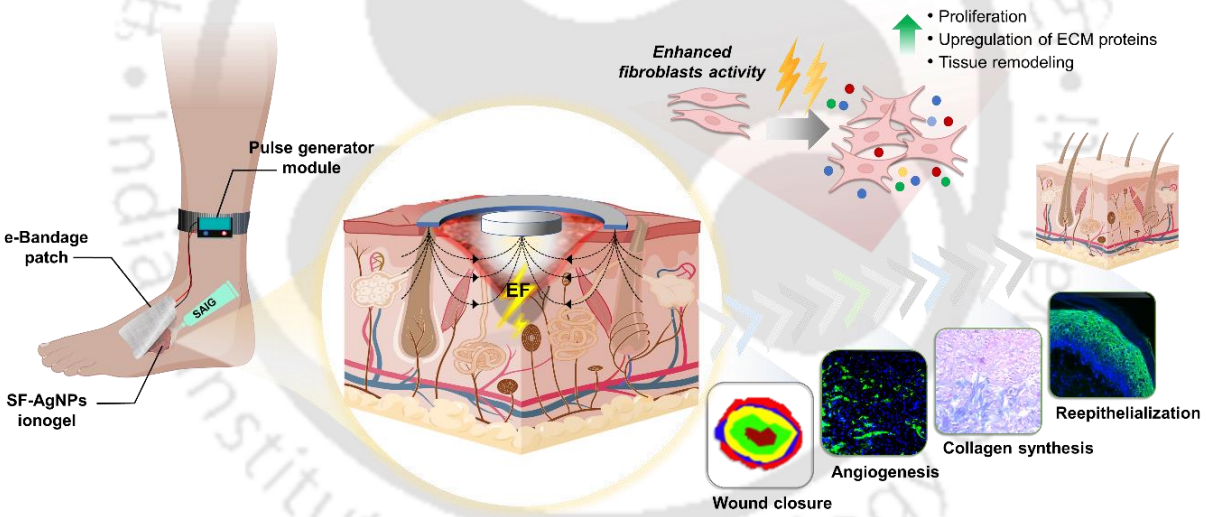


***The work embodied in this chapter is published as:***

Bibrita Bhar, Rajan Singh, Vaishak Gowda, Souradeep Dey, Samit K. Nandi, Roy Paily and Biman B. Mandal. "**Wearable e-Bandage with Antimicrobial Ionogel as an Integrated Electroceutical Device for Accelerated Wound Healing**." *ACS Materials Letters.* 2024; 3453-3461.

**Abstract**

Skin wound healing is a highly orchestrated and complex dynamic process, presenting a significant healthcare challenge when its natural progression is interrupted. Despite the known effectiveness of electrical stimulation (ES) in aiding wound recovery, its practical application remains limited by the use of large complicated equipments. Here, we present a miniaturized wearable electroceutical platform (WEP) that generates low-intensity electrical pulses, which are transmitted to wound site via a breathable electrical bandage patch through a silk-based antimicrobial ionogel interface. *In vivo* efficacy assessment of WEP demonstrated significantly rapid wound closure. Histological and immunostaining analysis exhibited accelerated granulation tissue formation, ECM remodeling, and reepithelization in presence of pulsed ES. *In vitro* studies showed ES-facilitated changes in fibroblast response, including proliferation, alignment, and ECM secretion, which potentially contributed to the observed improvements in healing process. The developed WEP possesses great translational potential, offering an advanced cost-effective therapeutic solution for wound care.

**Hypothesis**

The development of a miniaturized wearable electroceutical platform (WEP), capable of delivering low-intensity pulsed electrical stimulation, may effectively promote wound healing. The incorporation of silk-based ionogels at the electrode-wound interface is expected to enhance signal transmission and provide antimicrobial protection. By delivering controlled, low-intensity electrical pulses in a portable manner, this platform aims to overcome the challenges of bulky, power-consuming clinical equipments and provide a more effective and convenient alternative to traditional wound care strategies.

## 4.1. Introduction

Non-healing skin wounds often lead to the physiological imbalance in the body and result in fatal consequences [262]. These wounds require prolonged, intensive care, are highly susceptible to infections, and contribute to substantial healthcare costs, estimated to exceed $25 billion annually [7]. This susceptibility contributes significantly to lower limb amputations in diabetic patients [296]. Recent meta-analysis revealed a global prevalence of 6.3% for diabetic foot ulcers among adults with diabetes, affecting approximately 33 million individuals worldwide [297]. The significant economic burden on healthcare, coupled with the rising number of patients suffering from such conditions, necessitates advanced strategies that can quickly seal the wound and restore normal skin function. Due to significant progress in medical technology, recent decades have witnessed the development of various advanced treatment strategies for wound management, including compression bandaging, tissue-engineered wound dressings, negative pressure therapy, hyperbaric oxygen therapy, ultrasound, and electrical stimulation (ES) [126]. Externally applied ES is a promising adjunct therapy for wound care. It mimics the natural healing mechanism of endogenous electric fields (EEF) at the wound site. The presence of EEF at the site of skin injury was first discovered ~180 years ago [298]. The confirmation of DuBois-Reymond's discovery came later in 1980 through the detection of an electrical current exiting from amputated fingertips when dipped in a conductive fluid [299]. In most healing wounds, a lateral voltage gradient is generated in the vicinity of the injured area, allowing current to flow through the epidermis [300]. This EEF plays an essential role in the healing process by increasing growth, and mobility of host cells towards the center of the wound [301, 302]. It is notable that in the absence of this electrical current, the average healing rate is estimated to decline by 25% [303]. This phenomenon motivates further exploration of its use to facilitate tissue regeneration for various applications [304]. Exogenous ES imitates this mechanism to expedite the healing process. Numerous preclinical and clinical studies

demonstrated the beneficial effects of ES therapy in combination with standard wound care practices [305]. However, the field is currently facing a translational bottleneck [306]. The major hurdle lies in the cumbersome size and high cost of clinical equipment employed for ES. In addition, there are several risks associated with the use of high-intensity electrical pulses including overcurrent and short-circuit, hence, the protection circuitry needs to be employed along with the device. These requirements may make the devices more power-consuming and bulky. The use of large-sized extracorporeal devices is inconvenient, nearly unportable, and often necessitates patient hospitalization [307]. To address these challenges, low-intensity pulsed ES can be as a viable solution, minimizing the risk while circumventing the need for large instruments. The development of miniaturized wearable devices capable of generating the minimal required electrical signal for tissue regeneration is crucial in the current scenario [308].

Here, we developed a wearable electroceutical platform (WEP) that can deliver low intensity electrical pulses to accelerate the healing of wounds. The system comprises 3 primary components: 1) a disposable electrical bandage (e-Bandage) patch designed for application at the wound site, 2) silk-based ionogels utilized at the interface between the metal electrode and wound tissue to enhance signal transmission, and 3) a reusable pulse generating module (PGM). The e-Bandage patch is designed to be flexible and conform to the wound site, ensuring optimal contact and comfort for the patient. The incorporation of silk-based ionogels at the electrode-wound interface not only enhances signal transmission but also contributes to the biocompatibility, antimicrobial activity and overall performance of the device. The PGM is engineered to be lightweight, compact, and capable of generating precise electrical pulses required for effective wound healing. In this work, we not only assessed the efficacy of the e-Bandage device in promoting wound closure, but also optimized stimulation conditions by applying ionogel and investigated their effects on cellular targets to gain insights into the healing mechanism. Furthermore, the portability and ease of use of the designed device make it suitable for both clinical and home care settings. The development of an advanced wound care technologies has the potential to revolutionize the management of wounds. By providing a more effective, accessible, and less invasive treatment option, these innovations can improve patient outcomes and reduce the economic burden on healthcare systems.

## 4.2. Materials and methods

### 4.2.1. Fabrication of e-Bandage device

The e-Bandage device consists of two components: i) disposable bandage and ii) pulse generating module (PGM). The bandage patch contains the following layers: stainless steel ring-disk electrodes, a thermoplastic polyurethane (TPU) insulating rim, a cotton absorbing pad, and an adhesive back layer. The electrodes of the bandage were connected to PGM through connection wires. The PGM was designed in such a manner that its output can be easily reprogrammed and monitored during the treatment. It comprises three components- (i) Signal generator and tuning unit, (ii) Display unit, and (iii) Lithium-ion battery. The small dimension (18 mm × 45 mm), lightweight (~7 g), low power requirements (5 V, 19 mA), and versatile functionalities of Arduino Nano board make it suitable to be the foundation block of the signal generator and tuning unit. It has 6 PWM (Pulse Width Modulation) output pins, which can be programmed to tune the frequency and duty cycle of the pulses as per the desired levels. However, the board cannot control voltage levels after fixing the frequency and duty cycle, hence, a potentiometer arrangement is attached to the output of the PWM pin for fine-tuning the voltage level of the pulse before connecting it to the bandage. To avoid any errors in pulse levels while conducting the treatment, a small lightweight serial display board was attached to the board, which displays the programmed frequency and duty cycle of the pulses. Finally, the whole module was powered with a thin, small-sized lithium-ion battery so that the module can be rechargeable, which made it easy to use during the treatment.

### 4.2.2. Preparation of SF-AgNPs ionogel (SAIG)

The SF protein was isolated from *Bombyx mori* cocoons, following the established protocol [73]. Further, the isolated SF was mixed with isotonic 0.9 % w/v sodium chloride (NaCl) solution to prepare an ionic liquid-based SF solution. Anionic surfactant, sodium dodecyl sulfate (SDS), was used as a gelling agent to initiate sol-gel transition in SF solution for the formation of SF-based ionogels, containing predominantly β-sheet structure [309]. The ionogels were synthesized using a facile one-pot approach, wherein SF ionic solution was mixed with polyvinylpyrrolidone (PVP K-90, 1 % w/v), SDS (3 mM), and AgNPs (50 ppm), and incubated at 37 °C for 1 h. PVP was employed for its mucoadhesiveness and as a thickening agent [310]. AgNPs were synthesized by chemical reduction method following previously established protocol [311]. The antimicrobial property of AgNPs was determined by evaluating their minimum inhibitory concentration (MIC) and minimal bactericidal concentration (MBC) using the established broth microdilution method [312]. Bacterial cultures of *Escherichia coli*

(MTCC 40), *Staphylococcus aureus* (MTCC 3160), and *Pseudomonas aeruginosa* (MTCC 1688) were obtained from Microbial Type Culture Collection and Gene Bank (MTCC, India). The stock cultures were inoculated into 5 mL of sterile LB broth and incubated at 37 °C. Overnight inoculated cultures having viable count of $10^8$ CFU/mL were used further testing. AgNPs stock solutions were two-fold serially diluted to concentrations ranging from 128 ppm to 1 ppm. Each dilution was mixed with diluted bacterial suspension of ~$10^6$ CFU/mL in each well of a 96-well microtiter plate and incubated at 37 °C for 24 h. Negative control wells contained only medium, while positive control wells included medium with bacterial inoculum without AgNPs [313]. The MIC values present the lowest concentrations of AgNPs, at which the medium remained clear after 24 h of incubation. The MBC was determined by plating the samples from wells showing growth inhibition on LB agar plates and identifying the lowest concentration that resulted in no growth after overnight incubation at 37 °C. Further, the final concentration of AgNPs utilized for SAIG preparation was optimized through cellular viability assessment of HDF (Himedia, India) cultured on SF ionogels with different concentrations of AgNPs (0, 25, 50, and 100 ppm). AgNPS were characterized by transmission electron microscopy (TEM) imaging, selected area electron diffraction (SAED), and energy dispersive x-ray (EDX) analysis. The incorporation of AgNPs into the formulation aimed to enhance the electrical conductivity and antimicrobial properties of the gel.

### 4.2.3. Physico-chemical characterization of SAIG

The dynamics of the sol-gel transition were monitored by spectroscopic measurements at 600 nm using a Multiskan Sky microplate spectrophotometer. The increase in turbidity of the formulations was detected as the gelation progressed, and the completion of the formation of the gel was indicated by the curves reaching the plateau. The degradability of the fabricated ionogels was evaluated *in vitro* by immersing them in a solution containing 2 U/mL of protease XIV (Sigma–Aldrich, USA, ≥3.5 U/mg) derived from *Streptomyces griseus* at 37 °C. At regular intervals, the gels were retrieved and weighed to calculate the percentage of remaining mass using the following equation,

$$Mass\ remaining\ (\%) = \frac{Mt}{Mi}\ x\ 100$$

Where $M_i$ and $M_t$ are the initial mass and mass of the construct at the particular time, respectively.

For assessment of moisture retention ability, 1 mL of each gel was kept in a dry incubator at 37 °C. The weights of the gels were measured after 0, 6, 12, 24, 36, 48, and 60 h, and the gels were freeze-dried to measure their dry weights at last. The remaining water content percentage was calculated using the following equation,

$$Remaining\ water\ content\ (\%) = \frac{Wt - Wd}{Wi - Wd} \times 100$$

Where $W_i$, $W_t$, and $W_d$ are the initial weight of the gel, the weight of the hydrogel at the particular time (t), and weight of the lyophilized dry gel, respectively.

### 4.2.4. Antimicrobial assessments of SAIG

For the inhibition zone assessment, 100 µL of bacterial suspension ($OD_{600}$ = ~0.5) was evenly spread on 90 mm solidified nutrient agar petri dishes using the spread-plate method and kept in an incubator at 37 °C to obtain bacterial lawn. The study included a positive control group of SF gel incorporated with gentamicin (50 ppm) and a negative control group of only SF gel. For comparative efficacy assessment, a commercially available topical wound care product, Hydroheal™ AM (contains colloidal silver), was also included in the study. The experimental group SAIG contained 50 ppm AgNPs, chosen based on biocompatibility assessment. Four 6 mm diameter holes were made on each plate, one for each group, and 100 µL of gel was placed in each hole. The zones of inhibition were visualized and measured after 24 h of incubation.

### 4.2.5. Electroactivity assessment of SAIG

The electroactivity of SAIG was assessed through an analysis of its current-voltage (I–V) characteristics. This analysis was conducted using a two-probe I–V measurement setup using a Keithley 4200-SCS semiconductor characterization system. The probes were connected to copper sheets placed on both sides of SAIG (50 mm x 10 mm x 2 mm). The I–V measurements were performed by applying a DC voltage sweep from 0 to 1 V and measuring the resulting current (n=3). All measurements were conducted at room temperature (~25 °C). The resistance (R) was derived from the inverse of the slope of the I-V characteristics[314].

### 4.2.6. *In vitro* hemolysis study

*In vitro* hemolysis test was conducted to ensure the hemocompatibility of WEP following established protocol [315]. Erythrocytes were separated from whole blood by centrifugation at 1,000 rpm for 10 min and washed with 150 mM NaCl buffer twice. The obtained erythrocytes were then 20 x diluted with 150 mM NaCl buffer. The components of the WEP, which include disks of stainless-steel metal electrode (5 mm), cotton bandage (5 mm), absorbent tape (5 mm),

and SAIG (100 µL), were incubated separately and combined with 1 mL of diluted erythrocytes stock for 1 h. 1% triton X-100 (Sigma Aldrich, USA) and 150 mM NaCl buffer were used as positive and negative controls, respectively. The solution was then collected and centrifuged at 3000 rpm for 5 min to settle down the erythrocytes. 100 µL of supernatant was collected into a 96 well microplate, and absorbance was read at 540 nm in a Multiskan Sky multiplate reader (Thermo Scientific, USA). The hemolysis ratio (%) was calculated by following equation,

$$Hemolysis\ ratio\ (\%)\ = \frac{(As - An)}{(Ap - An)} x\ 100$$

Where $A_s$, $A_n$, and $A_p$ are the absorbance values of the sample, negative control, and positive control, respectively.

### 4.2.7. Breathability assessment

The breathability of the e-Bandage patch was evaluated by measuring the water vapor transmission rate (WVTR) following previously reported protocol in accordance with the European Pharmacopoeia standard [316]. Briefly, the bandages were affixed to the mouth of self-standing centrifuge tubes with an inner diameter of 25 mm, each containing 25 mL of distilled water. The bandages were secured with Teflon tape to ensure a tight seal. The initial weight of the sealed tubes was recorded. The tubes were then placed in an incubator set to 37 °C with a relative humidity of 35%. After 24 h, the tubes were removed from the incubator and weighed again to determine the final weight. The WVTR, expressed in grams per square meter per day (g/m²·day), was calculated using the following equation,

$$WVTR\ = \frac{(Wf - Wi)}{A}$$

Where $W_f$, $W_i$, and A are the final weight of tube, initial weight of tube, and area of opening of tube, respectively.

### 4.2.8. *In vivo* wound healing assessment in rabbit model

The animal experiment was conducted on adult rabbits weighing 1.5 to 1.8 kg. Ketamine hydrochloride (33 mg/kg; Ketalar®, Parke-Davis, India) and xylazine hydrochloride (6 mg/kg; Xylaxin®, Indian Immunologicals, India) were administered intramuscularly to anesthetize the rabbits before wounding. Full-thickness skin wounds were generated using a biopsy punch (8 mm diameter) on the dorsal region of the rabbits under anesthesia. 200 µL of ionogels were applied on the wounds for all the experimental groups except the untreated (UNT) group. The e-Bandage patches were applied on the wounds in the case of ES groups: ES1: 250 mV/mm,

250 ms, 2Hz; ES2: 500 mV/mm, 250 ms, 2Hz; and ES3: 1000 mV/mm, 250 ms, for 2 h per day. We discontinued further investigation of the effects of the ES3 group due to instances of skin irritation and damage, aiming to mitigate the discomfort or pain experienced by the animals. The wounds were regularly monitored and photographed on days 0, 4, 7, 10, and 14. The regenerated tissues were collected from the wound sites on day iongineering14. Animals of each group were administered Meloxicam (0.3 mg/kg body weight; Melonex Injection, Intas Pharmaceuticals Ltd., Ahmedabad, India) injection daily intramuscularly for 3 days. The experimental procedure was conducted with utmost care to minimize any discomfort experienced by the animals. Subsequently, the area of the wounds was measured from the gross wound images using ImageJ software. The relative wound area (%) was then calculated using the following equation.

$$Relative\ area\ of\ wound\ (\%) = \frac{At}{Ai} \times 100$$

Where $A_i$ and $A_t$ are initial wound area and wound area at the particular time (t), respectively.

### 4.2.9. Analyses of collected regenerated tissue from wound site

For histological analysis, the collected wound tissues were fixed using 10% neutral buffered formalin (NBF) and cryosectioned with a thickness of 10 µm using a cryomicrotome (Leica Biosystems, Germany). The initial histological analysis of the tissue involved staining the tissue sections with H&E. The examination of total collagen was conducted by MT staining using the Trichrome Stain (Masson) Kit (Sigma–Aldrich, USA), following the manufacturer's protocol. The hydroxyproline content of collected tissue was assessed following previously reported protocol [279]. The sGAG content was estimated from papain-digested total tissue samples following 1,9-dimethylmethylene blue (DMMB) assay [317]. Immunohistochemistry (IHC) of collagen type I (Col I) was conducted to evaluate Col I deposition using Vectastain Elite Universal ABC kit (Vector Laboratories Inc., USA), following the manufacturer's protocol. Following the staining, the sections were counterstained with hematoxylin, and the images were captured using a Nikon ECLIPSE Ti2 inverted microscope (Nikon Instruments Inc., Japan). The excised tissue sections were analyzed by immunofluorescence using the following primary antibodies: anti-CD31 and anti-CK14 (Abcam, UK). Subsequently, the sections were incubated with Alexa Fluor® 488-labeled secondary antibody, counterstained with 4′,6-diamidino-2-phenylindole (DAPI), and imaged using a fluorescence microscope.

### 4.2.10. Effect of pulsed ES on human dermal fibroblasts

The effect of pulsed ES was assessed on HDF (procured from Himedia, India). HDF were maintained in high glucose Dulbecco's Modified Eagle's Medium (DMEM) supplemented with 10 % FBS. Initially, the effect of pulsed ES with varying EF strengths (ES100: 100 mV/mm, 250 ms, 2Hz; ES250: 250 mV/mm, 250 ms, 2Hz; ES500: 500 mV/mm, 250 ms, 2Hz; and ES1000: 1000 mV/mm, 250 ms, 2Hz) were assessed on cells ($10^4$ cells/$cm^2$) seeded on 24 well plates. To assess the effect of ES, the experiments were conducted in reduced serum conditions (2% FBS) to minimize any masking effects on cellular behavior induced by undefined components present in FBS. The stimulation was provided for 2 h per day, and cellular viability was evaluated using MTT after 72 h. Further, HDF were seeded on a thin layer of SAIG for assessment of cellular proliferation rate in the presence of pulsed ES (+ES: 250 mV/mm, 250 ms, 2Hz) for 7 days using Alamar Blue assay. The unstimulated (-ES) group was taken as a reference for the study. To visualize the viable cells, the cells were stained with 4 μM calcein-AM (Sigma-Aldrich, USA) and 2 μM ethidium homodimer-1 (Sigma-Aldrich, USA) on days 1, 3, and 7. The fluorescent images were captured using a fluorescent microscope (Nikon ECLIPSE Ti2, Japan). The representative images were presented where viable cells were exhibiting green fluorescence from the calcein-AM dye, which passively crosses the cell membrane, indicating intact cell membranes. Dead cells appear red due to the penetration of ethidium homodimer-1 through damaged cell membranes [318]. Further, the cell nuclei were stained with 4',6-diamidino-2-phenylindole (DAPI, Invitrogen, USA).

### 4.2.11. Gene expression analysis using qRT-PCR

For gene expression analysis of stimulated HDF, the mRNA of the cells was extracted using TRIzol reagent (Invitrogen, USA) following the manufacturer's protocol. The complementary DNA (cDNA) was synthesized by reverse transcription of isolated mRNA using a reverse transcription kit (Applied Biosystems, USA). The cDNA was further used for qRT-PCR analysis using a High Capacity cDNA Reverse Transcription Kit (Applied Biosystems, USA) performed in QuantStudio™ 5 Real-Time PCR System (Applied Biosystems, USA) for the analysis of the following genes, MKI67, COL1A1, COL3A1, FN1, VIM, FGF2, EGF, and TGFB1. The $2^{-\Delta\Delta Ct}$ method was used to calculate the relative fold gene expression. The housekeeping gene, β-actin (ACTB), was used as an internal control for normalization. **Table 4.1** enlists the sequences of primers used in the qRT-PCR.

***Table 4.1.*** *Primer sequences used in the study for gene expression analysis.*

| Gene name | Protein name | Forward primer | Reverse primer | Accession number |
|---|---|---|---|---|
| **MKI67** | Ki-67 | TGACCCTGATGAGAA AGCTCAA | CCCTGAGCAACAC TGTCTTTT | NM_00241 7.5 |
| **COL1A1** | Collagen type I | TGGAGCAAGAGGCG AGAG | CACCAGCATCACC CTTAGC | NM_00008 8.4 |
| **COL3A1** | Collagen type III | GAGATGTCTGGAAGC CAGAACCAT | GATCTCCCTTGGG GCCTTGAGGT | NM_00009 0.4 |
| **FN1** | Fibronectin | CCATCGCAAACCGCT GCCAT | AACACTTCTCAGC TATGGGCTT | NM_00136 5522.2 |
| **VIM** | Vimentin | GACAATGCGTCTCTG GCACGTGTT | TCCTCCGCCTCCTG CAGGTTCTT | NM_00338 0.5 |
| **FGF2** | Fibroblast growth factor 2 | CGGGTGCCAGATTAG CGC | GGGTTCACGGATG GGTGT | NM_00200 6.6 |
| **EGF** | Epidermal growth factor | TTTCTGTCCTGAAGG CTCAGTGCT | AGGTCATACCCAG GAAAGCAACCA | NM_00117 8130.3 |
| **TGFB1** | Transforming growth factor β-1 | CCCAGCATCTGCAAA GCTC | GTCAATGTACAGC TGCCGCA | NM_00066 0.7 |
| **ACTB** | β-actin | GGCATCCTCACCCTG AAGTA | GGGGTGTTGAAGG TCTCAAA | NM_00110 1.5 |

### 4.2.12. Gene function analysis and construction of protein-protein interaction network

The GeneMANIA server was employed to analyze and predict the interactions among the differentially expressed target genes identified through the gene expression study. GeneMANIA (http://genemania.org/) is a web interface server that aids in the exploration of multiple aspects of target genes, such as physical interactions, co-expression, co-localization, pathways involved, shared protein domains, and genetic interactions [319]. Further, STRING v12.0 (http://string-db.org/), a database of known and predicted protein interactions, was utilized as a search tool to explore the interactions among proteins encoded by differentially expressed genes. These interactions were studied to understand the effects of provided pulsed ES on the critical biological processes associated with the wound healing process.

### 4.2.13. Statistical analysis

All experiments were conducted using n = 3 samples unless otherwise specified. Data analysis was performed using the statistical software OriginPro 2021 (OriginLab Corporation, USA). Graphical data are presented as mean ± standard deviation (SD). Statistical analysis involved comparison between groups and within groups using one-way analysis of variance (ANOVA) followed by Tukey's test at multiple significance levels (* $p \leq 0.05$, ** $p \leq 0.01$, *** $p \leq 0.001$). Histological and immunostaining examinations were carried out by capturing images of 5 fields per section, and subsequent image analysis was conducted using ImageJ software.

## 4.3. Results and discussion

### 4.3.1. Components of e-Bandage device and their functions

WEP comprises following key components: 1) a disposable e-Bandage patch for application on the wound, 2) silk-based ionogel, employed at the interface between the metal electrode and wound tissue to enhance signal transmission, and 3) a reusable PGM. The electrode setup within the patch is connected by wires to the PGM. PGM includes a programmable stimulator circuit, regulator, switches, and rechargeable battery capable of producing ES (**Figure 4.1A**). The patch consists of ring-disk electrodes made of stainless-steel sheets with a thickness of 0.05 mm. The electrodes were peripherally surrounded by a thin insulating casing of thermoplastic polyurethane (**Figure 4.1B**). A cotton absorbent pad and adhesive back layer were incorporated to cover the wound and absorb excess wound fluid, enhancing the functionality of the flexible patch (**Figure 4.1C**). The developed PGM generates pulsed ES and transmits the same at wound site through the single-use bandage patch (**Figure**

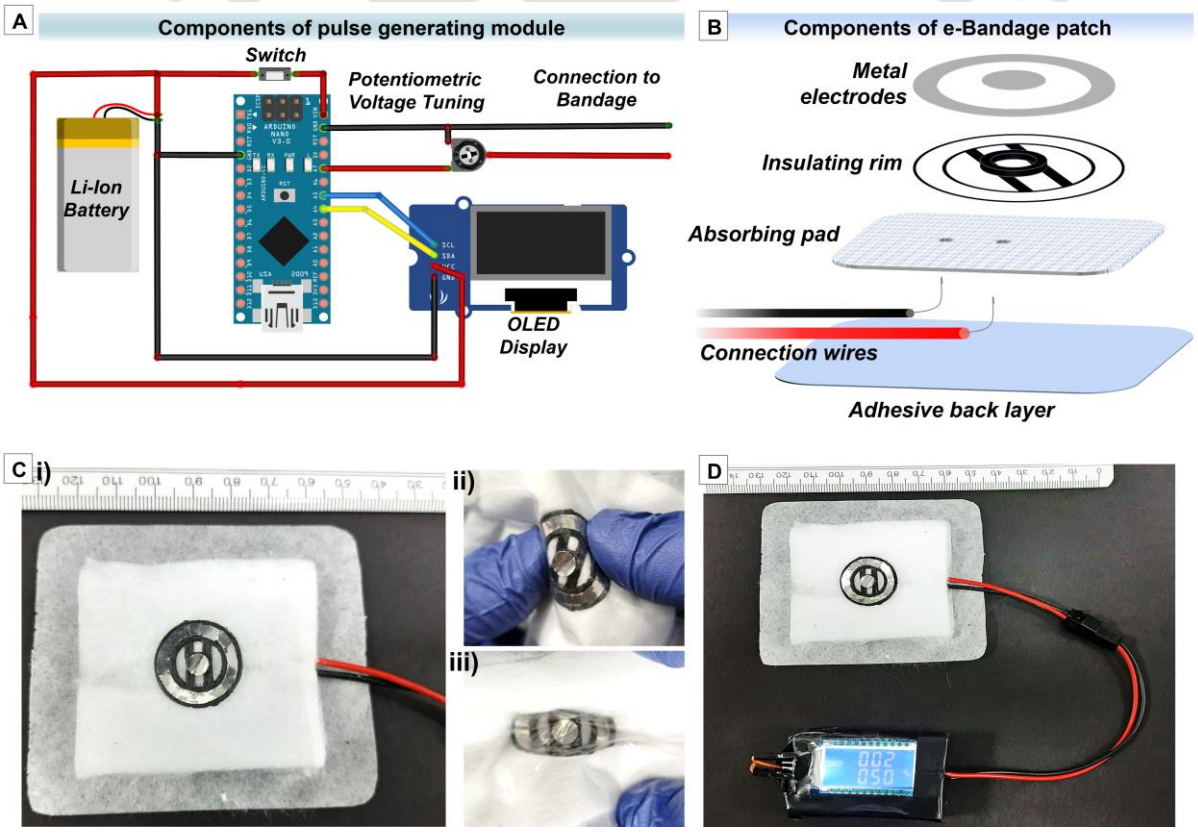


***Figure 4.1. Design and fabrication of e-Bandage device.*** *(A) Design diagram of the pulse generating module (PGM) comprising a stimulator circuit board and a rechargeable battery. The programmable stimulator circuit board is connected to the electrode setup through connection wires. (B) Schematic representation of different components of e-Bandage patch. (C) Photographic images of (i) the fabricated e-Bandage patch and (ii & iii) showcasing its flexible nature. (D) Photographic image of the whole e-Bandage device, including both the single-use bandage patch and the reusable PGM.*

**4.1D**). This design allows easy application of the disposable bandage patch, while enabling multiple uses of the PGM, enhancing cost-effectiveness and practicality in real-world applications.

### 4.3.2. Synthesis and characterization AgNPs

AgNPs are renowned for their antimicrobial activity and electrical conductivity, making them an excellent candidate for incorporation into the formulation of gels applied at the interface between electrodes and wound tissue. AgNPs were synthesized by chemical reduction of silver ions (from silver salt precursor, silver nitrate $AgNO_3$) using reducing agent trisodium citrate ($Na_3C_6H_5O_7$)[311]. Transmission electron microscopy (TEM) imaging revealed predominantly quasi-spherical nanoparticles (**Figure 4.2A**), with the majority falling within the size range of 25-35 nm and an average size of 29.2 nm (**Figure 4.2B**). Furthermore, the selected area electron diffraction (SAED) pattern of the nanoparticles indicated their polycrystalline nature [320] (**Figure 4.2C**), and while energy-dispersive X-ray (EDX) analysis confirmed the presence of silver in AgNPs, evidenced by a distinct peak at 3 keV [321] (**Figure 4.2D**).

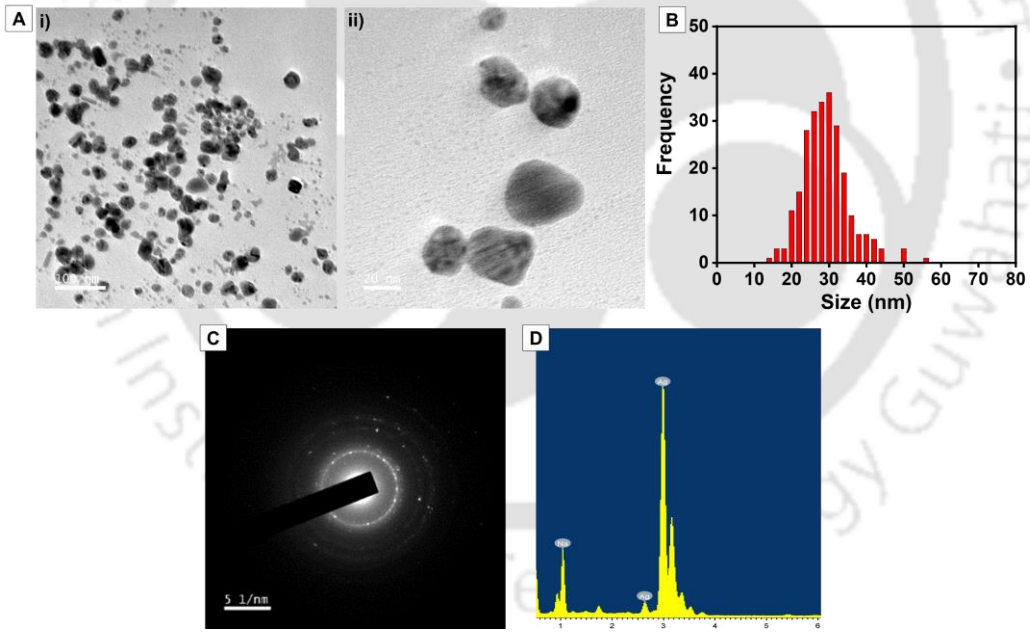


***Figure 4.2. Characterization of AgNPs.*** *(A) TEM images of AgNPs at different magnifications. (B) Particle size distribution curve. (C) The selected area electron diffraction (SAED) pattern. (D) Energy dispersive X-ray (EDX) analysis.*

The antimicrobial property of AgNPs was evaluated by determination of minimum inhibitory concentration (MIC) and minimum bactericidal concentration (MBC) values for following bacterial strains: *Escherichia coli, Staphylococcus aureus, and Pseudomonas aeruginosa*. The MIC values ranged from 13.3 ppm to 26.7 ppm, while the MBC values ranged from 18.7 ppm to 42.7 ppm (**Table 4.2**). The results demonstrated the effective bactericidal ability of the

synthesized AgNPs, as described in previous reports[312, 322], confirming their efficacy as antimicrobial agents against various bacterial pathogens.

**Table 4.2.** The MIC and MBC values of synthesized AgNPs for different bacterial strains

| Bacterial Strain | MIC (ppm) | MBC (ppm) |
|---|---|---|
| *Escherichia coli* | 13.3 ± 4.1 | 18.7 ± 6.5 |
| *Staphylococcus aureus* | 26.7 ± 8.3 | 42.7 ± 16.5 |
| *Pseudomonas aeruginosa* | 15 ± 5.6 | 29.3 ± 6.5 |

The optimal concentration of AgNPs included in the SF ionogel was determined through biocompatibility assessment. The results indicated that a maximum concentration of 50 ppm of AgNPs exhibited no significant cytotoxicity, while 100 ppm resulted in a statistically significant ($p \leq 0.05$) reduction in cell number on day 7 (**Figure 4.3**). Consequently, the 50 ppm concentration of AgNPs was selected for incorporation into the SF ionogel (SIG; containing SF, SDS, and PVP) for formulation of SF-AgNPs ionogels (SAIG).

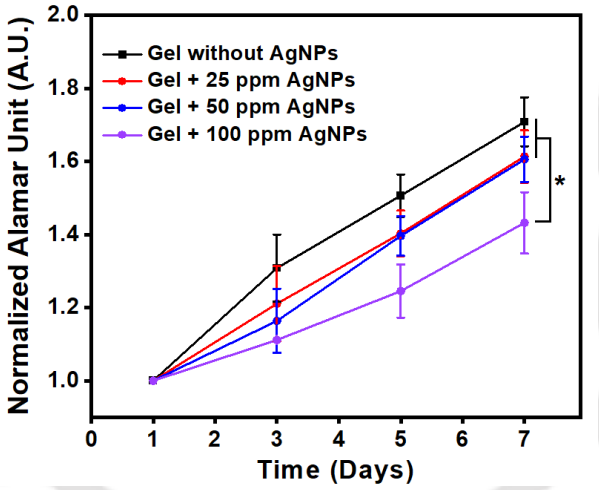


***Figure 4.3. Assessment of the effect different concentrations of AgNPs incorporated in the SF ionogels****. Alamar Blue assay for the assessment of growth and proliferation of HDF cultured on SF ionogels containing different concentrations of AgNPs.*

### 4.3.3. Formulation and characterization of SF ionogels

Biocompatible ionogels were formulated to be applied as solid electrolytic interfaces between wound tissue and metal electrodes. Ionogels, formed by entrapping ionic liquid in gelators like polymeric matrices, inherit the properties of ionic liquid, including ionic conductivity, making them excellent candidates for electronic devices. Natural biomaterials, such as SF, are gaining attention in wound care research [323]. It is being extensively explored due to its unique properties, including abundant supply, low cost, biodegradability, biocompatibility, and non-toxicity [324, 325]. The studies on SF for flexible electronics and sensing have primarily

emphasized its role as a substrate rather than as an active component[326]. Despite possessing favorable characteristics, SF has received limited attention for the development of ionogels. Therefore, we synthesized SF-based ionogels using a facile one-pot approach, wherein SF ionic (0.9 % w/v NaCl) solution was mixed with anionic surfactant, sodium dodecyl sulfate (SDS), polyvinylpyrrolidone (PVP), and AgNPs, followed by incubation at 37 °C (**Figure 4.4A**). We opted for 0.9% saline solution due to its isotonic nature, as hypertonic solutions, while potentially increasing ionic conductivity, may lead to adverse effects when applied to open wounds. The gelation process of the ionogels was evaluated using the turbidometric method by monitoring transmittance at 600 nm. The sol-gel transition in the formulated gels depends on the gelation dynamics of the SF-SDS system, with SDS acting as the gelling agent [327] (**Figure 4.4B**). The transmittance curves demonstrated a steady decrease in transmittance, i.e., an increase in turbidity over time, eventually reaching a plateau, signifying the completion of the gelation process and formation of ionogel matrices at 37 °C. The gelation was completed for both SIG and SAIG ionogels within 1.5 h. However, no gelation was observed for SF+PVP blend even after 2 h due to the absence of SDS (**Figure 4.4C**). To understand the gelation mechanism involving changes in the secondary structure of the SF chain, Fourier-transform infrared spectroscopy (FTIR) was conducted. FTIR analysis of the pregel formulation and postgel of the ionogels demonstrated the shifts of the signature peaks from 1646 $cm^{-1}$ to 1625

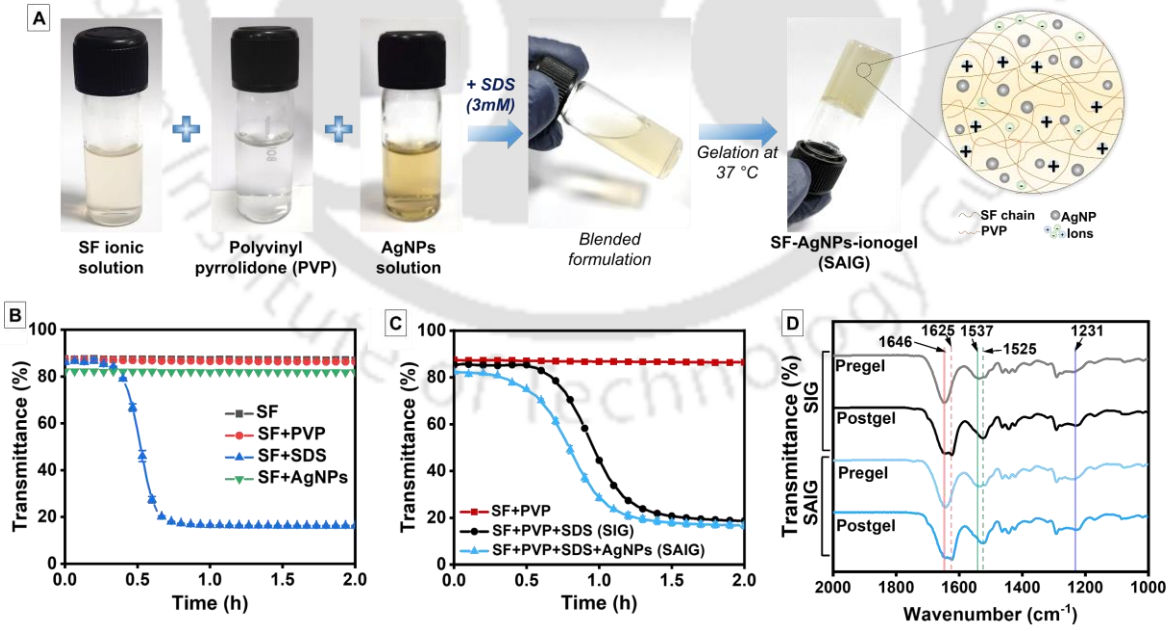


***Figure 4.4. Fabrication of SAIG.*** *(A) Formulation process of SAIG by blending the pristine materials. (B) Turbidimetric analysis of SF gelation in presence of other components of SAIG separately. (C) Turbidimetric analysis of gelation kinetics of SF composites. The result confirms the function of SDS as an effective gelling agent within the SAIG formulation. (D) FTIR analysis of pregel formulation and postgel of ionogels.*

$cm^{-1}$ at amide I region and from 1537 $cm^{-1}$ to 1525 $cm^{-1}$ at amide II region, indicating conformational changes in the SF polymeric chains, leading to β-sheet transition [328] (**Figure 4.4D**). The gelation mechanism involves the head groups of the SDS molecules gradually interacting with the tyrosine- and valine-containing segments of SF chains[309]. This interaction causes the SF chain to bend around the SDS molecules, aligning its hydrophobic blocks closer together and promoting the formation of β-sheet structures within these hydrophobic parts following the gelation of SF [309].

### 4.3.4. Evaluation of physico-chemical properties of SAIG

To assess the viscoelastic properties of ionogels, the ionogels were subjected to an amplitude sweep test, where the shear strain (γ) was varied while maintaining a constant frequency (**Figure 4.5A**). As γ increased, there was a reduction in the storage modulus (G′), intersecting the curve of the loss modulus (G″). The point at which G′ begins to decrease, indicating hydrogel deformation, is termed the limit of the linear viscoelastic (LVE) region. Both SIG and SAIG retained stability up to approximately 36% strain, indicating a range of strain values within which structural integrity of ionogels is maintained. Frequency sweep analysis conducted within the LVE region, with frequencies ranging from 1 to 100 rad/s (**Figure 4.5B)**, further affirmed the stability of both ionogels, with elastic responses observed across the specified frequency range. Moreover, the biodegradability of the ionogels was evaluated through protease treatment over a period of 28 days (**Figure 4.5C**). A significant difference in remaining weight ($p \leq 0.001$) was observed when the ionogels were immersed in protease solution than the control group (immersed in PBS) due to degradation of SF proteins by protease activity. No significant change in degradation rate was observed between SIG and SAIG. Both gels exhibited capacity to maintain moist environment **(Figure 4.5D)**. After 48 h, nearly 80 % of the water content was reduced at 37 °C in dry incubator, suggesting that the ionogels need to be applied every 48 h in order to maintain a moist and conducting environment at the tissue-metal interface.

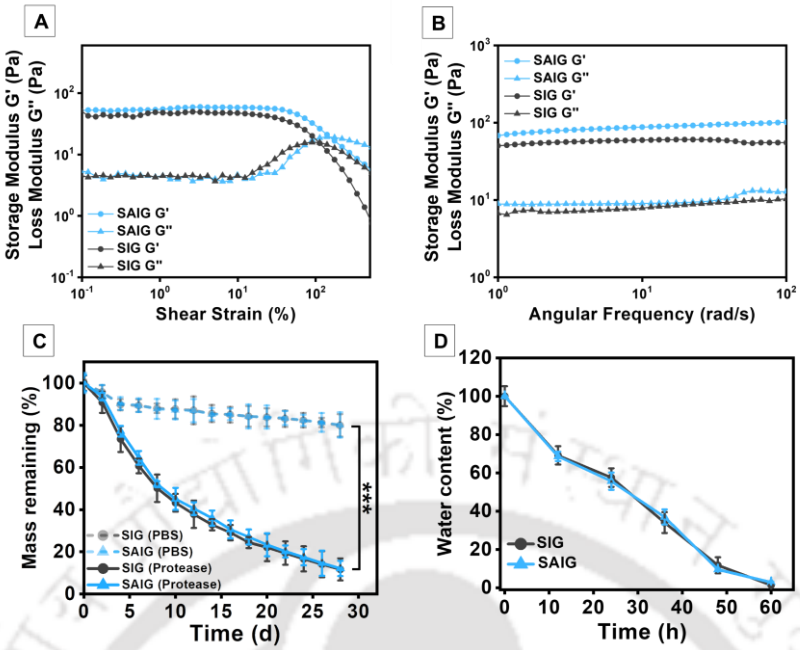


***Figure 4.5. Physicochemical properties of ionogels.*** *Assessment of viscoelastic properties of ionogels through (A) amplitude sweep and (B) frequency sweep test. (C) In vitro enzymatic degradation analysis. (D) Evaluation of water retention capacity of gels.*

### 4.3.5. Electroactivity and antimicrobial properties of SAIG

SAIG was further evaluated for its electrical properties (**Figure 4.6**), with the average resistance determined to be 5.26 ± 1.12 kΩ, at room temperature (~25 °C). The linearity observed in the I-V characteristics suggests ohmic behavior, indicating a stable and consistent interaction between the electrode and the ionogel. The observed electroactivity of SAIG indicated its potential effectiveness in ensuring reliable signal transmission from e-Bandage patch to wound tissue. The conformability of the hydrogel can allow it to easily adapt to the contours of irregularly shaped wounds, promoting optimal contact and facilitating effective treatment across the wound area.

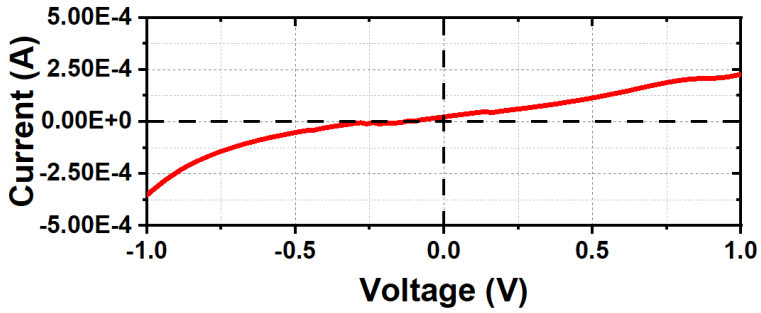


***Figure 4.6. Electroactivity of SAIG.*** *Current–voltage characteristic plot of SAIG.*

The antimicrobial activity of SAIG was evaluated using the agar diffusion method (**Figure 4.7A**). The study included a positive control group of SF gel supplemented with the

aminoglycoside antibiotic, Gentamicin, and a negative control group of only SF gel without AgNPs, which showed no inhibition zone. For comparative efficacy assessment, a commercially available wound care product, Hydroheal™ AM (contains colloidal silver), was also included in the study. Both SAIG containing AgNPs and the commercial gel demonstrated comparable antibacterial effects, with no significant difference in the zones of inhibition in case of all three bacterial strains (**Figure 4.7B**). The comparable efficacy observed with the commercial product validates the potential effectiveness of SAIG for microbial protection. Further, the zone of inhibition revealed that all three bacterial strains (*E. coli, S. aureus, and P. aeruginosa*) exhibited similar susceptibility to SAIG, demonstrating the broad-spectrum antimicrobial potential of the hydrogel. This observation is particularly relevant to wound infection management, as *S. aureus* and *P. aeruginosa* are common causative agents in chronic wound infections, especially in diabetic patients [329-331]. The ability of SAIG to effectively inhibit these pathogens suggests its potential as a protective barrier against microbial contamination, thus enhancing wound healing and addressing a critical challenge in chronic wound care. This finding highlights the potential application of the developed modality for protection against microbial infection, thereby expanding its clinical utility.

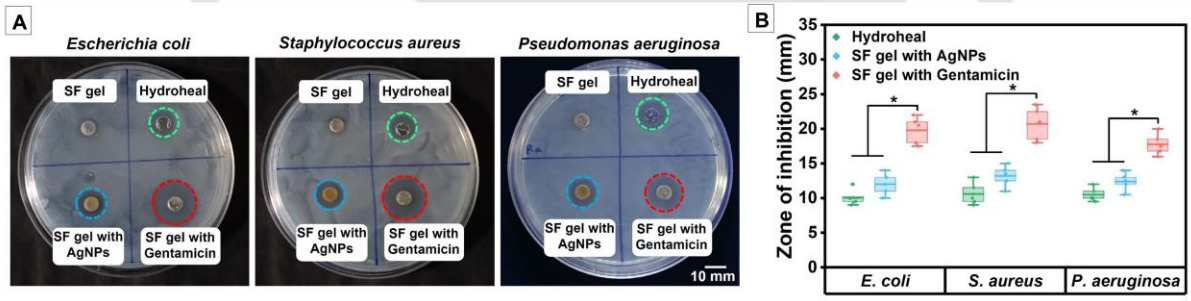


***Figure 4.7. Assessment of antimicrobial activity of fabricated SF gels and commercial gel.*** *(A) Agar well diffusion assay against different bacterial strains. (B) Estimation of corresponding inhibition zones. Values are plotted as mean ± standard deviation, where *p < 0.05.*

### 4.3.6. Hemocompatibility and breathability assessments

To ensure the safety of the developed WEP, we conducted a hemolysis assay to determine its hemocompatibility. In **Figure 4.8,** the results indicated that the hemolysis ratios of the WEP components were less than 5%, which is the critical safe hemolytic ratio according to the ASTM E2524-22 standard. The finding indicated no significant damage to erythrocytes, demonstrating biocompatibility and safety of WEP for application on wound sites. From the application point of view, assessing the water vapor transmission rate (WVTR) is critical for evaluating the suitability of wound dressing materials. A lower WVTR can lead to exudate

retention and promote bacterial growth, while a higher WVTR may cause excessive water loss, wound dehydration, and scar formation. Thus, an ideal wound dressing should balance preventing water loss and dryness while avoiding excess exudate formation [316]. The optimal WVTR for effective wound healing is approximately 2000-2500 g/m²·day [332]. The developed e-Bandage patch demonstrated a WVTR of 2343.4 ± 126.8 g/m²·day, indicating its suitability for maintaining proper moisture at the wound site.

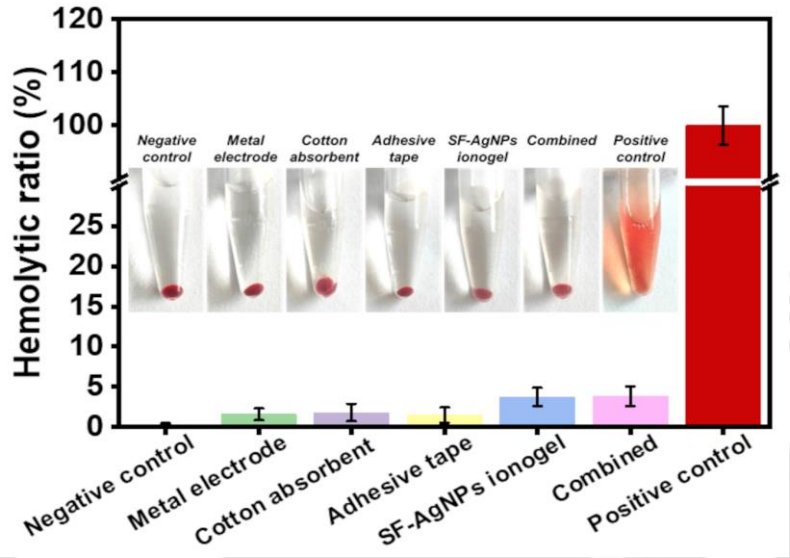


***Figure 4.8. In vitro hemolysis assay.*** *Assessment of hemocompatibility of WEP components.*

### 4.3.7. *In vivo* wound healing assessment of WEP

The wound healing efficacy of the e-Bandage modality was assessed in the full-thickness wound model in rabbits (**Figure 4.9A**). The experiment was performed in accordance with "Principles of Laboratory Animal Care" from the Institutional Animal Ethics Committee (IAEC), West Bengal University of Animal and Fishery Sciences (WBUAFS), West Bengal, India (Proposal No. 763/GO/Re/SL/03/CPCSEA/04/2021-22). The full-thickness wound was created using an 8 mm biopsy punch on the dorsal side of the animal. SAIG were applied on the wounds of all the experimental groups except the untreated (UNT) control group. The test was performed to assess the effect of monophasic pulsed ES with a pulse width of 250 ms, frequency 2Hz, of different field strengths: 250 mV/mm (ES1), 500 mV/mm (ES2), and 1000 mV/mm (ES3) for 2 h per day. The e-Bandages were applied on top of the applied SAIG to provide EF on the wounds in case of ES groups (**Figure 4.9B**). Due to incidences of skin irritation and damage observed in the ES3 group (**Figure A4.1**), further exploration of the effects of that particular group was discontinued in order to minimize animal discomfort and

pain. The wounds were monitored and photographed on days 0, 4, 7, 10, and 14, and the tissue samples were collected on day 14 (**Figure 4.9C**). The gross examination of photographic images of the wounds revealed that the healing of UNT wounds was significantly delayed compared to the experimental groups **(Figure 4.9D)**. The wound contraction was apparent for all the groups between days 7 to 14 **(Figure 4.9E)**. The wound areas were calculated from the photographic images using Image J software for quantitative analysis **(Figure 4.9F)**. The relative percentage areas of wounds on a postoperative day 7 were 69.3 ± 8.7% in UNT group, 60.5 ± 4.7% in SAIG group, 50.8 ± 8.7% in ES1+SAIG group, and 36.9 ± 7.8% in ES2+SAIG group. A significant difference in the wound area percentages between ES2+SAIG and control groups ($p \leq 0.01$) was observed on postoperative day 7 **(Figure 4.9G)**. The e-Bandage system

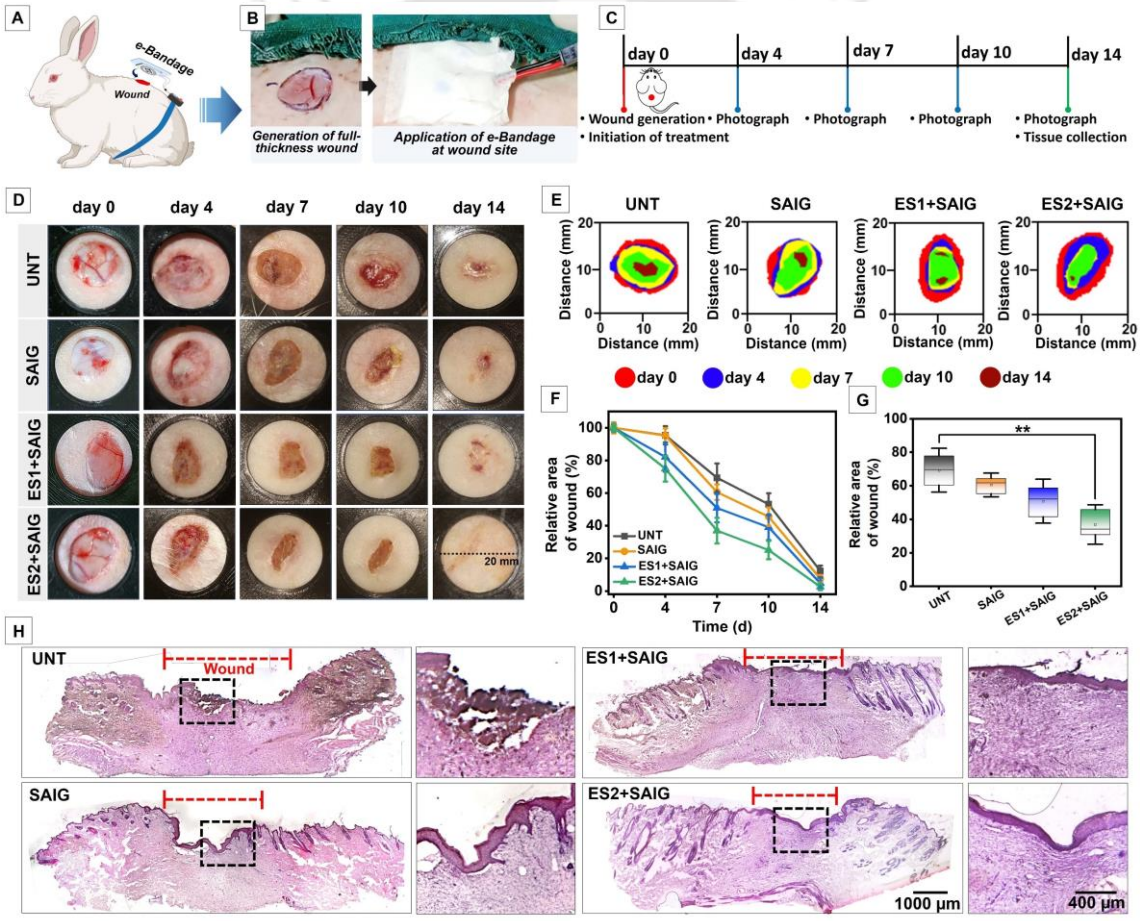


***Figure 4.9. In vivo assessment of healing efficacy of e-Bandage and SAIG.*** *(A) Schematic showing application of e-Bandage device on full-thickness wound generated on rabbit model. (B) Photographic images of application of e-Bandage patch at wound site. (C) Timeline of the in vivo study. (D) Digital images of wound closure in experimental groups and untreated (UNT) control group on days 0, 4, 7, 10, and 14. (E) Wound traces of the healing process were drawn. (F) Quantification of the wound area, determined by measuring the area of wounds using ImageJ software. (G) Quantification of relative wound area on day 7 after treatment. (H) H&E staining of regenerated tissues to depict the wound morphologies after treatment with different experimental groups and UNT control on day 14. Values are plotted as mean ± standard deviation, where ** $p \leq 0.01$.*

providing pulsed ES of 500 mV/mm, 2Hz along with SAIG was observed to be favorable for faster closure of the wounds in comparison to other experimental groups, indicating an effective influence of ES on cellular growth, proliferation, and migration, essential for wound closure. On day 14, the UNT wounds showed delayed closure and took another 2-3 days for complete closure. H&E staining was performed on the collected regenerated tissues to evaluate the healing effect of the WEP from a histological perspective. During the proliferation phase, cell proliferation is crucial to populate the wound with an adequate number of matrix-producing fibroblasts, facilitating the formation of granulation tissue [333]. This tissue partially restores the structure and function of the wounded skin. H&E stained sections revealed incomplete closure of wounds even after 14 days in the UNT group, whereas an intact regenerated epidermis layer was formed at the wound sites in all treated groups **(Figure 4.9H)**. Quantitative analysis showed that ES2+SAIG treatment significantly reduced the width of granulation tissue compared to UNT group ($p \leq 0.01$), suggesting accelerated wound closure and dermal tissue regeneration (**Figure A4.2**).

### 4.3.8. Granulation tissue formation and ECM deposition

The rapid formation of granulation tissue and accelerated wound contraction observed in the ES2+SAIG group potentially signify the effective influence of pulsed ES at the wound site (**Figure 4.10A**). The synthesis of ECM, including its primary constituent, collagen, is crucial for tissue healing. Collagens provide structural support and integrity to skin tissues, playing a significant role in the repair mechanisms of wound healing [334]. Quantification of total collagen was performed by estimating its biochemical marker hydroxyproline level (**Figure 4.10B**). The result indicates higher collagen deposition in wounds treated with ES2+SAIG compared to SAIG and UNT groups ($p \leq 0.01$) on day 14. Additionally, the increased presence of sulfated glycosaminoglycans (sGAG) further supports faster ECM deposition in ES2+SAIG-treated wounds (**Figure 4.10C**). The findings from MT stained images corroborated this observation by demonstrating an increased presence of blue-stained collagen fiber bundles in ES2+SAIG-treated wounds (**Figure 4.10D**). Further, immunohistochemistry (IHC) staining of tissue sections revealed a similar trend, with comparatively lesser collagen type I (Col I) deposition observed in UNT wound tissues (**Figure 4.10E**).

### 4.3.9. Assessment of angiogenic and reepithelialization potential

During healing, angiogenesis occurs as blood vessels invade the wound site, generating an organized microvascular network [335]. ES2+SAIG-treated wounds exhibited enhanced angiogenic responses compared to other groups (**Figure 4.10F**). The relative fluorescence

intensity of anti-CD31 (angiogenic marker) indicated a higher vessel density in the dermis of ES2+SAIG-treated wounds compared to the UNT group ($p \leq 0.05$) **(Figure A4.3)**. The enhancement in vascularization supports the faster healing process. This observation is consistent with previous studies [336], including the randomized controlled clinical trial by Ud-Din et al. 2015 [337]. The study demonstrated that electrical stimulation (ES) promotes wound healing in human skin by reducing wound dimensions and upregulating the expression of VEGF-A and placental growth factor (PLGF). These factors contribute to new blood vessel formation by stimulating the proliferation and migration of endothelial cells and activating endothelial cell precursors, thereby enhancing the healing process [337]. Further, reepithelialization was assessed through immunostaining of regenerated tissue with the epithelial differentiation marker, cytokeratin 10 (CK10). It was evident that all experimental groups exhibited newly formed epidermal layers, with evident expression of CK10. In contrast, the UNT group exhibited breaches in the epidermal layers, along with a notably lower expression of CK10 compared to other groups (**Figure 4.10G**). The significant expression of CK10 in ES2+SAIG-treated regenerated tissue signifies accelerated keratinocyte differentiation, indicating improved structural integrity of the epidermal layer. The outcomes align with the known effects of ES in enhancing keratinocyte function and promoting epithelial differentiation, leading to the organization of a functional epidermis, as reported in prior studies [338, 339]. These findings emphasize the therapeutic potential of ES2+SAIG in facilitating wound closure by effectively influencing keratinocyte activity and epidermal maturation.

### 4.3.10. *In vitro* validation of pulsed ES of e-Bandage device

To understand the effect of ES on the cells, we simulated the microenvironment *in vitro* using a custom-built 3D-printed electro-stimulator chamber connected to the PGM (**Figure 4.11A & A4.4A**). Initially, the HDF were stimulated with similar ES parameters, pulse width: 250, frequency: 2Hz with varying EF strengths. Unlike *in vivo* conditions, pulsed ES of 250 mV/mm group showed a significant increase ($p \leq 0.05$) in cell number compared to both the unstimulated control group and the higher intensity groups (**Figure A4.4B**). This disparity may be attributed to the increased electrical impedance encountered within biological tissues *in vivo*, necessitating higher electrical stimuli for cellular response. Under *in vitro* conditions, the absence of biological tissue impediments eliminates the need for high-intensity stimuli. To mimic the conditions of cells with the application of SAIG, HDF were seeded on a thin layer of SAIG and cultured both with and without the presence of ES for 7 days with 2 h of daily stimulation. The cellular proliferation in presence of ES was significantly increased ($p \leq 0.05$),

as observed by Alamar Blue assay (**Figure 4.11B**). Live-dead stained images of HDF showed a similar trend in viable cell numbers in presence of ES **(Figure 4.11C)**. Cellular morphological changes were evident in the presence of ES, with elongated and directionally aligned cells observed upon stimulation. This indicates the occurrence of galvanotropism, including somatic elongation and alignment of the fibroblasts in response to the applied EF [340] (**Figure 4.11D**). To assess the potential effect of pulsed ES on molecular level, gene expression analysis was performed (**Figure 4.11E**). The expression of MKI67, the proliferation marker, was increased ~2.5 fold by ES, providing further confirmation of the observed cellular proliferation data. The enhanced expressions of ECM protein-encoding genes, including COL1A1($p \leq 0.01$), FN1 ($p \leq 0.05$), and VIM ($p \leq 0.01$), were observed. However, there was no statistically significant difference in the expression of COL3A1 in response to ES. The gene expression of typical growth factors involved in wound healing, such as epidermal growth factor (EGF), fibroblast growth factor (FGF), and transforming growth factor beta (TGF-β), significantly increased when cells were stimulated. This analysis suggested that the improved fibroblast proliferation could be a result of elevated levels of growth factors stimulated by ES. Further, we explored the GeneMANIA database to predict essential genes involved in ES-mediated cellular response on the basis of the differentially expressed genes as the query genes (**Figure 4.11F)**. The predicted TGF-β receptor genes (TGFRB1-3), integral to TGF-β signaling, are potentially involved in ES-mediated cellular responses. This interacting network highlights the role of TGF-β signaling in enhancing the therapeutic effects of ES on wound healing, corroborating previous findings in the field[339, 341]. Along with TGF-β, metalloproteinases, including MMP-9 secreted by dermal fibroblasts, regulate the remodeling stage of wound healing[342]. The predicted involvement of SPARC (Secreted Protein, Acidic and Rich in Cysteine) suggests its influence on fibronectin-induced stress fiber formation, thereby mediating cell-ECM interactions[343]. During wound healing, fibroblasts actively assemble an initial matrix primarily made of fibronectin, gradually replacing the provisional fibrin clot, crucial for stabilizing the mature ECM. The influence of ES on these key events suggests a potential mechanism for expediting the healing process. Furthermore, protein-protein interaction network analysis, conducted using STRING among the same set of differentially expressed genes investigated using GeneMANIA, revealed the involvement of various proteins (details enlisted in **Table A4.1**) in several important biological processes. These processes include positive regulation of fibroblast proliferation, regulation of cell division/cell cycle, cellular response to fibroblast growth factor stimulus, response to wounding and wound healing

(**Figure 4.11G**). The findings provide an overview of how monophasic pulsed ES influences fibroblasts in the dermis, prompting them to proliferate, increase secretion of growth factors, and stimulate ECM synthesis. Rapid ECM deposition may promote cellular migration towards the wound bed for wound closure [344]. Therefore, ES-mediated induction of these crucial biological processes directly contributes to prompt tissue repair.

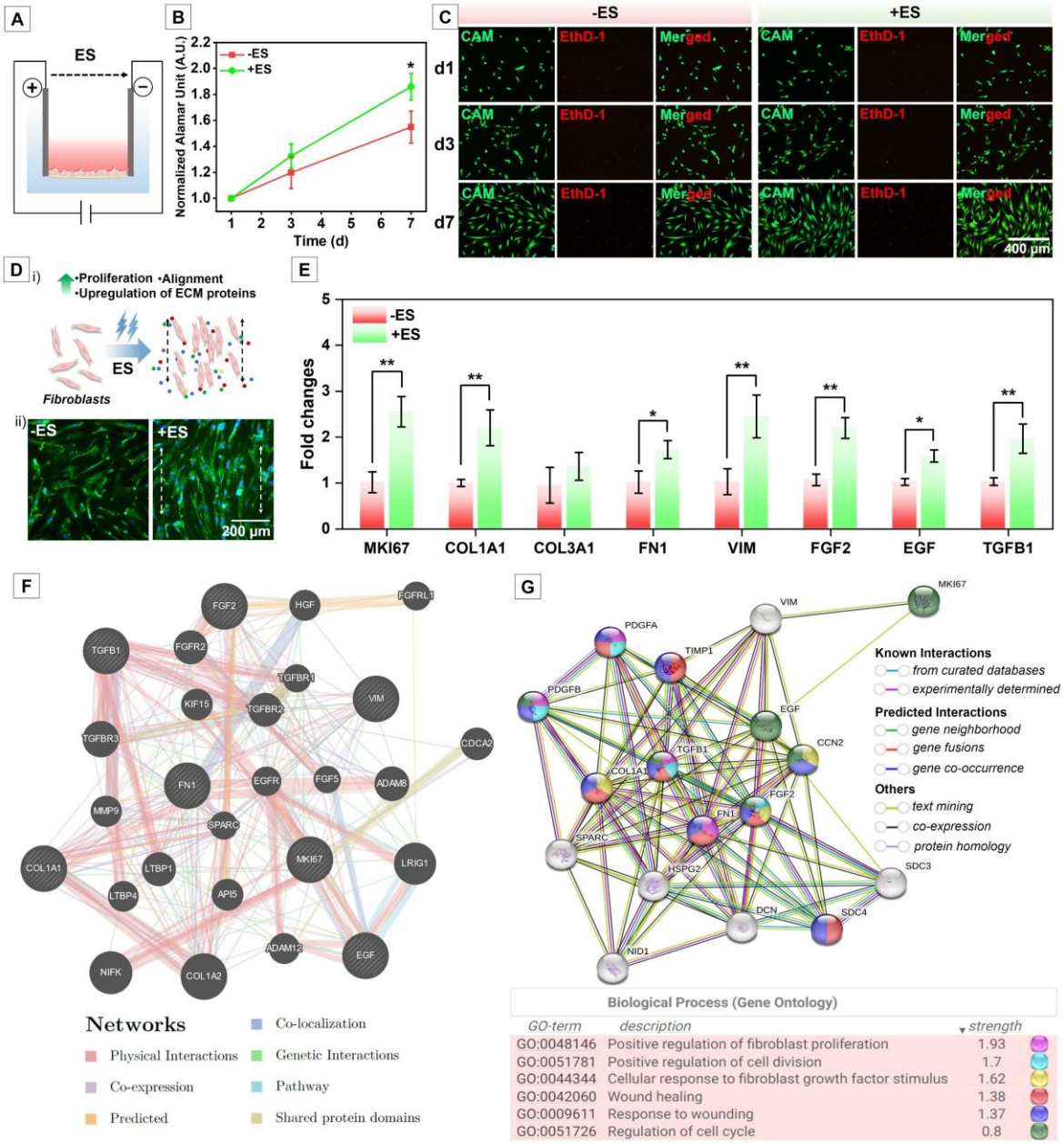


***Figure 4.10. Effect of ES of e-Bandage device on HDF under in vitro condition.*** *(A) Schematic image of cells cultured on SAIG in wells with stimulation from the device. (B) Quantification of cellular proliferation through Alamar blue assay. (C) Cellular viability assessment using live-dead assay. CAM: Calcein-AM, EthD-1: Ethidium homodimer-1. (D) Cellular morphology and alignment without (-ES) and with (+ES) pulsed ES. (E) Gene expression analysis of following genes: i) MKI67, ii) COL1A1, COL3A1, iv) FN1, v) VIM, vi) FGF2, vii) EGF, and viii) TGFB1. (F) Gene interaction network of target and predicted genes constructed using GeneMANIA. (G) STRING analysis to identify the predicted protein-protein interaction involved in specific biological processes. Values are plotted as mean ± standard deviation, where * $p \leq 0.05$, ** $p \leq 0.01$.*

In summary, the study explored an efficient wound healing strategy based on a WEP. The device generated a safe level of electric pulses over the wounds, minimizing discomfort, while the antimicrobial property of SAIG offers additional protection against potential infections. This modality promoted the healing of wounds by accelerating fibroblast proliferation, ECM secretion, enhancing angiogenesis and epithelialization, suggesting potential future clinical applications. Unlike traditional cotton or tulle dressings, which are considered passive or nonocclusive dressings as they mainly serve to cover the wound area and absorb wound exudate without directly contributing to the healing mechanism [345], the e-Bandage patch can serve as a breathable active secondary dressing. It not only covers the wound but also generates electrical pulses to stimulate cellular behaviour. Interestingly, the results showed that WEP-mediated stimulation enhanced specific growth factor expression. The induction of host cells to secrete growth factors involved in regeneration circumvents the need for conventional growth factor-based therapies. While growth factor-based therapies are generally effective in clinical practices, they encounter difficulties related to rapid degradation and loss of bioactivity [346, 347]. In contrast, the cost-effectiveness of WEP arises from its utilization of readily available materials, including cotton absorbent and stainless-steel electrodes, with SF serving as the base material for SAIG. The reusability of the PGM further enhances cost-efficiency of the platform. Collectively, these features position WEP as a practical and economical option, overcoming the need for frequent and expensive growth factor applications. We acknowledge that while this study introduces the healing potential of WEP, further validation in animal models with diabetic or infected wounds would allow us to comprehensively understand the potential of the developed technology to treat the diseased conditions. The developed electroceutical can also offer potential use for addressing cosmetic concerns and providing pain relief. In addition, future investigations could focus on integrating sensors into the bandage patch for real-time wound condition assessment and optimizing ES parameters for enhanced therapeutic efficacy. In conclusion, the study highlights the promising potential of the developed wearable electroceutical for wound management in household settings.

### 4.4. Salient findings and outcomes

1. The work presents an integrated platform which contains 3 primary components: 1) a disposable electrical bandage (e-Bandage) patch designed for application at the wound site, 2) silk-based ionogel (SAIG) utilized at the interface between the metal electrode and wound tissue to enhance signal transmission, and 3) a reusable pulse generating module (PGM).
2. The device generates pulsed electric field over the wounds, while the antimicrobial property of SAIG offers additional protection against potential infections.
3. The modality promoted the healing of wounds by accelerating fibroblast proliferation, ECM secretion, enhancing angiogenesis and epithelialization, suggesting potential future clinical applications.
4. The developed technology offers an integrated solution in the form of a miniaturized device for low-cost household use, potentially transforming the wound care market.
5. The WEP is a robust and versatile platform with significant potential for a wide range of applications, including chronic wound healing, addressing cosmetic concerns, and providing pain relief.

***Limitations of the chapter***

The study highlights the promising potential of WEP in enhancing the healing process. However, several factors require further consideration. The correlation of data obtained from the preclinical rabbit model with human cases presents a key challenge, as results from animal studies may not always directly translate to clinical outcomes due to species differences in healing processes, which are beyond the scope of the current work. Additionally, while its efficacy in normal wound models has been demonstrated, its performance in more complex conditions, such as diabetic or infected wounds, remains to be explored. Further work is needed to integrate real-time sensors for wound monitoring and to evaluate the practicality and durability of the device for continuous use in home care settings. Nonetheless, despite the need for further research and optimization, the study provides a potential breakthrough, with the WEP demonstrating significant promise as an innovative, cost-effective, and portable solution for enhancing healing in advanced wound care.

# Chapter 5: Development of silk-based 3D bioprinted immunocompetent skin model as an advanced platform for skin sensitization assessment

*The chapter provides the details of an innovative approach of fabrication of 3D bioprinted immunocompetent in vitro skin model. This model was developed using a tunable silk-based photopolymerizable bioink that supports cellular growth and proliferation. Functional evaluations of the matured model demonstrated its effectiveness in classifying skin irritants and non-irritants, thus establishing itself as a suitable pre-clinical screening platform for toxicity testing and sensitization assessments.*

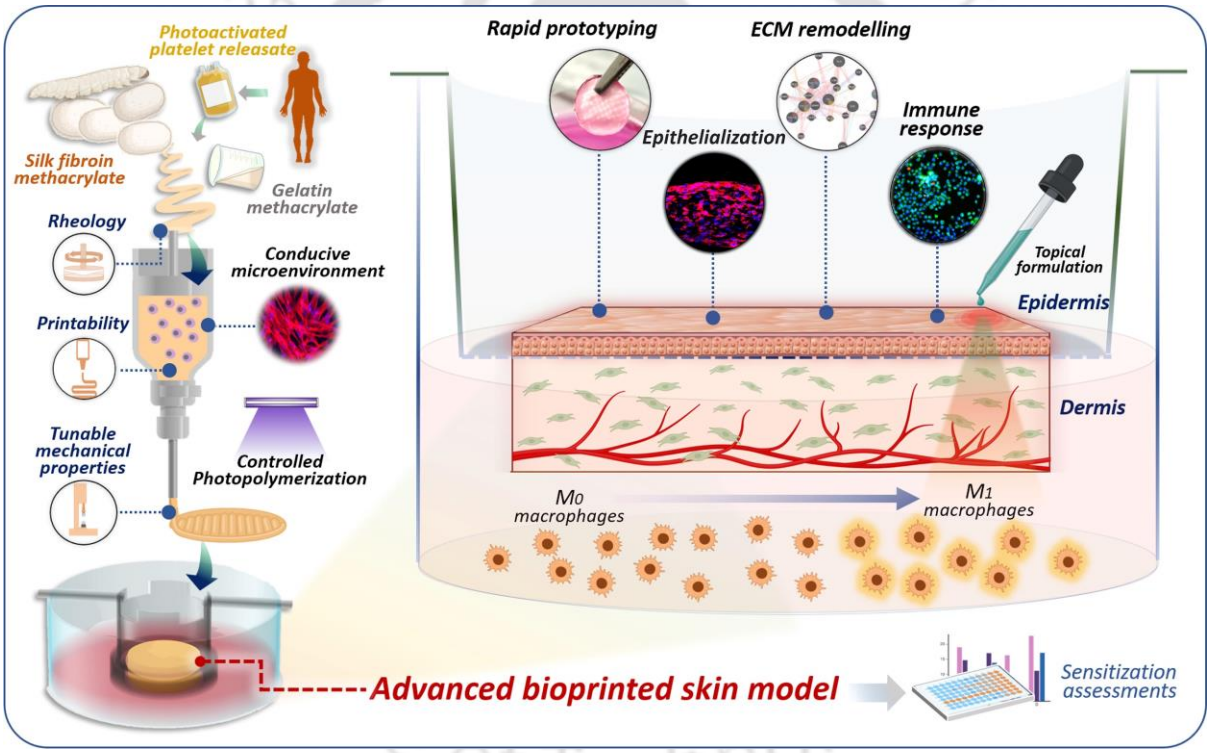


***The work embodied in this chapter is published as:***

1. Bibrita Bhar, Eshani Das, Kodieswaran Manikumar, and Biman B. Mandal. "**3D Bioprinted Human Skin Model Recapitulating Native-like Tissue Maturation and Immunocompetence as an Advanced Platform for Skin Sensitization Assessment**." *Advanced Healthcare Materials*. 2024:2303312.
Reprinted (adapted) here with permission from *Advanced Healthcare Materials* (John Wiley and Sons), Copyright 2024.

**Abstract**

Physiologically-relevant *in vitro* skin models hold utmost importance for efficacy assessments of pharmaceutical and cosmeceutical formulations, offering valuable alternatives to animal testing. Here, we present an advanced immunocompetent three-dimensional (3D) bioprinted human skin model to assess skin sensitization. Initially, a photopolymerizable bioink is formulated using silk fibroin methacrylate (SilkMA), gelatin methacrylate (GelMA), and photoactivated human platelet releasate (PPR). The developed bioink shows desirable physicochemical and rheological attributes for microextrusion bioprinting. The tunable physical and mechanical properties of bioink were modulated through variable photocuring time, aiding control over mechanoresponsive cellular behaviour. Thereafter, the bioink is utilized to 3D bioprint "sandwich type" skin construct where an artificial basement membrane supports a biomimetic epidermal layer on one side and a printed pre-vascularized dermal layer on the other side within a transwell system. The printed construct is further cultured in air-liquid interface for maturation. Immunofluorescence staining demonstrated a differentiated keratinocyte layer and dermal ECM-remodelling by fibroblasts and endothelial cell innervation. The biochemical estimations and gene-expression analysis validate the maturation of the printed model. Incorporation of macrophages further enhances physiological relevance of the model. The model effectively classifies skin irritative and non-irritative substances, thus establishing itself as a suitable pre-clinical screening platform for sensitization tests.

**Hypothesis**

The development of a silk-based 3D bioprinted immunocompetent skin model will enable the fabrication of a physiologically relevant *in vitro* platform that mimics the structural and functional attributes of native skin. By incorporating tunable and mechanically stable biomaterials and relevant skin cell types, the model can support cellular proliferation, differentiation, and extracellular matrix remodeling. Furthermore, integrating immune components, such as macrophages, will enhance the ability of the model to predict skin sensitization and irritation responses, thus providing a reliable and reproducible tool for pre-clinical toxicity testing.

## 5.1. Introduction

Over the past decade, there has been a remarkable upsurge in scientific attention directed at improving the physiological relevance of *in vitro* systems, aligning with the 3Rs principles (replacement, reduction, and refinement) to minimize animal testing. Regulatory agencies such as the U.S. FDA, European Chemicals Agency (ECHA), and European Medicines Agency (EMA) are promoting the adoption of alternative techniques, offering guidelines for their validation and approval [187, 188]. Similarly, the Government of India's recent amendment in 2023 to the New Drugs and Clinical Trial Rules, 2019, aims to reduce the reliance on animal use in research, allowing non-animal methods such as cell-based assays, organs-on-chip, and computational techniques for drug testing [348]. Additionally, the limitation of animal models extends beyond ethical concerns, as their physiological disparities to human skin often lead to ambiguous research outcomes [176]. The aforementioned limitations prompted the necessity for the development of suitable models for *in vitro* pre-clinical testing. The gold standard for *in vitro* skin permeation and irritability assessments is the use of cadaveric skin explants [349]. However, the challenges in using skin explants include limited availability, ethical concerns, variations in skin thickness, skin conditions, storage conditions, donor age, and high laboratory costs [349]. To address these challenges and provide an alternative, synthetic artificial membranes are engineered to mimic skin properties, offering reproducibility in testing. Usually, these membranes primarily act as filters with specific pore sizes, allowing measurement of the diffused molecules from the formulation. However, human skin studies require insights into the potential interactions of the formulations with the cells and the reservoir function of the epidermis alongside the diffusion profile [349]. Therefore, three-dimensional (3D) *in vitro* skin models fabricated with human skin cells have shown the potential to enable more reliable and accurate assessments of pharmaceutical and

cosmeceutical agents as these provide a more biologically relevant microenvironment [350]. Skin is the first organ to be reconstructed *in vitro* and reach clinical translation [351]. Commercially available mono or bi-layered skin constructs, such as EpiSkin™, SkinEthic™ (L'Oreal, France), Phenion® (Henkel, Germany), Epi-DermFT™ (MatTek Corporation, USA), LabCyte® (J-TEC, Japan), and NeoDerm® (Tegoscience, Korea) have significantly advanced the field of skin engineering and are commonly utilized for basic research and toxicological testing of drugs and cosmeceutical agents. The global tissue-engineered skin substitutes market was valued at $2.2 Billion in 2022 and is projected to reach $4.8 Billion by 2030, expanding at a compound annual growth rate (CAGR) of 10.6 % over the period 2022-2030 [352]. Despite extensive research efforts towards the fabrication of 3D *in vitro* skin models, the available collagen-based models predominantly rely on multi-step manual cell-seeding methods, resulting in low reproducibility, fixed sizes, high costs, and limited applicability[353]. Compared to conventional tissue-engineered strategies, 3D bioprinting technology provides an advanced and automated manufacturing platform that enables simulating the complexity of skin in a spatially controlled manner by controlling the deposition of multiple bioinks containing various types of skin cells in a layer-by-layer fashion [189, 190]. The primary advantage of 3D bioprinting is its capacity to generate on-demand models with precise spatial architecture in a consistent and reproducible manner [191]. The extrusion-based printing, in particular, has revolutionized the field of skin bioprinting due to its technical ease, scalability, and, notably, its ability to deposit bioink with high cell density, rendering it well-suited for fabrication of skin models [176, 354].

The currently available *in vitro* models lack essential components such as an inflammatory system and blood vessels, highlighting the need for the development of more physiologically relevant models [355, 356]. Hence, we aimed to develop an immunocompetent 3D bioprinted skin model using an innovative single-step extrusion-based bioprinting strategy in order to gain insights into inflammatory response in presence of skin irritants. To achieve this, it is imperative to ensure the preparation of tissue-specific bioink to support encapsulated human skin cells. A photopolymerizable bioink was formulated by blending silk fibroin methacrylate (SilkMA), gelatin methacrylate (GelMA), and photoactivated human platelet releasate (PPR) **(Figure 5.1A)**. SilkMA sourced from *Bombyx mori* silk cocoons provides an essential foundation for the engineered material due to the excellent biocompatibility, strength, stability, and elasticity of the SF molecule[357]. The inclusion of GelMA serves to enhance the printability and cytocompatibility of bioinks, owing to the cell attachment motifs of the

gelatin molecule[358]. The platelets isolated from human blood were stimulated by exposure to polychromatic light (wavelengths in the range of 600–1200 nm) for photo-activated release of numerous growth factors and interleukins[359]. The PPR comprises a concoction of these essential bioactive molecules in patient-specific levels and ratios, which will further influence the functional responses of the fabricated model in a patient-specific manner. These combined components create a biomimetic environment conducive to tissue remodelling and biological responses, enhancing the overall functionality of the printed model. The optimal concentrations of the pristine materials for the formulation and the printing parameters were determined through comprehensive evaluations of printability, physicochemical attributes, and rheological properties. The *in vitro* stability and tunable mechanical properties, achieved by varying the photocuring time of the bioink, were investigated. Utilizing extrusion-based bioprinting technology, we fabricated pre-vascularized dermal and epidermal layers on opposing sides of a polycarbonate (PC) membrane within a customized transwell system. The printed skin construct was matured in air-liquid interface (ALI) culture for 14 days (**Figure 5.1B**). The formation and differentiation of the keratinocyte layer were assessed by immunostaining against epidermal differentiation markers. Further, maturation of full-thickness skin construct was evaluated by biochemical estimations and detection of alteration in gene expression profile. We have also performed gene network analysis to understand the role of complex molecular components involved during the cell-substrate attachment, ECM deposition and remodelling, epidermal differentiation, and keratinization in the 3D bioprinted model. The barrier property of the model was also evaluated through the permeation of fluorescently-labelled molecules and compared its ability with native skin explants. The phorbol 12-myristate 13-acetate (PMA)-differentiated human macrophages (M0 type) were introduced in the model to assess its inflammatory response after topical application of skin irritative and non-irritative chemicals. We conducted a comprehensive assessment of the predictive capacity of the printed model in accordance with the Organization for Economic Cooperation and Development (OECD) guidelines to evaluate its aptness as a pre-clinical screening platform for skin sensitization tests.

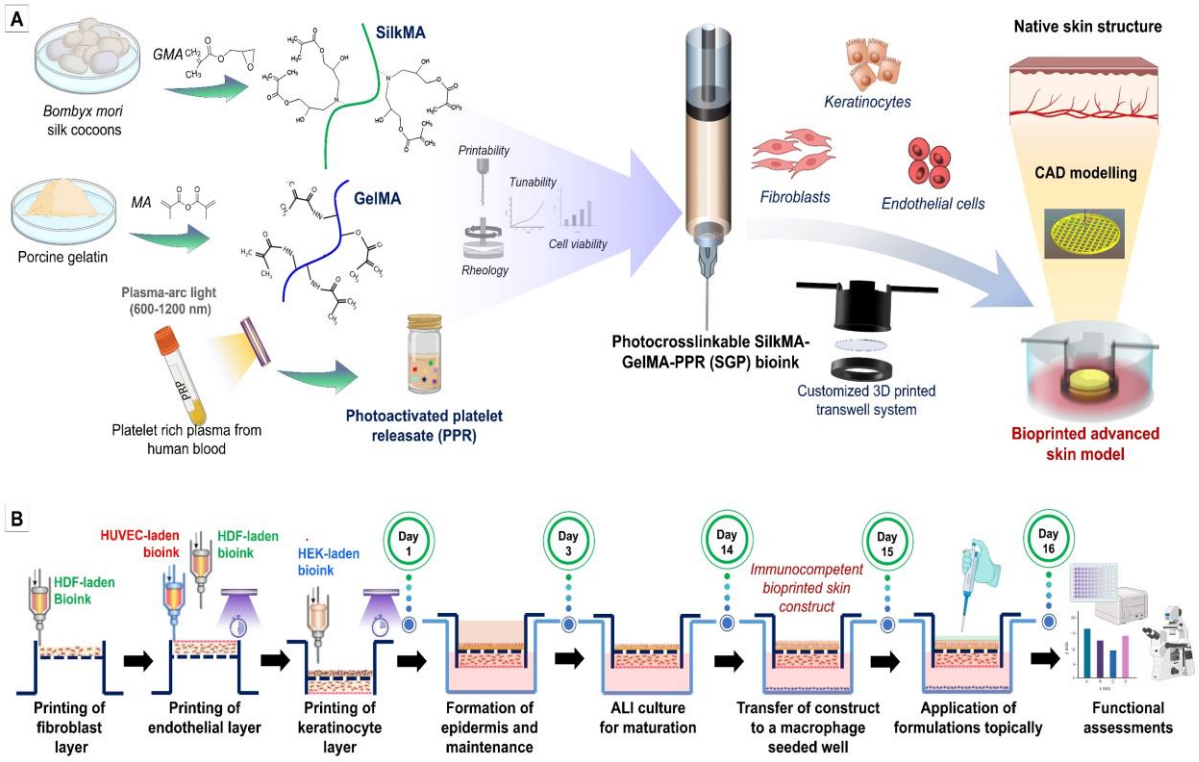


***Figure 5.1. Schematics and timeline of the study. (A)*** *Formulation of the bioink using SilkMA, GelMA, and PPR encapsulated with human skin cells for bioprinting of advanced immunocompetent 3D in vitro skin model.* ***(B)*** *Chronological steps of the study including bioprinting, maturation and functional assessment of the skin model. Created with BioRender.com.*

## 5.2. Materials and methods

### 5.2.1. Preparation of silk methacrylate from *Bombyx mori*

Silk methacrylate (SilkMA) was prepared from *Bombyx mori* cocoons, following previously established protocol [360, 361]. Briefly, the cocoons were cut into small pieces and were degummed in boiling 0.02 M $Na_2CO_3$ solution for 15 min to remove sericin. The degummed fibers were thoroughly washed with distilled water, air dried, and dissolved in 9.3 M lithium bromide (LiBr; Sigma-Aldrich, USA) solution. Subsequently, 6% (v/v) glycidyl methacrylate (GMA; (Sigma-Aldrich, USA) was added dropwise to the silk fibroin-LiBr solution, while stirring at 300 rpm for 3 h at 60 °C, facilitating a substantial reaction between GMA and SF. Further, the solution was dialyzed against Milli-Q water using a dialysis membrane with a molecular weight cutoff of 12 kDa (Sigma-Aldrich, USA) for 4 days. After dialysis, the concentration of protein was measured using gravimetric method. The solution was stored in 4°C for further use.

### 5.2.2. Synthesis of gelatin methacrylate

Gelatin methacrylate (GelMA) was synthesized from porcine skin gelatin by following a previously established protocol[358]. In brief, 10 g of type A gelatin (Sigma-Aldrich, USA) was dissolved in 100 mL of phosphate buffered saline (PBS) at 60°C. Methacrylic anhydride (MA) was dropwise added to the gelatin solution, achieving a final concentration of 6% MA. The resultant mixture was stirred at 50°C for 3 h, then the solution was dialyzed against Milli-Q water for 4 days in dialysis bag (12 kDa) at 40°C. Subsequently, the solution was lyophilized and stored at 4°C until further use.

### 5.2.3. Preparation of photoactivated platelet releasate (PPR)

The preparation of photoactivated platelet releasate (PPR) was conducted with minor modifications to a previously reported protocol [359]. Platelet concentrate bags were obtained from the blood bank of GNRC hospital (Guwahati, Assam, India), following proper processing, and handling protocols reviewed and approved by the Institutional Ethics Committee, Institute of Neurological Sciences Trust, GNRC Hospitals (Reference no. Inst/AS/2015/RR-2018/EC-104). Initially, the platelets were concentrated through centrifugation at 300 x g for 8 min at 12°C, effectively isolating the platelet and buffy coat layer from residual cells. The resulting suspension underwent further centrifugation at 1000 x g for 10 min at 16°C, yielding a platelet pellet and plasma supernatant. The supernatant was reduced to 1/3$^{rd}$ of its initial volume, while the platelet pellet was gently resuspended to form a platelet-rich plasma suspension. The

prepared suspension was poured onto petri dishes placed in an ice bath for photoactivation of platelet and secretion of growth factors. This involved employing a polychromatic infrared light source (600-1300nm, Philips R95) positioned at a distance of 30 cm along the central axis of the lamp, and the process was conducted for 15 min. Further, the suspension was centrifuged at 1000 x g for 15 min at 16°C to pellet down the platelets. The supernatant, rich in growth factors, was collected, freeze-dried, and stored under sterile conditions at -20°C for future use.

### 5.2.4. Formulation of bioink and rheological characterization

The pristine materials i.e., SilkMA, GelMA and PPR were blended with 3 mg/mL of LAP (Sigma-Aldrich, USA) as the photoinitiator due to its high polymerization efficiency, water solubility, and cytocompatibility[362]. LAP allowed the crosslinking of the formulation under visible light (wavelength of 405 nm, 60W LED source, 10 cm), which eliminates the concerns related to UV damage to the cells. In order to optimize the printability of the bioink formulation, different concentrations of SilkMA (0-4% w/v) with GelMA (5-15% w/v) were mixed. The printability of bioink was evaluated by examining the gelation, stability, shear-thinning behavior, and self-standing capability of different bioink compositions. Various concentrations of SilkMA and GelMA were employed, and the printability of each combination was assessed. Further, the optimized acellular bioink was subjected to rheological characterization using a MCR 302 rheometer (Anton Par, Austria). 500 µl of bioink formulation was kept on the sample stage, followed by adjusting the distance between two plates to 1 mm for all tests. To determine the optimal printing temperature, the temperature sweep was conducted at the range of 10–22 °C at a constant shear strain ($\gamma$ = 1 %) and angular frequency ($\omega$ = 10 rad/s). Based on the result of the temperature sweep analysis, the temperature of the sample stage of the rheometer was maintained at 16 °C for the following experiments. The limit of LVER of bioink was evaluated through amplitude sweep analysis at a constant angular frequency ($\omega$ = 10 rad/s) while shear strain ($\gamma$) was increased in the range of 0.01–1000%. The variation in corresponding complex viscosity ($\eta^*$) was also plotted against shear strain ($\gamma$). The obtained LVER from the amplitude sweep analysis was noted and further used for performing frequency sweep tests over a wide frequency range ($\omega$ = 0.1–1000 rad/s) and at a constant shear strain ($\gamma$ = 1%). Furthermore, the shear thinning property of the bioink were analyzed using a thixotropic analysis by alternating shear strain from lower ($\gamma$ = 1%) to higher ($\gamma$ = 1000%) value and repeated for 2 cycles.

### 5.2.5. Assessment of physicochemical properties of formulated bioink

To determine the optimal light-exposure time for each layer of the skin model, 1 mL of optimized bioink mixed with LAP photoinitiator was exposed to the light source for different

durations: 5, 10, 15, 30, and 45 s. The confirmation of gelation was assessed by the tube inversion method. After fabrication of hydrogels, they were kept in PBS at 37°C for assessment of swelling property. The weights of constructs were measured at different time intervals till 24 h. The swelling ratio was calculated by following the Eq. (1),

$$Swelling\ ratio\ (\%) = \frac{Wt - Wi}{Wi}\ x\ 100$$

Where $W_i$ and $W_t$ are initial weight and weight of the construct at the particular time, respectively. Further, *in vitro* stability of the printed constructs was assessed for 28 days by keeping them immersed in PBS with 0.05 % (w/v) sodium azide (Sigma-Aldrich, USA) at 37°C in a humidified incubator. Weights of constructs were measured on 0,1,3,7,10,14,17,21 and 28 days. The percent mass remaining was calculated by following the Eq. (2),

$$Mass\ remaining\ (\%) = \frac{Mt}{Mi}\ x\ 100$$

Where $M_i$ and $M_t$ are the initial mass and mass of the construct at the particular time, respectively. The mechanical properties of the constructs printed using optimized bioink were assessed through tensile and compression tests. All tests were conducted using a computer-controlled universal testing machine, Instron 5944 (Instron, USA). For the tensile test, dumbbell-shaped samples (60 mm x 10 mm x 1.5 mm) were printed and photocrosslinked. The test was performed in accordance with the ASTM D412 test method. The uniaxial tension experiment was conducted at room temperature with a deformation rate of 1 mm/min until the constructs ruptured. The UTS were estimated from the stress-strain curves. For compression test, cylindrical constructs of 10 mm × 10 mm × 10 mm were fabricated and photocrosslinked for 15 s, 30 s, and 45 s. The constructs were compressed up to 60% strain at 1 mm/min rate in unconfined condition. The strain–stress curves were plotted, and the compressive moduli were calculated from the strain–stress curve.

### 5.2.6. Cell culture maintenance

HDF (Himedia, India) cells were maintained in high glucose DMEM (Gibco, Thermo Scientific Fisher, USA) supplemented with 10 % (v/v) FBS (Gibco, Thermo Scientific Fisher, USA) and 1 X antimycotic/antibiotic solution (Gibco, Thermo Scientific Fisher, USA). Human umbilical vein endothelial cells (HUVEC) were obtained from ScienCell (Carlsbad, CA, USA), and cultured in endothelial cell medium (ScienCell, Carlsbad, CA, USA), supplemented with 5% (v/v) FBS, 1 X antimycotic/antibiotic solution. Human epidermal keratinocytes (HEK; from juvenile foreskin procured from Himedia, India) cells were maintained in Keratinocyte

Expansion Medium (Himedia, India). The HDF, HUVEC and HEK were subcultured at 70-80% confluency, and cells at ≤ 5 passage were further used for bioprinting. Further, THP-1, a human monocyte cell line, obtained from NCCS, was cultured in suspension using RPMI 1640 media (Gibco, Thermo Scientific Fisher, USA) following established protocol.

### 5.2.7. Biocompatibility and cellular proliferation assessment of SGP bioink

The effect of PPR on the dermal fibroblasts was evaluated through MTT assay and RP staining. Image analysis with ImageJ software was conducted to examine the distribution of F-actin and measure cellular axes based on stained images. To assess the biocompatibility of formulated bioink, HDF cells were encapsulated in the bioink with PPR (SGP) and without PPR (SG). Collagen gel was taken as control group for the experiment. For DNA estimation, the samples were digested at 60°C for 16 h in papain digestion buffer consisting of 125 µg/mL papain (Sigma-Aldrich, USA), 5 mM l-cysteine (Sigma-Aldrich, USA), 100 mM $Na_2HPO_4$ (Merck, India), 5 mM ethylenediaminetetraacetic acid (EDTA, Sigma-Aldrich, USA). The digested sample was centrifuged at 12,000 rpm for 3 min and supernatant was used for further estimations. Quant-iT™ PicoGreen® dsDNA assay kit (Invitrogen, Life Technologies, USA) was used to quantify the DNA content, following the manufacturer's protocol. In brief, 25 µL of solution of the papain digested constructs were mixed with 75 µL of 1x TE buffer in a 96-well plate. 100 µL of Quant-iT PicoGreen reagent (1:200 dilution) was mixed with the samples in each well, and fluorescence (480 nm/520 nm, Ex/Em) was measured using a fluorescence microplate reader (Tecan infinite M200 PRO, Switzerland). Further, the cellular viability of bioink was evaluated using HDF on days 1, 3, 7, and 14 with calcein AM/ethidium homodimer-1 staining (Thermo Fisher Scientific, USA). The cell-laden constructs were incubated in PBS containing 4 µM calcein–AM and 2 µM ethidium homodimer for 30 min. The fluorescence images were acquired using a Nikon ECLIPSE Ti2 inverted microscope (NIKON Instruments Inc., Japan) and processed using ImageJ software to obtain 3D surface plots. Alamar blue assay was performed to analyze the cellular viability and proliferation of HUVEC cultured in SGP bioink at different time points on day 1, 3, 7, and 14.

### 5.2.8. Preparation of cell-laden bioinks for bioprinting

The optimized SilkMA (2% w/v) and GelMA (10% w/v) solution was blended and sterilized by autoclaving it at 121°C. Syringe filtered (0.2 µm) PPR (10 mg/mL) and LAP (3 mg/mL) solutions were mixed with the blend after autoclaving. Further, the cells were mixed with respective bioinks for printing. The constituents of the bioinks used in this study are listed in **Table 5.1**.

**Table 5.1.** Concentration of each constituent in formulated bioinks.

| Bioinks | GelMA (% w/v) | SilkMA (% w/v) | PPR (mg/mL) | LAP (mg/mL) | Cell density (cells/mL) |
|---|---|---|---|---|---|
| HDF-laden bioink-1 | 10 | 2 | 10 | 3 | $2 \times 10^6$ |
| HUVEC-laden bioink-2 | 10 | 2 | 10 | 3 | $8 \times 10^6$ |
| HEK-laden bioink-3 | 10 | 2 | 10 | 3 | $10 \times 10^6$ |

### 5.2.9. Bioprinting of dermal and epidermal layers on the printed transwell system

The cell-laden bioinks were loaded in CELLINK syringes. The instructed G-code was imported to the Bio X 3D printer (CELLINK, USA), and the bioink was extruded through 25G (ID = 0.25 mm) needle at 16°C following extrusion-based bioprinting at 3-4 mm $s^{-1}$ speed and 100-120 kPa pressure. The dermal layer was printed at the bottom side of the customized transwell system. At first, 4 layers of HDF-laden bioink-1 were printed in layer-by-layer fashion alternatively in both horizontal and vertical directions. The last layer of the dermis was printed with HDF-laden bioink-1 and HUVEC-laden bioink-2 in alternate parallel lines. The bioprinted dermal layer was then crosslinked with exposure to visible light (405 nm) for 30 s. Further, the transwell was inverted to print the epidermal layer on the upper side. A single layer of HEK-laden bioink 3 was printed using 27G needle (ID = 0.2 mm) onto the PC membrane and then subjected to photocrosslinking for 15 s. Subsequently, the transwell containing the printed construct was submerged in a mixed culture medium. The upper chamber of the transwell was filled with HEK-supplemented media, while the lower chamber contained a mixture of high glucose DMEM and endothelial cell medium in a 1:1 ratio. The transwells with printed constructs were kept in the incubator for 48 h at 37°C, 5% $CO_2$. After 48 h, the upper keratinocyte layer was exposed to the air–liquid interface (ALI) by removing media from the upper chamber and adjusting the level of the media in the lower chamber to ensure cell growth and differentiation. Parallelly, the cells were stained with different CellTracker™ Fluorescent Probes (Thermo Fisher Scientific, USA) before printing to observe their distribution while encapsulated in bioinks, following the manufacturer's protocol. Subsequently, the cell imaging was performed after 48 h of printing using the fluorescent microscope. The H&E staining of the printed construct was performed to examine the membrane interface between the keratinocyte and fibroblast layers.

### 5.2.10. Maintenance and maturation conditions for bioprinted construct

After bioprinting of the skin model, the different media were added in the upper and lower chambers of the transwell system based on the specific cell types present in each layer. The upper chamber was filled with HEK-supplemented media (basal medium containing keratinocyte growth supplement with the additives, 1.5 mM calcium chloride, and 50 μg $mL^{-1}$ ascorbic acid) [363]. The lower chamber contained a mixture of high glucose DMEM and endothelial cell medium in a 1:1 ratio. After 2 days, the epidermal layer was exposed to an air-liquid interface (ALI) by removing the medium with a micropipette. The printed constructs were subsequently cultured in a mixed medium (HEK supplemented media/DMEM/ endothelial cell medium in 1:1:1 ratio) placed in the lower chamber, with the volume adjusted to ensure that the epidermal layer remained in the air-liquid interface for maturation. The medium was changed every alternative day for 14 days.

### 5.2.11. Assessments of epidermal differentiation and dermal maturation of bioprinted model

The behavior of encapsulated keratinocytes was examined by RP staining. For immunofluorescence staining, the bioprinted skin models matured for 14 days were cryosectioned using a manual rotary microtome (Leica Biosystems, Germany) and further used for the staining. The sections were permeabilized in permeabilization buffer (PBS containing 0.1% (v/v) Triton X-100), and subjected to blocking buffer (PBS containing 1% (w/v) BSA, 2% (v/v) horse serum, and 0.2% (v/v) tween 20). Next, the sections were incubated with the following primary antibodies, anti-cytokeratin 14, anti-cytokeratin 10, anti-collagen I, and anti-collagen III (Abcam, 1:200 dilution). The sections of human foreskin samples were used as control group for comparison of epidermal markers. The samples were obtained from young healthy donors undergoing circumcisions in GNRC Hospital. The collection and processing protocols were approved by the Institute Human Ethics Committee, IIT Guwahati (Ref no. IHEC/BBM/21/2023). For staining of the endothelial network, the printed construct was incubated with anti-von Willebrand factor antibody (Abcam, 1:100 dilution) suspended in blocking buffer and kept at 4 °C overnight. Then, the sections and constructs were incubated with corresponding secondary antibodies for 2 h, and nuclei were counterstained with 4′,6-diamidino-2-phenylindole (DAPI, Thermofisher Scientific, USA). The images were taken using a fluorescent microscope (NIKON Instruments Inc., Japan), and representative images are presented. DNA quantification of the samples was performed using Quant-iT™ PicoGreen® dsDNA assay kit according to the above-mentioned protocol. For sGAG estimation, 50 μL of

the papain-digested samples or the collected secreted media was mixed with 200 µL of DMMB reagent, and absorbance was measured immediately at 525 nm [325]. Collagen estimation of the samples was performed using Sirius red assay following previously established protocol [224]. A standard calibration curve was plotted, using rat collagen type-1 (0-100 µg/mL) for the estimation.

### 5.2.12. Analyzing maturation of the model through assessment of functional gene expression

The maturation of advanced bioprinted skin model (abp-SM) was further evaluated by examining the expression profile of functional genes (COL1A1, COL3A1, FN1, ELN, EGF, KRT14, KRT10). The printed constructs were disintegrated in Tri® reagent (Sigma-Aldrich, USA) in ice, and the RNA was isolated following acidic chloroform-phenol extraction[364]. The cDNA was prepared from 500 ng of extracted RNA using a high-capacity reverse transcription kit (Applied Biosystems, USA) and a thermal cycler (Veriti PCR, Applied Biosystem, USA). The relative gene expression of target genes was quantified using Power SYBR PCR master mix (Applied Biosystems, USA) in a real-time PCR machine (Applied Biosystems, Quant Studio 5, USA). The primer sequences of the target genes are listed in **Table 5.2**. The relative expression of genes was quantified by comparative $2^{-\Delta\Delta Ct}$ method. The human β-actin gene (ACTB) was used as a housekeeping gene. Further, GeneMANIA server was used to analyze and predict the gene-gene interactions of the differentially expressed target genes used for the study [319] **(Table A5.1)**. GeneMANIA (http://genemania.org/) is a web interface server designed to explore various aspects of target genes, including physical interactions, co-expression, co-localization, involved pathways, and shared protein domains, in addition to genetic interactions.

**Table 5.2.** Primer sequences used for gene expression analysis.

| Gene name | Protein name | Forward primer | Reverse primer | Accession number |
|---|---|---|---|---|
| **COL1A1** | Collagen type I | TGGAGCAAGAGGCGAGAG | CACCAGCATCACCCTTAGC | NM_000088.4 |
| **COL3A1** | Collagen type III | GAGATGTCTGGAAGCCAGAACCAT | GATCTCCCTTGGGGCCTTGAGGT | NM_000090.4 |
| **FN1** | Fibronectin | CCATCGCAAACCGCTGCCAT | AACACTTCTCAGCTATGGGCTT | NM_001365522.2 |

| | | | | |
|---|---|---|---|---|
| **ELN** | Elastin | AGGCTCCAGGTGTAGGTG | TGTGGTGTAGGGCAGTCC | NM_001278939.2 |
| **EGF** | Epidermal growth factor | TTTCTGTCCTGAAGGCTCAGTGCT | AGGTCATACCCAGGAAAGCAACCA | NM_001178130.3 |
| **KRT14** | Cytokeratin 14 | TGAGAAGGTGACCATGCAGA | ATTGTCCACTGTGGCTGTGA | NM_000526.5 |
| **KRT10** | Cytokeratin 10 | AGGGGGCAGTTTCGGAGGTG | AAGTAGGAAGCCAGGCGGTCATT | NM_000421.5 |
| **ACTB** | β-actin | GGCATCCTCACCCTGAAGTA | GGGGTGTTGAAGGTCTCAAA | NM_001101.5 |

### 5.2.13. Evaluation of skin permeability to assess barrier function

The printed samples and skin explants were fixed in transwells (diameter of 1 cm), and these transwells were placed over wells containing 1 mL of 1X PBS solution in a 24-well plate. 200 µL of 5 mg/mL fluorescence-labeled FITC-inulin (2-5 kDa; Sigma-Aldrich, USA) and FITC-dextran (20 kDa; Sigma-Aldrich, USA) were added on the top of the samples in the upper chamber of the insert. The samples were incubated at 37°C in a humidified incubator. At various time intervals (0. 0.5, 1, 2, 3, 4, 5, 6 h), 100 µL of the solution from the bottom of the insert was transferred into a 96-well plate. Subsequently, the fluorescence values were recorded (495 nm/520 nm, Ex/Em) using a fluorescence microplate reader. Then, the amounts of fluorescent molecules were determined based on standard curves plotted using various concentrations of FITC-inulin and FITC-dextran.

### 5.2.14. Assessment of skin inflammatory response of the skin models

The skin models attached to the transwell were transferred to 24 well plates containing PMA-differentiated THP-1 cells[232] seeded on the bottom surface of the well at a cellular density of $5 \times 10^4$ cells per well. Next day, the irritation tests were conducted following the OECD test guidelines 431 and 439. The reference substances comprised one skin corrosive (category 1), one skin irritant (category 2), and one non-irritant (no category) according to the United Nations Globally Harmonized System of Classification and Labelling of Chemicals (UN GHS), mentioned in **Table 5.3**. 1X PBS and 5% (w/v) aqueous solution of SDS (Sigma-Aldrich, USA) were used as negative and positive controls, respectively. The following are the details of the substances used for the skin sensitization experiment.

**Table 5.3.** List of chemicals used for the experiment to evaluate the predictive capacity of the fabricated skin models.

| Sl no. | Substance Name | CAS no. | Physical state of application | Chemical class | MTT reducer | Conc. | *In vivo* UN GHS class | Ref. |
|---|---|---|---|---|---|---|---|---|
| 1 | Hydrochloric acid (HCl) | 7647-01-0 | Liquid | Inorganic acid | No | 14.4% aq. | Category 1 (Skin corrosive) | [365] |
| 2 | Potassium hydroxide (KOH) | 1310-58-3 | Liquid | Inorganic base | No | 5% aq. | Category 2 (Skin irritant) | [366] |
| 3 | Isopropyl alcohol (IPA) | 67-63-0 | Liquid | Neutral organic | No | 100% | No category | [366] |

The skin irritation test was conducted following the protocol mentioned in previous reports with some modifications [367, 368]. Briefly, 100 µL of the liquid test substances were added on the skin models and treated for 30 min at room temperature. The skin models were washed six times with 1X PBS. After 42 h at 37 °C and 5% $CO_2$, the cellular viability of the models was assessed via MTT assay. The constructs were cut out of the inserts and incubated with MTT reagent for 3 h at 37 °C and 5% $CO_2$. The MTT reduction was quantified by measuring the absorbance at a wavelength of 595 nm using a micro-plate reader. Cellular viability of treated models was normalized with respect to the negative control (PBS). To assess the cytokine response following skin irritation, the media samples were collected before and after 42h of the irritation test. The inflammatory cytokines IL-1β and TNF-α secreted in media were quantified by ELISA (Krishgen Biosystems, India) following the manufacturer's instructions. The immunostaining of macrophages was performed by staining them for antibodies against CD68 and CCR7 markers (Abcam, USA), followed by counterstaining with DAPI. The fluorescent micrographs were obtained using the fluorescence microscope. The obtained images were used to calculate the field of view area stained with CD68 and CCR7 to calculate their ratio using ImageJ software.

### 5.2.15. Statistical Analysis

All the experiments were performed in n = 3 samples unless otherwise mentioned. Data are represented as mean ± SD (standard deviation). OriginPro 2021 software (OriginLabs, USA) was used for processing data and determining statistical significance. The one-way analysis of variance (ANOVA) test followed by Tukey's test was performed to determine statistical analysis considering significance levels at $p \leq 0.05$, $p \leq 0.01$, and $p \leq 0.001$.

## 5.3. Results and discussion

### 5.3.1. Assessment of printability and rheological properties of formulated bioink

Biomaterials for fabrication of the skin bioink must possess mechanical, rheological, and biological properties of native ECM of skin tissue. The native ECM is composed of a complex milieu of soluble and non-soluble extracellular components, and recapitulating such a composition is challenging. In this context, we formulated a photocrosslinkable bioink (SGP) containing multiple components, such as SilkMA, GelMA, and PPR. SilkMA from *Bombyx mori* provides mechanical strength, stability, and elasticity to the material[357]. On the other hand, GelMA contains natural arginine-glycine-aspartic acid (RGD) sequences, which promote cellular attachment and spreading of encapsulated cells [358]. In addition, PPR suspension mimics the patient-specific soluble factors of native ECM as it contains a broad spectrum of signaling molecules and growth factors, including platelet-derived growth factor (PDGF), basic fibroblast growth factor (bFGF), and vascular endothelial growth factor (VEGF) **(Figure 5.2A)** [359]. The concentration of 10 mg/mL of PPR markedly enhanced the cellular viability of HDF, thus being selected as the optimal concentration for inclusion in the bioink formulation **(Figure 5.2B)**.

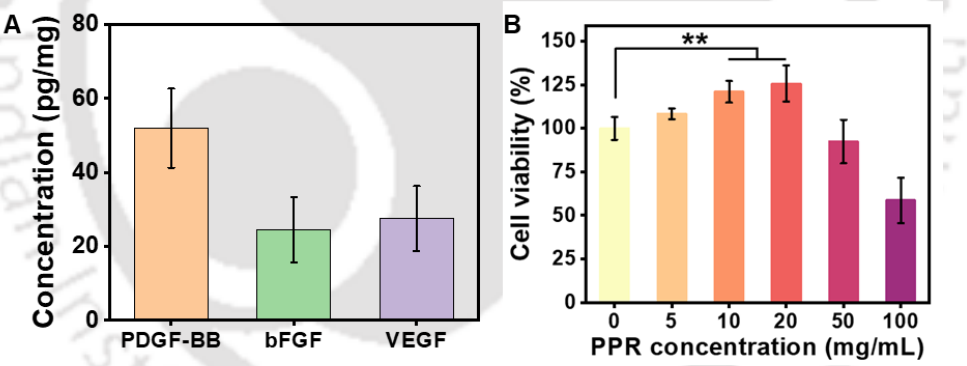


***Figure 5.2. Evaluation of isolated PPR.*** *(A) Estimation of growth factors present in PPR through ELISA. (B) Assessment of cellular viability of HDF treated with different concentrations of PPR.*

The printability of the blended formulation was assessed by mixing the components in various ratios and categorizing them as printable/non-printable based on their extrudability, self-standing nature, and shear thinning property **(Figure 5.3A)**. At the lowest concentration, a combination of 2% (w/v) SilkMA and 5% (w/v) GelMA in the final blend was determined to be extrudable; however, it showed inadequate shear thinning and self-standing properties. Therefore, a final composition of 2% (w/v) SilkMA and 10% (w/v) GelMA was selected for further experimentation due to its appropriate shear-thinning and self-standing behavior after extrusion. This composition has been referred to as the optimized bioink composition, or bioink, in subsequent experiments. Scaled-up printing of constructs with heights of ~1.3 mm

(5 layers) and ~3.5 mm (15 layers) was effectively achieved using the optimized bioink **(Figure 5.3B)**. Rheological properties significantly influence the printability of hydrogel, depicting material deformation under applied forces. In an extrusion-based process, the bioink hydrogel, initially present in a bulk resting state, undergoes a shift to a high shear state as it passes through the nozzle, forms a new shape, and ultimately settles into a new resting state[369]. This transition involves key rheological factors such as viscosity, viscoelastic shear moduli, yield stress, and elastic recovery **(Figure 5.3C)**. The temperature-dependent changes in viscoelastic properties of the bioink were observed in the uncrosslinked bioink. The storage modulus (G') is a measure of the elastic (solid-like) behaviour of the hydrogel associated with energy storage, while the loss modulus (G") is a measure of viscous (fluid-like) behaviour associated with energy dissipation[370]. For extrusion-based printing, the bioink hydrogel should possess a balance of both of these moduli. At low temperatures (10-16°C), the developed bioink showed gel-like properties (G' > G") **(Figure 5.3D)**. As the temperature increases, there is a continuous decrease in both the storage modulus (G') and the loss modulus (G"). The intersection point of G' and G" (19°C) indicates a change in the elastic/viscous behavior of the bioink; it started to show more fluid-like properties (G" > G'). Over the temperature range of 10-15°C, the loss factor (tan δ) remained almost constant **(Figure 5.3E)**. The increase of tan δ started occurring from 16 °C. The extrusion state of bioink changes with the change in temperature. At low temperatures (10-14°C), the developed bioink is in an over-gelation phase and cannot be printed. At the optimal temperature (15-18°C), the bioink enters the printable phase, where it possesses the right balance of viscosity and elasticity to be extruded and printed into 3D structures. As the temperature increases more (19-22°C), the bioink undergoes a phase transition and enters the liquid state, where it becomes too fluidic to be extruded **(Figure 5.3F)**. Further, the amplitude sweep was performed by applying varying shear strain (γ) of 0.1 to 1000 % at a constant angular frequency of 10 rad/s to determine the linear viscoelastic range (LVER) of the bioinks. The point of intersection of G' and G" gives the yield point where the hydrogel loses its integrity (G'=G") and is known as limit of LVER **(Figure 5.3G)**. The frequency sweep was performed over a wide frequency range of 1-100 rad/s by applying a constant strain (γ = 1%) to assess the frequency dependent viscoelastic properties of the bioink **(Figure 5.3H)**. The shear thinning property of the bioink was assessed using a thixotropic test by alternating shear strain at 16°C from lower (γ = 1%) to higher (γ = 1000%) range. G′ gradually recovered after removal of high strain that occurred due to the shear-thinning property of bioink in LVER

**(Figure 5.3I)**. This indicates that the bioink possesses the capability of regaining its elastic nature and maintaining structural stability after exposure to high shear strain during extrusion.

### 5.3.2. Evaluation of physicochemical properties of formulated photopolymerizable bioink

Photoinitiated polymerization technique allows *in situ* formation of hydrogel with excellent spatio-temporal control [371]. This technique is advantageous for cellular encapsulation due to its rapid reaction rate, which prevents cells from settling during gelation. In addition, it circumvents the need for extreme temperature or pH conditions or the addition of chemical crosslinkers for gelation. The duration of light exposure is an essential parameter as it determines the extent of free radical chain polymerization of the formulation. Therefore, the formulated bioink mixed with photoinitiator LAP was exposed to visible light with a

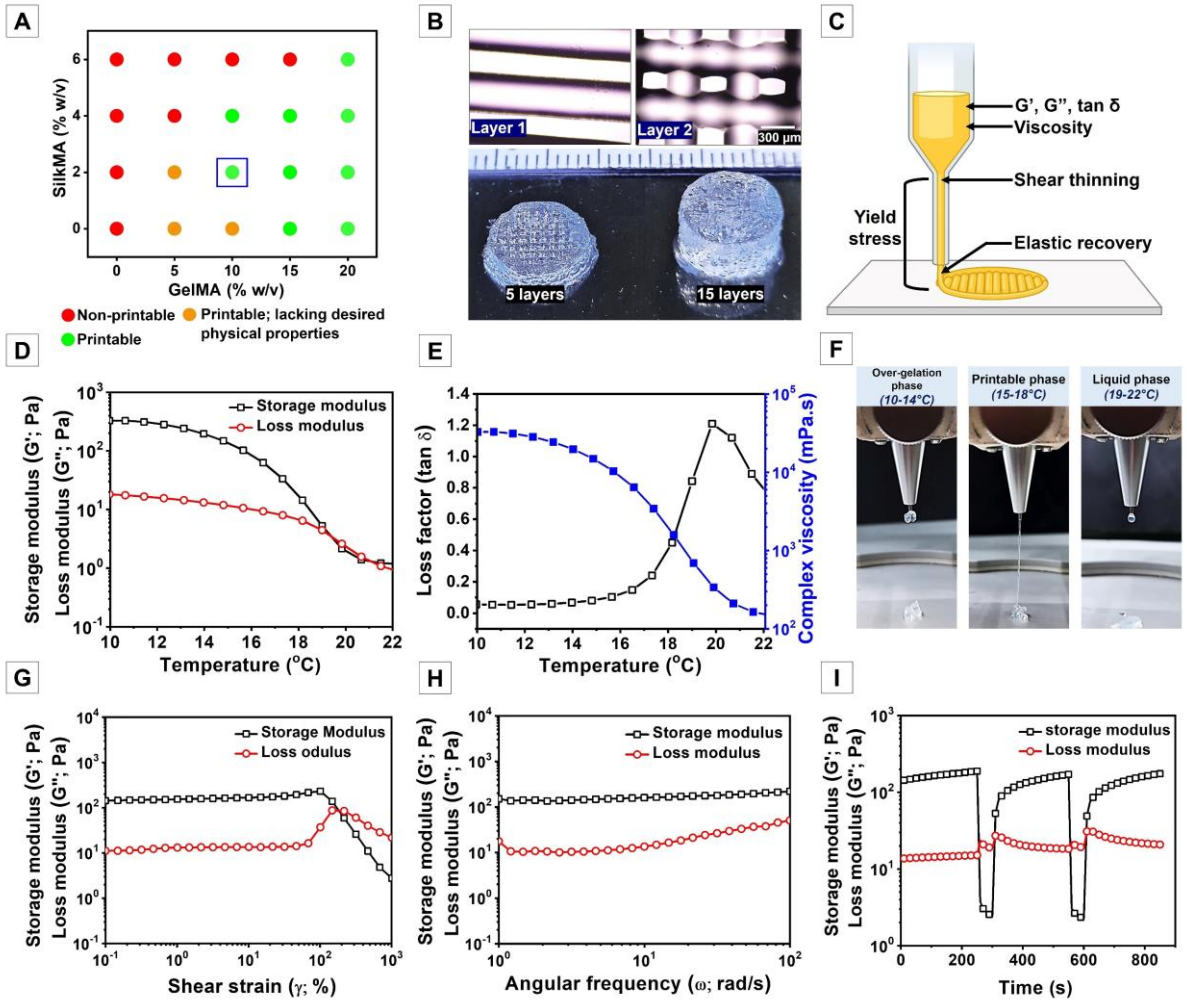


***Figure 5.3. Printability and rheological analysis of bioink.*** *(A) Printability assessment of formulated bioink. (B) Layers of printed constructs. (C) Schematic representing rheological properties influencing printability and shape fidelity. (D) Temperature sweep. (E) Changes in complex viscosity and loss factor in response of temperature. (F) Extrusion state of the bioink at different temperatures, showing liquid, overgelation, and printable phases. (G) Amplitude sweep to determine the linear viscoelastic region (LVR). (H) Frequency sweep. (I) Thixotropic analysis of bioink.*

wavelength of 405 nm for different durations of 5, 10, 15, 30, and 45 s **(Figure 5.4A)**. The projection of light triggered the solidification of the formulation, and a viscous liquid was observed after 5 s of light exposure. After 10 s of light exposure, the formulation begins to set, and after 15 s it forms a self-standing hydrogel. Subsequent exposure for 30 and 45 s results in continued crosslinking, leading to the hardening of the hydrogel. After photopolymerization the constructs were kept immersed in phosphate buffered saline (PBS) for the assessment of swelling property. The swelling ratios of the constructs photopolymerized for 15 s, 30 s, and 45 s were 11.75 ± 2.09%, 9.79 ± 1.90%, and 9.78 ± 1.12%, respectively, after 24 h **(Figure 5.4B)**. The swelling of constructs photocured for 15 s showed comparatively more swelling than that of other groups but the difference was not statistically significant. Further, the *in vitro* stability of the constructs was assessed for 28 days, by immersing the constructs in PBS at 37°C to ensure the long-term stability of the model under *in vitro* condition **(Figure 5.4C)**. The constructs photocured for 15 s (82.52 ± 5.33%) showed a slight reduction in mass compared to the constructs photocured for 30 s (92.55 ± 5.64%) and 45 s (94.25 ± 5.64%) after 28 days. Hence, the mass loss observed in all the groups was not significantly pronounced, confirming the stability of the constructs for at least 28 days following fabrication. Further, the printed grid constructs were assessed for mechanical properties through tensile and compression tests using universal testing machine. The tensile stress-strain responses of the dumbbell-shaped constructs were recorded until the breakage of the constructs **(Figure 5.4D)**. The tensile modulus was observed to be highest in the constructs with 45 s exposure (65.7 ± 5.3) compared to 30 s (54.7 ± 4.5) and 15 s (36.9 ± 5.1) groups **(Figure 5.4E)**. Skin tissue exhibits high anisotropy and viscoelasticity, with tensile modulus within a wide range of 5 kPa-140 MPa, depending on the anatomical location, age, and lifestyle of the individual [372]. Hence, the tensile strengths of printed constructs were towards the lower end of this spectrum but are in alignment with the elastic property of skin. Further, we focused on analyzing the stiffness of printed constructs concerning cellular responses. The constructs were subjected to a compressive strain of up to 60% **(Figure 5.4F)**. The compressive moduli of the constructs were found to be highest in 45 s constructs (13.1 ± 1.9 kPa), followed by 30 s constructs (7.6 ± 1.8 kPa) followed by 15 s (2.5 ± 1.2 kPa), suggesting compressive properties of the soft hydrogels **(Figure 5.4G)**. As per previous reports, fibroblasts and endothelial cells exhibit elongated morphology in the presence of substrate stiffness above 2 kPa [373]. Dermal fibroblasts typically display an elongated spindle-like morphology and attain maximum spreading when

cultured on substrates with a stiffness ~10 kPa [374]. Therefore, light exposure of 30 s has been selected as the photocuring duration of the printed dermal layer of the skin model.

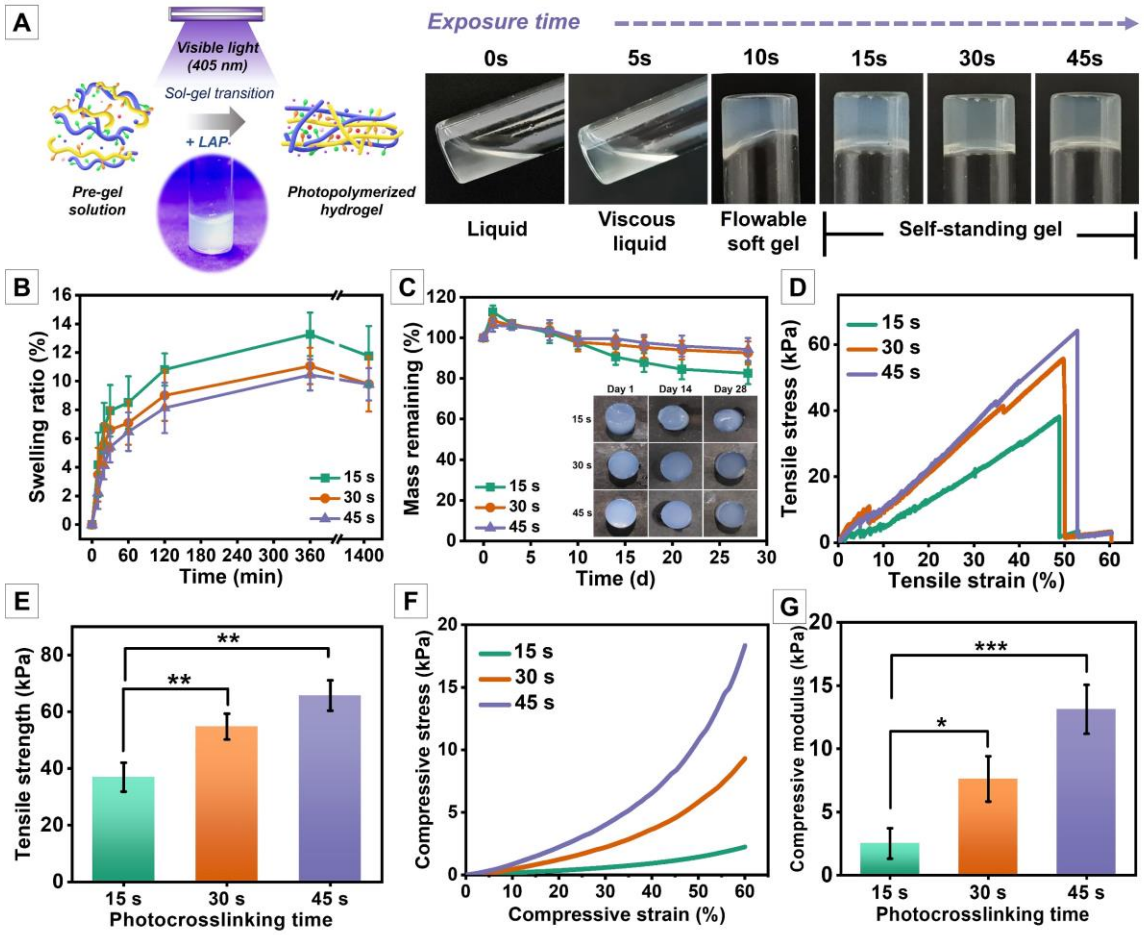


***Figure 5.4. Effect of light-exposure time on physicochemical properties of formulated SGP bioink.*** *(A) Schematic and photographic images showing the effect of photocuring time for gelation of formulated SGP bioink. (B) Swelling ratios of the bioink hydrogels photocured for different exposure time durations. (C) In vitro stability of the constructs, immersed in PBS (pH 7.2-7.4) at 37°C. (D) Representative tensile stress/strain plots of printed constructs with varying crosslinking time and (E) corresponding average tensile strength. (F) Representative compressive stress/strain plots of printed constructs with varying crosslinking time and (G) corresponding compressive moduli. Values are plotted as mean ± standard deviation, where * $p \leq 0.05$, ** $p \leq 0.01$, and *** $p \leq 0.001$.*

### 5.3.3. Influences of PPR on cellular growth and proliferation aiding in cell-instructive property of SGP bioink

Photoactivation of platelet concentrates involves exposing them to plasma arc light source emitting near-infrared (NIR) wavelengths (600-1200 nm), which stimulates the release of growth factors and bioactive molecules (**Figure 5.5A**) [359]. The released secretomes enrich the microenvironments with biologically active proteins and cytokines, which directly influence cellular growth, proliferation, and ECM secretion in a patient-specific manner. A

concentration of 10 mg/mL of isolated PPR significantly increased the number of cells compared to the control group without PPR **(Figure 5.2B)**. The cells exhibited more prominent F-actin filaments in presence of PPR, suggesting the influence of PPR on the dynamic reorganization of the cytoskeleton during substrate adhesion **(Figure 5.5B)**. The image-based quantification analysis showed a significant increase in the area of F-actin distribution per field of view (FOV), normalized by cell numbers ($p \leq 0.05$) in presence of PPR **(Figure 5.5C)**. Further, the significant increase in the length of minor and major axes of the cells infers the greater spreading of fibroblasts when treated with PPR **(Figure 5.5D)**[375].

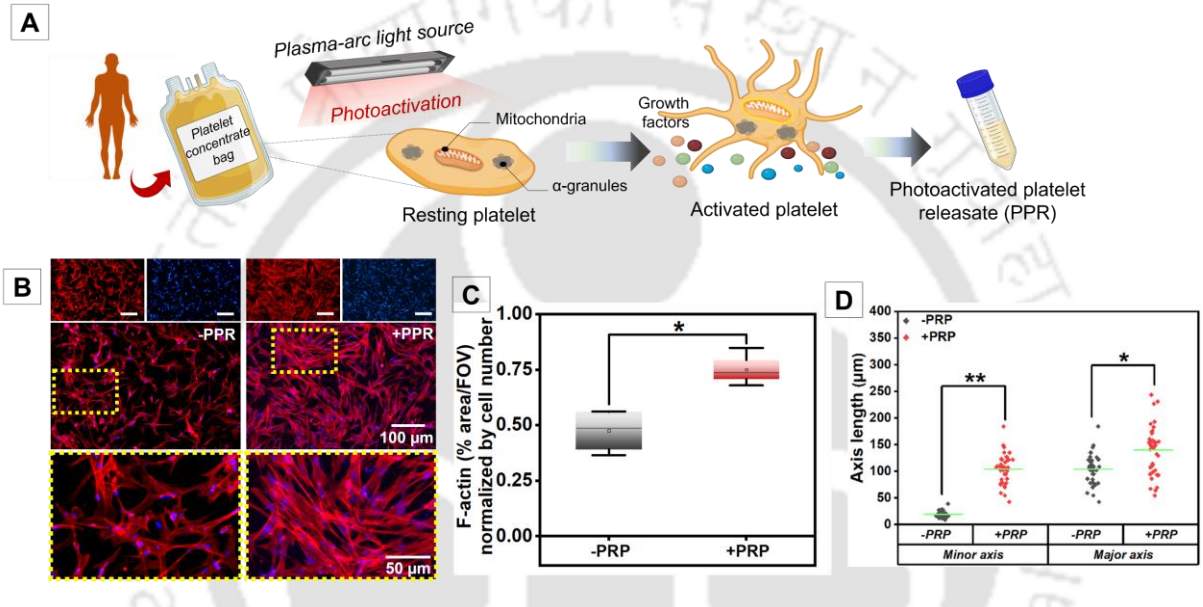


***Figure 5.5. Effect of photoactivated platelet releasate (PPR) on HDF.*** *(A) Schematic diagram illustrating isolation process of PPR from platelet concentrate through photo-activation. Created with BioRender.com. (B) Assessment of the effect of PPR on cellular morphology by rhodamine phalloidin (RP) staining. (C) Estimation of F-actin distribution area per field of view (FOV) normalized by cell number measured using ImageJ software. (D) Measurement of length of minor and major axes of cultured fibroblasts. The image analysis revealed a significant increase in cellular area induced by PPR through cytoskeletal reorganization, facilitating cellular spreading.*

The PPR suspension was further mixed with biomaterial ink solution along with HDF to assess the effect of PPR-laden formulated bioink on the fibroblasts. The HDF cells were encapsulated in the bioink with (SGP) and without PPR (SG) and were cultured for 14 days. HDF cells were encapsulated in collagen gel (Col) to be used as the control group. The significant increase in DNA was evident in case of all the groups on day 14 from day 1. DNA content of collagen gel constructs showed a significant increment ($p \leq 0.01$) compared to the bioink constructs on day 3 and day 7. Interestingly, SGP constructs showed significantly more DNA content than SG and collagen gel constructs on day 14, indicating the proliferative effect of platelet releasate on fibroblasts **(Figure 5.6A)**. This effect could potentially be mediated through the activation of

the ERK1/2 pathway, aligning with observations in previous studies[376, 377]. The viability of the encapsulated fibroblasts in the constructs was visualized using live/dead staining **(Figure 5.6B)**. The presence of live cells in all the groups till day 14 was confirmed by the green fluorescence, which resulted from the uptake of calcein-AM into the cells and its subsequent hydrolysis by intracellular esterases, leading to green fluorescence emission [328]. While all the groups supported HDF adhesion to the hydrogels and promoted cell spreading and proliferation, it was noted that the collagen gel underwent significant shrinkage, and SG and SGP groups maintained their size throughout the culture period **(Figure A5.1)**. The observed contraction in collagen-based skin models has been recognized as a significant drawback due to its association with tissue necrosis, reduced lifespan, and faster degradation [156]. A greater number of elongated fibroblasts were observed in the SGP group compared to the SG group on day 14, indicating that microniche is more conducive for cellular growth and attachment due to the presence of platelet-released growth factors. In addition, the formulated SGP bioink also supported the growth and proliferation of HUVEC (**Figure A5.2**), suggesting its ability to be utilized as bioink for the fabrication of vascular network in the model.

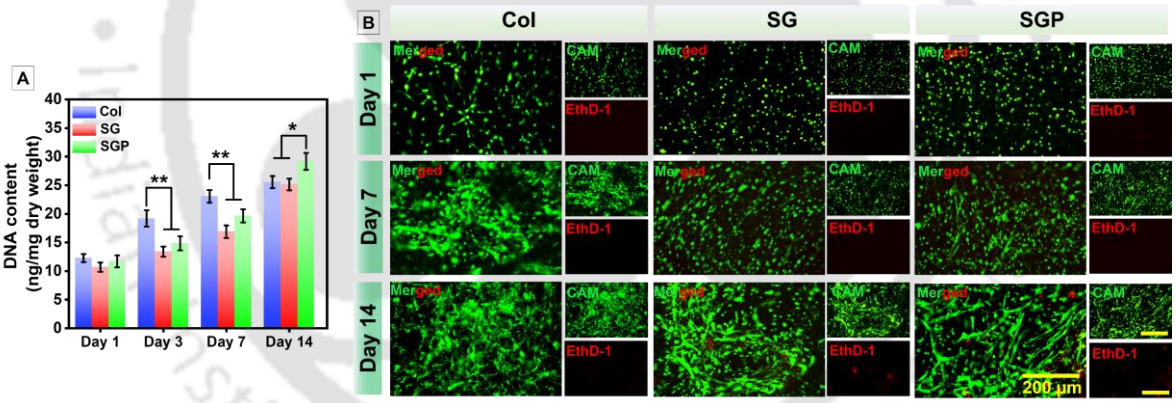


***Figure 5.6. Influence of PPR on HDF encapsulated in formulated bioink.*** *A) Cellular proliferation assessment of HDF encapsulated hydrogels through quantification of DNA content at different time points (day 1, 3, 7, and 14) . (B) Representative fluorescence images of cell viability assessment of composite bioinks using live/dead assay and 3D surface plot analysis. Values are plotted as mean ± standard deviation, where * $p \leq 0.05$, and ** $p \leq 0.01$. CAM: Calcein-AM, EthD-1: ethidium homodimer-1.*

### 5.3.4. Strategy and setup for extrusion-based bioprinting contributed to the fabrication of an advanced skin model

The multi-layered structure of skin reflects the significance of the organ in terms of its functions and physiology. The outer epidermal layer is separated from the underlying dermis by the basal membrane or basement membrane. The basement membrane, a thin layer of ECM, provides structural support and serves as a physical barrier between the epidermis and dermis. It crucially anchors the epidermis to the dermis and facilitates interlayer communication and nutrient exchange. In this study, a customized 3D printed transwell system (1 cm in diameter) was printed, which contains a PC membrane in the middle **(Figure 5.7)**. The PC membrane functioned as an artificial basement membrane, allowing adherence of bioprinted dermal layer on one side and the epidermal layer on the other.

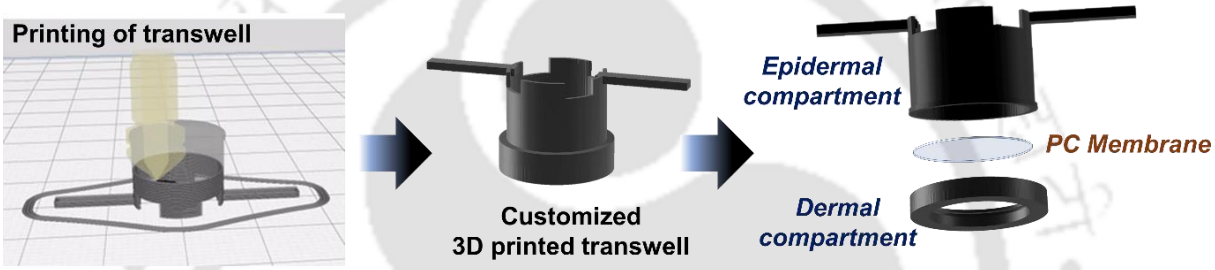


***Figure 5.7. Fabrication of 3D printed transwell system.*** *3D Printing of customized insert with different components.*

Further, we developed an innovative bioprinting strategy to produce an advanced 3D skin tissue model with the transwell system in a rapid single-step process (**Figure 5.8A**). A 3D skin mimetic computer-aided design (CAD) was modelled using AutoCAD software, wherein the structure emphasizes the epidermal and dermal layers of skin. Initially, the dermal layer with 4 layers of HDF-laden bioink-1 and the 5$^{th}$ layer with an alternate fashion of HDF-laden bioink-1 and HUVEC-laden bioink-2 were printed on one side of PC membrane (at the bottom side of the transwell) in order to achieve complementary cellular arrangements of fibroblasts and endothelial cells which would resemble the vascularized dermal layer of the native skin. The printed dermal layer was photopolymerized for 30 s, and the transwell was inverted to print the epidermal layer on the other side. A single layer of HEK-laden bioink-3 was printed on top of the PC membrane and photopolymerized for 15 s to form the abp-SM. For visualization of specific cell types in each layer, the cells were stained with CellTrackers with different dyes (HDF: green, HUVEC: red, and HEK: blue) prior to incorporation into the bioink to depict the distribution of cells within the printed construct **(Figure 5.8B & C)**. H&E stained image of the

printed construct showed the interface between the keratinocyte and fibroblast layers printed on the opposite sides of the membrane (**Figure A5.3**).

### 5.3.5. Establishment of extrusion-based bioprinting conditions to form a uniform and matured epidermal layer

To form a uniform matured epidermal layer on bioprinted model, we utilized the tunable mechanical properties of SGP bioink by varying the duration of photocuring time. Prior research reported that keratinocyte differentiation tends to be more pronounced on substrates with lower elastic modulus, indicating a correlation between substrate softness and enhanced keratinocyte differentiation and nascent epithelial sheet formation [378, 379]. *Trappmann et*

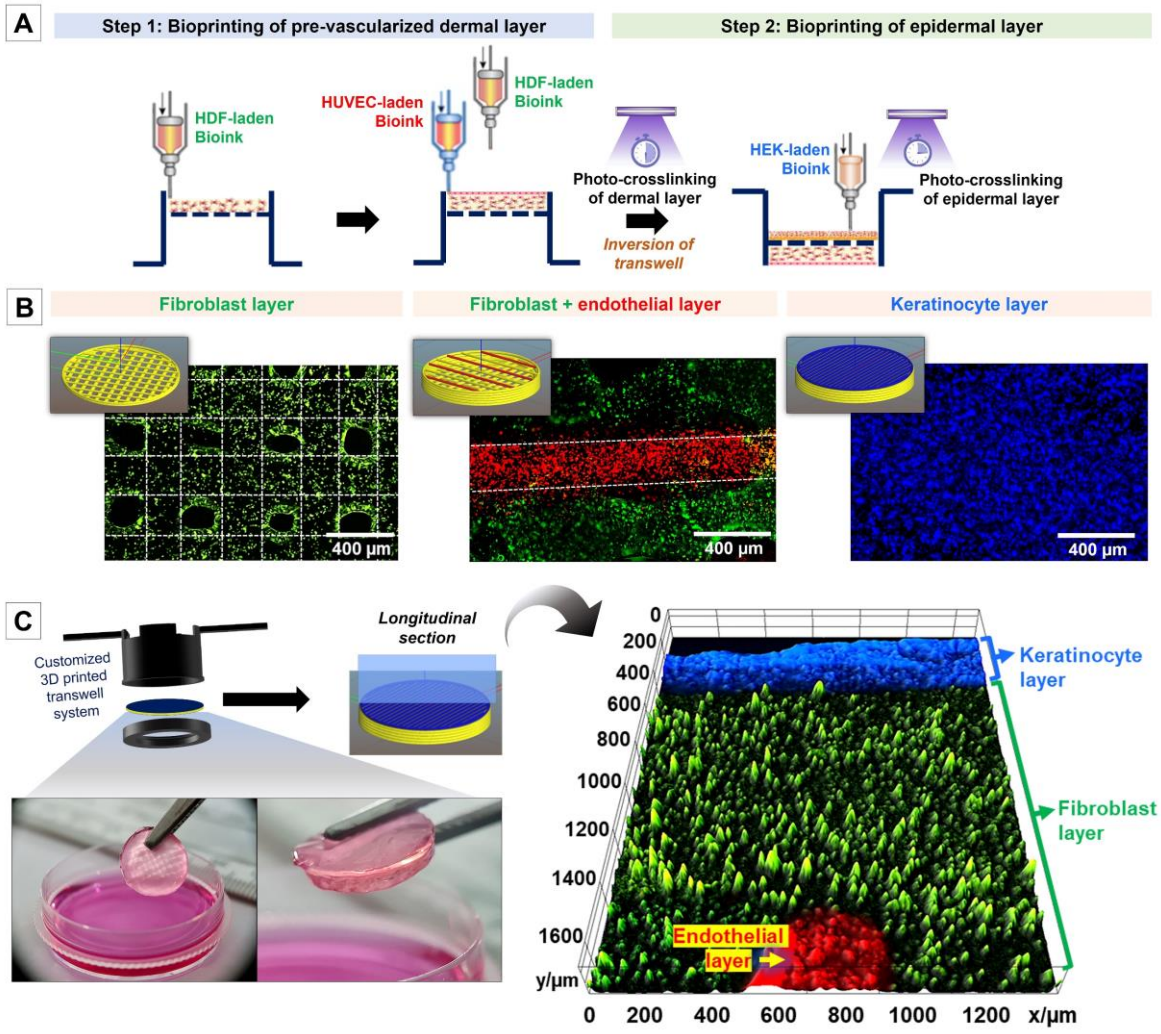


***Figure 5.8. Extrusion-based bioprinting of advanced skin model.*** *(A) Diagrammatic representation of bioprinting of pre-vascularized biomimetic skin model. (B) Representative Z stacked fluorescence images of individual layers of the fabricated skin model. The cells were stained with CellTrackers (HDF: green, HUVEC: red and HEK: blue), showing cellular distribution in printed construct. (C) Photographic images of developed skin model (left) and 3D surface plot of longitudinal section of printed skin model (right), showing the arrangement of the cell layers in the model.*

*al.* demonstrated a notable increase in the expression of differentiation markers when keratinocytes were cultured in soft hydrogels within the stiffness range of 0.5-2 kPa in contrast to stiffer hydrogels [378]. Based on the obtained compressive moduli of the printed constructs in compression test **(Figure 5.4G)**, we selected the photocuring time of 15 s for the epidermal layer to closely emulate the mechanical stiffness of the hydrogel that promotes keratinocyte differentiation **(Figure 5.9A)**. After the photopolymerization, the cellular behaviour was studied through F-actin staining of the printed keratinocyte layer using rhodamine phalloidin (RP) dye. The images demonstrated that round-shaped HEK were sparsely distributed on day 1 after printing. However, over time, the cells gradually regained their original, more physiological shape on day 3, and formed an organized epidermal layer on day 14 in ALI culture **(Figure 5.9B)**. Furthermore, the maturation of epidermis was evaluated using immunofluorescence staining of cryosectioned constructs against basal (CK14) and suprabasal (CK10) epidermal differentiation markers **(Figure 5.9C)**. The immunofluorescence analysis revealed the expression of CK14, indicative of basal keratinocytes, with a distribution pattern closely resembling that of native human skin. Moreover, the differentiation of keratinocytes are characterized by the expression of CK10, which plays a crucial role in regulating the skin's epidermal function [380]. The presence of CK10 expression in abp-SM suggested the maturation and terminal differentiation of the keratinocytes, contributing to the development of the matured epidermal layer while cultured at air-liquid interface. Although the immunofluorescence images demonstrated the formation of an organized epidermal arrangement in the bioprinted model, it is evident that achieving the same level of compactness of the epidermal layer and the expression of differentiated markers to the extent observed in native skin still remains a challenge. This implies that achieving barrier functionality and permeability similar to human epidermis in the fabricated model may require *in vivo*-like dynamic conditions for enhanced compaction. Further, a comprehensive assessment of the whole skin construct, including the dermal layer, was conducted to ensure the maturation of the printed construct.

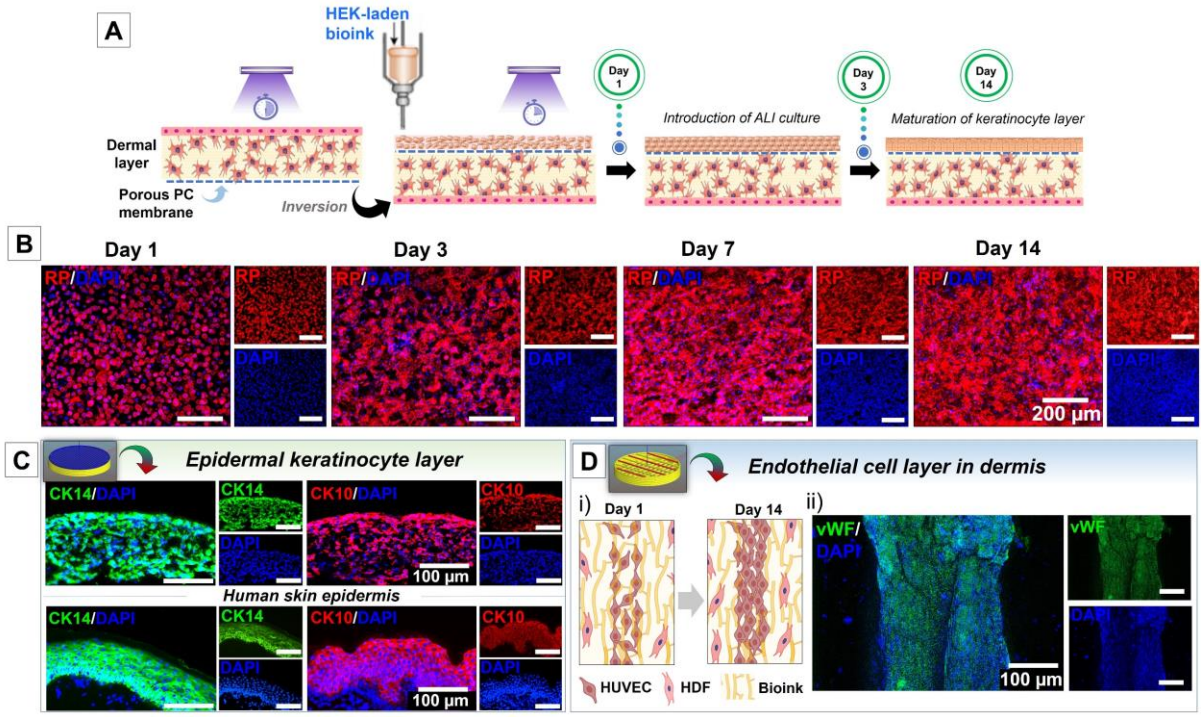


***Figure 5.9. Bioprinting and maturation of HEK and HUVEC layers.*** *(A) Diagrammatic representation of bioprinting strategy used for formation of uniform epidermal layer using exposure time-dependent tunability of SGP bioink. (B) RP stained images of printed keratinocyte layer, showing changes in cellular morphology and confluency of the cells during the 14 day-culture period of the model. (C) Representative immunofluorescence images of epidermal layers of abp-SM and human skin tissue, stained against epidermal differentiation markers (left: CK14, green and right: CK10, red). (D) i) Schematic diagram showing endothelial cell layer inside dermal layer. Created with BioRender.com. ii) Immunofluorescence z-stacked image of endothelialized microvascular structure in the dermal layer after 14 days.*

### 5.3.6. Engineering a functional full-thickness skin model through synthesis and remodelling of key ECM components

For development of a functional skin model, the maturation of the dermal layer holds equal significance, alongside that of the epidermal layer. Here, the dermal layer was primarily constructed using HDF-laden bioink-1, accompanied by a single layer of HUVEC-laden bioink-2 in an alternating pattern with bioink-2 to ensure interaction between HDF and HUVEC. Immunofluorescence images stained against vWF, a selective endothelial marker, demonstrated the formation of endothelialized vasculature in dermal layer after day 14 **(Figure 5.9D)**. Furthermore, the skin construct was evaluated through biochemical and gene expression analysis to ensure its *in vitro* maturation. The first step in the analysis involved the estimation of DNA content, a reliable and accurate method for assessing cell proliferation. The DNA content on day 14 exhibited a highly significant increment ($p \leq 0.001$) in the constructs when compared to day 1 **(Figure 5.10A)**. A similar trend was observed on the normalization of DNA with the dry weight of the construct, showing a 3-fold increase on the 14th day from day 1 (p

≤ 0.001) **(Figure 5.10B)**. The total sulfated glycosaminoglycan (sGAG) content, which was both secreted into the culture media and deposited within the construct, was quantified using the DMMB assay to assess the ECM composition. A significant increase in sGAG content was observed after a 2-week culture period. The total sGAG content increased from 0.49 ± 0.09 µg on day 1 to 2.81 ± 0.19 µg on day 14 **(Figure 5.10C)**. Further, collagen fibers constitute a significant portion of ECM in skin, comprising approximately 75% of dry weight of skin[381]. The total collagen content within the construct also increased significantly from 66.36 ± 20.49 µg on day 1 to 419.09 ± 50.71 µg (approximately 6.3-fold) on day 14 ($p \leq 0.001$) **(Figure 5.10D)**. When normalized to DNA content, the collagen content exhibited an approximately 3.1-fold increase on day 14 compared to day 1 ($p \leq 0.01$) **(Figure 5.10E)**. Immunofluorescence staining revealed the deposition of specific collagen types, collagen type I (Col I), and collagen type III (Col III) after 14 days in culture **(Figure 5.10F)**.

Maturation of abp-SM was also validated through gene expression analysis of the markers mentioned in **Table 5.2** after 1, 3, 7, and 14 days. The gene expression of ECM constituents such as COL1A1, COL3A1, FN1, and ELN have increased significantly from day 1 to day 7 and further to day 14 **(Figure 5.10G)**. A significant 7.1-fold increase in COL1A1 and 4.7-fold increase in COL3A1 validates the collagen deposition and ECM remodelling during the maturation phase of model. Fibronectin and elastin are major components of the ECM and play essential roles in cellular adhesion and the elastic resilience of tissues, respectively. The increased expression of FN1 (~15.8 fold on day 14) and ELN (~13.3 fold on day 14) suggests improved regulation of ECM formation and remodelling to mimic tissue homeostasis [382]. EGF expression was gradually upregulated (~2.4 fold on day 3, ~7.9 fold on day 7) and maintained till day 14 (~5.5 fold). Further, the matured model also exhibited upregulation of epidermal maturation markers related to keratinocyte differentiation, including cytokeratins encoded by KRT14 and KRT10 **(Figure 5.10G)**. KRT14 expression was highest on day 7 (~15.6 fold) and decreased on day 14 (~9.7 fold). In contrary, KRT10 expression showed a gradual increase and highest expression on day 14 (~29.24 fold), indicating maturation of the printed epidermal layer. Further, GeneMANIA was used to identify partner genes that might be involved in the pathways of the maturation process based on their predicted functions **(Figure 5.10H)**. The predicted genes possess important roles in the following functions: expression of ECM structural constituents and organization, cell-substrate adhesion, skin development, epidermal cell differentiation, and keratinization. The predicted genes possess specific functions for tissue remodelling, such as, SPARC encoding ECM protein that

influences fibroblast proliferation and collagen deposition [383]. Fibulins (FBLN-1,2, and 5) are a family of secreted glycoproteins that regulate cellular attachment and stabilize other ECM proteins [384]. NID2 encodes a member of the nidogen family of basal membrane proteins, acting as a cell-adhesion protein with an affinity for collagens, laminin, and fibronectin, potentially contributing to the structural integrity and maintenance of the basement membrane [385]. For the formation of epidermis, keratin genes such as KRT5, encoding keratin 5, dimerizes with keratin 14 to form cytoskeletal structure of basal epithelial cells [386]. Similarly, keratin 16 (KRT16) plays a crucial role in maintenance of innate immunity, barrier function, and network signalling of the skin epidermis [387]. In addition, EGFR is also predicted to be involved during the maturation of abp-SM, which initiates the EGFR signalling pathway, one of the most important pathways to regulate survival, proliferation, and migration of keratinocytes[388]. Overall, the expression of genes related to ECM production, regulation, and differentiation proteins serves as confirmation of the functionality of the encapsulated cells within the 3D bioprinted construct and indicates the presence of distinctive molecular signatures associated with the development of skin tissue. In addition, maintaining the integrity of the barrier is crucial in skin models, as it guarantees the reliability of *in vitro* testing. The permeability assays using fluorescently labelled molecules, FITC-inulin (2-5 kDa) and FITC-dextran (40 kDa), were carried out using the printed constructs and skin explants **(Figure 5.10I)**. The introduction of the PC membrane resulted in a notable reduction in the penetrability of both the molecules in case of abp-SM compared to the bioprinted skin model (bp-SM) without the PC membrane **(Figure 5.10J & K)**. It is important to note that even with this reduction, the abp-SM remained considerably more permeable when compared to skin explant. As lipid forms the main barrier for diffusion of formulations through skin, a comprehensive analysis of the lipid composition of the bioprinted epidermal layer can be conducted in future study. Although utilizing the PC membrane as artificial basement membrane has significantly improved the barrier property of the printed skin construct, the maturation of the model within a dynamic bioreactor system could further facilitate the development of an epidermis with a lipid organization more closely resembling that of native skin and improve barrier function.

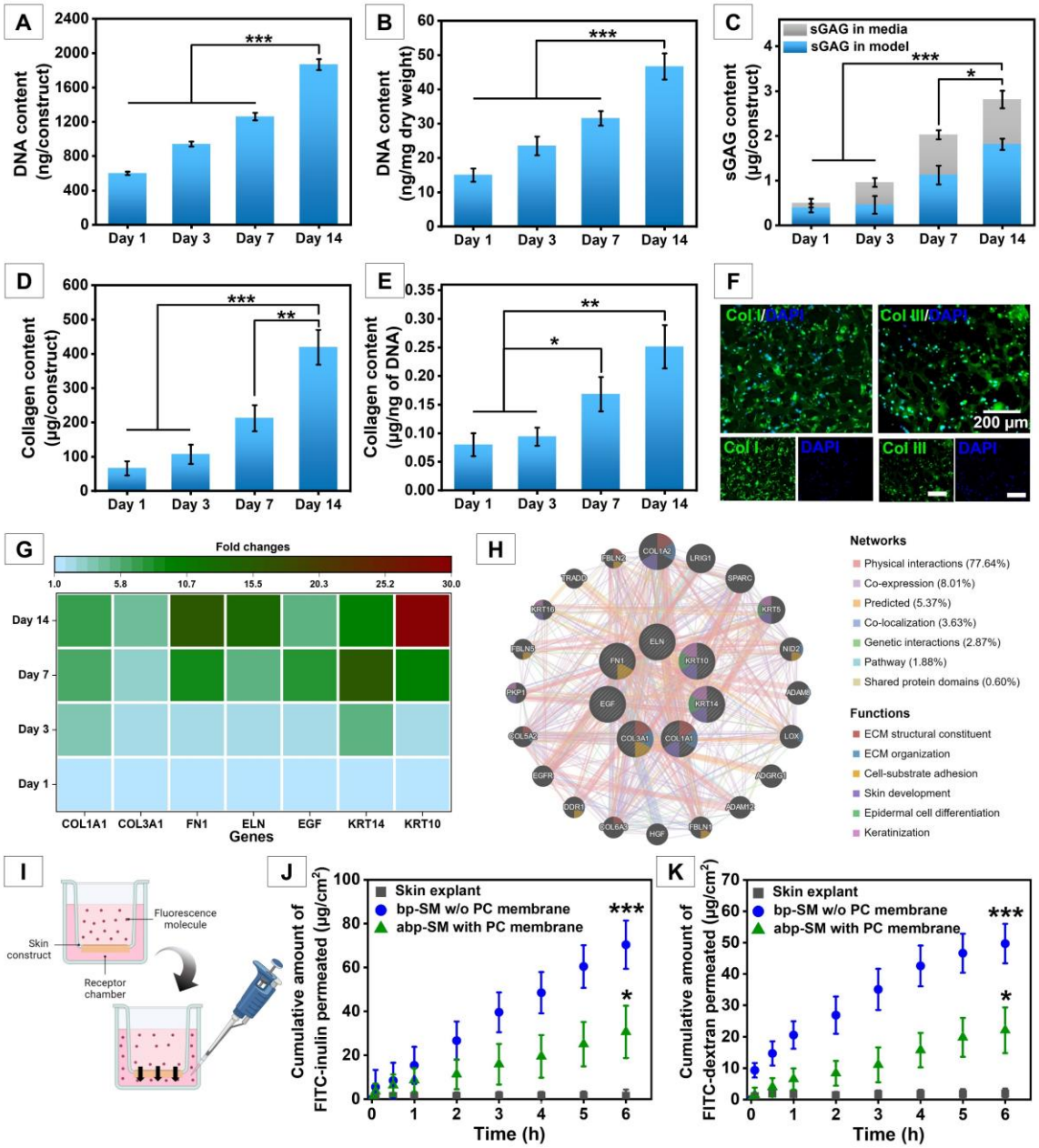


***Figure 5.10. In vitro maturation of advanced bioprinted skin model (apb-SM).*** *(A) DNA content per construct, (B) dry weight normalized DNA content. (C) Estimation of sGAG content in the printed model. (D) Collagen content per construct, (E) DNA normalized collagen content. (F) Immunofluorescence staining of cryosections of dermal layer of abp-SM on day 14 for Col I and Col III markers. (G) Heatmap profile depicting relative expression levels of the genes involved in maturation of skin model. (H) Gene interaction network of query and predicted genes built in GeneMANIA. (I) Schematic representation of permeation assay using developed skin model. Permeation profiles of (J) FITC-inulin (2-5 kDa) and (K) FITC-Dextran (20 kDa) through different groups: skin explant, bioprinted construct with and without polycarbonate (PC) membrane. Values are plotted as mean ± standard deviation, where * $p \leq 0.05$, ** $p \leq 0.01$, and *** $p \leq 0.001$.*

### 5.3.7. Importance of human macrophages in immunocompetent skin model for sensitization

The development of skin models remains a formidable challenge due to the intricate structural and functional complexity of skin, involving a diverse array of specialized cells and physiological subsystems [355]. This complexity extends to include components responsible for regulating immune responses within the skin. We incorporated human THP-1 macrophages in the fabricated model for predicting skin inflammation under *in vitro* condition by mimicking the response of tissue-resident macrophages in *in vivo* condition. PMA-differentiated M0-macrophages were seeded at the bottom of the transwell plate with abp-SM on day 14. Next day, the holistic model was subjected to topical applications of formulations for skin irritation assessment **(Figure 5.11A)**. The assessment was performed to evaluate the prediction ability of the models to effectively classify the applied substances and compare the classification with United Nations Globally Harmonized System of Classification and Labelling of Chemicals (UN GHS). Typically, the potential for substances to cause skin irritation is determined by assessing the cell viability of the model. MTT assay was performed after 42 h of exposure time following OECD test guidelines (TG) 431 and 439. A negative control (1X PBS) and positive control (5% sodium dodecyl sulfate, SDS) were included in the sensitization test. The cell viability of the negative control was considered as 100%. The obtained result of MTT assay was compared to the reference classification according to the UN GHS to validate the predictive capacity of the skin models. The data obtained from the printed skin model was compared with a traditional manually deposited collagen-based skin model. Both skin models classified the skin corrosive substance HCl (GHS category 1) and skin irritant KOH (GHS category 2) aptly. However, the traditional bilayered col-SM misclassified IPA (GHS no category) as skin irritating, whereas abp-SM classified the solution correctly as non-irritating, similar to *in vivo* UN GHS classification **(Figure 5.11B)**. Similar misclassification of substances in *in vitro* irritation testing by conventional bi-layered collagen-based skin models was also previously reported, limiting its application as *in vitro* platform for skin sensitization assessments [368]. Further, the effect of the skin irritation reaction could be correlated to the release of inflammatory cytokines from the macrophages and fibroblasts. The secreted cytokines (IL-1β, and TNF-α) were measured pre- and 42 h post-exposure of the applied substances using ELISA **(Figure 5.11C & D)**. The PBS treatment, negative control group, showed a very limited impact on the cytokine release in both the skin models. The treatment with skin irritants such as SDS, HCl, and KOH showed a significant increase in inflammatory cytokines release in both models. The treatment of IPA led to an increase of IL-1β only in col-

SM ($p \leq 0.05$), while the change in secretion is not significant in case of abp-SM. However, the increase of secretion of TNF-α after treatment with IPA was evident in both model systems but at different significance levels i.e., $p \leq 0.01$ in case of col-SM and $p \leq 0.05$ in case of abp-SM. The macrophages were further visualized using cell-specific markers, including a pan-macrophage marker (CD68, green) and a pro-inflammatory M1 marker (CCR7, red) **(Figure 5.11E)**. CD68, a glycosylated type I transmembrane glycoprotein, is prominently expressed in cells of the mononuclear phagocyte lineage, such as monocytes, dendritic cells, circulating and tissue macrophages[389]. This includes both undifferentiated (M0) macrophages and pro-inflammatory M1 macrophages. The process of M0 to M1 polarization in THP-1 cells under the influence of inflammatory agents is a key aspect of the assessment of immune response and plays a significant role in various inflammatory conditions. A comparatively lower count of CCR7+ cells was observed in abp-SM compared to the col-SM, indicating a reduced extent of macrophage polarization from the M0 to M1 type after the application of IPA **(Figure 5.11E)**. The negative control group, PBS treatment, showed no significant difference in CCR7/CD68 populations in abp-SM and col-SM **(Figure 5.11F.i)**. However, application of IPA led to significantly increased ($p \leq 0.05$) CCR7/CD68 population in col-SM compared to abp-SM **(Figure 5.11F.ii)**, validating improved epidermal property of fabricated bioprinted model over the collagen-based skin model. These findings illustrate that the release of mentioned pro-inflammatory cytokines and macrophage polarization can serve as indicators to reveal the effects of mild irritation caused by non-classified substances like IPA, along with cell viability studies.

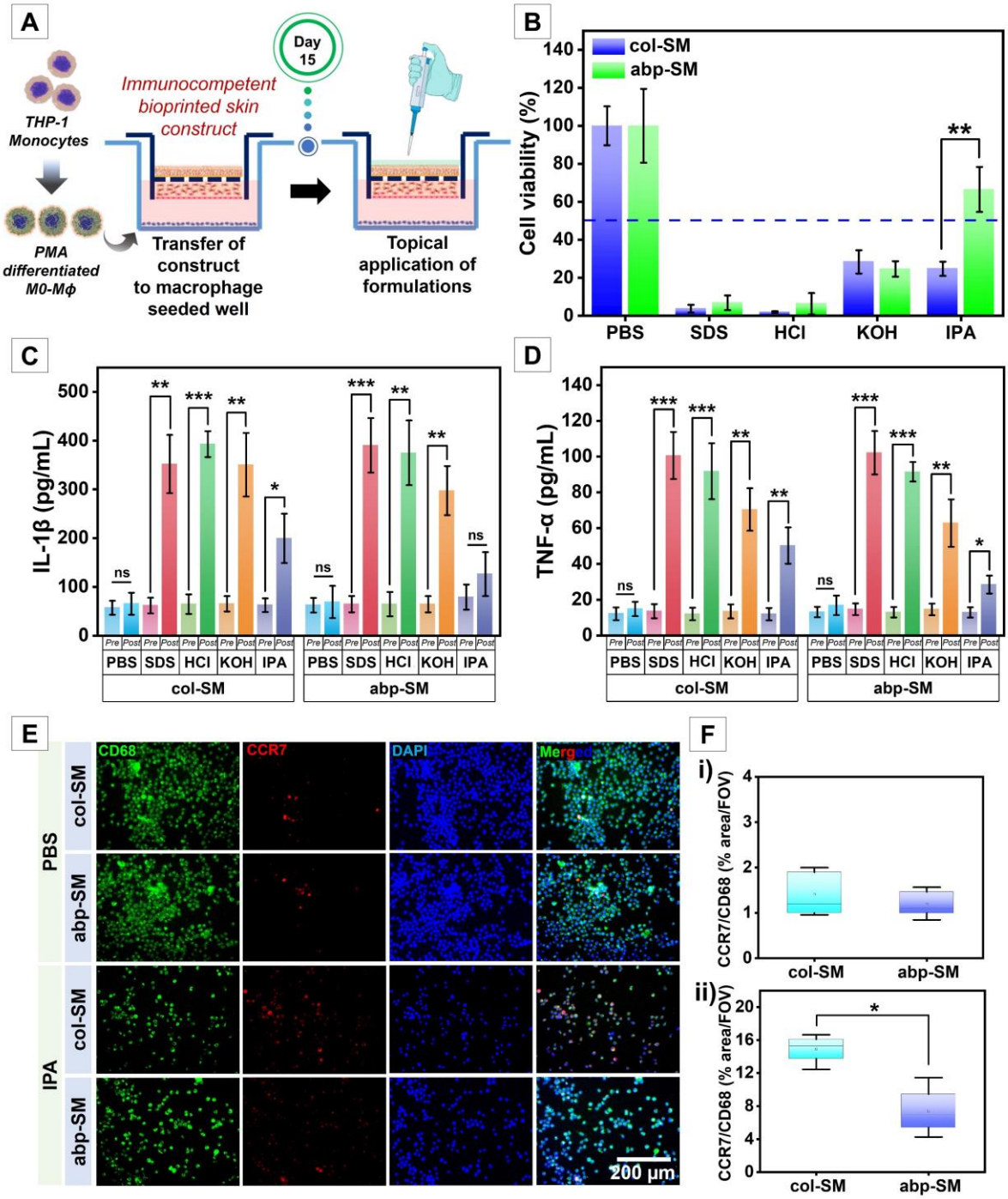


***Figure 5.11. Skin inflammatory test to assess the predictive capacity of the 3D models in effectively classifying topically applied skin irritants and non-irritants.*** *(A) Schematic representation of irritation test performed with different UN GHS classified substances. (B) Skin irritation assessment of abp-SM and col-SM, through cellular viability assay. (C) IL-1β, (D) TNF-α levels before and 48 h after application of skin irritating substances were estimated using ELISA, indicating activated immune response in the skin models. (E) Immunostaining of THP-1 macrophages seeded on bottom surface of skin model-transwell system to evaluate the presence of pan macrophage marker (CD68, green) and M1 macrophage marker (CCR7, red) against DAPI (blue) staining. (F) Image-based analysis to quantify the distribution of M1 cell population in (i) PBS- and (ii) IPA-treated groups. Values are plotted as mean ± standard deviation, where * $p \leq 0.05$, ** $p \leq 0.01$, *** $p \leq 0.001$,* and *ns= not significant.*

The advent of 3D skin bioprinting as a fully automated system represents a promising technological advancement, addressing the limitations associated with manual approaches by offering precise control and organized fabrication processes [178]. The manual cell seeding method often requires seeding of cells multiple times to achieve desirable layer height[390] and is also plagued by issues such as uneven distribution of cells, void formation, and irregular clustering of keratinocytes, resulting in reduced productivity and reproducibility [391]. The notable advantage of extrusion-based bioprinting is its ability to fabricate constructs with a higher cell density compared to other types of printing [392]. Therefore, we harnessed the extrusion-based technique, leveraging the tunable mechanical properties of the photopolymerizable SGP bioink. The unique property of photopolymerizable polymers to be mechanically tailored through controlled photocuring time holds significant scientific and practical implications for fabricating printed constructs with variable stiffness resembling native tissues. During the generation of *in vitro* models, achieving mechanical properties of biomaterial akin to native condition is crucial for eliciting desired cellular responses. Here, this phenomenon facilitated the development of matured epidermal and dermal layers within the *in vitro* skin model.

The currently marketed *in vitro* models encounter limitations due to the absence of critical characteristics of native skin tissue, such as an inflammatory system and a vascular network. Consequently, there is a pressing need for the development of more physiologically relevant skin models that can better emulate the intricacies of native skin tissue. In this study, we presented a unique extrusion-based bioprinting strategy of single-step fabrication of a 3D bioprinted *in vitro* human skin model with native skin-like-epithelialization and inflammatory response. For printing of the skin model, the silk-based photopolymerizable composite bioink was formulated with a patient-specific composition and optimized rheological properties designed for extrusion-based bioprinting applications. After printing and maturation of the model, immunofluorescence staining of abp-SM showed a well-defined matured epidermal layer and a dermal layer comprising fibroblast-secreted essential ECM component innervated with vascular endothelial cells. Moreover, the incorporation of advanced micro-architectural design and the use of alternative biomaterials have overcome the limitations associated with the conventional bilayered collagen-based skin model, which serves as the control group in this study. The current trend in skin tissue engineering has shifted from conventional manual deposition to automated technologies that enable large-scale generation of highly reproducible models. The recent emergence of 3D bioprinting technology has revolutionized the field by

providing a powerful technique to automate and scale-up the production of complex *in vitro* models. This study serves as the proof-of-concept endeavour to develop a less permeable 3D bioprinted skin model compared to the standard macroporous printed constructs, aiming to mimic native skin functions. The strategy allowed us to develop a matured immunocompetent skin-like printed model, enabling the evaluation of inflammatory responses following the topical application of various substances. More importantly, the study is a pioneering report where a printed skin model effectively classified skin irritants and non-irritants, demonstrating mild irritation effects of non-classified substances similar to in vivo condition. However, the importance of incorporating a perfusable endothelial network into the skin model is acknowledged to closely replicate the native microarchitecture of skin [393, 394]. Future studies may focus on the fabrication of perfusable microvessels in dermal layer using formulated SilkMA-based bioink to develop more physiologically relevant tissue models. The bioink is envisioned to be harnessed by integrating additional skin cell types, such as adipocytes, hair follicle stem cells, dermal papilla cells, and melanocytes, to replicate more intricate skin functions for both *in vitro* skin models and *in vivo* skin substitutes. Further, the model can be explored for evaluating the safety, efficacy, and irritation potential of cosmetic products, such as creams, lotions, and topical formulations. As a future strategy, expanding the scope of this construct to include studies on anti-aging, pigmentation regulation, and hydration mechanisms could significantly enhance its applicability and relevance in the cosmetic industry.

### 5.4. Salient findings and outcomes

1. The work presents a tunable photopolymerizable bioink by blending silk fibroin methacrylate (SilkMA), gelatin methacrylate (GelMA), and photoactivated human platelet releasate (PPR), which exhibited excellent printability, tunable physicochemical properties, and cell-instructive property conducive to cellular growth and proliferation.
2. The bioink was utilized to bioprint the immunocompetent skin model where an artificial basement membrane supports a biomimetic epidermal layer on one side and a pre-vascularized dermal layer on the other side within a customized transwell system containing macrophages on its bottom surface.
3. The innovative setup mimics the complex architecture of skin tissue along with tissue-resident macrophages essential for skin inflammatory response.
4. The printed model demonstrated a proficient classification of skin irritants and non-irritants in accordance with *in vivo* UN GHS classifications while also replicating mild irritation effects observed in human skin for non-classified substances.
5. The advanced micro-architectural design and use of alternative biomaterials have overcome the drawbacks of the widely-used collagen-based skin model considered as the control group in the study.
6. The developed model represents a robust and versatile platform with significant potential for a wide range of applications in the fields of toxicity testing, biomaterial assessment, and the study of fundamental biological processes such as wound healing.

***Limitations of the chapter***

Though the positive outcomes of the in vitro skin model demonstrate its ability to effectively classify skin irritants and non-irritants, certain limitations of the study still remain. The absence of a perfusable endothelial network limits the ability to fully replicate the native microcirculatory functions of the skin. Future advancements could focus on the integration of additional skin cell types, such as adipocytes, hair follicle stem cells, dermal papilla cells, and melanocytes, to enhance the physiological relevance of the model. While the study represents significant progress, comprehensive screening of topical and transdermal drugs is necessary to validate the predictive capacity of the model across a broader range of applications. Nonetheless, this innovative approach holds substantial potential for advancing the development of physiologically relevant tissue models and expanding their translational applicability in dermatological research and therapeutic development.

# *Summary and future perspectives*

# Summary and future perspectives

The thesis is a comprehensive study that explores the innovative use of silk-based materials for skin regeneration and *in vitro* screening applications. The thesis is structured into five chapters, each addressing different facets of this multifaceted research. Chapter 1 provided an overview of skin tissue engineering. It included the details of the cellular composition and functions of the different layers of skin, emphasizing the complexity and importance of this organ. The chapter discussed various types of skin injuries and regeneration. The introduction also outlined the primary objectives of the thesis, which aim to address the limitations of current skin regeneration techniques and explore innovative solutions. A significant portion of chapter 1 is dedicated to a comprehensive literature review. This review traced the evolution of materials used in skin tissue engineering, highlighting a paradigm shift from conventional materials to advanced biomaterials. The review focused on the significance of silk proteins derived from both mulberry and non-mulberry sources, emphasizing their unique properties such as biocompatibility, mechanical strength, and ability to support cell adhesion and proliferation. These properties make silk an attractive material for developing scaffolds and matrices for skin regeneration. It also explored various cellular strategies employed in skin tissue engineering, discussing the use of different cell types, including keratinocytes, fibroblasts, and stem cells, and their roles in promoting skin regeneration. The chapter examined the incorporation of exogenous growth factors, which are crucial in enhancing the regenerative capacity of engineered tissues. These growth factors can stimulate cell proliferation, migration, and differentiation, thereby accelerating the healing process. Innovative approaches in skin tissue engineering are another focal point of the chapter. It explored the potential of nanotherapeutics, which involve the use of nanoparticles to deliver therapeutic agents directly to the wound site. This targeted delivery system can enhance the efficacy of treatments and reduce side effects. Wearable devices, such as smart bandages equipped with sensors and drug/stimuli delivery systems, were also discussed. These devices can monitor the wound environment in real-time and provide timely interventions, thereby improving the healing process. One of the most promising advancements highlighted in this chapter is the use of 3D bioprinting technology. This technique allows for the precise fabrication of complex tissue structures by depositing layers of bioink containing cells and biomaterials. The chapter discussed the importance of 3D bioprinted *in vitro* skin models, showcasing their potential in mimicking the complex structure

and function of native skin tissue for drug testing, disease modeling, and personalized medicine. The clinical relevance and future trajectory of these advancements were emphasized, underlining their potential to provide cost-effective and efficient skin regenerative solutions, ultimately improving patient outcomes and quality of life. Lastly, the chapter outlined the motivation and objectives of the research, aiming to advance the field of skin tissue engineering by developing more effective and innovative solutions for skin regeneration. Chapter 2 described the fabrication of a composite hydroscaffold using silk and dECM derived from porcine omentum tissue. This chapter explored the regenerative efficacy of the hydroscaffold in a diabetic wound model, which presents unique challenges due to impaired healing processes associated with diabetes. The composite hydroscaffold was designed to mimic the natural ECM, providing a supportive environment for cell growth and tissue regeneration. The results indicated that the SF-dECM composite hydroscaffold significantly improves wound healing in diabetic models, promoting faster and more effective tissue regeneration. The findings highlight the promise of the SF-dECM composite hydroscaffold as a novel therapeutic approach for treating chronic wounds. From a translational perspective, the chapter 3 focused on fabricating a SF-based matrix using alternative natural bioactive agents, such as phytochemicals from *Aloe vera*. The study developed silk-aloe composite matrix which can release aloe phytochemicals at the wound site and possesses long-term stability. This chapter provided a detailed account of the experimental design and methodology used to fabricate the matrix. Along with *in vitro* assessments, its healing efficacy was evaluated using a full-thickness wound model in rabbits. The results demonstrated that the composite matrix significantly accelerated the regeneration through modulating multiple stages of the healing process. The comparable efficacy of the hydrogel with a widely used commercial product suggested its potential to be used as an alternative natural remedy for wound care at an affordable cost. Next, chapter 4 presented the design and fabrication of a wearable ES generating bandage patch along with a silk-based antimicrobial ionogel. The chapter included the *in vivo* functional assessments in rabbit models, demonstrating its effectiveness in promoting accelerated wound closure and tissue regeneration. Further *in vitro* assessments validated that the generated ES was able to significantly enhance the cellular proliferation and accelerated the healing process. The findings suggested that the developed combined strategy of e-Bandage and SF gel could be a valuable addition to advanced wound care products, offering a multifunctional solution for managing complex wounds. Lastly, chapter 5 detailed the fabrication of a 3D bioprinted immunocompetent skin model using a photocrosslinkable

silk composite with platelet releasate. The photocrosslinkable silk composite provided a robust and biocompatible 3D printed construct, abled to support cellular growth and proliferation. The chapter discussed the experimental procedures used to fabricate and assess the bioprinted skin model, including its ability to differentiate between skin irritative and non-irritative substances. The bioprinted skin model effectively mimicked the immune response of native skin tissue, providing a reliable platform for pre-clinical screening of sensitization tests. The findings suggest that the 3D bioprinted immunocompetent skin model could serve as a valuable tool for advancing skin tissue engineering and improving the accuracy and efficiency of pre-clinical testing.

Throughout the thesis, each chapter provides a thorough rationale for the research, outlines the experimental plans, highlights significant findings, and discusses future implications. The research presented in this thesis aims to advance the field of skin tissue engineering by developing innovative bioengineered silk-based matrices that not only enhance skin regeneration but also serve as effective platforms for *in vitro* screening applications. The research highlights the versatility and potential of silk-based materials for generating effective and multifunctional matrices for skin tissue engineering. By addressing the limitations of current treatments and exploring new approaches, the thesis contributes to the advancement of the field and offers promising prospects for improving the quality of life of patients.

The future prospects of the thesis work are promising and multifaceted, with following potential directions for further research and application.

1. One significant area for future exploration is the development of complex organotypic models using perfusion-based bioreactors to more accurately replicate flow patterns, shear stress, and mass transfer. By utilizing the developed silk-based materials, advanced 3D models can be fabricated that closely resemble the native skin tissue environment. These models can be employed for more precise drug testing, disease modeling, and personalized medicine, ultimately leading to more effective and tailored therapeutic interventions.

2. The integration of silk-based smart bioink in bioprinting represents another exciting prospect. Smart bioinks, which can respond to various stimuli such as temperature, pH, or light, can enhance the precision and functionality of bioprinted tissues. By incorporating smart bioinks into the bioprinting process, researchers can fabricate more dynamic and adaptable tissue constructs. These advanced bioinks can improve cell viability, promote better tissue integration, and enable the creation of more complex and functional tissue structures.

3. The development of stimuli-responsive automated bandages is also a promising avenue for future research. These bandages can respond to changes in the wound environment, such as pH shifts or the presence of specific biomarkers, to deliver targeted therapeutic interventions. This technology can significantly enhance wound care by providing real-time, adaptive treatment, reducing the need for frequent bandage changes, and improving patient outcomes.

4. Another important direction is testing the developed technologies in larger animal models. While the current research has demonstrated efficacy in smaller animal models, it is crucial to validate these findings in larger, more complex organisms. This step is essential for understanding the scalability and translational potential of the developed matrices.

5. Finally, the ultimate goal of this research is to move towards human clinical trials and technology transfer. The successful translation of these bioengineered silk-based matrices from the laboratory to clinical settings will require rigorous testing, regulatory approval, and collaboration with industry partners. By focusing on clinical applications and technology commercialization, the research can have a tangible impact on patient care, offering new and effective solutions for skin regeneration and in vitro screening.

# *Bibliography*

# Bibliography

[1] A. Amirsadeghi, A. Jafari, L.J. Eggermont, S.-S. Hashemi, S.A. Bencherif, M. Khorram, Vascularization strategies for skin tissue engineering, Biomaterials science 8(15) (2020) 4073-4094.
[2] W.C. Yan, P. Davoodi, S. Vijayavenkataraman, Y. Tian, W.C. Ng, J.Y. Fuh, K.S. Robinson, C.H. Wang, 3D bioprinting of skin tissue: from pre-processing to final product evaluation, Advanced drug delivery reviews 132 (2018) 270-295.
[3] T.A. Harris-Tryon, E.A. Grice, Microbiota and maintenance of skin barrier function, Science 376(6596) (2022) 940-945.
[4] K.R. Feingold, Thematic review series: skin lipids. The role of epidermal lipids in cutaneous permeability barrier homeostasis, Journal of lipid research 48(12) (2007) 2531-2546.
[5] L. Bento-Lopes, L.C. Cabaço, J. Charneca, M.V. Neto, M.C. Seabra, D.C. Barral, Melanin's journey from melanocytes to keratinocytes: Uncovering the molecular mechanisms of melanin transfer and processing, International journal of molecular sciences 24(14) (2023) 11289.
[6] M.J. Randall, A. Jüngel, M. Rimann, K. Wuertz-Kozak, Advances in the biofabrication of 3D skin in vitro: healthy and pathological models, Frontiers in bioengineering and biotechnology 6 (2018) 154.
[7] G. Han, R. Ceilley, Chronic wound healing: a review of current management and treatments, Advances in therapy 34 (2017) 599-610.
[8] N. Bhardwaj, D. Chouhan, B. B Mandal, Tissue engineered skin and wound healing: current strategies and future directions, Current pharmaceutical design 23(24) (2017) 3455-3482.
[9] G.D. Mogoşanu, A.M. Grumezescu, Natural and synthetic polymers for wounds and burns dressing, International journal of pharmaceutics 463(2) (2014) 127-136.
[10] R.V. Shevchenko, S.L. James, S.E. James, A review of tissue-engineered skin bioconstructs available for skin reconstruction, Journal of the royal society interface 7(43) (2010) 229-258.
[11] D. Chouhan, T.u. Lohe, P.K. Samudrala, B.B. Mandal, In situ forming injectable silk fibroin hydrogel promotes skin regeneration in full thickness burn wounds, Advanced healthcare materials 7(24) (2018) 1801092.
[12] P. Martin, Wound healing--aiming for perfect skin regeneration, Science 276(5309) (1997) 75-81.
[13] R.A. Clark, Fibrin and wound healing, Annals of the New York academy of sciences 936 (2001) 355-367.
[14] R.A. Clark, K. Ghosh, M.G. Tonnesen, Tissue engineering for cutaneous wounds, Journal of investigative dermatology 127(5) (2007) 1018-1029.
[15] H.N. Wilkinson, M.J. Hardman, Wound healing: cellular mechanisms and pathological outcomes, Open biology 10(9) (2020) 200223.
[16] D. Chouhan, T.U. Lohe, N. Thatikonda, V. Naidu, M. Hedhammar, B.B. Mandal, Silkworm silk scaffolds functionalized with recombinant spider silk containing a fibronectin motif promotes healing of full-thickness burn wounds, ACS Biomaterials science & engineering 5(9) (2019) 4634-4645.
[17] D. Chouhan, P. Das, N. Thatikonda, S.K. Nandi, M. Hedhammar, B.B. Mandal, Silkworm silk matrices coated with functionalized spider silk accelerate healing of diabetic wounds, ACS Biomaterials science & engineering 5(7) (2019) 3537-3548.

[18] D. Chouhan, N. Thatikonda, L. Nileback, M. Widhe, M. Hedhammar, B.B. Mandal, Recombinant spider silk functionalized silkworm silk matrices as potential bioactive wound dressings and skin grafts, ACS applied materials & interfaces 10(28) (2018) 23560-23572.
[19] D. Chouhan, N. Dey, N. Bhardwaj, B.B. Mandal, Emerging and innovative approaches for wound healing and skin regeneration: Current status and advances, Biomaterials 216 (2019) 119267.
[20] M. Mir, M.N. Ali, A. Barakullah, A. Gulzar, M. Arshad, S. Fatima, M. Asad, Synthetic polymeric biomaterials for wound healing: a review, Progress in biomaterials 7 (2018) 1-21.
[21] A. Sood, M.S. Granick, N.L. Tomaselli, Wound dressings and comparative effectiveness data, Advances in wound care 3(8) (2014) 511-529.
[22] H.S. Kim, X. Sun, J.-H. Lee, H.-W. Kim, X. Fu, K.W. Leong, Advanced drug delivery systems and artificial skin grafts for skin wound healing, Advanced drug delivery reviews 146 (2019) 209-239.
[23] S.L. Percival, S.M. McCarty, Silver and alginates: role in wound healing and biofilm control, Advances in wound care 4(7) (2015) 407-414.
[24] M. Zhang, X. Zhao, Alginate hydrogel dressings for advanced wound management, International journal of biological macromolecules 162 (2020) 1414-1428.
[25] S. Nazarnezhada, G. Abbaszadeh-Goudarzi, H. Samadian, M. Khaksari, J.M. Ghatar, H. Khastar, N. Rezaei, S.R. Mousavi, S. Shirian, M. Salehi, Alginate hydrogel containing hydrogen sulfide as the functional wound dressing material: In vitro and in vivo study, International journal of biological macromolecules 164 (2020) 3323-3331.
[26] X. Yang, B. Wang, D. Sha, Y. Liu, J. Xu, K. Shi, C. Yu, X. Ji, Injectable and antibacterial ε-poly (l-lysine)-modified poly (vinyl alcohol)/chitosan/AgNPs hydrogels as wound healing dressings, Polymer 212 (2021) 123155.
[27] D. Chouhan, B. Chakraborty, S.K. Nandi, B.B. Mandal, Role of non-mulberry silk fibroin in deposition and regulation of extracellular matrix towards accelerated wound healing, Acta biomaterialia 48 (2017) 157-174.
[28] N. Kovtyukhova, B. Martin, J. Mbindyo, T. Mallouk, M. Cabassi, T. Mayer, Layer-by-layer self-assembly strategy for template synthesis of nanoscale devices, Materials science and engineering: C 19(1-2) (2002) 255-262.
[29] G.M. Whitesides, B. Grzybowski, Self-assembly at all scales, Science 295(5564) (2002) 2418-2421.
[30] M. Chi, Y. Zhao, Q. Fan, W. Han, The synthesis of PrB6 nanowires and nanotubes by the self-catalyzed method, Ceramics international 40(6) (2014) 8921-8924.
[31] L. Xia, L. Lu, Y. Liang, B. Cheng, Fabrication of centrifugally spun prepared poly (lactic acid)/gelatin/ciprofloxacin nanofibers for antimicrobial wound dressing, RSC Advances 9(61) (2019) 35328-35335.
[32] A. Ota, R. Beyer, U. Hageroth, A. Müller, P. Tomasic, F. Hermanutz, M.R. Buchmeiser, Chitin/cellulose blend fibers prepared by wet and dry-wet spinning, Polymers for advanced technologies 32(1) (2021) 335-342.
[33] S. Homaeigohar, A.R. Boccaccini, Antibacterial biohybrid nanofibers for wound dressings, Acta biomaterialia 107 (2020) 25-49.
[34] N. Bhardwaj, D. Chouhan, B.B. Mandal, 3D functional scaffolds for skin tissue engineering, Functional 3D tissue engineering scaffolds, Elsevier2018, pp. 345-365.
[35] S. Gilotra, D. Chouhan, N. Bhardwaj, S.K. Nandi, B.B. Mandal, Potential of silk sericin based nanofibrous mats for wound dressing applications, Materials science and engineering: C 90 (2018) 420-432.
[36] M. Abrigo, S.L. McArthur, P. Kingshott, Electrospun nanofibers as dressings for chronic wound care: advances, challenges, and future prospects, Macromolecular bioscience 14(6) (2014) 772-792.

[37] S. Ojha, Structure–property relationship of electrospun fibers, Electrospun nanofibers, Elsevier 2017, pp. 239-253.
[38] B. Pant, M. Park, S.-J. Park, Drug delivery applications of core-sheath nanofibers prepared by coaxial electrospinning: a review, Pharmaceutics 11(7) (2019) 305.
[39] D. Chouhan, G. Janani, B. Chakraborty, S.K. Nandi, B.B. Mandal, Functionalized PVA–silk blended nanofibrous mats promote diabetic wound healing via regulation of extracellular matrix and tissue remodelling, Journal of tissue engineering and regenerative medicine 12(3) (2018) e1559-e1570.
[40] R.M. Walker, B.M. Gillespie, L. Thalib, N.S. Higgins, J.A. Whitty, Foam dressings for treating pressure ulcers, Cochrane database of systematic reviews (10) (2017).
[41] P. Chaganti, I. Gordon, J.H. Chao, S. Zehtabchi, A systematic review of foam dressings for partial thickness burns, The American journal of emergency medicine 37(6) (2019) 1184-1190.
[42] A. Alkhalil, A. Day, K. Monger, J. Zhang, B. Carney, H. Hoffman, L. Moffatt, J. Shupp, Hydroconductive and silver-impregnated foam dressings: a comparison, Journal of wound care 26(Sup7) (2017) S15-S22.
[43] S. MacNeil, Progress and opportunities for tissue-engineered skin, Nature 445(7130) (2007) 874-880.
[44] M. Downer, C.E. Berry, J.B. Parker, L. Kameni, M. Griffin, Current biomaterials for wound healing, Bioengineering 10(12) (2023) 1378.
[45] A.B.M. Hilmi, A.S. Halim, Vital roles of stem cells and biomaterials in skin tissue engineering, World journal of stem cells 7(2) (2015) 428.
[46] M. Sheikholeslam, M.E. Wright, M.G. Jeschke, S. Amini-Nik, Biomaterials for skin substitutes, Advanced healthcare materials 7(5) (2018) 1700897.
[47] M. Modrák, M. Trebuňová, A.F. Balogová, R. Hudák, J. Živčák, Biodegradable materials for tissue engineering: development, classification and current applications, Journal of functional biomaterials 14(3) (2023) 159.
[48] Y. Yang, W. Zhang, Y. Li, G. Fang, K. Zhang, Scalded skin of rat treated by using fibrin glue combined with allogeneic bone marrow mesenchymal stem cells, Ann Dermatol 26(3) (2014) 289-95.
[49] T. Sun, J. Haycock, S. Macneil, In situ image analysis of interactions between normal human keratinocytes and fibroblasts cultured in three-dimensional fibrin gels, Biomaterials 27(18) (2006) 3459-65.
[50] D.J. Gilmartin, A. Soon, C. Thrasivoulou, A.R. Phillips, S.N. Jayasinghe, D.L. Becker, Sustained release of Cx43 antisense oligodeoxynucleotides from coated collagen scaffolds promotes wound healing, Advanced healthcare materials 5(14) (2016) 1786-99.
[51] D.C. Koppenol, F.J. Vermolen, F.B. Niessen, P.P.M. van Zuijlen, K. Vuik, A biomechanical mathematical model for the collagen bundle distribution-dependent contraction and subsequent retraction of healing dermal wounds, Biomechanics and modeling in mechanobiology 16(1) (2017) 345-361.
[52] J. Chen, Z. Liu, M. Chen, H. Zhang, X. Li, Electrospun gelatin fibers with a multiple release of antibiotics accelerate dermal regeneration in infected deep burns, Macromolecular Bioscience 16(9) (2016) 1368-80.
[53] S. Huang, Y. Zhang, L. Tang, Z. Deng, W. Lu, F. Feng, X. Xu, Y. Jin, Functional bilayered skin substitute constructed by tissue-engineered extracellular matrix and microsphere-incorporated gelatin hydrogel for wound repair, Tissue engineering Part A 15(9) (2009) 2617-24.
[54] P.S. Nunes, A.S. Rabelo, J.C. Souza, B.V. Santana, T.M. da Silva, M.R. Serafini, P. Dos Passos Menezes, B. Dos Santos Lima, J.C. Cardoso, J.C. Alves, L.A. Frank, S.S. Guterres, A.R. Pohlmann, M.S. Pinheiro, R.L.J. de Albuquerque, A.A. Araujo, Gelatin-based membrane

containing usnic acid-loaded liposome improves dermal burn healing in a porcine model, International journal of pharmaceutics 513(1-2) (2016) 473-482.
[55] V.T. Tchemtchoua, G. Atanasova, A. Aqil, P. Filee, N. Garbacki, O. Vanhooteghem, C. Deroanne, A. Noel, C. Jerome, B. Nusgens, Y. Poumay, A. Colige, Development of a chitosan nanofibrillar scaffold for skin repair and regeneration, Biomacromolecules 12(9) (2011) 3194-204.
[56] Y. Kong, R. Xu, M.A. Darabi, W. Zhong, G. Luo, M.M. Xing, J. Wu, Fast and safe fabrication of a free-standing chitosan/alginate nanomembrane to promote stem cell delivery and wound healing, International journal of nanomedicine 11 (2016) 2543-55.
[57] A. Skardal, S.V. Murphy, K. Crowell, D. Mack, A. Atala, S. Soker, A tunable hydrogel system for long-term release of cell-secreted cytokines and bioprinted in situ wound cell delivery, Journal of biomedical materials research Part B: Applied biomaterials 105(7) (2017) 1986-2000.
[58] T. Tokatlian, C. Cam, T. Segura, Porous hyaluronic acid hydrogels for localized nonviral DNA delivery in a diabetic wound healing model, Advanced healthcare materials 4(7) (2015) 1084-91.
[59] M. Farokhi, F. Mottaghitalab, Y. Fatahi, A. Khademhosseini, D.L. Kaplan, Overview of silk fibroin use in wound dressings, Trends in biotechnology, 36(9), 907-922.
[60] E.S. Gil, B. Panilaitis, E. Bellas, D.L. Kaplan, Functionalized silk biomaterials for wound healing, Advanced healthcare materials 2(1) (2013) 206-17.
[61] S.Z. Fu, X.H. Meng, J. Fan, L.L. Yang, Q.L. Wen, S.J. Ye, S. Lin, B.Q. Wang, L.L. Chen, J.B. Wu, Y. Chen, J.M. Fan, Z. Li, Acceleration of dermal wound healing by using electrospun curcumin-loaded poly(epsilon-caprolactone)-poly(ethylene glycol)-poly(epsilon-caprolactone) fibrous mats, Journal of biomedical materials research Part B: Applied biomaterials 102(3) (2014) 533-42.
[62] W.L. Hinrichs, E.J. Lommen, C.R. Wildevuur, J. Feijen, Fabrication and characterization of an asymmetric polyurethane membrane for use as a wound dressing, Journal of Applied Biomaterials 3(4) (1992) 287-303.
[63] M.S. Khil, D.I. Cha, H.Y. Kim, I.S. Kim, N. Bhattarai, Electrospun nanofibrous polyurethane membrane as wound dressing, Journal of biomedical materials research Part B: Applied biomaterials 67(2) (2003) 675-9.
[64] G. Chen, T. Sato, H. Ohgushi, T. Ushida, T. Tateishi, J. Tanaka, Culturing of skin fibroblasts in a thin PLGA-collagen hybrid mesh, Biomaterials 26(15) (2005) 2559-66.
[65] W.A. Marston, Dermagraft, a bioengineered human dermal equivalent for the treatment of chronic nonhealing diabetic foot ulcer, Expert Review of Medical Devices 1(1) (2004) 21-31.
[66] E.A. Kamoun, E.R.S. Kenawy, X. Chen, A review on polymeric hydrogel membranes for wound dressing applications: PVA-based hydrogel dressings, Journal of advanced research, 8(3), 217-233.
[67] M.Z. Li, N. Minoura, L.X. Dai, L.S. Zhang, Preparation of porous poly(vinyl alcohol)-silk fibroin (PVA/SF) blend membranes, Macromolecular materials and engineering 286(9) (2001) 529-534.
[68] G.H. Altman, F. Diaz, C. Jakuba, T. Calabro, R.L. Horan, J. Chen, H. Lu, J. Richmond, D.L. Kaplan, Silk-based biomaterials, Biomaterials 24(3) (2003) 401-416.
[69] C. Holland, K. Numata, J. Rnjak-Kovacina, F.P. Seib, The biomedical use of silk: past, present, future, Advanced healthcare materials 8(1) (2019) 1800465.
[70] S. Kundu, B. Kundu, S. Talukdar, S. Bano, S. Nayak, J. Kundu, B.B. Mandal, N. Bhardwaj, M. Botlagunta, B.C. Dash, Nonmulberry silk biopolymers, Biopolymers 97(6) (2012) 455-467.

[71] M. Widhe, J. Johansson, M. Hedhammar, A. Rising, Current progress and limitations of spider silk for biomedical applications, Biopolymers 97(6) (2012) 468-478.
[72] Y. Qi, H. Wang, K. Wei, Y. Yang, R.-Y. Zheng, I.S. Kim, K.-Q. Zhang, A review of structure construction of silk fibroin biomaterials from single structures to multi-level structures, International journal of molecular sciences 18(3) (2017) 237.
[73] D.N. Rockwood, R.C. Preda, T. Yücel, X. Wang, M.L. Lovett, D.L. Kaplan, Materials fabrication from Bombyx mori silk fibroin, Nature protocols 6(10) (2011) 1612-1631.
[74] D. Chouhan, B.B. Mandal, Silk biomaterials in wound healing and skin regeneration therapeutics: From bench to bedside, Acta biomaterialia 103 (2020) 24-51.
[75] S. Inoue, K. Tanaka, F. Arisaka, S. Kimura, K. Ohtomo, S. Mizuno, Silk fibroin of Bombyx mori is secreted, assembling a high molecular mass elementary unit consisting of H-chain, L-chain, and P25, with a 6: 6: 1 molar ratio, Journal of biological chemistry 275(51) (2000) 40517-40528.
[76] A.R. Murphy, D.L. Kaplan, Biomedical applications of chemically-modified silk fibroin, Journal of materials chemistry 19(36) (2009) 6443-6450.
[77] X. Wang, J.A. Kluge, G.G. Leisk, D.L. Kaplan, Sonication-induced gelation of silk fibroin for cell encapsulation, Biomaterials 29(8) (2008) 1054-1064.
[78] T. Yucel, P. Cebe, D.L. Kaplan, Vortex-induced injectable silk fibroin hydrogels, Biophysical journal 97(7) (2009) 2044-2050.
[79] G.G. Leisk, T.J. Lo, T. Yucel, Q. Lu, D.L. Kaplan, Electrogelation for protein adhesives, Advanced materials 22(6) (2010) 711-715.
[80] A. Gupta K, K. Mita, K.P. Arunkumar, J. Nagaraju, Molecular architecture of silk fibroin of Indian golden silkmoth, Antheraea assama, Scientific reports 5(1) (2015) 12706.
[81] B.B. Mandal, S. Kundu, A novel method for dissolution and stabilization of non-mulberry silk gland protein fibroin using anionic surfactant sodium dodecyl sulfate, Biotechnology and bioengineering 99(6) (2008) 1482-1489.
[82] P. Gupta, M. Kumar, N. Bhardwaj, J.P. Kumar, C. Krishnamurthy, S.K. Nandi, B.B. Mandal, Mimicking form and function of native small diameter vascular conduits using mulberry and non-mulberry patterned silk films, ACS applied materials & interfaces 8(25) (2016) 15874-15888.
[83] S.T. Boyce, Cultured skin substitutes: a review, Tissue engineering 2(4) (1996) 255-266.
[84] D. Marino, J. Luginbühl, S. Scola, M. Meuli, E. Reichmann, Bioengineering dermo-epidermal skin grafts with blood and lymphatic capillaries, Science translational medicine 6(221) (2014) 221ra14-221ra14.
[85] W. Pu, J. Ren, Y. Chen, J. Shu, L. Cui, Y. Han, J. Xi, X. Pei, W. Yue, Y. Han, Injectable human decellularized adipose tissue hydrogel containing stem cells enhances wound healing in mouse, Colloids and surfaces A: Physicochemical and engineering aspects 604 (2020) 125268.
[86] Q. Bo, L. Yan, H. Li, Z. Jia, A. Zhan, J. Chen, Z. Yuan, W. Zhang, B. Gao, R. Chen, Decellularized dermal matrix-based photo-crosslinking hydrogels as a platform for delivery of adipose derived stem cells to accelerate cutaneous wound healing, Materials & design 196 (2020) 109152.
[87] C. Mohanty, J. Pradhan, A human epidermal growth factor-curcumin bandage bioconjugate loaded with mesenchymal stem cell for in vivo diabetic wound healing, Materials science and engineering: C 111 (2020) 110751.
[88] S. Danner, M. Kremer, A.E. Petschnik, S. Nagel, Z. Zhang, U. Hopfner, A.K. Reckhenrich, C. Weber, T.L. Schenck, T. Becker, The use of human sweat gland–derived stem cells for enhancing vascularization during dermal regeneration, Journal of investigative dermatology 132(6) (2012) 1707-1716.

[89] A. Pourmoussa, D.J. Gardner, M.B. Johnson, A.K. Wong, An update and review of cell-based wound dressings and their integration into clinical practice, Annals of translational medicine 4(23) (2016).
[90] W. Srifa, N. Kosaric, A. Amorin, O. Jadi, Y. Park, S. Mantri, J. Camarena, G.C. Gurtner, M. Porteus, Cas9-AAV6-engineered human mesenchymal stromal cells improved cutaneous wound healing in diabetic mice, Nature communications 11(1) (2020) 2470.
[91] N. Papanas, E. Maltezos, Becaplermin gel in the treatment of diabetic neuropathic foot ulcers, Clinical interventions in aging 3(2) (2008) 233-240.
[92] S. Akita, K. Akino, T. Imaizumi, A. Hirano, Basic fibroblast growth factor accelerates and improves second-degree burn wound healing, Wound repair and regeneration 16(5) (2008) 635-641.
[93] J.I. Fernández-Montequín, E. Infante-Cristiá, C. Valenzuela-Silva, N. Franco-Pérez, W. Savigne-Gutierrez, H. Artaza-Sanz, L. Morejón-Vega, C. González-Benavides, O. Eliseo-Musenden, E. García-Iglesias, Intralesional injections of Citoprot-P®(recombinant human epidermal growth factor) in advanced diabetic foot ulcers with risk of amputation, International wound journal 4(4) (2007) 333-343.
[94] V.K. Mohan, Recombinant human epidermal growth factor (REGEN-D™ 150): Effect on healing of diabetic foot ulcers, Diabetes research and clinical practice 78(3) (2007) 405-411.
[95] P. Tayalia, D.J. Mooney, Controlled growth factor delivery for tissue engineering, Advanced materials 21(32-33) (2009) 3269-3285.
[96] H.-J. Lai, C.-H. Kuan, H.-C. Wu, J.-C. Tsai, T.-M. Chen, D.-J. Hsieh, T.-W. Wang, Tailored design of electrospun composite nanofibers with staged release of multiple angiogenic growth factors for chronic wound healing, Acta biomaterialia 10(10) (2014) 4156-4166.
[97] M. Berthet, Y. Gauthier, C. Lacroix, B. Verrier, C. Monge, Nanoparticle-based dressing: the future of wound treatment?, Trends in biotechnology 35(8) (2017) 770-784.
[98] F. Reyes-Ortega, A. Cifuentes, G. Rodríguez, M.R. Aguilar, Á. González-Gómez, R. Solis, N. García-Honduvilla, J. Buján, J. García-Sanmartin, A. Martínez, Bioactive bilayered dressing for compromised epidermal tissue regeneration with sequential activity of complementary agents, Acta biomaterialia 23 (2015) 103-115.
[99] J. Tian, K.K. Wong, C.M. Ho, C.N. Lok, W.Y. Yu, C.M. Che, J.F. Chiu, P.K. Tam, Topical delivery of silver nanoparticles promotes wound healing, ChemMedChem: Chemistry enabling drug discovery 2(1) (2007) 129-136.
[100] G. Nam, S. Rangasamy, B. Purushothaman, J.M. Song, The application of bactericidal silver nanoparticles in wound treatment, Nanomaterials and nanotechnology 5 (2015) 23.
[101] A. Munteanu, I. Florescu, C. Nitescu, A modern method of treatment: The role of silver dressings in promoting healing and preventing pathological scarring in patients with burn wounds, Journal of medicine and life 9(3) (2016) 306.
[102] O. Akturk, K. Kismet, A.C. Yasti, S. Kuru, M.E. Duymus, F. Kaya, M. Caydere, S. Hucumenoglu, D. Keskin, Collagen/gold nanoparticle nanocomposites: a potential skin wound healing biomaterial, Journal of biomaterials applications 31(2) (2016) 283-301.
[103] H. Nurhasni, J. Cao, M. Choi, I. Kim, B.L. Lee, Y. Jung, J.-W. Yoo, Nitric oxide-releasing poly (lactic-co-glycolic acid)-polyethylenimine nanoparticles for prolonged nitric oxide release, antibacterial efficacy, and in vivo wound healing activity, International journal of nanomedicine (2015) 3065-3080.
[104] K. Blecher, L.R. Martinez, C. Tuckman-Vernon, P. Nacharaju, D. Schairer, J. Chouake, J.M. Friedman, A. Alfieri, C. Guha, J.D. Nosanchuk, Nitric oxide-releasing nanoparticles accelerate wound healing in NOD-SCID mice, Nanomedicine: Nanotechnology, Biology and Medicine 8(8) (2012) 1364-1371.

[105] A. Tamayol, M. Akbari, Y. Zilberman, M. Comotto, E. Lesha, L. Serex, S. Bagherifard, Y. Chen, G. Fu, S.K. Ameri, Flexible pH-sensing hydrogel fibers for epidermal applications, Advanced healthcare materials 5(6) (2016) 711-719.
[106] W. Honda, S. Harada, T. Arie, S. Akita, K. Takei, Printed wearable temperature sensor for health monitoring, Sensors, 2014 IEEE, pp. 2227-2229.
[107] S.D. Milne, I. Seoudi, H. Al Hamad, T.K. Talal, A.A. Anoop, N. Allahverdi, Z. Zakaria, R. Menzies, P. Connolly, A wearable wound moisture sensor as an indicator for wound dressing change: an observational study of wound moisture and status, International wound journal 13(6) (2016) 1309-1314.
[108] M. Messaoud, C. Marsiquet, F. Revol-Cavalier, V. Rat, G. Marchand, Flexible sensors for real-time monitoring of moisture levels in wound dressings, Journal of wound care 27(6) (2018) 385-391.
[109] E.S. Papazoglou, L. Zubkov, X. Mao, M. Neidrauer, N. Rannou, M.S. Weingarten, Image analysis of chronic wounds for determining the surface area, Wound repair and regeneration 18(4) (2010) 349-358.
[110] T.E. Serena, K. Harrell, L. Serena, R.A. Yaakov, Real-time bacterial fluorescence imaging accurately identifies wounds with moderate-to-heavy bacterial burden, Journal of wound care 28(6) (2019) 346-357.
[111] M. Ochoa, R. Rahimi, J. Zhou, H. Jiang, C.K. Yoon, D. Maddipatla, B.B. Narakathu, V. Jain, M.M. Oscai, T.J. Morken, Integrated sensing and delivery of oxygen for next-generation smart wound dressings, Microsystems & nanoengineering 6(1) (2020) 46.
[112] G. Baura, Medical device technologies: a systems based overview using engineering standards, Academic Press2011.
[113] P. Kassal, J. Kim, R. Kumar, W.R. de Araujo, I.M. Steinberg, M.D. Steinberg, J. Wang, Smart bandage with wireless connectivity for uric acid biosensing as an indicator of wound status, Electrochemistry communications 56 (2015) 6-10.
[114] S. RoyChoudhury, Y. Umasankar, J. Jaller, I. Herskovitz, J. Mervis, E. Darwin, P.A. Hirt, L.J. Borda, H.A. Lev-Tov, R. Kirsner, Continuous monitoring of wound healing using a wearable enzymatic uric acid biosensor, Journal of the electrochemical society 165(8) (2018) B3168.
[115] A. Lockmann, T. Schill, F. Hartmann, L.-L. Grönemeyer, R. Holzkamp, M.P. Schön, K.-M. Thoms, Testing elevated protease activity: prospective analysis of 160 wounds, Advances in skin & wound care 31(2) (2018) 82-88.
[116] T.F. O'Connor, S. Savagatrup, D.J. Lipomi, Soft power: stretchable and ultra-flexible energy sources for wearable and implantable devices, Stretchable bioelectronics for medical devices and systems (2016) 69-82.
[117] P. Mostafalu, A. Tamayol, R. Rahimi, M. Ochoa, A. Khalilpour, G. Kiaee, I.K. Yazdi, S. Bagherifard, M.R. Dokmeci, B. Ziaie, Smart bandage for monitoring and treatment of chronic wounds, Small 14(33) (2018) 1703509.
[118] R. Rahimi, M. Ochoa, A. Tamayol, S. Khalili, A. Khademhosseini, B. Ziaie, Highly stretchable potentiometric pH sensor fabricated via laser carbonization and machining of Carbon− Polyaniline composite, ACS applied materials & interfaces 9(10) (2017) 9015-9023.
[119] S.K. Beidler, C.D. Douillet, D.F. Berndt, B.A. Keagy, P.B. Rich, W.A. Marston, Inflammatory cytokine levels in chronic venous insufficiency ulcer tissue before and after compression therapy, Journal of vascular surgery 49(4) (2009) 1013-1020.
[120] G. Wang, H. Huang, G. Zhang, X. Zhang, B. Fang, L. Wang, Dual amplification strategy for the fabrication of highly sensitive interleukin-6 amperometric immunosensor based on poly-dopamine, Langmuir 27(3) (2011) 1224-1231.
[121] J. Mok, M.N. Mindrinos, R.W. Davis, M. Javanmard, Digital microfluidic assay for protein detection, Proceedings of the national academy of sciences 111(6) (2014) 2110-2115.

[122] S. Mandal, J.M. Goddard, D. Erickson, A multiplexed optofluidic biomolecular sensor for low mass detection, Lab on a chip 9(20) (2009) 2924-2932.
[123] H.J. Sismaet, A. Banerjee, S. McNish, Y. Choi, M. Torralba, S. Lucas, A. Chan, V.K. Shanmugam, E.D. Goluch, Electrochemical detection of Pseudomonas in wound exudate samples from patients with chronic wounds, Wound repair and regeneration 24(2) (2016) 366-372.
[124] A. Pal, D. Goswami, H.E. Cuellar, B. Castro, S. Kuang, R.V. Martinez, Early detection and monitoring of chronic wounds using low-cost, omniphobic paper-based smart bandages, Biosensors and bioelectronics 117 (2018) 696-705.
[125] M. Ashrafi, T. Alonso-Rasgado, M. Baguneid, A. Bayat, The efficacy of electrical stimulation in lower extremity cutaneous wound healing: a systematic review, Experimental dermatology 26(2) (2017) 171-178.
[126] J. Hunckler, A. De Mel, A current affair: electrotherapy in wound healing, Journal of multidisciplinary healthcare 10 (2017) 179-194.
[127] Y. Shen, T. Pfluger, F. Ferreira, J. Liang, M.F. Navedo, Q. Zeng, B. Reid, M. Zhao, Diabetic cornea wounds produce significantly weaker electric signals that may contribute to impaired healing, Scientific reports 6(1) (2016) 26525.
[128] X.-F. Wang, M.-L. Li, Q.-Q. Fang, W.-Y. Zhao, D. Lou, Y.-Y. Hu, J. Chen, X.-Z. Wang, W.-Q. Tan, Flexible electrical stimulation device with Chitosan-Vaseline® dressing accelerates wound healing in diabetes, Bioactive materials 6(1) (2021) 230-243.
[129] G. Tai, M. Tai, M. Zhao, Electrically stimulated cell migration and its contribution to wound healing, Burns & trauma 6 (2018).
[130] K.C. Balakatounis, A.G. Angoules, Low-intensity electrical stimulation in wound healing: review of the efficacy of externally applied currents resembling the current of injury, Eplasty 8 (2008).
[131] B. Palmieri, M. Vadalà, C. Laurino, Electromedical devices in wound healing management: A narrative review, Journal of wound care 29(7) (2020) 408-418.
[132] M.R. Asadi, G. Torkaman, Bacterial inhibition by electrical stimulation, Advances in wound care 3(2) (2014) 91-97.
[133] A. Ramadan, M. Elsaidy, R. Zyada, Effect of low-intensity direct current on the healing of chronic wounds: a literature review, Journal of wound care 17(7) (2008) 292-296.
[134] K.M. Bogie, The modular adaptive electrotherapy delivery system (MAEDS): An electroceutical approach for effective treatment of wound infection and promotion of healing, Military Medicine 184(Supplement_1) (2019) 92-96.
[135] D.S. Howe, J.L. Dunning, M.K. Henzel, J.K. Graebert, K.M. Bogie, A wearable stimulation bandage for electrotherapy studies in a rat ischemic wound model, 2011 Annual International Conference of the IEEE engineering in medicine and biology society, IEEE, 2011, pp. 298-301.
[136] C. Yu, Z.X. Xu, Y.-H. Hao, Y.-B. Gao, B.-W. Yao, J. Zhang, B. Wang, Z.-Q. Hu, R.-Y. Peng, A novel microcurrent dressing for wound healing in a rat skin defect model, Military medical research 6 (2019) 1-9.
[137] S.T. Sultana, E. Atci, J.T. Babauta, A. Mohamed Falghoush, K.R. Snekvik, D.R. Call, H. Beyenal, Electrochemical scaffold generates localized, low concentration of hydrogen peroxide that inhibits bacterial pathogens and biofilms, Scientific reports 5(1) (2015) 1-10.
[138] R. Heald, M. Bennett, V.V. Subramaniam, D. Dusane, V. Lochab, P.M. Sundaram, S. Salyer, J. West, P. Stoodley, S. Prakash, Printed electroceutical dressings for the inhibition of biofilms and treatment of chronic wounds, Journal of microelectromechanical systems 29(5) (2020) 918-923.
[139] D. Chapman-Jones, S. Young, M. Tadej, Assessment of wound healing following electrical stimulation with Accel-Heal®, Wounds UK 6(3) (2010) 67-71.

[140] H. Kim, I. Makin, J. Skiba, A. Ho, G. Housler, A. Stojadinovic, M. Izadjoo, Antibacterial efficacy testing of a bioelectric wound dressing against clinical wound pathogens, The open microbiology journal 8 (2014) 15.
[141] L.C. Kloth, Electrical stimulation technologies for wound healing, Advances in wound care 3(2) (2014) 81-90.
[142] H. Kai, T. Yamauchi, Y. Ogawa, A. Tsubota, T. Magome, T. Miyake, K. Yamasaki, M. Nishizawa, Accelerated wound healing on skin by electrical stimulation with a bioelectric plaster, Advanced healthcare materials 6(22) (2017) 1700465.
[143] H.-K. Jang, J.Y. Oh, G.-J. Jeong, T.-J. Lee, G.-B. Im, J.-R. Lee, J.-K. Yoon, D.-I. Kim, B.-S. Kim, S.H. Bhang, A disposable photovoltaic patch controlling cellular microenvironment for wound healing, International journal of molecular sciences 19(10) (2018) 3025.
[144] Y. Long, H. Wei, J. Li, G. Yao, B. Yu, D. Ni, A.L. Gibson, X. Lan, Y. Jiang, W. Cai, Effective wound healing enabled by discrete alternative electric fields from wearable nanogenerators, ACS nano 12(12) (2018) 12533-12540.
[145] S.H. Jeong, Y. Lee, M.G. Lee, W.J. Song, J.U. Park, J. Y. Sun, Accelerated wound healing with an ionic patch assisted by a triboelectric nanogenerator, Nano energy 79 (2021) 105463.
[146] P.G. Wirsing, A.D. Habrom, T.M. Zehnder, S. Friedli, M. Blatti, Wireless micro current stimulation–an innovative electrical stimulation method for the treatment of patients with leg and diabetic foot ulcers, International wound journal 12(6) (2015) 693-698.
[147] S.E. Vidal Yucha, K.A. Tamamoto, H. Nguyen, D.M. Cairns, D.L. Kaplan, Human skin equivalents demonstrate need for neuro-immuno-cutaneous system, Advanced biosystems 3(1) (2019) 1800283.
[148] R. Augustine, Skin bioprinting: a novel approach for creating artificial skin from synthetic and natural building blocks, Progress in biomaterials 7(2) (2018) 77-92.
[149] V. Lee, G. Singh, J.P. Trasatti, C. Bjornsson, X. Xu, T.N. Tran, S.-S. Yoo, G. Dai, P. Karande, Design and fabrication of human skin by three-dimensional bioprinting, Tissue engineering Part C: Methods 20(6) (2014) 473-484.
[150] N. Cubo, M. Garcia, J.F. Del Cañizo, D. Velasco, J.L. Jorcano, 3D bioprinting of functional human skin: production and in vivo analysis, Biofabrication 9(1) (2016) 015006.
[151] L.J. Pourchet, A. Thepot, M. Albouy, E.J. Courtial, A. Boher, L.J. Blum, C.A. Marquette, Human skin 3D bioprinting using scaffold-free approach, Advanced healthcare materials 6(4) (2017) 1601101.
[152] N. Hakimi, R. Cheng, L. Leng, M. Sotoudehfar, P.Q. Ba, N. Bakhtyar, S. Amini-Nik, M.G. Jeschke, A. Günther, Handheld skin printer: in situ formation of planar biomaterials and tissues, Lab on a chip 18(10) (2018) 1440-1451.
[153] M. Albanna, K.W. Binder, S.V. Murphy, J. Kim, S.A. Qasem, W. Zhao, J. Tan, I.B. El-Amin, D.D. Dice, J. Marco, In situ bioprinting of autologous skin cells accelerates wound healing of extensive excisional full-thickness wounds, Scientific reports 9(1) (2019) 1856.
[154] R.Y. Cheng, G. Eylert, J.-M. Gariepy, S. He, H. Ahmad, Y. Gao, S. Priore, N. Hakimi, M.G. Jeschke, A. Günther, Handheld instrument for wound-conformal delivery of skin precursor sheets improves healing in full-thickness burns, Biofabrication 12(2) (2020) 025002.
[155] G. Ying, J. Manríquez, D. Wu, J. Zhang, N. Jiang, S. Maharjan, D.H. Medina, Y.S. Zhang, An open-source handheld extruder loaded with pore-forming bioink for in situ wound dressing, Materials today bio 8 (2020) 100074.
[156] B.S. Kim, Y.W. Kwon, J.-S. Kong, G.T. Park, G. Gao, W. Han, M.-B. Kim, H. Lee, J.H. Kim, D.-W. Cho, 3D cell printing of in vitro stabilized skin model and in vivo pre-vascularized skin patch using tissue-specific extracellular matrix bioink: A step towards advanced skin tissue engineering, Biomaterials 168 (2018) 38-53.

[157] W. Lee, J.C. Debasitis, V.K. Lee, J.-H. Lee, K. Fischer, K. Edminster, J.-K. Park, S.-S. Yoo, Multi-layered culture of human skin fibroblasts and keratinocytes through three-dimensional freeform fabrication, Biomaterials 30(8) (2009) 1587-1595.
[158] K.W. Binder, W. Zhao, T. Aboushwareb, D. Dice, A. Atala, J.J. Yoo, In situ bioprinting of the skin for burns, Journal of the american college of surgeons 211(3) (2010) S76.
[159] L. Koch, A. Deiwick, S. Schlie, S. Michael, M. Gruene, V. Coger, D. Zychlinski, A. Schambach, K. Reimers, P.M. Vogt, Skin tissue generation by laser cell printing, Biotechnology and bioengineering 109(7) (2012) 1855-1863.
[160] S. Michael, H. Sorg, C.-T. Peck, L. Koch, A. Deiwick, B. Chichkov, P.M. Vogt, K. Reimers, Tissue engineered skin substitutes created by laser-assisted bioprinting form skin-like structures in the dorsal skin fold chamber in mice, PloS one 8(3) (2013) e57741.
[161] W. Wan, F. Cai, J. Huang, S. Chen, Q. Liao, A skin-inspired 3D bilayer scaffold enhances granulation tissue formation and anti-infection for diabetic wound healing, Journal of materials chemistry B 7(18) (2019) 2954-2961.
[162] N. Mori, Y. Morimoto, S. Takeuchi, Skin integrated with perfusable vascular channels on a chip, Biomaterials 116 (2017) 48-56.
[163] H.E. Abaci, Z. Guo, A. Coffman, B. Gillette, W.h. Lee, S.K. Sia, A.M. Christiano, Human skin constructs with spatially controlled vasculature using primary and iPSC-derived endothelial cells, Advanced healthcare materials 5(14) (2016) 1800-1807.
[164] T. Baltazar, J. Merola, C. Catarino, C.B. Xie, N.C. Kirkiles-Smith, V. Lee, S. Hotta, G. Dai, X. Xu, F.C. Ferreira, Three dimensional bioprinting of a vascularized and perfusable skin graft using human keratinocytes, fibroblasts, pericytes, and endothelial cells, Tissue engineering part A 26(5-6) (2020) 227-238.
[165] D. Min, W. Lee, I.H. Bae, T.R. Lee, P. Croce, S.S. Yoo, Bioprinting of biomimetic skin containing melanocytes, Experimental dermatology 27(5) (2018) 453-459.
[166] W.L. Ng, J.T.Z. Qi, W.Y. Yeong, M.W. Naing, Proof-of-concept: 3D bioprinting of pigmented human skin constructs, Biofabrication 10(2) (2018) 025005.
[167] D. Duscher, J. Barrera, V.W. Wong, Z.N. Maan, A.J. Whittam, M. Januszyk, G.C. Gurtner, Stem cells in wound healing: the future of regenerative medicine? A mini-review, Gerontology 62(2) (2016) 216-225.
[168] A. Skardal, D. Mack, E. Kapetanovic, A. Atala, J.D. Jackson, J. Yoo, S. Soker, Bioprinted amniotic fluid-derived stem cells accelerate healing of large skin wounds, Stem cells translational medicine 1(11) (2012) 792-802.
[169] V.W. Wong, B. Levi, J. Rajadas, M.T. Longaker, G.C. Gurtner, Stem cell niches for skin regeneration, International journal of biomaterials 2012(1) (2012) 926059.
[170] B. Yao, R. Wang, Y. Wang, Y. Zhang, T. Hu, W. Song, Z. Li, S. Huang, X. Fu, Biochemical and structural cues of 3D-printed matrix synergistically direct MSC differentiation for functional sweat gland regeneration, Science advances 6(10) (2020) eaaz1094.
[171] S. Huang, B. Yao, J. Xie, X. Fu, 3D bioprinted extracellular matrix mimics facilitate directed differentiation of epithelial progenitors for sweat gland regeneration, Acta biomaterialia 32 (2016) 170-177.
[172] Y. Fu, L. Karbaat, L. Wu, J. Leijten, S.K. Both, M. Karperien, Trophic effects of mesenchymal stem cells in tissue regeneration, Tissue engineering Part B: Reviews 23(6) (2017) 515-528.
[173] M. Wang, C. Wang, M. Chen, Y. Xi, W. Cheng, C. Mao, T. Xu, X. Zhang, C. Lin, W. Gao, Efficient angiogenesis-based diabetic wound healing/skin reconstruction through bioactive antibacterial adhesive ultraviolet shielding nanodressing with exosome release, ACS Nano 13(9) (2019) 10279-10293.

[174] B.S. Kim, G. Gao, J.Y. Kim, D.W. Cho, 3D cell printing of perfusable vascularized human skin equivalent composed of epidermis, dermis, and hypodermis for better structural recapitulation of native skin, Advanced healthcare materials 8(7) (2019) 1801019.
[175] B. Zhang, L. Gao, L. Ma, Y. Luo, H. Yang, Z. Cui, 3D bioprinting: a novel avenue for manufacturing tissues and organs, Engineering 5(4) (2019) 777-794.
[176] A. Olejnik, J.A. Semba, A. Kulpa, A. Danczak-Pazdrowska, J.D. Rybka, J. Gornowicz-Porowska, 3D bioprinting in skin related research: recent achievements and application perspectives, ACS Synthetic biology 11(1) (2021) 26-38.
[177] H. Yoon, J.-S. Lee, H. Yim, G. Kim, W. Chun, Development of cell-laden 3D scaffolds for efficient engineered skin substitutes by collagen gelation, RSC Advances 6(26) (2016) 21439-21447.
[178] B.S. Kim, J.-S. Lee, G. Gao, D.-W. Cho, Direct 3D cell-printing of human skin with functional transwell system, Biofabrication 9(2) (2017) 025034.
[179] Y. Shi, T. Xing, H. Zhang, R. Yin, S. Yang, J. Wei, W. Zhang, Tyrosinase-doped bioink for 3D bioprinting of living skin constructs, Biomedical materials 13(3) (2018) 035008.
[180] Z. Zheng, D. Eglin, M. Alini, G.R. Richards, L. Qin, Y. Lai, Visible light-induced 3D bioprinting technologies and corresponding bioink materials for tissue engineering: a review, Engineering 7(7) (2021) 966-978.
[181] D. Sreedhar, N. Manjula, A. Pise, S. Pise, Ban of cosmetic testing on animals: A brief overview, International journal of current research and review 12(14) (2020) 113.
[182] N. Bhardwaj, S. Dey, B. Bhar, B.B. Mandal, Bioprinted in vitro tissue models: an emerging platform for developing therapeutic interventions and disease modelling, Progress in biomedical engineering 6(1) (2023) 012003.
[183] B.S. Kim, M. Ahn, W.-W. Cho, G. Gao, J. Jang, D.-W. Cho, Engineering of diseased human skin equivalent using 3D cell printing for representing pathophysiological hallmarks of type 2 diabetes in vitro, Biomaterials 272 (2021) 120776.
[184] Z. Wang, Z. Wang, W.W. Lu, W. Zhen, D. Yang, S. Peng, Novel biomaterial strategies for controlled growth factor delivery for biomedical applications, NPG Asia materials 9(10) (2017) e435-e435.
[185] V. Volarevic, B.S. Markovic, M. Gazdic, A. Volarevic, N. Jovicic, N. Arsenijevic, L. Armstrong, V. Djonov, M. Lako, M. Stojkovic, Ethical and safety issues of stem cell-based therapy, International journal of medical sciences 15(1) (2018) 36.
[186] J.S. Meena, S.B. Choi, S.-B. Jung, J.-W. Kim, Electronic textiles: New age of wearable technology for healthcare and fitness solutions, Materials today bio 19 (2023) 100565.
[187] M. Portugal-Cohen, D. Cohen, R. Kohen, M. Oron, Exploitation of alternative skin models from academia to industry: proposed functional categories to answer needs and regulation demands, Frontiers in physiology 14 (2023) 1215266.
[188] D. Sreedhar, N. Manjula, S. Pise, V. Ligade, Ban of cosmetic testing on animals: a brief overview, International journal of current research and review 12(14) (2020) 113.
[189] B. Bhar, D. Chouhan, N. Pai, B.B. Mandal, Harnessing multifaceted next-generation technologies for improved skin wound healing, ACS Applied bio materials 4(11) (2021) 7738-7763.
[190] P. Jain, H. Kathuria, N. Dubey, Advances in 3D bioprinting of tissues/organs for regenerative medicine and in-vitro models, Biomaterials 287 (2022) 121639.
[191] E.S. Bishop, S. Mostafa, M. Pakvasa, H.H. Luu, M.J. Lee, J.M. Wolf, G.A. Ameer, T.-C. He, R.R. Reid, 3-D bioprinting technologies in tissue engineering and regenerative medicine: Current and future trends, Genes & diseases 4(4) (2017) 185-195.
[192] S.F. Spampinato, G.I. Caruso, R. De Pasquale, M.A. Sortino, S. Merlo, The treatment of impaired wound healing in diabetes: looking among old drugs, Pharmaceuticals 13(4) (2020) 60.

[193] T.I. Oliver, M. Mutluoglu, Diabetic foot ulcer, (2019).
[194] G. Ragnarson Tennvall, J. Apelqvist, Health-economic consequences of diabetic foot lesions, Clinical infectious diseases 39(Supplement_2) (2004) S132-S139.
[195] W. Huang, Y. Chen, N. Wang, G. Yin, C. Wei, W. Xu, The efficacy and safety of acellular matrix therapy for diabetic foot ulcers: a meta-analysis of randomized clinical trials, Journal of diabetes research 2020 (2020).
[196] J.S. Choi, J.D. Kim, H.S. Yoon, Y.W. Cho, Full-thickness skin wound healing using human placenta-derived extracellular matrix containing bioactive molecules, Tissue engineering Part A 19(3-4) (2013) 329-339.
[197] A. Chiu, D. Sharma, F. Zhao, Tissue Engineering-Based Strategies for Diabetic Foot Ulcer Management, Advances in wound care (2021).
[198] P. Goodarzi, K. Falahzadeh, M. Nematizadeh, P. Farazandeh, M. Payab, B. Larijani, A. Tayanloo Beik, B. Arjmand, Tissue engineered skin substitutes, Cell Biology and Translational Medicine, Volume 3: Stem Cells, Bio-materials and tissue engineering (2018) 143-188.
[199] C. Dai, S. Shih, A. Khachemoune, Skin substitutes for acute and chronic wound healing: an updated review, Journal of dermatological treatment 31(6) (2020) 639-648.
[200] M. Song, W. Wang, Q. Ye, S. Bu, Z. Shen, Y. Zhu, The repairing of full-thickness skin deficiency and its biological mechanism using decellularized human amniotic membrane as the wound dressing, Materials science and engineering: C 77 (2017) 739-747.
[201] V.A. Solarte David, V.R. Güiza-Argüello, M.L. Arango-Rodríguez, C.L. Sossa, S.M. Becerra-Bayona, Decellularized tissues for wound healing: Towards closing the gap between scaffold design and effective extracellular matrix remodeling, Frontiers in bioengineering and biotechnology 10 (2022) 194.
[202] A. Eweida, M. Marei, Naturally occurring extracellular matrix scaffolds for dermal regeneration: do they really need cells?, BioMed research international 2015 (2015).
[203] J.A. Van Dongen, V. Getova, L.A. Brouwer, G.R. Liguori, P.K. Sharma, H.P. Stevens, B. van der Lei, M.C. Harmsen, Adipose tissue-derived extracellular matrix hydrogels as a release platform for secreted paracrine factors, Journal of tissue engineering and regenerative medicine 13(6) (2019) 973-985.
[204] T. Stasch, J. Hoehne, T. Huynh, R. De Baerdemaeker, S. Grandel, C. Herold, Debridement and autologous lipotransfer for chronic ulceration of the diabetic foot and lower limb improves wound healing, Plastic and reconstructive surgery 136(6) (2015) 1357-1366.
[205] G. Vicenti, G. Solarino, V. Pesce, L. Moretti, A. Notarnicola, M. Carrozzo, F. Rifino, B. Moretti, Autologous lipotransfer versus stromal vascular fraction enriched lipoinjection for diabetic foot wounds healing: a pilot study, Journal of biological regulators and homeostatic agents 31(4 suppl 1) (2017) 141-146.
[206] Y.C. Choi, J.S. Choi, B.S. Kim, J.D. Kim, H.I. Yoon, Y.W. Cho, Decellularized extracellular matrix derived from porcine adipose tissue as a xenogeneic biomaterial for tissue engineering, Tissue engineering Part C: Methods 18(11) (2012) 866-876.
[207] L. Wang, J.A. Johnson, Q. Zhang, E.K. Beahm, Combining decellularized human adipose tissue extracellular matrix and adipose-derived stem cells for adipose tissue engineering, Acta biomaterialia 9(11) (2013) 8921-8931.
[208] A. Bandyopadhyay, S.K. Chowdhury, S. Dey, J.C. Moses, B.B. Mandal, Silk: a promising biomaterial opening new vistas towards affordable healthcare solutions, Journal of the Indian Institute of Science 99(3) (2019) 445-487.
[209] Y.R. Park, M.T. Sultan, H.J. Park, J.M. Lee, H.W. Ju, O.J. Lee, D.J. Lee, D.L. Kaplan, C.H. Park, NF-κB signaling is key in the wound healing processes of silk fibroin, Acta biomaterialia 67 (2018) 183-195.
[210] C.M. Srivastava, R. Purwar, R. Kannaujia, D. Sharma, Flexible silk fibroin films for wound dressing, Fibers and polymers 16(5) (2015) 1020-1030.

[211] X. Li, B. Li, J. Ma, X. Wang, S. Zhang, Development of a silk fibroin/HTCC/PVA sponge for chronic wound dressing, Journal of bioactive and compatible polymers 29(4) (2014) 398-411.
[212] I. Firlar, M. Altunbek, C. McCarthy, M. Ramalingam, G. Camci-Unal, Functional hydrogels for treatment of chronic wounds, Gels 8(2) (2022) 127.
[213] H. Zheng, B. Zuo, Functional silk fibroin hydrogels: preparation, properties and applications, Journal of materials chemistry B 9(5) (2021) 1238-1258.
[214] M. Gholipourmalekabadi, S. Sapru, A. Samadikuchaksaraei, R.L. Reis, D.L. Kaplan, S.C. Kundu, Silk fibroin for skin injury repair: where do things stand?, Advanced drug delivery reviews 153 (2020) 28-53.
[215] S. Ghosh, F. Pati, Decellularized extracellular matrix and silk fibroin-based hybrid biomaterials: A comprehensive review on fabrication techniques and tissue-specific applications, International journal of biological macromolecules 253(Pt 8) (2023) 127410.
[216] A.P. Rameshbabu, K. Bankoti, S. Datta, E. Subramani, A. Apoorva, P. Ghosh, P.P. Maity, P. Manchikanti, K. Chaudhury, S. Dhara, Silk sponges ornamented with a placenta-derived extracellular matrix augment full-thickness cutaneous wound healing by stimulating neovascularization and cellular migration, ACS applied materials & interfaces 10(20) (2018) 16977-16991.
[217] M. Gholipourmalekabadi, A. Samadikuchaksaraei, A.M. Seifalian, A.M. Urbanska, H. Ghanbarian, J.G. Hardy, M.D. Omrani, M. Mozafari, R.L. Reis, S.C. Kundu, Silk fibroin/amniotic membrane 3D bi-layered artificial skin, Biomedical materials 13(3) (2018) 035003.
[218] B.K. Bhunia, B.B. Mandal, Exploring gelation and physicochemical behavior of in situ bioresponsive silk hydrogels for disc degeneration therapy, ACS Biomaterials science & engineering 5(2) (2018) 870-886.
[219] M. Shevach, R. Zax, A. Abrahamov, S. Fleischer, A. Shapira, T. Dvir, Omentum ECM-based hydrogel as a platform for cardiac cell delivery, Biomedical materials 10(3) (2015) 034106.
[220] A. Inui, H. Sekine, K. Sano, I. Dobashi, A. Yoshida, K. Matsuura, E. Kobayashi, M. Ono, T. Shimizu, Generation of a large-scale vascular bed for the in vitro creation of three-dimensional cardiac tissue, Regenerative therapy 11 (2019) 316-323.
[221] B.B. Mandal, S.C. Kundu, Cell proliferation and migration in silk fibroin 3D scaffolds, Biomaterials 30(15) (2009) 2956-2965.
[222] D. Moffat, K. Ye, S. Jin, Decellularization for the retention of tissue niches, Journal of tissue engineering 13 (2022) 20417314221101151.
[223] R.W. Farndale, D.J. Buttle, A.J. Barrett, Improved quantitation and discrimination of sulphated glycosaminoglycans by use of dimethylmethylene blue, Biochimica et Biophysica Acta (BBA)-General Subjects 883(2) (1986) 173-177.
[224] J.P. Kumar, B.B. Mandal, Inhibitory role of silk cocoon extract against elastase, hyaluronidase and UV radiation-induced matrix metalloproteinase expression in human dermal fibroblasts and keratinocytes, Photochemical & photobiological sciences 18(5) (2019) 1259-1274.
[225] A.M. Schor, I. Ellis, S.L. Schor, Collagen gel assay for angiogenesis: induction of endothelial cell sprouting, Angiogenesis Protocols (2001) 145-162.
[226] B.L. Furman, Streptozotocin-induced diabetic models in mice and rats, Current protocols in pharmacology 70(1) (2015) 5.47. 1-5.47. 20.
[227] A.E. Anderson, I. Wu, A.J. Parrillo, M.T. Wolf, D.R. Maestas Jr, I. Graham, A.J. Tam, R.M. Payne, J. Aston, C.M. Cooney, An immunologically active, adipose-derived extracellular matrix biomaterial for soft tissue reconstruction: concept to clinical trial, NPJ Regenerative medicine 7(1) (2022) 6.

[228] U. Mendibil, R. Ruiz-Hernandez, S. Retegi-Carrion, N. Garcia-Urquia, B. Olalde-Graells, A. Abarrategi, Tissue-specific decellularization methods: Rationale and strategies to achieve regenerative compounds, International journal of molecular sciences 21(15) (2020) 5447.
[229] P.M. Crapo, T.W. Gilbert, S.F. Badylak, An overview of tissue and whole organ decellularization processes, Biomaterials 32(12) (2011) 3233-3243.
[230] K.-Z. Liu, M. Jackson, M.G. Sowa, H. Ju, I.M. Dixon, H.H. Mantsch, Modification of the extracellular matrix following myocardial infarction monitored by FTIR spectroscopy, Biochimica et Biophysica Acta (BBA)-Molecular basis of disease 1315(2) (1996) 73-77.
[231] G. Janani, S.K. Nandi, B.B. Mandal, Functional hepatocyte clusters on bioactive blend silk matrices towards generating bioartificial liver constructs, Acta biomaterialia 67 (2018) 167-182.
[232] C. Jaiswal, T. Gupta, P.K. Jadi, J.C. Moses, B.B. Mandal, Injectable anti-cancer drug loaded silk-based hydrogel for the prevention of cancer recurrence and post-lumpectomy tissue regeneration aiding triple-negative breast cancer therapy, Biomaterials advances 145 (2023) 213224.
[233] C. Ergun, M. Parmaksiz, M.T. Vurat, A.E. Elçin, Y.M. Elçin, Decellularized liver ECM-based 3D scaffolds: Compositional, physical, chemical, rheological, thermal, mechanical, and in vitro biological evaluations, International journal of biological macromolecules 200 (2022) 110-123.
[234] S.S. Garakani, M. Khanmohammadi, Z. Atoufi, S.K. Kamrava, M. Setayeshmehr, R. Alizadeh, F. Faghihi, Z. Bagher, S.M. Davachi, A. Abbaspourrad, Fabrication of chitosan/agarose scaffolds containing extracellular matrix for tissue engineering applications, International journal of biological macromolecules 143 (2020) 533-545.
[235] L. Bacakova, E. Filova, M. Parizek, T. Ruml, V. Svorcik, Modulation of cell adhesion, proliferation and differentiation on materials designed for body implants, Biotechnology advances 29(6) (2011) 739-767.
[236] J. Li, Y.P. Zhang, R.S. Kirsner, Angiogenesis in wound repair: angiogenic growth factors and the extracellular matrix, Microscopy research and technique 60(1) (2003) 107-114.
[237] S.Y. Chun, J.O. Lim, E.H. Lee, M.-H. Han, Y.-S. Ha, J.N. Lee, B.S. Kim, M.J. Park, M. Yeo, B. Jung, Preparation and characterization of human adipose tissue-derived extracellular matrix, growth factors, and stem cells: a concise review, Tissue engineering and regenerative medicine 16 (2019) 385-393.
[238] G. Hausman, R. Richardson, Adipose tissue angiogenesis, Journal of animal science 82(3) (2004) 925-934.
[239] Q.X. Zhang, C.J. Magovern, C.A. Mack, K.T. Budenbender, W. Ko, T.K. Rosengart, Vascular endothelial growth factor is the major angiogenic factor in omentum: mechanism of the omentum-mediated angiogenesis, Journal of surgical research 67(2) (1997) 147-154.
[240] V. Di Nicola, Omentum a powerful biological source in regenerative surgery, Regenerative therapy 11 (2019) 182-191.
[241] T. Szkudelski, The mechanism of alloxan and streptozotocin action in B cells of the rat pancreas, Physiological research 50(6) (2001) 537-546.
[242] J. Y. Won, M.-H. Lee, M.-J. Kim, K.-H. Min, G. Ahn, J.-S. Han, S. Jin, W.-S. Yun, J.-H. Shim, A potential dermal substitute using decellularized dermis extracellular matrix derived bio-ink, Artificial cells, nanomedicine, and biotechnology 47(1) (2019) 644-649.
[243] D.M. Hoganson, E.M. O'Doherty, G.E. Owens, D.O. Harilal, S.M. Goldman, C.M. Bowley, C.M. Neville, R.T. Kronengold, J.P. Vacanti, The retention of extracellular matrix proteins and angiogenic and mitogenic cytokines in a decellularized porcine dermis, Biomaterials 31(26) (2010) 6730-6737.

[244] A.K. Leonard, E.A. Loughran, Y. Klymenko, Y. Liu, O. Kim, M. Asem, K. McAbee, M.J. Ravosa, M.S. Stack, Methods for the visualization and analysis of extracellular matrix protein structure and degradation, Methods in cell biology, Elsevier2018, pp. 79-95.
[245] N. Raina, R. Rani, M. Gupta, Angiogenesis: Aspects in wound healing, endothelial signaling in vascular dysfunction and disease, Elsevier2021, pp. 77-90.
[246] J. Herold, J. Kalucka, Angiogenesis in adipose tissue: the interplay between adipose and endothelial cells, Frontiers in physiology 11 (2021) 624903.
[247] K. Kim, Z. Siddiqui, A.M. Acevedo-Jake, A. Roy, M. Choudhury, J. Grasman, V. Kumar, Angiogenic hydrogels to accelerate early wound healing, Macromolecular bioscience 22(7) (2022) 2200067.
[248] S.A. Eming, T.A. Wynn, P. Martin, Inflammation and metabolism in tissue repair and regeneration, Science 356(6342) (2017) 1026-1030.
[249] A.E. Boniakowski, A.S. Kimball, B.N. Jacobs, S.L. Kunkel, K.A. Gallagher, Macrophage-mediated inflammation in normal and diabetic wound healing, The Journal of immunology 199(1) (2017) 17-24.
[250] A.T. Rowley, R.R. Nagalla, S.W. Wang, W.F. Liu, Extracellular matrix-based strategies for immunomodulatory biomaterials engineering, Advanced healthcare materials 8(8) (2019) 1801578.
[251] W. Xiao, Y. Yang, C. Chu, S.-A. Rung, Z. Wang, Y. Man, J. Lin, Y. Qu, Macrophage response mediated by extracellular matrix: Recent progress, Biomedical materials (2022).
[252] F. Pati, J. Jang, D.-H. Ha, S. Won Kim, J.-W. Rhie, J.-H. Shim, D.-H. Kim, D.-W. Cho, Printing three-dimensional tissue analogues with decellularized extracellular matrix bioink, Nature communications 5(1) (2014) 3935.
[253] W. Pu, Y. Han, M. Yang, Human decellularized adipose tissue hydrogels as a culture platform for human adipose-derived stem cell delivery, Journal of applied biomaterials & functional materials 19 (2021) 2280800020988141.
[254] S. Chae, S.-S. Lee, Y.-J. Choi, G. Gao, J.H. Wang, D.-W. Cho, 3D cell-printing of biocompatible and functional meniscus constructs using meniscus-derived bioink, Biomaterials 267 (2021) 120466.
[255] Y. Zhu, D. Wang, X. Yao, M. Wang, Y. Zhao, Y. Lu, Z. Wang, Y. Guo, Biomimetic hybrid scaffold of electrospun silk fibroin and pancreatic decellularized extracellular matrix for islet survival, Journal of Biomaterials Science, Polymer Edition 32(2) (2021) 151-165.
[256] N. Alevra Sarika, V.L. Payen, M. Fléron, J. Ravau, D. Brusa, M. Najimi, E. De Pauw, G. Eppe, G. Mazzucchelli, E.M. Sokal, Human liver-derived extracellular matrix for the culture of distinct human primary liver cells, Cells 9(6) (2020) 1357.
[257] T. Zhang, J.H. Day, X. Su, A.G. Guadarrama, N.K. Sandbo, S. Esnault, L.C. Denlinger, E. Berthier, A.B. Theberge, Investigating fibroblast-induced collagen gel contraction using a dynamic microscale platform, Frontiers in bioengineering and biotechnology 7 (2019) 196.
[258] F. Pallaske, A. Pallaske, K. Herklotz, J. Boese-Landgraf, The significance of collagen dressings in wound management: a review, Journal of wound care 27(10) (2018) 692-702.
[259] C.K. Sen, G.M. Gordillo, S. Roy, R. Kirsner, L. Lambert, T.K. Hunt, F. Gottrup, G.C. Gurtner, M.T. Longaker, Human skin wounds: a major and snowballing threat to public health and the economy, Wound repair and regeneration 17(6) (2009) 763-771.
[260] M. Olsson, K. Järbrink, U. Divakar, R. Bajpai, Z. Upton, A. Schmidtchen, J. Car, The humanistic and economic burden of chronic wounds: A systematic review, Wound repair and regeneration 27(1) (2019) 114-125.
[261] C. Sasanka, Venous ulcers of the lower limb: where do we stand?, Indian Journal of Plastic Surgery 45(2) (2012) 266.
[262] C.K. Sen, Human wounds and its burden: an updated compendium of estimates, Advances in Wound Care 8(2) (2019) 39-48.

[263] Y. Niu, Q. Li, Y. Ding, L. Dong, C. Wang, Engineered delivery strategies for enhanced control of growth factor activities in wound healing, Advanced drug delivery reviews 146 (2019) 190-208.
[264] T. Bhojani-Lynch, Late-onset inflammatory response to hyaluronic acid dermal fillers, Plastic and Reconstructive Surgery–Global Open 5(12) (2017) e1532.
[265] J. Alijotas-Reig, M.T. Fernández-Figueras, L. Puig, Inflammatory, immune-mediated adverse reactions related to soft tissue dermal fillers, Seminars in arthritis and rheumatism, Elsevier, 2013, pp. 241-258.
[266] N.E. Thomford, D.A. Senthebane, A. Rowe, D. Munro, P. Seele, A. Maroyi, K. Dzobo, Natural products for drug discovery in the 21st century: innovations for novel drug discovery, International journal of molecular sciences 19(6) (2018) 1578.
[267] F.-S. Li, J.-K. Weng, Demystifying traditional herbal medicine with modern approach, Nature plants 3(8) (2017) 1-7.
[268] M. Leonti, R. Verpoorte, Traditional Mediterranean and European herbal medicines, Journal of ethnopharmacology 199 (2017) 161-167.
[269] M. Shi, H. Zhang, T. Song, X. Liu, Y. Gao, J. Zhou, Y. Li, Sustainable dual release of antibiotic and growth factor from pH-responsive uniform alginate composite microparticles to enhance wound healing, ACS applied materials & interfaces 11(25) (2019) 22730-22744.
[270] M. Qu, X. Jiang, X. Zhou, C. Wang, Q. Wu, L. Ren, J. Zhu, S. Zhu, P. Tebon, W. Sun, Stimuli-responsive delivery of growth factors for tissue engineering, Advanced healthcare materials 9(7) (2020) 1901714.
[271] J. Zarubova, M.M. Hasani-Sadrabadi, L. Bacakova, S. Li, Nano-in-micro dual delivery platform for chronic wound healing applications, Micromachines 11(2) (2020) 158.
[272] J.L. Drury, D.J. Mooney, Hydrogels for tissue engineering: scaffold design variables and applications, Biomaterials 24(24) (2003) 4337-4351.
[273] A. Francesko, P. Petkova, T. Tzanov, Hydrogel dressings for advanced wound management, Current medicinal chemistry 25(41) (2018) 5782-5797.
[274] A. Balaji, M.V. Vellayappan, A.A. John, A.P. Subramanian, S.K. Jaganathan, M. SelvaKumar, A.A. bin Mohd Faudzi, E. Supriyanto, M. Yusof, Biomaterials based nano-applications of Aloe vera and its perspective: a review, RSC advances 5(105) (2015) 86199-86213.
[275] M.H. Radha, N.P. Laxmipriya, Evaluation of biological properties and clinical effectiveness of Aloeávera: áAásystematic review, Journal of traditional and complementary medicine 5(1) (2015) 21-26.
[276] R. Kumar, A.K. Singh, A. Gupta, A. Bishayee, A.K. Pandey, Therapeutic potential of Aloe vera—A miracle gift of nature, Phytomedicine 60 (2019) 152996.
[277] T.J. McKee, G. Perlman, M. Morris, S.V. Komarova, Extracellular matrix composition of connective tissues: a systematic review and meta-analysis, Scientific reports 9(1) (2019) 10542.
[278] A.R. Eberendu, G. Luta, J.A. Edwards, B.H. Mcanalley, B. Davis, S. Rodriguez, C. Ray Henry, Quantitative colorimetric analysis of aloe polysaccharides as a measure of Aloe vera quality in commercial products, Journal of AOAC international 88(3) (2005) 684-691.
[279] S. Murthy, M. Gautam, S. Goel, V. Purohit, H. Sharma, R. Goel, Evaluation of in vivo wound healing activity of Bacopa monniera on different wound model in rats, BioMed research international 2013(1) (2013) 972028.
[280] M.P. Quezada, C. Salinas, M. Gotteland, L. Cardemil, Acemannan and fructans from Aloe vera (Aloe barbadensis Miller) plants as novel prebiotics, Journal of agricultural and food chemistry 65(46) (2017) 10029-10039.

[281] J.C. Moses, S.K. Nandi, B.B. Mandal, Multifunctional cell instructive silk-bioactive glass composite reinforced scaffolds toward osteoinductive, proangiogenic, and resorbable bone grafts, Advanced healthcare materials 7(10) (2018) 1701418.
[282] J. Wu, Y. Hong, Enhancing cell infiltration of electrospun fibrous scaffolds in tissue regeneration, Bioactive materials 1(1) (2016) 56-64.
[283] G. Eke, N. Mangir, N. Hasirci, S. MacNeil, V. Hasirci, Development of a UV crosslinked biodegradable hydrogel containing adipose derived stem cells to promote vascularization for skin wounds and tissue engineering, Biomaterials 129 (2017) 188-198.
[284] I. Pastar, O. Stojadinovic, N.C. Yin, H. Ramirez, A.G. Nusbaum, A. Sawaya, S.B. Patel, L. Khalid, R.R. Isseroff, M. Tomic-Canic, Epithelialization in wound healing: a comprehensive review, Advances in wound care 3(7) (2014) 445-464.
[285] M. Xue, C.J. Jackson, Extracellular matrix reorganization during wound healing and its impact on abnormal scarring, Advances in wound care 4(3) (2015) 119-136.
[286] V.R. Krishnaswamy, D. Mintz, I. Sagi, Matrix metalloproteinases: the sculptors of chronic cutaneous wounds, Biochimica et Biophysica Acta (BBA)-Molecular Cell Research 1864(11) (2017) 2220-2227.
[287] A. Page-McCaw, A.J. Ewald, Z. Werb, Matrix metalloproteinases and the regulation of tissue remodelling, Nature reviews Molecular cell biology 8(3) (2007) 221-233.
[288] S.Y. Kim, M.G. Nair, Macrophages in wound healing: activation and plasticity, Immunology and cell biology 97(3) (2019) 258-267.
[289] H. Sorg, D.J. Tilkorn, S. Hager, J. Hauser, U. Mirastschijski, Skin wound healing: an update on the current knowledge and concepts, European surgical research 58(1-2) (2017) 81-94.
[290] K.E. Martin, A.J. García, Macrophage phenotypes in tissue repair and the foreign body response: Implications for biomaterial-based regenerative medicine strategies, Acta biomaterialia 133 (2021) 4-16.
[291] B.Z. Johnson, A.W. Stevenson, C.M. Prêle, M.W. Fear, F.M. Wood, The role of IL-6 in skin fibrosis and cutaneous wound healing, Biomedicines 8(5) (2020) 101.
[292] S. Löffek, O. Schilling, C.-W. Franzke, Biological role of matrix metalloproteinases: a critical balance, European respiratory journal 38(1) (2011) 191-208.
[293] M. Dyson, S.R. Young, J. Hart, J.A. Lynch, S. Lang, Comparison of the effects of moist and dry conditions on the process of angiogenesis during dermal repair, Journal of investigative dermatology 99(6) (1992) 729-733.
[294] D.K. Kim, B.R. Sim, G. Khang, Nature-derived aloe vera gel blended silk fibroin film scaffolds for cornea endothelial cell regeneration and transplantation, ACS applied materials & interfaces 8(24) (2016) 15160-15168.
[295] P. Inpanya, A. Faikrua, A. Ounaroon, A. Sittichokechaiwut, J. Viyoch, Effects of the blended fibroin/aloe gel film on wound healing in streptozotocin-induced diabetic rats, Biomedical Materials 7(3) (2012) 035008.
[296] O. Hoffstad, N. Mitra, J. Walsh, D.J. Margolis, Diabetes, lower-extremity amputation, and death, Diabetes care 38(10) (2015) 1852-1857.
[297] K. McDermott, M. Fang, A.J. Boulton, E. Selvin, C.W. Hicks, Etiology, epidemiology, and disparities in the burden of diabetic foot ulcers, Diabetes care 46(1) (2023) 209-221.
[298] E.H. Du Bois-Reymond, Vorläufiger Abriss einer Untersuchung über den sogenannten Froschstrom und über die elektromotorischen Fische, 1843.
[299] C.M. Illingworth, A. Barker, Measurement of electrical currents emerging during the regeneration of amputated finger tips in children, Clinical physics and physiological measurement 1(1) (1980) 87.
[300] R. Nuccitelli, A role for endogenous electric fields in wound healing, Current topics in developmental biology 58(2) (2003) 1-26.

[301] J. Banerjee, P.D. Ghatak, S. Roy, S. Khanna, C. Hemann, B. Deng, A. Das, J.L. Zweier, D. Wozniak, C.K. Sen, Silver-zinc redox-coupled electroceutical wound dressing disrupts bacterial biofilm, PloS one 10(3) (2015) e0119531.
[302] K.Y. Nishimura, R.R. Isseroff, R. Nuccitelli, Human keratinocytes migrate to the negative pole in direct current electric fields comparable to those measured in mammalian wounds, Journal of cell science 109(1) (1996) 199-207.
[303] S. Hampton, F. Collins, Treating a pressure ulcer with bio-electric stimulation therapy, British journal of nursing 15(Sup1) (2006) S14-S18.
[304] S.E. Gardner, R.A. Frantz, F.L. Schmidt, Effect of electrical stimulation on chronic wound healing: a meta-analysis, Wound repair and regeneration 7(6) (1999) 495-503.
[305] R. Luo, J. Dai, J. Zhang, Z. Li, Accelerated skin wound healing by electrical stimulation, Advanced healthcare materials 10(16) (2021) 2100557.
[306] M. Verdes, K. Mace, L. Margetts, S. Cartmell, Status and challenges of electrical stimulation use in chronic wound healing, Current opinion in biotechnology 75 (2022) 102710.
[307] F.C. Kao, H.-H. Ho, P.-Y. Chiu, M.K. Hsieh, J.C. Liao, P.-L. Lai, Y.-F. Huang, M.-Y. Dong, T.T. Tsai, Z.-H. Lin, Self-assisted wound healing using piezoelectric and triboelectric nanogenerators, Science and technology of advanced materials 23(1) (2022) 1-16.
[308] Y. Long, J. Li, F. Yang, J. Wang, X. Wang, Wearable and implantable electroceuticals for therapeutic electrostimulations, Advanced science 8(8) (2021) 2004023.
[309] S. Hirlekar, D. Ray, V.K. Aswal, A. Prabhune, A. Nisal, S. Ravindranathan, Silk Fibroin–sodium dodecyl sulfate gelation: molecular, structural, and rheological insights, Langmuir 35(46) (2019) 14870-14878.
[310] M. Kurakula, G.K. Rao, Pharmaceutical assessment of polyvinylpyrrolidone (PVP): As excipient from conventional to controlled delivery systems with a spotlight on COVID-19 inhibition, Journal of drug delivery science and technology 60 (2020) 102046.
[311] P. Van Dong, C.H. Ha, L.T. Binh, J. Kasbohm, Chemical synthesis and antibacterial activity of novel-shaped silver nanoparticles, International nano letters 2(1) (2012) 1-9.
[312] V. Platania, A. Kaldeli-Kerou, T. Karamanidou, M. Kouki, A. Tsouknidas, M. Chatzinikolaidou, Antibacterial effect of colloidal suspensions varying in silver nanoparticles and ions concentrations, Nanomaterials 12(1) (2021) 31.
[313] L. Barnes, D.M. Heithoff, S.P. Mahan, J.K. House, M.J. Mahan, Antimicrobial susceptibility testing to evaluate minimum inhibitory concentration values of clinically relevant antibiotics, STAR protocols 4(3) (2023) 102512.
[314] A. Gangrade, B. Gawali, P.K. Jadi, V.G. Naidu, B.B. Mandal, Photo-electro active nanocomposite silk hydrogel for spatiotemporal controlled release of chemotherapeutics: an in vivo approach toward suppressing solid tumor growth, ACS applied materials & interfaces 12(25) (2020) 27905-27916.
[315] S. Morang, A. Bandyopadhyay, B.B. Mandal, N. Karak, Asymmetric hard domain-induced robust resilient biocompatible self-healable waterborne polyurethane for biomedical applications, ACS Applied Bio Materials 6(7) (2023) 2771-2784.
[316] M. Sadeghi, M. Rahimnejad, H. Adeli, F. Feizi, Matrix–drug interactions for the development of pH-sensitive alginate-based nanofibers as an advanced wound dressing, Journal of Polymers and the Environment 31(3) (2023) 1242-1256.
[317] V.J. Coulson-Thomas, T.F. Gesteira, Dimethylmethylene blue assay (DMMB), Bio-protocol 4(18) (2014) e1236-e1236.
[318] M.N. Kavaldzhiev, J.E. Perez, R. Sougrat, P. Bergam, T. Ravasi, J. Kosel, Inductively actuated micro needles for on-demand intracellular delivery, Scientific reports 8(1) (2018) 9918.

[319] S. Mostafavi, D. Ray, D. Warde-Farley, C. Grouios, Q. Morris, GeneMANIA: a real-time multiple association network integration algorithm for predicting gene function, Genome biology 9(Suppl 1) (2008) 1-15.
[320] D. Garibo, H.A. Borbón-Nuñez, J.N.D. de León, E. García Mendoza, I. Estrada, Y. Toledano-Magaña, H. Tiznado, M. Ovalle-Marroquin, A.G. Soto-Ramos, A. Blanco, Green synthesis of silver nanoparticles using Lysiloma acapulcensis exhibit high-antimicrobial activity, Scientific reports 10(1) (2020) 12805.
[321] K. Anandalakshmi, J. Venugobal, V. Ramasamy, Characterization of silver nanoparticles by green synthesis method using Pedalium murex leaf extract and their antibacterial activity, Applied nanoscience 6(3) (2016) 399-408.
[322] V. Holubnycha, Y. Husak, V. Korniienko, S. Bolshanina, O. Tveresovska, P. Myronov, M. Holubnycha, A. Butsyk, T. Borén, R. Banasiuk, Antimicrobial activity of two different types of silver nanoparticles against wide range of pathogenic bacteria, Nanomaterials 14(2) (2024) 137.
[323] S. Indrakumar, T.K. Dash, V. Mishra, B. Tandon, K. Chatterjee, Silk fibroin and its nanocomposites for wound care: a comprehensive review, ACS Polymers Au 4(3) (2024) 168-188.
[324] S. Dey, A. Bhat, G. Janani, V. Shandilya, R. Gupta, B.B. Mandal, Microfluidic human physiomimetic liver model as a screening platform for drug induced liver injury, Biomaterials 310 (2024) 122627.
[325] B. Bhar, P. Ranta, P.K. Samudrala, B.B. Mandal, Omentum extracellular matrix-silk fibroin hydroscaffold promotes wound healing through vascularization and tissue remodeling in the diabetic rat model, ACS Biomaterials science & engineering 10(2) (2024) 1090–1105.
[326] I.P. Moreira, C. Esteves, S.I. Palma, E. Ramou, A.L. Carvalho, A.C. Roque, Synergy between silk fibroin and ionic liquids for active gas-sensing materials, Materials today bio 15 (2022) 100290.
[327] X. Wu, J. Hou, M. Li, J. Wang, D.L. Kaplan, S. Lu, Sodium dodecyl sulfate-induced rapid gelation of silk fibroin, Acta biomaterialia 8(6) (2012) 2185-2192.
[328] B. Bhar, B. Chakraborty, S.K. Nandi, B.B. Mandal, Silk-based phyto-hydrogel formulation expedites key events of wound healing in full-thickness skin defect model, International journal of biological macromolecules 203 (2022) 623-637.
[329] S. DeLeon, A. Clinton, H. Fowler, J. Everett, A.R. Horswill, K.P. Rumbaugh, Synergistic interactions of Pseudomonas aeruginosa and Staphylococcus aureus in an in vitro wound model, Infection and immunity 82(11) (2014) 4718-4728.
[330] M. Garousi, S. MonazamiTabar, H. Mirazi, Z. Farrokhi, A. Khaledi, A. Shakerimoghaddam, Epidemiology of Pseudomonas aeruginosa in diabetic foot infections: a global systematic review and meta-analysis, Germs 13(4) (2023) 362.
[331] T.C. Goh, M.Y. Bajuri, S. C. Nadarajah, A.H. Abdul Rashid, S. Baharuddin, K.S. Zamri, Clinical and bacteriological profile of diabetic foot infections in a tertiary care, Journal of foot and ankle research 13 (2020) 1-8.
[332] M.T. Khorasani, A. Joorabloo, A. Moghaddam, H. Shamsi, Z. MansooriMoghadam, Incorporation of ZnO nanoparticles into heparinised polyvinyl alcohol/chitosan hydrogels for wound dressing application, International journal of biological macromolecules 114 (2018) 1203-1215.
[333] M.S. Sakar, J. Eyckmans, R. Pieters, D. Eberli, B.J. Nelson, C.S. Chen, Cellular forces and matrix assembly coordinate fibrous tissue repair, Nature communications 7(1) (2016) 11036.
[334] B. Sun, The mechanics of fibrillar collagen extracellular matrix, Cell reports physical science 2(8) (2021).

[335] A.P. Veith, K. Henderson, A. Spencer, A.D. Sligar, A.B. Baker, Therapeutic strategies for enhancing angiogenesis in wound healing, Advanced drug delivery reviews 146 (2019) 97-125.
[336] Y.-t. Wang, X.-t. Meng, A review of the evidence to support electrical stimulation-induced vascularization in engineered tissue, Regenerative therapy 24 (2023) 237-244.
[337] S. Ud-Din, A. Sebastian, P. Giddings, J. Colthurst, S. Whiteside, J. Morris, R. Nuccitelli, C. Pullar, M. Baguneid, A. Bayat, Angiogenesis is induced and wound size is reduced by electrical stimulation in an acute wound healing model in human skin, PloS one 10(4) (2015) e0124502.
[338] A. Sebastian, S.A. Iqbal, J. Colthurst, S.W. Volk, A. Bayat, Electrical stimulation enhances epidermal proliferation in human cutaneous wounds by modulating p53–SIVA1 interaction, Journal of investigative dermatology 135(4) (2015) 1166-1174.
[339] K. Katoh, Effects of electrical stimulation of the cell: wound healing, cell proliferation, apoptosis, and signal transduction, Medical sciences 11(1) (2023) 11.
[340] H.F. Tsai, J.Y. Cheng, H.F. Chang, T. Yamamoto, A.Q. Shen, Uniform electric field generation in circular multi-well culture plates using polymeric inserts, Scientific reports 6(1) (2016) 26222.
[341] Y. Wang, M. Rouabhia, Z. Zhang, Pulsed electrical stimulation benefits wound healing by activating skin fibroblasts through the TGFβ1/ERK/NF-κB axis, Biochimica et Biophysica Acta (BBA)-General Subjects 1860(7) (2016) 1551-1559.
[342] B. Kuehlmann, C.A. Bonham, I. Zucal, L. Prantl, G.C. Gurtner, Mechanotransduction in wound healing and fibrosis, Journal of clinical medicine 9(5) (2020) 1423.
[343] T.H. Barker, G. Baneyx, M. Cardó-Vila, G.A. Workman, M. Weaver, P.M. Menon, S. Dedhar, S.A. Rempel, W. Arap, R. Pasqualini, SPARC regulates extracellular matrix organization through its modulation of integrin-linked kinase activity, Journal of biological chemistry 280(43) (2005) 36483-36493.
[344] P. Rousselle, M. Montmasson, C. Garnier, Extracellular matrix contribution to skin wound re-epithelialization, Matrix biology 75 (2019) 12-26.
[345] M. Farahani, A. Shafiee, Wound healing: from passive to smart dressings, Advanced healthcare materials 10(16) (2021) 2100477.
[346] A. Nurkesh, A. Jaguparov, S. Jimi, A. Saparov, Recent advances in the controlled release of growth factors and cytokines for improving cutaneous wound healing, Frontiers in cell and developmental biology 8 (2020) 638.
[347] P. Kolimi, S. Narala, D. Nyavanandi, A.A.A. Youssef, N. Dudhipala, Innovative treatment strategies to accelerate wound healing: trajectory and recent advancements, Cells 11(15) (2022) 2439.
[348] G.S.R. 175(E) dt_09.03.2023_ Amendment to the New Drugs and Clinical Trials Rules, 2019, in: D.o.H.a.F. Welfare (Ed.) The Gazette of India, India, 2023.
[349] A. Kovács, S. Zsikó, F. Falusi, E. Csányi, M. Budai-Szűcs, I. Csóka, S. Berkó, Comparison of synthetic membranes to heat-separated human epidermis in skin permeation studies in vitro, Pharmaceutics 13(12) (2021) 2106.
[350] M. Cui, C. Wiraja, M. Zheng, G. Singh, K.T. Yong, C. Xu, Recent Progress in Skin-on-a-Chip Platforms, Advanced therapeutics 5(1) (2022) 2100138.
[351] H.-G. Machens, A. Berger, P. Mailaender, Bioartificial skin, Cells tissues organs 167(2-3) (2000) 88-94.
[352] Tissue Engineered Skin Substitutes - Global Strategic Business Report, 2023, p. 89.
[353] M. Li, L. Sun, Z. Liu, Z. Shen, Y. Cao, L. Han, S. Sang, J. Wang, 3D bioprinting of heterogeneous tissue-engineered skin containing human dermal fibroblasts and keratinocytes, Biomaterials science 11(7) (2023) 2461-2477.

[354] H.W. Kang, S.J. Lee, I.K. Ko, C. Kengla, J.J. Yoo, A. Atala, A 3D bioprinting system to produce human-scale tissue constructs with structural integrity, Nature biotechnology 34(3) (2016) 312-319.
[355] A. Pupovac, B. Senturk, C. Griffoni, K. Maniura-Weber, M. Rottmar, S.L. McArthur, Toward immunocompetent 3D skin models, Advanced healthcare materials 7(12) (2018) 1701405.
[356] L.J. Van den Broek, L.I. Bergers, C.M. Reijnders, S. Gibbs, Progress and future prospectives in skin-on-chip development with emphasis on the use of different cell types and technical challenges, Stem cell reviews and reports 13 (2017) 418-429.
[357] S. Dey, C. Jaiswal, S. Shome, B. Bhar, A. Bandyopadhyay, K. Manikumar, R. Dadheech, B.B. Mandal, Photocrosslinkable silk-based biomaterials for regenerative medicine and healthcare applications, Regenerative engineering and translational medicine (2022) 1-21.
[358] D. Loessner, C. Meinert, E. Kaemmerer, L.C. Martine, K. Yue, P.A. Levett, T.J. Klein, F.P. Melchels, A. Khademhosseini, D.W. Hutmacher, Functionalization, preparation and use of cell-laden gelatin methacryloyl–based hydrogels as modular tissue culture platforms, Nature protocols 11(4) (2016) 727-746.
[359] G. Irmak, T.T. Demirtaş, M. Gümüşderelioğlu, Sustained release of growth factors from photoactivated platelet rich plasma (PRP), European Journal of pharmaceutics and biopharmaceutics 148 (2020) 67-76.
[360] S.H. Kim, Y.K. Yeon, J.M. Lee, J.R. Chao, Y.J. Lee, Y.B. Seo, M.T. Sultan, O.J. Lee, J.S. Lee, S. Yoon, I. Hong, C. H. Park, Precisely printable and biocompatible silk fibroin bioink for digital light processing 3D printing, Nature communications 9(1) (2018) 1620.
[361] A. Bandyopadhyay, B.B. Mandal, N. Bhardwaj, 3D bioprinting of photo-crosslinkable silk methacrylate (SilMA)-polyethylene glycol diacrylate (PEGDA) bioink for cartilage tissue engineering, Journal of biomedical materials research Part A 110(4) (2022) 884-898.
[362] G. Irmak, M. Gümüşderelioğlu, Photo-activated platelet-rich plasma (PRP)-based patient-specific bio-ink for cartilage tissue engineering, Biomedical materials 15(6) (2020) 065010.
[363] I.M. Dijkhoff, B. Petracca, R. Prieux, G. Valacchi, B. Rothen-Rutishauser, M. Eeman, Cultivating a three-dimensional reconstructed human epidermis at a large scale, JoVE (Journal of visualized experiments) (171) (2021) e61802.
[364] P. Chomczynski, N. Sacchi, The single-step method of RNA isolation by acid guanidinium thiocyanate–phenol–chloroform extraction: twenty-something years on, Nature protocols 1(2) (2006) 581-585.
[365] N. Alépée, C. Robert, C. Tornier, J. Cotovio, The usefulness of the validated SkinEthic™ RHE test method to identify skin corrosive UN GHS subcategories, Toxicology in vitro 28(4) (2014) 616-625.
[366] N. Alépée, M.H. Grandidier, C. Tornier, J. Cotovio, An integrated testing strategy for in vitro skin corrosion and irritation assessment using SkinEthic™ Reconstructed Human Epidermis, Toxicology in vitro 29(7) (2015) 1779-1792.
[367] F. Groeber, L. Schober, F.F. Schmid, A. Traube, S. Kolbus-Hernandez, K. Daton, S. Hoffmann, D. Petersohn, M. Schaefer-Korting, H. Walles, Catch-up validation study of an in vitro skin irritation test method based on an open source reconstructed epidermis (phase II), Toxicology in vitro 36 (2016) 254-261.
[368] F.F. Schmidt, S. Nowakowski, P.J. Kluger, Improvement of a three-layered in vitro skin model for topical application of irritating substances, Frontiers in bioengineering and biotechnology 8 (2020) 388.
[369] A. Schwab, R. Levato, M. D'Este, S. Piluso, D. Eglin, J. Malda, Printability and shape fidelity of bioinks in 3D bioprinting, Chemical reviews 120(19) (2020) 11028-11055.

[370] S. Mourtas, M. Haikou, M. Theodoropoulou, C. Tsakiroglou, S.G. Antimisiaris, The effect of added liposomes on the rheological properties of a hydrogel: A systematic study, Journal of colloid and interface science 317(2) (2008) 611-619.
[371] C.N. Bowman, C.J. Kloxin, Toward an enhanced understanding and implementation of photopolymerization reactions, AIChE journal 54(11) (2008) 2775-2795.
[372] C.M. Tringides, D.J. Mooney, Materials for implantable surface electrode arrays: current status and future directions, Advanced materials 34(20) (2022) 2107207.
[373] T. Yeung, P.C. Georges, L.A. Flanagan, B. Marg, M. Ortiz, M. Funaki, N. Zahir, W. Ming, V. Weaver, P.A. Janmey, Effects of substrate stiffness on cell morphology, cytoskeletal structure, and adhesion, Cell motility and the cytoskeleton 60(1) (2005) 24-34.
[374] J. Solon, I. Levental, K. Sengupta, P.C. Georges, P.A. Janmey, Fibroblast adaptation and stiffness matching to soft elastic substrates, Biophysical journal 93(12) (2007) 4453-4461.
[375] M. Caceres, R. Hidalgo, A. Sanz, J. Martínez, P. Riera, P.C. Smith, Effect of platelet-rich plasma on cell adhesion, cell migration, and myofibroblastic differentiation in human gingival fibroblasts, Journal of periodontology 79(4) (2008) 714-720.
[376] T. Hara, N. Kakudo, N. Morimoto, T. Ogawa, F. Lai, K. Kusumoto, Platelet-rich plasma stimulates human dermal fibroblast proliferation via a Ras-dependent extracellular signal-regulated kinase 1/2 pathway, Journal of artificial organs 19 (2016) 372-377.
[377] E.B. Cho, G.S. Park, S.S. Park, Y.J. Jang, K.H. Kim, K.J. Kim, E.J. Park, Effect of platelet-rich plasma on proliferation and migration in human dermal fibroblasts, Journal of cosmetic dermatology 18(4) (2019) 1105-1112.
[378] B. Trappmann, J.E. Gautrot, J.T. Connelly, D.G. Strange, Y. Li, M.L. Oyen, M.A. Cohen Stuart, H. Boehm, B. Li, V. Vogel, Extracellular-matrix tethering regulates stem-cell fate, Nature materials 11(7) (2012) 642-649.
[379] H. Zarkoob, S. Bodduluri, S.V. Ponnaluri, J.C. Selby, E.A. Sander, Substrate stiffness affects human keratinocyte colony formation, Cellular and molecular bioengineering 8 (2015) 32-50.
[380] J. Zhao, S. Jia, P. Xie, E. Friedrich, R.D. Galiano, S. Qi, R. Mao, T.A. Mustoe, S.J. Hong, Knockdown of sodium channel Nax reduces dermatitis symptoms in rabbit skin, Laboratory investigation 100(5) (2020) 751-761.
[381] J.W. Shin, S.H. Kwon, J.-Y. Choi, J.-I. Na, C.-H. Huh, H.-R. Choi, K.-C. Park, Molecular mechanisms of dermal aging and antiaging approaches, International journal of molecular sciences 20(9) (2019) 2126.
[382] D. Pezzoli, J. Di Paolo, H. Kumra, G. Fois, G. Candiani, D.P. Reinhardt, D. Mantovani, Fibronectin promotes elastin deposition, elasticity and mechanical strength in cellularised collagen-based scaffolds, Biomaterials 180 (2018) 130-142.
[383] S. Jiang, H. F. Sun, S. Li, N. Zhang, J. S. Chen, J. X. Liu, SPARC: a potential target for functional nanomaterials and drugs, Frontiers in Molecular Biosciences 10 (2023).
[384] G. Liu, A.M. Philp, T. Corte, M.A. Travis, H. Schilter, N.G. Hansbro, C.J. Burns, M.S. Eapen, S.S. Sohal, J.K. Burgess, Therapeutic targets in lung tissue remodelling and fibrosis, Pharmacology & therapeutics 225 (2021) 107839.
[385] P. Jain, S.B. Rauer, M. Möller, S. Singh, Mimicking the natural basement membrane for advanced tissue engineering, Biomacromolecules 23(8) (2022) 3081-3103.
[386] C.H. Lee, P.A. Coulombe, Self-organization of keratin intermediate filaments into cross-linked networks, Journal of Cell Biology 186(3) (2009) 409-421.
[387] J.C. Lessard, S. Piña-Paz, J.D. Rotty, R.P. Hickerson, R.L. Kaspar, A. Balmain, P.A. Coulombe, Keratin 16 regulates innate immunity in response to epidermal barrier breach, Proceedings of the national academy of sciences 110(48) (2013) 19537-19542.

[388] S. Pastore, F. Mascia, V. Mariani, G. Girolomoni, The epidermal growth factor receptor system in skin repair and inflammation, Journal of investigative dermatology 128(6) (2008) 1365-1374.
[389] D.A. Chistiakov, M.C. Killingsworth, V.A. Myasoedova, A.N. Orekhov, Y.V. Bobryshev, CD68/macrosialin: not just a histochemical marker, Laboratory investigation 97(1) (2017) 4-13.
[390] N.R. Barros, H.J. Kim, M.J. Gouidie, K. Lee, P. Bandaru, E.A. Banton, E. Sarikhani, W. Sun, S. Zhang, H.-J. Cho, Biofabrication of endothelial cell, dermal fibroblast, and multilayered keratinocyte layers for skin tissue engineering, Biofabrication 13(3) (2021) 035030.
[391] M. Ahn, W.W. Cho, H. Lee, W. Park, S.H. Lee, J.W. Back, Q. Gao, G. Gao, D.W. Cho, B.S. Kim, Engineering of Uniform Epidermal Layers via Sacrificial Gelatin Bioink-Assisted 3D Extrusion Bioprinting of Skin, Advanced healthcare materials (2023) 2301015.
[392] S. Mehrotra, J.C. Moses, A. Bandyopadhyay, B.B. Mandal, 3D printing/bioprinting based tailoring of in vitro tissue models: Recent advances and challenges, ACS Applied bio materials 2(4) (2019) 1385-1405.
[393] S. Salameh, N. Tissot, K. Cache, J. Lima, I. Suzuki, P.A. Marinho, M. Rielland, J. Soeur, S. Takeuchi, S. Germain, A perfusable vascularized full-thickness skin model for potential topical and systemic applications, Biofabrication 13(3) (2021) 035042.
[394] S. Sun, L. Jin, Y. Zheng, J. Zhu, Modeling human HSV infection via a vascularized immune-competent skin-on-chip platform, Nature communications 13(1) (2022) 5481.

# *Appendix*

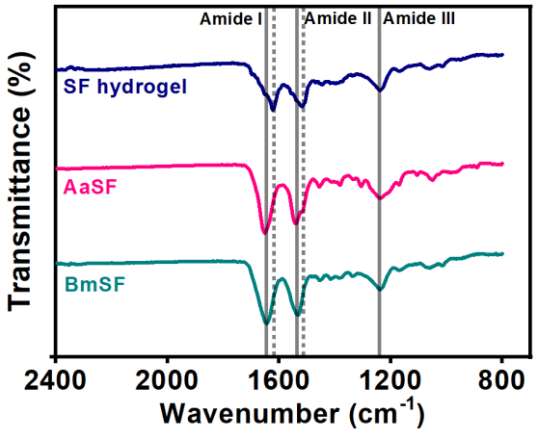


***Figure A2.1.*** *FTIR spectra of pristine SF solutions and blended SF hydrogel, showing shift in characteristic peaks of amide (I,II, and III) bands of SF proteins.*

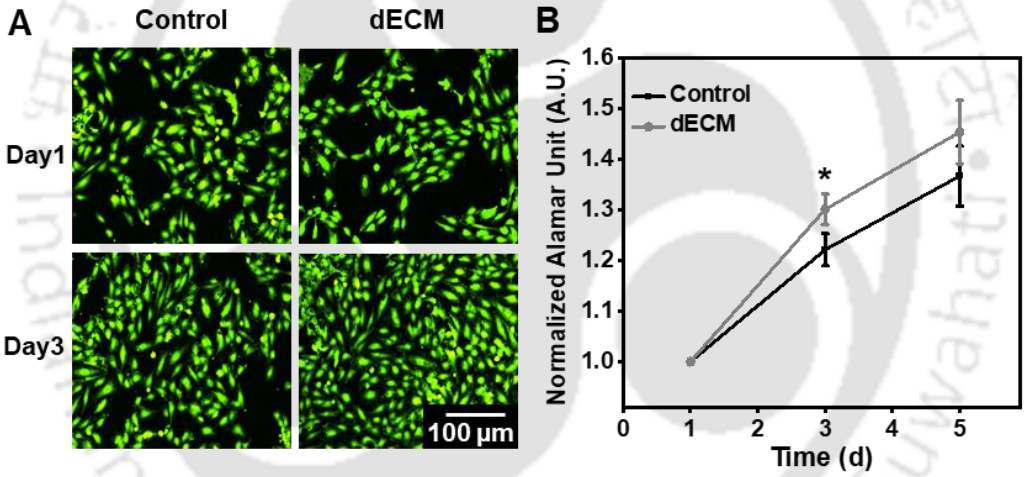


***Figure A2.2.*** *(A) Live/dead stained images of HUVEC in presence of dECM leachate. (B) Assessment of cellular proliferation of HUVEC treated with dECM leachate using Alamar Blue assay. Values are plotted as mean ± standard deviation, where * $p \leq 0.05$.*

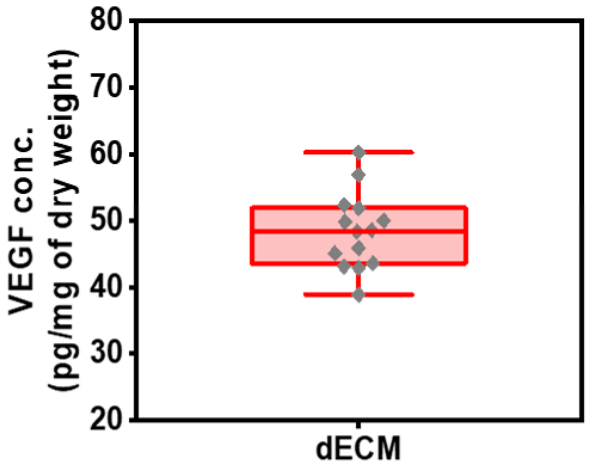


***Figure A2.3.*** *Quantification of VEGF present in dECM through ELISA.*

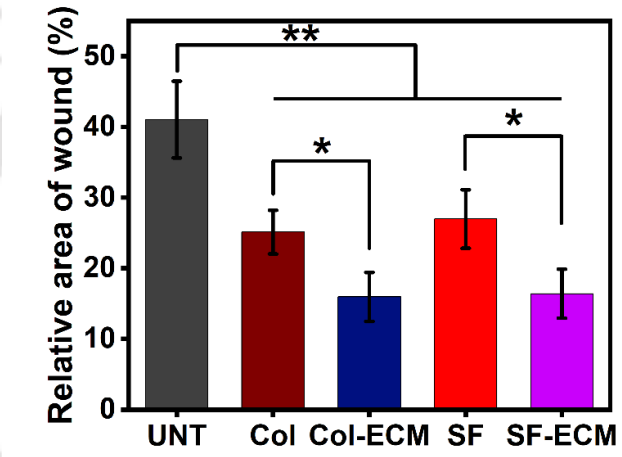


***Figure A2.4.*** *Quantification of percentages of wound area of the untreated control and experimental groups on day 14, determined using ImageJ software. Values are plotted as mean ± standard deviation, where * $p \leq 0.05$ and ** $p \leq 0.01$.*

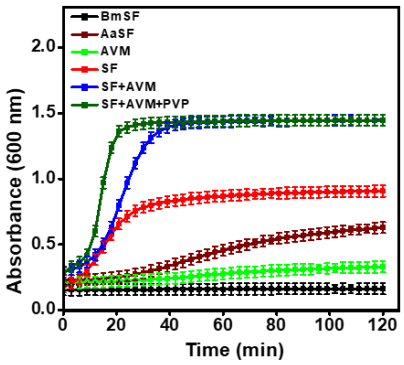


***Figure A3.1.*** *Gelation kinetics of the blended solutions and pristine solutions was assessed at 37 °C. The gelation of SAP (SF+AVM+PVP) was completed within 20 min.*

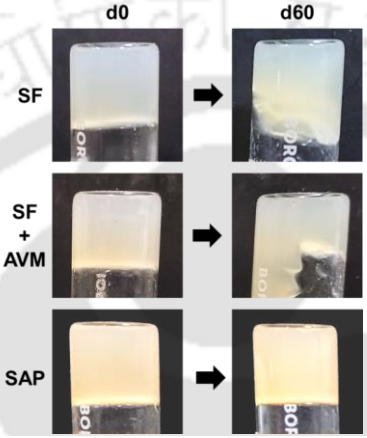


***Figure A3.2.*** *Assessment of long-term stability of hydrogels by tube inversion method. Fragmentation and liquefaction of SF and SF+AVM hydrogel were observed but SAP hydrogel was intact after day 60 (d60).*

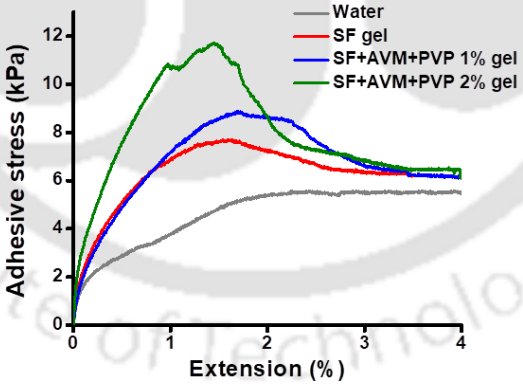


***Figure A3.3.*** *Adhesive stress curves of SF hydrogels with different concentrations of PVP on porcine skin and control group with only water between two skin explants. Presence of PVP has improved the mucoadhesive property of the hydrogel.*

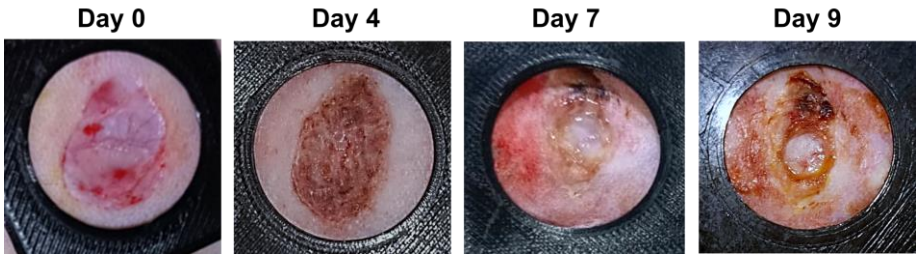


***Figure A4.1.*** *Photographic images depict wounds treated with the ES group using an amplitude of 1000 mV/mm, pulse width of 250 ms, and frequency of 2 Hz. The images demonstrate the skin irritation and damage caused by the higher intensity ES applied via the e-Bandage.*

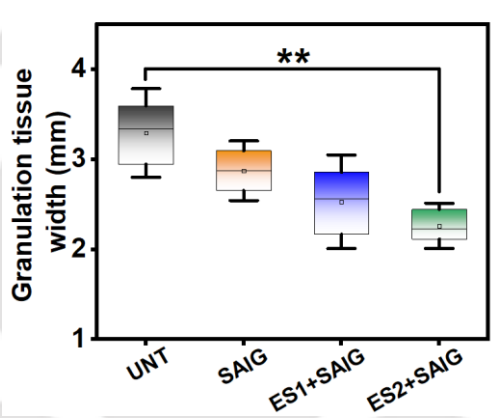


***Figure A4.2.*** *Quantitative analysis of regenerated granulation tissue widths. Values are plotted as mean ± standard deviation, where ** P < 0.01.*

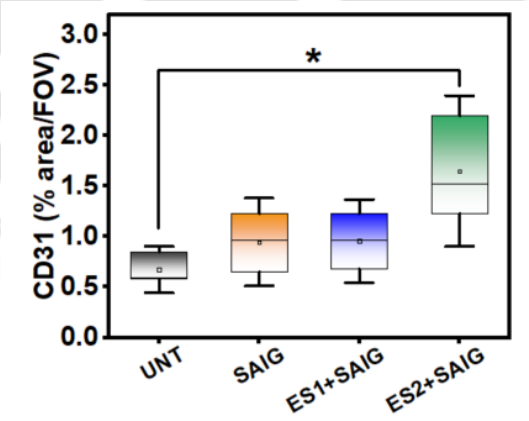


***Figure A4.3.*** *Quantification of percentage area of CD31 expression per field of view (FOV) processed from the fluorescent images. Values are plotted as mean ± standard deviation, where *p ≤ 0.05.*

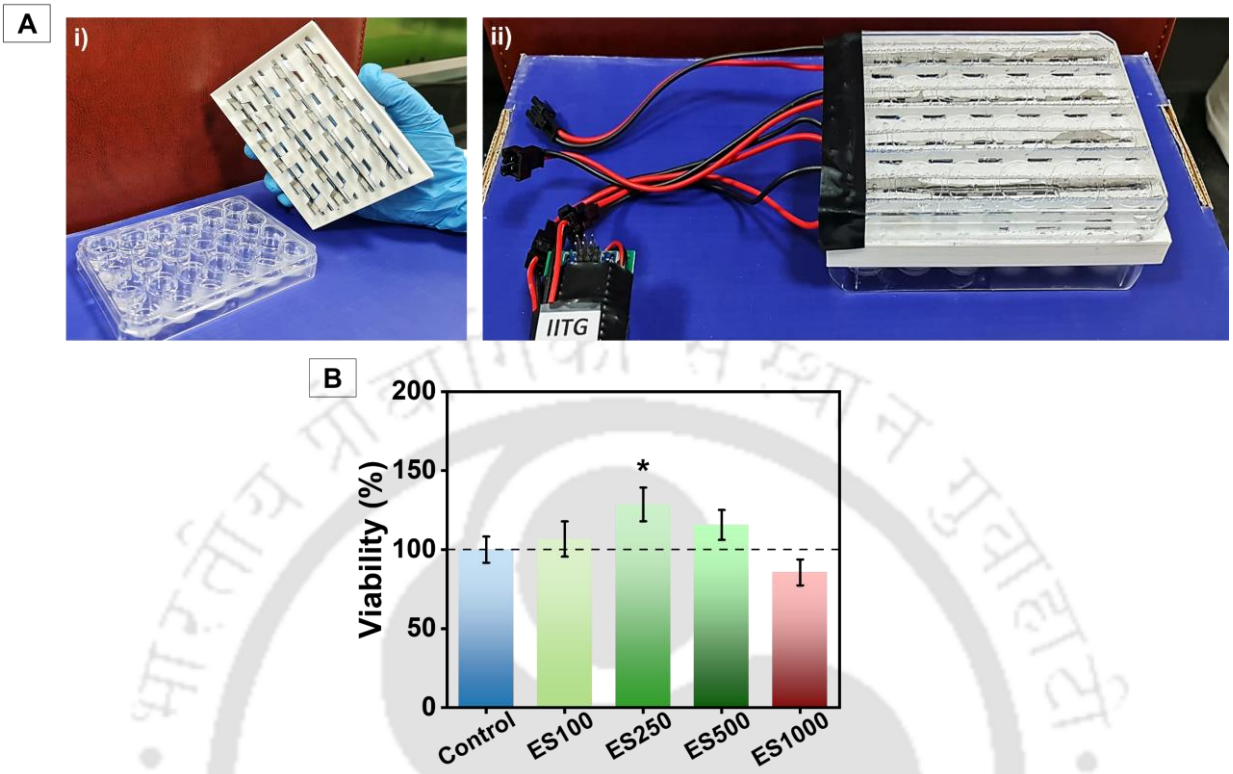


***Figure A4.4.*** *(A) In-house-developed 3D printed electro-stimulator with precisely placed stainless steel electrodes for cell culture. (B) Quantification of viability of HDF cultured in presence of pulsed ES after 72 h through MTT assay. (ES100: 100 mV/mm, 250 ms, 2Hz; ES250: 250 mV/mm, 250 ms, 2Hz; ES500: 500 mV/mm, 250 ms, 2Hz; and ES1000: 1000 mV/mm, 250 ms, 2Hz). Mean ± SD; * P < 0.05.*

**Table A4.1.** Details of proteins of interaction network built using STRING

| **Input** | |
|---|---|
| **COL1A1** | Collagen alpha-1(I) chain; Type I collagen is a member of group I collagen (fibrillar forming collagen). (1464 aa) |
| **EGF** | Pro- epidermal growth factor; EGF stimulates the growth of various epidermal and epithelial tissues in vivo and in vitro and of some fibroblasts in cell culture. Magnesiotropic hormone that stimulates magnesium reabsorption in the renal distal convoluted tubule via engagement of EGFR and activation of the magnesium channel TRPM6. Can induce neurite outgrowth in motoneurons of the pond snail Lymnaea stagnalis in vitro. (1207 aa) |
| **MKI67** | Proliferation marker protein Ki-67; Required to maintain individual mitotic chromosomes dispersed in the cytoplasm following nuclear envelope disassembly. |

| | |
|---|---|
| | Associates with the surface of the mitotic chromosome, the perichromosomal layer, and covers a substantial fraction of the chromosome surface. Prevents chromosomes from collapsing into a single chromatin mass by forming a steric and electrostatic charge barrier: the protein has a high net electrical charge and acts as a surfactant, dispersing chromosomes and enabling independent chromosome motility. (3256 aa) |
| **FGF2** | Fibroblast growth factor 2; Acts as a ligand for FGFR1, FGFR2, FGFR3 and FGFR4. Also acts as an integrin ligand which is required for FGF2 signaling. Binds to integrin ITGAV:ITGB3. Plays an important role in the regulation of cell survival, cell division, cell differentiation and cell migration. Functions as a potent mitogen in vitro. Can induce angiogenesis. (288 aa) |
| **TGFB1** | Transforming growth factor beta-1 proprotein; Transforming growth factor beta-1 proprotein: Precursor of the Latency-associated peptide and Transforming growth factor beta-1 (TGF-beta-1) chains, which constitute the regulatory and active subunit of TGF-beta-1, respectively. Transforming growth factor beta-1: Multifunctional protein that regulates the growth and differentiation of various cell types and is involved in various processes, such as normal development, immune function, microglia function and responses to neurodegeneration (By similarity). (390 aa) |
| **FN1** | Fibronectin; Fibronectins bind cell surfaces and various compounds including collagen, fibrin, heparin, DNA, and actin. Fibronectins are involved in cell adhesion, cell motility, opsonization, wound healing, and maintenance of cell shape. Involved in osteoblast compaction through the fibronectin fibrillogenesis cell-mediated matrix assembly process, essential for osteoblast mineralization. Participates in the regulation of type I collagen deposition by osteoblasts. (2477 aa) |
| **VIM** | Vimentin; Vimentins are class-III intermediate filaments found in various non-epithelial cells, especially mesenchymal cells. Vimentin is attached to the nucleus, endoplasmic reticulum, and mitochondria, either laterally or terminally. (466 aa) |
| **Predicted Functional Partners** | **Score** |
| **SDC4** | Syndecan-4; Cell surface proteoglycan that bears heparan sulfate. Regulates exosome biogenesis in concert with SDCBP and PDCD6IP. 0.999 |

| | | |
|---|---|---|
| **PDGFA** | Platelet- derived growth factor subunit A; Growth factor that plays an essential role in the regulation of embryonic development, cell proliferation, cell migration, survival and chemotaxis. Potent mitogen for cells of mesenchymal origin. Required for normal lung alveolar septum formation during embryogenesis, normal development of the gastrointestinal tract, normal development of Leydig cells and spermatogenesis. Required for normal oligodendrocyte development and normal myelination in the spinal cord and cerebellum. | 0.950 |
| **NID1** | Nidogen-1; Sulfated glycoprotein widely distributed in basement membranes and tightly associated with laminin. Also binds to collagen IV and perlecan. It probably has a role in cell-extracellular matrix interactions. | 0.997 |
| **DCN** | Decorin; May affect the rate of fibrils formation. | 0.999 |
| **HSPG2** | Basement membrane-specific heparan sulfate proteoglycan core protein; Integral component of basement membranes. Component of the glomerular basement membrane (GBM), responsible for the fixed negative electrostatic membrane charge, and which provides a barrier which is both size- and charge-selective. It serves as an attachment substrate for cells. Plays essential roles in vascularization. Critical for normal heart development and for regulating the vascular response to injury. | 0.998 |
| **CCN2** | CCN family member 2; Major connective tissue mitoattractant secreted by vascular endothelial cells. Promotes proliferation and differentiation of chondrocytes. Mediates heparin- and divalent cation-dependent cell adhesion in many cell types including fibroblasts, myofibroblasts, endothelial and epithelial cells. Enhances fibroblast growth factor-induced DNA synthesis; Belongs to the CCN family. | 0.969 |
| **PDGFB** | Platelet- derived growth factor subunit B; Growth factor that plays an essential role in the regulation of embryonic development, cell proliferation, cell migration, survival and chemotaxis. Potent mitogen for cells of mesenchymal origin. Required for normal proliferation and | 0.955 |

| | | |
|---|---|---|
| | recruitment of pericytes and vascular smooth muscle cells in the central nervous system, skin, lung, heart and placenta. Required for normal blood vessel development, and for normal development of kidney glomeruli. Plays an important role in wound healing. | |
| **SPARC** | SPARC; Appears to regulate cell growth through interactions with the extracellular matrix and cytokines. Binds calcium and copper, several types of collagen, albumin, thrombospondin, PDGF and cell membranes. There are two calcium binding sites; an acidic domain that binds 5 to 8 $Ca^{(2+)}$ with a low affinity and an EF-hand loop that binds a Ca(2+) ion with a high affinity. | 0.969 |
| **SDC3** | Syndecan-3; Cell surface proteoglycan that may bear heparan sulfate (By similarity). May have a role in the organization of cell shape by affecting the actin cytoskeleton, possibly by transferring signals from the cell surface in a sugar-dependent mechanism. | 0.867 |
| **TIMP1** | Metalloproteinase inhibitor 1; Metalloproteinase inhibitor that functions by forming one to one complex with target metalloproteinases, such as collagenases, and irreversibly inactivates them by binding to their catalytic zinc cofactor. Acts on MMP1, MMP2, MMP3, MMP7, MMP8, MMP9, MMP10, MMP11, MMP12, MMP13 and MMP16. Does not act on MMP14. Also functions as a growth factor that regulates cell differentiation, migration and cell death and activates cellular signaling cascades via CD63 and ITGB1. Plays a role in integrin signaling. | 0.954 |

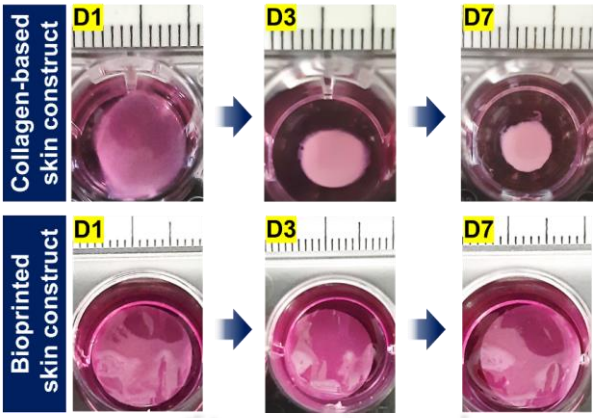


***Figure A5.1***. *Photographic images of collagen-based and bioprinted skin constructs, showing contraction in collagen-based construct, but the bioprinted construct maintained its shape consistently throughout the culture period.*

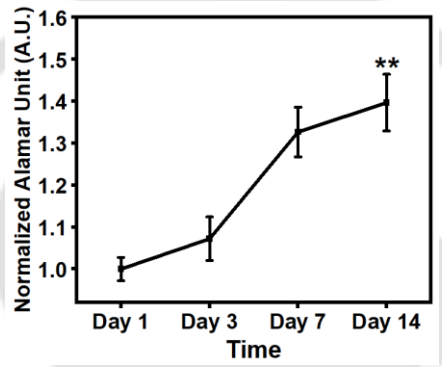


***Figure A5.2.*** *Cellular proliferation assessment of the HUVEC cultured in SGP using the Alamar blue assay. Data are represented as mean ± SD, where **p ≤ 0.01, compared to day 1.*

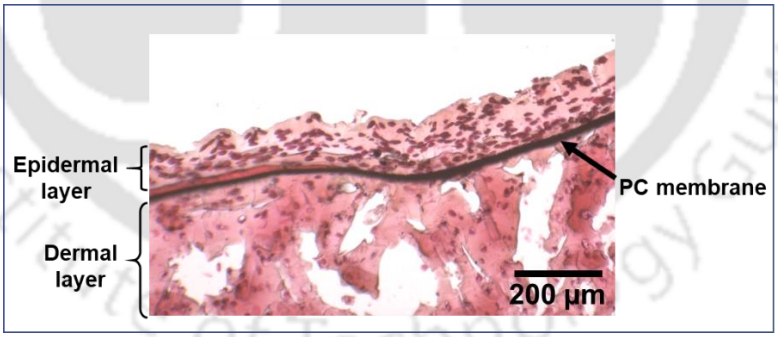


***Figure A5.3.*** *H&E stained image of printed skin model showing interface between keratinocyte and fibroblast layers.*

**Table A5.1.** Details of genes of the network obtained from GeneMANIA

| Sl no. | Gene | Functions (as described in NCBI) | Score | Description link |
|---|---|---|---|---|
| 1. | COL1A1 | It encodes pro-α1 chains of type I collagen, which form a triple helix consisting of two α1 chains and one α2 chain. Type I collagen is a fibril-forming collagen that is present in most connective tissues and is abundant in skin, bone, cornea, and tendon. | 0.896567 | http://www.ncbi.nlm.nih.gov/sites/entrez?db=gene&cmd=search&term=1277 |
| 2. | COL3A1 | It encodes pro-α1 chains of type III collagen, which is a fibrillar collagen typically found in extensible connective tissues such as skin, lung, intestine, vascular system, and uterus, often in conjunction with type I collagen. | 0.896376 | http://www.ncbi.nlm.nih.gov/sites/entrez?db=gene&cmd=search&term=1281 |
| 3. | EGF | It encodes a member of the epidermal growth factor (EGF) superfamily. The encoded preproprotein undergoes proteolytic processing to produce the 53-amino acid epidermal growth factor peptide. This protein functions as a potent mitogenic factor, playing a crucial role in the growth, proliferation, and differentiation of various cell types. Its mechanism of action involves high-affinity binding to the cell surface receptor, EGFR (epidermal growth factor receptor). | 0.886304 | http://www.ncbi.nlm.nih.gov/sites/entrez?db=gene&cmd=search&term=1950 |
| 4. | FN1 | It encodes fibronectin, a glycoprotein that is found in a soluble dimeric form in blood plasma, and in a dimeric or multimeric form at the cell surface and in ECM. The encoded preproprotein undergoes proteolytic processing to yield the mature protein. | 0.868767 | http://www.ncbi.nlm.nih.gov/sites/entrez?db=gene&cmd=search&term=2335 |
| 5. | KRT10 | It encodes cytokeratin-10 (CK-10) or keratin-10 (K10) protein belonging to the type I (acidic) cytokeratin family, which is part of the superfamily of intermediate filament (IF) proteins. Keratins are structural proteins that form heteropolymeric intermediate filaments, constituting a significant component of the cytoskeleton alongside actin microfilaments and microtubules in epithelial cells. | 0.92634 | http://www.ncbi.nlm.nih.gov/sites/entrez?db=gene&cmd=search&term=3858 |
| 6. | KRT14 | It encodes cytokeratin-14 (CK-14) or keratin-14 (K14) protein, a type I keratin, the most diverse group of intermediate filaments. The gene product typically forms a heterotetramer with two keratin 5 molecules, a type II keratin, collectively constituting the cytoskeleton of epithelial cells. | 0.900583 | http://www.ncbi.nlm.nih.gov/sites/entrez?db=gene&cmd=search&term=3861 |

| | | | | |
|---|---|---|---|---|
| 7. | ELN | It encodes the protein, elastin, primary component of elastic fibers, which comprise part of the ECM for providing elasticity to various organs and tissues including the skin, heart, lungs, ligaments, and blood vessels. The encoded protein is characterized by its abundance of hydrophobic amino acids like glycine and proline, forming flexible hydrophobic regions linked by crosslinks between lysine residues. | 0.933234 | http://www.ncbi.nlm.nih.gov/sites/entrez?db=gene&cmd=search&term=2006 |
| 8. | COL1A2 | It encodes pro-α2 chain of type I collagen, which, along with two α1 chains, forms the triple helix characteristic of this fibril-forming collagen. Type I collagen is prevalent in various connective tissues, notably bone, skin, cornea, and tendon. | 0.005626 | http://www.ncbi.nlm.nih.gov/sites/entrez?db=gene&cmd=search&term=1278 |
| 9. | LRIG1 | The encoded protein is rredicted to act upstream of or within various processes, such as innervation, otolith morphogenesis; and sensory perception of sound. Additionally, it is predicted to be located in the plasma membrane and to be active in the ECM and extracellular space. | 0.003928 | http://www.ncbi.nlm.nih.gov/sites/entrez?db=gene&cmd=search&term=26018 |
| 10. | SPARC | It encodes a cysteine-rich acidic matrix-associated protein. It plays a crucial role in the calcification of bone collagen, while also contributing to ECM synthesis and the regulation of cell shape changes. | 0.003927 | http://www.ncbi.nlm.nih.gov/sites/entrez?db=gene&cmd=search&term=6678 |
| 11. | KRT5 | The encoded protein is part of the keratin gene family. It belongs to the type II cytokeratins, which are basic or neutral proteins found in pairs of heterotypic keratin chains expressed during the differentiation of simple and stratified epithelial tissues. Specifically, this type II cytokeratin is expressed in the basal layer of the epidermis where it coexists with KRT14. | 0.003586 | http://www.ncbi.nlm.nih.gov/sites/entrez?db=gene&cmd=search&term=3852 |
| 12. | NID2 | It encodes a member of the nidogen family of basement membrane proteins. It functions as a cell-adhesion protein, binding to collagens I and IV as well as laminin, and is thought to play a role in maintaining the structure of the basement membrane. | 0.002609 | http://www.ncbi.nlm.nih.gov/sites/entrez?db=gene&cmd=search&term=22795 |
| 13. | ADAM8 | It encodes a member of the ADAM (a disintegrin and metalloprotease domain) family, which consists of membrane-anchored proteins structurally related to snake venom disintegrins. These proteins have been implicated in various biological processes involving cell-cell and cell-matrix interactions. | 0.00259 | http://www.ncbi.nlm.nih.gov/sites/entrez?db=gene&cmd=search&term=101 |

| | | | | |
|---|---|---|---|---|
| 14. | LOX | It encodes protein which belongs to the lysyl oxidase family of proteins and undergoes alternative splicing to produce multiple transcript variants. One of these variants encodes a preproprotein that IS proteolytic processed to yield a regulatory propeptide and the mature enzyme. This enzyme exhibits copper-dependent amine oxidase activity, crucial for the crosslinking of collagens and elastin. | 0.002577 | http://www.ncbi.nlm.nih.gov/sites/entrez?db=gene&cmd=search&term=4015 |
| 15. | ADGRG1 | It encodes a member of the G protein-coupled receptor family and plays a role in regulating brain cortical patterning. It specifically binds to transglutaminase 2, which is a component of tissue and tumor stroma known to inhibit tumor progression. | 0.002542 | http://www.ncbi.nlm.nih.gov/sites/entrez?db=gene&cmd=search&term=9289 |
| 16. | ADAM12 | It encodes a member of a family of proteins, structurally related to snake venom disintegrins and playing roles in various biological processes like fertilization, neurogenesis and muscle development through cell-cell and cell-matrix interactions. | 0.00237 | http://www.ncbi.nlm.nih.gov/sites/entrez?db=gene&cmd=search&term=8038 |
| 17. | FBLN1 | It encodes Fibulin 1, a secreted glycoprotein that integrates into the fibrillar ECM. Calcium-binding is essential for its interaction with laminin and nidogen, while it also facilitates platelet adhesion by binding fibrinogen. | 0.002232 | http://www.ncbi.nlm.nih.gov/sites/entrez?db=gene&cmd=search&term=2192 |
| 18. | HGF | It encodes a protein crucial for regulating cell growth, motility, and morphogenesis across various cell and tissue types by binding to the hepatocyte growth factor receptor. This protein functions as a multifunctional cytokine primarily affecting epithelial cells and is implicated in processes like angiogenesis, tumorogenesis, and tissue regeneration. | 0.002202 | http://www.ncbi.nlm.nih.gov/sites/entrez?db=gene&cmd=search&term=3082 |
| 19. | COL6A3 | It encodes the α-3 chain, one of the three α chains of type VI collagen, present in most of connective tissues. Notably, the α-3 chain of type VI collagen exhibits a much larger size compared to the α-1 and -2 chains, primarily attributed to a greater number of subdomains. These domains are known to interact with ECM proteins, highlighting the significance of this protein in organizing matrix components. | 0.002161 | http://www.ncbi.nlm.nih.gov/sites/entrez?db=gene&cmd=search&term=1293 |
| 20. | DDR1 | The encoded protein belongs to a subfamily of tyrosine kinase receptors, which play a crucial role in mediating cellular communication with the microenvironment. These kinases are pivotal | 0.002108 | http://www.ncbi.nlm.nih.gov/sites/entrez?db=gene&cmd=search&term=780 |

| | | | | |
|---|---|---|---|---|
| | | in regulating cell growth, differentiation, and metabolism. | | |
| 21. | EGFR | It encodes a transmembrane glycoprotein, a member of the protein kinase superfamily. It serves as a receptor for members of the EGF family, facilitating cell surface binding to epidermal growth factor. This interaction induces receptor dimerization and subsequent tyrosine autophosphorylation, ultimately promoting cell proliferation. | 0.002081 | http://www.ncbi.nlm.nih.gov/sites/entrez?db=gene&cmd=search&term=1956 |
| 22. | COL5A2 | It encodes an α chain for one of the low abundance fibrillar collagens. Type V collagen is typically found in tissues that also contain type I collagen and plays a role in mediating the assembly of heterotypic fibers composed of both type I and type V collagen. | 0.00201 | http://www.ncbi.nlm.nih.gov/sites/entrez?db=gene&cmd=search&term=1290 |
| 23. | PKP1 | It encodes a member of the arm-repeat (armadillo) and plakophilin gene families. Proteins belonging to the plakophilin family contain multiple armadillo repeats, localize to cell desmosomes and nuclei, and contribute in linking cadherins to intermediate filaments in the cytoskeleton. | 0.001976 | http://www.ncbi.nlm.nih.gov/sites/entrez?db=gene&cmd=search&term=5317 |
| 24. | FBLN5 | It encodes a secreted ECM protein that contains an Arg-Gly-Asp (RGD) motif and calcium-binding EGF-like domains. It facilitates endothelial cell adhesion by interacting with integrins through the RGD motif. While prominently expressed in developing arteries, its expression is less prominent in adult vessels. | 0.001937 | http://www.ncbi.nlm.nih.gov/sites/entrez?db=gene&cmd=search&term=10516 |
| 25. | KRT16 | It encodes a member of the keratin gene family, which are intermediate filament proteins vital for the structural integrity of epithelial cells. This particular keratin is coexpressed with keratin 14 in various epithelial tissues | 0.001841 | http://www.ncbi.nlm.nih.gov/sites/entrez?db=gene&cmd=search&term=3868 |
| 26. | TRADD | It encodes a death domain containing adaptor molecule which interacts with TNFRSF1A/TNFR1 and regulates programmed cell death signaling and activation of NF- κB. | 0.001767 | http://www.ncbi.nlm.nih.gov/sites/entrez?db=gene&cmd=search&term=8717 |
| 27. | FBLN2 | It encodes an ECM protein, a member of the fibulin family, known to bind various extracellular ligands and calcium. It is implicated in organ development, such as in the differentiation of heart, neuronal, and skeletal. | 0.00174 | http://www.ncbi.nlm.nih.gov/sites/entrez?db=gene&cmd=search&term=2199 |

# *List of Publications, Presentations and Achievements*

**Publications from Ph.D. Thesis**

**A. Journal Publications:**

1. **Bibrita Bhar**, Rajan Singh, Vaishak Gowda, Souradeep Dey, Samit K. Nandi, Roy Paily and Biman B. Mandal. "Wearable e-Bandage with Antimicrobial Ionogel as an Integrated Electroceutical Device for Accelerated Wound Healing." *ACS Materials Letters.* 2024; 3453-3461.
2. **Bibrita Bhar**, Eshani Das, Kodieswaran Manikumar, and Biman B. Mandal. "3D Bioprinted Human Skin Model Recapitulating Native-like Tissue Maturation and Immunocompetence as an Advanced Platform for Skin Sensitization Assessment." *Advanced Healthcare Materials*. 2024:2303312.
3. **Bibrita Bhar**, Priyanka Ranta, Pavan Kumar Samudrala, and Biman B. Mandal. "Omentum Extracellular Matrix-Silk Fibroin Hydroscaffold Promotes Wound Healing through Vascularization and Tissue Remodeling in the Diabetic Rat Model." *ACS Biomaterials Science & Engineering.* 2024;10(2):1090–105.
4. **Bibrita Bhar**, Bijayashree Chakraborty, Samit K Nandi, and Biman B Mandal. "Silk-Based Phyto-Hydrogel Formulation Expedites Key Events of Wound Healing in Full-Thickness Skin Defect Model." *International Journal of Biological Macromolecules.* 2022; 203: 623-37.
5. **Bibrita Bhar**, Dimple Chouhan, Nakhul Pai, and Biman B Mandal. "Harnessing Multifaceted Next-Generation Technologies for Improved Skin Wound Healing." *ACS Applied Bio Materials*. 2021;4(11):7738-63.

**B. Patents:**

1. Biman B. Mandal, **Bibrita Bhar**, Roy P. Paily, Rajan Singh. ***Wearable Electrotherapeutic Device for Wound Healing.*** Indian Patent Application No. 202431027630.
2. Biman B. Mandal and **Bibrita Bhar**. ***Silk-based 3D bioprinted skin model for in vitro screening applications.*** Indian Patent Application No. 202431102555.

**C. Conference Publications:**

1. **Bibrita Bhar**, Biman B Mandal. "Rapid Prototyping Of Silk-based Bioprinted Immunocompetent Skin Model: An Advanced Pre-clinical Platform For Skin Sensitization Assessments." *Tissue Engineering Part A.* 2024.
2. **Bibrita Bhar**, Eshani Das, Kodieswaran Manikumar, Ashutosh Bandyopadhyay, Biman B Mandal. "Silk based 3D printed human skin model for high-throughput screening of topical formulations." *Tissue Engineering Part A.* 2023;29.

**D. Conference, Seminar, Workshop Participation/Presentations:**

1. **Bibrita Bhar**, Biman B Mandal. "Rapid Prototyping Of Silk-based Bioprinted Immunocompetent Skin Model: An Advanced Pre-clinical Platform For Skin Sensitization Assessments", **Poster** presentation at *TERMIS-World Congress* 2024, organized by Tissue Engineering and Regenerative Medicine International Society (TERMIS), June 25-28 2024.

2. **Bibrita Bhar**, Eshani Das, Kodieswaran Manikumar, and Biman B. Mandal, "Development of pre-clinical 3D bioprinted full-thickness skin model for screening of sensitization effects of topical formulations", **Oral** presentation at *BioRemedi 2022* organized by Tissue Engineering

and Regenerative Medicine India (STERMI) and Society for Biomaterials & Artificial Organs India (SBAOI), Dec 15-18, 2022. (**Best oral presentation for *In vitro* models**)

3. **Bibrita Bhar**, Rajan Singh, Souradeep Dey, Janani G, Roy P. Paily, and Biman B. Mandal, "Affordable Electronic Smart Bandage for Accelerated Wound Healing". **Poster** presentation at *Innovation & Entrepreneurship Conclave (IEC)* 2022 organized by IITG Research park, April 20, 2022.

4. **Bibrita Bhar**, Biman B. Mandal, "Exploring regenerative potential of composite hydroscaffold of silk fibroin and omentum tissue derived extracellular matrix for diabetic wound healing". **Oral** presentation at *3rd National Biomedical Research Competition* 2021 organized by Society of Young Biomedical Scientists, India, Dec 6-10, 2021.

5. **Bibrita Bhar**, Biman B. Mandal, "Functionalized Silk-based Topical Gel with Aloe Extract Facilitates Wound Healing via Modulation of Inflammation and Tissue Remodeling". **Oral** presentation at *International Conference on Advanced Materials for Better Tomorrow (AMBT)* 2021 organized by Indian Institute of Technology (BHU) Varanasi in association with SIRMB, Jul 13-17, 2021.

6. **Bibrita Bhar**, Bijayashree Chakraborty, Samit K Nandi, and Biman B. Mandal, "Development of a Silk-based Composite Hydrogel Functionalized with Bioactive Molecules for Potential Wound Healing Applications". **Oral** presentation at *International e Symposium on Smart Polymers: Application in Current Scenario (SPACS)* 2021 organized by Asian Polymer Association (APA) in association with Amity Institute of Applied Science, Jan 15-16, 2021. (**Best Flash Talk Presentation**)

7. **Bibrita Bhar**, Dimple Chouhan, and Biman B. Mandal, "Silk-based Natural Formulation for Wound Healing and Skin Regeneration". **Poster** presented at *International Conference on Smart Materials for Sustainable Technology* 2020 organized by Society for interdisciplinary Research in Materials and Biology (SIRMB) in association with IIT BHU, Feb 22-25, 2020.

8. **Bibrita Bhar**, Dimple Chouhan, and Biman B. Mandal, "Harnessing regenerative properties of naturally derived silk biomaterials to develop smart wound care matrices". **Poster** presented at *Research Conclave* 2019 organized by Indian Institute of Technology Guwahati, Mar 14-17, 2019.

**Selected Awards & Achievements**

1. **TERMIS-AP SYIS Award 2024** from Student and Young Investigator Section (SYIS), Tissue Engineering and Regenerative Medicine International Society (TERMIS).

2. **DST-SERB Travel Award 2024** to attend the 7$^{th}$ TERMIS World Congress 2024 in Seattle, USA, scheduled from June 25$^{th}$ to 28$^{th}$, 2024.

3. **New Generation Innovation and Entrepreneurship Development Centre (Newgen-IEDC) Student project grant** awarded for project titled, "*In vitro 3D skin model for high throughput drug screening applications*", (Grant of Rs. 2,50,000), 2022-2023.

4. **Best oral presentation** for *In vitro* models on "*Development of pre-clinical 3D bioprinted full-thickness skin model for screening of sensitization effects of topical formulations*", in

International Conference, BioRemedi 2022 organized by Tissue Engineering and Regenerative Medicine India (STERMI) and Society for Biomaterials & Artificial Organs India (SBAOI), Dec 15-18, 2022.

5. **Best Flash talk Presentation** on "*Development of a Silk-based Composite Hydrogel Functionalized with Bioactive Molecules for Potential Wound Healing Applications*" in International e Symposium on Smart Polymers: Application in Current Scenario (SPACS) 2021 organized by Asian Polymer Association (APA) in association with Amity Institute of Applied Science, Jan 15-16, 2021.

6. **New Generation Innovation and Entrepreneurship Development Centre (Newgen-IEDC) Student project grant** awarded for project titled**,** *"Affordable Electronic Smart Bandage for Accelerated Wound Healing"*, (Grant of Rs. 2,50,000), 2020-2021.

**Publications from Other Collaborative Research Projects**

**A. Journal Publications:**

1. Nandana Bhardwaj, Souradeep Dey, **Bibrita Bhar**, and Biman Mandal. "Bioprinted in vitro tissue models: An emerging platform for developing therapeutic interventions and disease modeling." *Progress in Biomedical Engineering.* 2023;6(1):012003.
2. Santanu Mandal, Anyam VVNGSV Kishore, Sumantra Mandal, **Bibrita Bhar**, Biman B Mandal, Samit Kumar Nandi, and Mangal Roy. "Controlled Nano Cu Precipitation through Age Treatment: A Method to Enhance the Biodegradation, Mechanical, Antimicrobial Properties and Biocompatibility of Fe-20mn-3cu Alloys." *Acta Biomaterialia*. 2023; 168:650-69.
3. Souradeep Dey, Chitra Jaiswal, Sayanti Shome, **Bibrita Bhar**, Ashutosh Bandyopadhyay, Kodieswaran Manikumar, Rajat Dadheech, Biman B Mandal. "Photocrosslinkable silk-based biomaterials for regenerative medicine and healthcare applications." *Regenerative Engineering and Translational Medicine*. 2023; 9(2):181-201.
4. Nobomi Borah, Muzamil Ahmad Rather, **Bibrita Bhar**, Biman B Mandal, Manabendra Mandal, Niranjan Karak. "A robust epoxy nanocomposite with iron oxide decorated cellulose nanofiber as a sustained drug delivery vehicle for antibacterial drugs." *New Journal of Chemistry*. 2023; 47(43): 20010-20025.

**B. Book chapter:**

1. Yogendra Pratap Singh, Joseph Christakiran Moses, Ashutosh Bandyopadhyay, **Bibrita Bhar,** Bhaskar Birru, Nandana Bhardwaj, and Biman B. Mandal. "State-of-the-art strategies and future interventions in bone and cartilage repair for personalized regenerative therapy: Regenerated Organs." *Academic press;* 2021. p. 203-48.

**C. Conference Publications:**

1. Ashutosh Bandyopadhyay, **Bibrita Bhar**, Biman B Mandal. "Evaluating Ultrasound Augmented Healing Potential of Autologous Growth Factor Loaded 3d Printed Photopolymerized Silk-based Constructs for Meniscus Tears". *Tissue Engineering Part A.* 2024.
2. Souradeep Dey, Pragya Mehra, Chitra Jaiswal, **Bibrita Bhar**, Biman B Mandal. "3D Bioprinted Microphysiological In Vitro Osteochondral Model to Study Osteoarthritic Niche." *Tissue Engineering Part A.* 2024.